

Biochemical characterisation of Parkinson's disease models

Haya Alrashidi

Great Ormond Street Institute of Child Health

University College London

This thesis is submitted for the degree of Doctor of Philosophy (PhD) awarded by

University College London

Funded by Kuwait University, Kuwait.

Declaration

I, Haya Alrashidi, confirm that the work presented in this thesis is my own. Where information has been derived from other sources, I confirm that this has been indicated in the thesis. Some ideas and figures have been previously published in the following publications (see Publications):

- ❖ Alrashidi H, Eaton S, Heales S. Biochemical characterization of proliferative and differentiated SH-SY5Y cell line as a model for Parkinson's disease. *Neurochem Int.* 2021 May;145:105009. doi: 10.1016/j.neuint.2021.105009. Epub 2021 Mar 5. PMID: 33684546.
- ❖ Rossignoli G, Krämer K, Lugarà E, Alrashidi H, Pope S, De La Fuente Barrigon C, Barwick K, Bisello G, Ng J, Counsell J, Lignani G, Heales SJR, Bertoldi M, Barral S, Kurian MA. Aromatic l-amino acid decarboxylase deficiency: a patient-derived neuronal model for precision therapies. *Brain.* 2021 Sep 4;144(8):2443-2456. doi: 10.1093/brain/awab123. PMID: 33734312; PMCID: PMC8418346.

Signed.....

Date

*For the 18-year-old girl,
who sat on a park bench one afternoon,
and dreamt this into reality.*

Abstract

Parkinson's disease (PD) is the second most common neurodegenerative disorder. The exact molecular mechanism of disease remains unclear. Several factors are proposed to play part including, but not limited to, decreased activity of mitochondrial complex I and lysosomal glucocerebrosidase enzymes and disrupted cellular antioxidant defence and lysosomal acidification. In addition, there is growing support for a role of organelle crosstalk between mitochondria and lysosome, the disruption of which is proposed to play part in PD pathology. The nature and consequence of this crosstalk remains unclear. The SH-SY5Y neuronal cell line model is commonly used to investigate PD mechanisms and potential therapeutics. However, functional analysis of the suitability of the cell line in its proliferative state or the necessity for differentiation remains unclear. Furthermore, iPSC-derived dopaminergic neurons are another commonly used model for PD and related diseases however, validating their functional dopamine metabolism is important to determine disease mechanism and test potential therapeutics. In this thesis, a host of biochemical tools, including HPLC measurement of neurotransmitter metabolites and enzyme activity assays, were used to elucidate the aforementioned ambiguities. The findings demonstrate that although there are similarities between proliferative and differentiated phenotypes of SH-SY5Y cells, there are also significant differences. Notably, the rate of dopamine turnover and the activity of lysosomal glucocerebrosidase were significantly higher in differentiated SH-SY5Y cells. In contrast, mitochondrial electron transport chain complexes' activities were similar between the two phenotypes, despite a significant difference in mitochondrial content. Therefore, care should be taken when choosing either phenotype as a PD model. In addition,

the findings demonstrate that inhibition of either mitochondrial complex I or lysosomal glucocerebrosidase affect both the ratio of pro-cathepsin D/cathepsin D protein expression and enzyme activity. Cathepsin D is one of the most ubiquitous lysosomal enzymes, the state of which can be used as reflection of the degree of lysosomal acidification. This shines a light on the potential involvement of both lysosomal glucocerebrosidase and mitochondrial complex I in maintenance of lysosomal acidification. This could be a consequence of a more dynamic crosstalk between mitochondria and lysosomes than previously thought. Moreover, the work presented provides a method for validation of the dysfunctional dopamine metabolism in iPSC derived dopaminergic neuronal disease models for aromatic amino acid decarboxylase deficiency and PD patients carrying mutations in *PINK1*. In addition, it provides a proof of concept for the effectiveness of both lentivirus-based gene therapy and levodopa treatment to restore dopamine metabolism in aromatic amino acid decarboxylase deficiency.

Impact statement

Parkinson's disease (PD) is the second most common neurodegenerative disorder, estimated to affect about 1% of people over the age of 60. With the increase in life expectancy, PD prevalence is projected to increase by 50% by 2030. It is a progressive and life debilitating disease that mainly result from death of brain nerve cells that control movement. The cause of the cell death remains unclear. Currently, there is no cure for PD and available therapies only alleviate the symptoms. Cellular disease models are a great asset in understanding how diseases arise and in investigation of potential therapies. This is especially true for neurodegenerative disorders, such as PD, where direct examination of the pathological process is not possible. Such preclinical studies form the foundation of clinical trials through which rigorous examination of therapies take place, ultimately leading to a cure. However, the choice of disease models is a difficult process that requires careful evaluation of the model to determine its suitability. Two of the most commonly used models in PD research are the neuronal cell line, SH-SY5Y, and human induced pluripotent stem cell (iPSC)-derived dopaminergic neurons. Despite their common use, functional validation of their suitability is lacking in the literature, specifically with regards to dopamine metabolism. Therefore, the aim of this thesis was to undertake a careful biochemical characterisation and comparison of the key pathways affected in PD in proliferative and differentiated phenotypes of SH-SY5Y cells to determine their suitability as a dopaminergic neuronal model for PD. The findings in this thesis help guide future scientific research into the choice of phenotype to be used in fundamental research of PD and related diseases. This thesis also demonstrates a method for functional validation of disease phenotype in iPSC derived

dopaminergic neurons generated from patients with PD and primary monoamine disorders affecting the dopamine system, through analysis of dopamine metabolism. It allows assessment of the benefit of experimental therapies on disease modification through a translational precision medicine approach, which is a promising area in the healthcare sector.

Contents

Declaration.....	2
Abstract.....	3
Impact statement.....	6
List of figures:.....	17
List of tables:.....	21
List of abbreviations:.....	22
Declaration of collaborations.....	25
Acknowledgement.....	26
Chapter 1. Introduction.....	28
1.1. Parkinson’s disease:.....	29
1.2. Dopamine:.....	34
1.2.1. Dopamine metabolism:.....	35
1.2.2. Enzymes of the dopamine pathway:.....	39
1.2.3. Dopamine toxicity:.....	44
1.3. Serotonin:.....	48
1.4. Molecular mechanisms of Parkinson’s Disease.....	50
1.4.1. Mitochondria.....	50
1.4.1.1. Mitochondrial citric acid cycle.....	52

1.4.1.2. Mitochondrial electron transport chain.....	55
1.4.1.3. Mitochondrial impairment in PD.....	60
1.4.2. Lysosomes:.....	66
1.4.2.1. Lysosomal impairment in PD.....	71
1.4.3. Glutathione.....	74
1.5. Mitochondrial-lysosomal crosstalk	80
1.5.1. Impact of mitochondrial dysfunction on lysosomes	83
1.5.2. Impact of lysosomal dysfunction on mitochondria	86
1.5.3. Mechanisms of mitochondrial and lysosomal crosstalk.....	87
1.6. SH-SY5Y cells in Parkinson’s research	88
1.7. Induced pluripotent stem cell neurons in Parkinson’s research:	93
1.8. Hypotheses	95
1.9. Aims.....	96
Chapter 2. Materials and Methods.....	97
2.1. Materials.....	98
2.2. Cell culture.....	100
2.2.1. Cell storage and recovery:	100
2.2.2. L-DOPA treatment	101
2.3. SH-SY5Y cell differentiation	102
2.3.1. Differentiation protocol:.....	103

2.4. Sample preparation.....	105
2.4.1. Bradford protein assay, western blot, and enzyme assays:.....	105
2.4.2. HPLC-ED sample preparation:	105
2.4.2.1. Extracellular metabolites:.....	105
2.4.2.2. Intracellular metabolites:	105
2.4.3. Glutathione:	106
2.5. Bradford assay:.....	107
2.6. Western blot for protein expression	109
2.7. Enzyme assays:.....	113
2.7.1. Citrate synthase assay:	113
2.7.2. Mitochondrial NADH-Ubiquinone oxidoreductase (Complex I):.....	116
2.7.3. Mitochondrial succinate dehydrogenase-cytochrome c reductase (complex II-III):.....	120
2.7.4. Mitochondrial cytochrome c oxidase (complex IV):	123
2.7.5. Lysosomal glucocerebrosidase (GBA):.....	126
2.8. Measurement of glutathione using HPLC-ED:	130
2.8.1. Equipment:.....	130
2.8.2. Method:	130
2.9. Statistical Analysis	134

Chapter 3. Development of a High-Performance Liquid Chromatography Method for Measurement of Dopamine and Serotonin Metabolites 135

3.1. Introduction..... 136

3.2. Method development:..... 140

3.2.1. Equipment: 140

3.2.2. Method conditions: 142

3.2.3. Method optimisation: 145

3.2.3.1. Cyclic voltammetry: 145

3.2.3.2. Calibration curve:..... 147

3.2.3.3. Metabolite temperature sensitivity: 149

3.2.3.4. Quality and accuracy of the method:..... 151

3.2.4. Identification and quantification of integrated peaks:..... 153

3.2.5. Internal standard: 157

Chapter 4. Biochemical Comparison Between Proliferative and Differentiated SH-SY5Y Cell Models for Parkinson’s Disease 162

4.1. Introduction..... 163

4.2. Materials and methods:..... 166

4.2.1. Cell culture..... 166

4.2.2. SH-SY5Y differentiation..... 166

4.2.3. Western blot for neuronal marker expression..... 166

4.2.4. L-DOPA treatment	166
4.2.5. Sample preparation	166
4.2.1. HPLC-ED analysis	166
4.2.2. Enzyme assays	166
4.2.3. GSH measurement	167
4.3. Results	168
4.3.1. Morphology	168
4.3.2. Expression of neuronal markers:	170
4.3.3. Extracellular and intracellular dopamine and serotonin metabolism	174
4.3.4. Mitochondrial ETC	179
4.3.5. Lysosomal glucocerebrosidase activity	181
4.3.6. Glutathione levels	183
4.4. Discussion	185

Chapter 5. Biochemical Effects of L-DOPA Treatment on Proliferative and

Differentiated SH-SY5Y Cells	192
5.1. Introduction	193
5.2. Materials and methods:	196
5.2.1. Cell culture	196
5.2.2. L-DOPA treatment	196
5.2.3. Sample preparation	196

5.2.4. Enzyme assays	196
5.2.5. GSH measurement.....	196
5.3. Results	197
5.3.1. Effect of L-DOPA treatment on mitochondrial ETC complex activity:	197
5.3.2. Lysosomal GBA enzyme activity.....	202
5.3.3. GSH levels	204
5.4. Discussion	208
Chapter 6. Cathepsin D as an Indicator of Lysosomal Acidification	211
6.1. Introduction.....	212
6.2. Materials and methods:.....	219
6.2.1. Materials:.....	219
6.2.2. Cell culture and differentiation:.....	219
6.2.3. Cell treatment:.....	219
6.2.3.1. Bafilomycin A1:	219
6.2.3.2. Conduritol B epoxide:	219
6.2.3.3. Rotenone:	220
6.2.4. Cathepsin D enzyme activity assay	220
6.2.5. Western blot for proCTSD and mCTSD:.....	222
6.3. Results:	223
6.3.1. Creating a pH calibration curve using LysoSensor dyes:	223

6.3.2. Choice of CTSD antibody:	227
6.3.3. Effect of baf on CTSD maturation and activity:.....	229
6.3.4. The effect of inhibition of lysosomal GBA on CTSD function	235
6.3.5. The effect of inhibition of mitochondrial complex I on CTSD function	239
6.4. Discussion:.....	242

Chapter 7. Investigation of Potential Therapies for Treatment of Aromatic Amino

Acid Decarboxylase deficiency	249
7.1. Introduction	250
7.2. Materials and methods:	254
7.2.1. Generation of iPSC-derived dopaminergic neuronal model for AADC: ...	254
7.2.2. Lentivirus gene rescue of AADC mutant iPSC derived dopaminergic neurons:	254
7.2.3. L-DOPA treatment and HPLC sample preparation:.....	255
7.2.4. HPLC-ED measurement of extracellular dopamine metabolites.....	255
7.3. Results.....	256
7.3.1. Confirmation of AADC deficiency phenotype	256
7.3.2. Lentivirus gene rescue of <i>DDC</i> gene	258
7.3.3. L-DOPA as potential therapy for AADC	261
7.4. Discussion.....	264

Chapter 8. Assessing Dopamine Metabolism in an iPSC Dopaminergic Neuronal

Model	267
8.1. Introduction.....	268
8.2. Methods	271
8.2.1. Generation of iPSC dopaminergic neuronal model.....	271
8.2.2. HPLC sample preparation	272
8.2.3. HPLC-ED analysis.....	272
8.3. Results	273
8.3.1. Comparison of basal dopamine metabolism between 3 and 4-weeks differentiated dopaminergic neurons:.....	273
8.3.2. Effect of L-DOPA stimulation on 3- and 4-week differentiated dopaminergic neurons:	275
8.3.3. Dopamine metabolism in iPSC dopaminergic neuronal model for PD:	280
8.4. Discussion:.....	287
 Chapter 9. General Discussion	 291
9.1. Discussion:.....	292
9.2. Conclusion:	307
9.3. Further work:.....	309
 Bibliography.....	 313
Publications	367

Abstracts 369

List of figures:

Figure 1 Dopamine and serotonin metabolic pathways. _____	37
Figure 2 Potential cellular toxicity of dopamine. _____	47
Figure 3 The citric acid cycle. _____	54
Figure 4 The mitochondrial electron transport chain. _____	59
Figure 5 Lysosomal v-ATPase mechanism of action. _____	70
Figure 6 Regulation of glutathione. _____	76
Figure 7 TFEB activation induces mitochondrial and lysosomal biogenesis. _____	82
Figure 9 Protein standard curve for Bradford assay. _____	108
Figure 10 Order of assembly of the Bio Rad Trans-Blot turbo transfer pack. _____	111
Figure 11 Correlation between citrate synthase (CS) activity and protein concentration in SH-SY5Y cells. _____	115
Figure 12 Correlation between mitochondrial complex I activity and protein concentration in SH-SY5Y cells. _____	119
Figure 13 Correlation between mitochondrial complex II-III activity and protein concentration in SH-SY5Y cells. _____	122
Figure 14 Correlation between mitochondrial complex IV activity and protein concentration in SH-SY5Y cells. _____	125
Figure 15 Correlation between GBA activity and protein concentration in SH-SY5Y cells. _____	128
Figure 16 Fluorescence intensity calibration curve for 4-methylumbelliferone (4-MU). _____	129
Figure 17 Cyclic voltammogram for glutathione. _____	131
Figure 18 Linear calibration curve for glutathione. _____	132

Figure 19 Effect of working electrode voltages on the specificity of HPLC detection.	133
Figure 20 HPLC instrumentation.	141
Figure 21 The effect of different method conditions on the resolution of the chromatogram.	144
Figure 22 Cyclic voltammograms for dopamine and serotonin metabolites.	146
Figure 23 Linear regression curve for dopamine and serotonin metabolites.	148
Figure 24 The temperature sensitivity of dopamine and serotonin metabolites.	150
Figure 25 Quality control samples for DOPAC.	152
Figure 26 The order and retention times of the external standards.	154
Figure 27 A chromatogram of an experimental sample and external standard.	154
Figure 28 Example of an extracellular neurotransmitter metabolite profile in L-DOPA treated differentiated SH-SY5Y cells.	156
Figure 29 Example of a cell lysate neurotransmitter metabolite profile in L-DOPA treated proliferative SH-SY5Y cells.	156
Figure 30 DHBA stability test.	159
Figure 31 DHBA peak interference with 5-HIAA.	159
Figure 32 Elution time of external standards and isoproterenol internal standard.	161
Figure 33 Proliferative and differentiated SH-SY5Y cell morphology as observed under light microscope.	169
Figure 34 Expression level of the neuronal-specific enolase in proliferative and differentiated SH-SY5Y cells.	172
Figure 35 Expression level of the NeuN in proliferative and differentiated SH-SY5Y cells.	172

Figure 36 Tyrosine hydroxylase protein expression in proliferative and differentiated SH-SY5Y cells. _____	173
Figure 37 Extracellular level of 5-HIAA under basal conditions. _____	177
Figure 38 Extracellular and intracellular dopamine and serotonin metabolites in proliferative and differentiated SH-SY5Y cells. _____	178
Figure 39 Lysosomal glucocerebrosidase activity in proliferative and differentiated SH-SY5Y cells. _____	182
Figure 40 Glutathione level in proliferative and differentiated SH-SY5Y cells. _____	184
Figure 41 Effect of L-DOPA on citrate synthase enzyme activity. _____	199
Figure 42 The effect of L-DOPA on mitochondrial complex I, II-III and IV activity. ____	201
Figure 43 Effect of L-DOPA on glucocerebrosidase enzyme activity. _____	203
Figure 44 Effect of L-DOPA on glutathione levels. _____	205
Figure 45 Cathepsin D synthesis pathway. _____	216
Figure 46 Correlation between cathepsin D enzyme activity and protein concentration in SH-SY5Y cells. _____	221
Figure 47 A pH calibration curve of the LysoSensor™ Yellow/Blue DND-160. _____	223
Figure 48 A pH calibration curve of proliferative SH-SY5Y cells incubated with the LysoSensor™ Yellow/Blue DND-160. _____	224
Figure 49 A pH calibration curve of the LysoSensor™ Blue DND-167. _____	225
Figure 50 A pH calibration curve of fibroblast cells incubated with the LysoSensor™ Blue DND-167. _____	226
Figure 51 A representative western blot blotted with (A) anti-cathepsin D polyclonal antibody (Cell Signalling #2284) and (B) anti-proCTSD and anti-mCTSD monoclonal	

antibodies (Abcam #ab134169 and #ab75852) in proliferative and differentiated SH-SY5Y cells. _____	228
Figure 52 Effect of baf treatment on CTSD maturation. _____	231
Figure 53 Effect of lysosomal alkalinisation on CTSD enzyme activity. _____	233
Figure 54 Effect of GBA inhibition on CTSD maturation. _____	236
Figure 55 Effect of inhibition of GBA activity on CTSD enzyme activity. _____	238
Figure 56 Effect of inhibition of complex I activity on CTSD enzyme activity. _____	240
Figure 57 Dopamine metabolites in AADC patient-derived dopaminergic neurons.	257
Figure 58 Lentivirus DDC gene rescue of AADC dopaminergic neurons. _____	260
Figure 59 Dopamine metabolites in L-DOPA treated AADC dopaminergic neurons.	263
Figure 60 Basal dopamine metabolism at different differentiation time points. _____	274
Figure 61 Dopamine metabolism following L-DOPA stimulation at different dopaminergic differentiation time points. _____	276
Figure 62 Dopamine turnover following L-DOPA stimulation at different dopaminergic differentiation time points. _____	277
Figure 63 Basal dopamine metabolism in control and PINK1 patient dopaminergic neurons. _____	282
Figure 64 Dopamine metabolism following L-DOPA stimulation in control and PINK1 patient neurons. _____	283
Figure 65 Dopamine turnover in L-DOPA treated dopaminergic neurons. _____	284
Figure 66 Mitochondrial-lysosomal contact tethering facilitates ATP delivery to lysosomes. _____	304

List of tables:

Table 1 Gel electrophoresis loading sample composition.	110
Table 2 List of antibodies used and dilutions.....	112
Table 3 HPLC mobile phase composition.	142
Table 4 Activity of mitochondrial electron transport chain complexes in proliferative and differentiated SH-SY5Y cells.....	180
Table 5 The effect of L-DOPA on proliferative and differentiated SH-SY5Y cell biochemistry.....	207
Table 6 Ratio of proCTSD/mCTSD protein expression in control and bafilomycin A1 treated SH-SY5Y cells.....	232
Table 7 CTSD enzyme activity in control and bafilomycin A1 treated SH-SY5Y cells.	234
Table 8 Ratio of proCTSD/mCTSD protein expression in control and CBE treated SH-SY5Y cells.....	237
Table 9 CTSD enzyme activity in control, CBE and rotenone treated SH-SY5Y cells.....	241
Table 10 Extracellular dopamine metabolites.	278
Table 11 Intracellular dopamine metabolites.....	278
Table 12 Dopamine turnover.....	279
Table 13 Extracellular dopamine metabolites.	285
Table 14 Intracellular dopamine metabolites.....	285
Table 15 Dopamine turnover.....	286
Table 16 Percent reduction in CTSD enzyme activity in response to different toxins...	298

List of abbreviations:

3-MT	3-methoxytyramine
3-OMD	3-methyldopa
5-HIAA	5-hydroxyindolacetic acid
5-HTP	5-hydroxytryptophan
AADC	aromatic amino acid decarboxylase
AADCDD	aromatic amino acid decarboxylase deficiency
AD	Alzheimer disease
AIF	apoptosis-induced factor
ALDH	aldehyde dehydrogenase
ALS	Amyotrophic lateral sclerosis
BDNF	brain-derived neurotrophic factor
BH₄	tetrahydrobiopterin
Ca²⁺	Calcium
CCCP	carbonyl cyanide m-chlorophenylhydrazone
CLEAR	coordinated lysosomal expression and regulation network
CNS	central nervous system
COMT	catechol-O-methyl transferase
CS	citrate synthase
CSF	cerebrospinal fluid
DAT	dopamine transporter
DOPAC	3,4-Dihydroxyphenylacetic acid
DOPAL	3,4-Dihydroxyphenylacetaldehyde

DQ	Dopamine quinones
DRD	L-DOPA-responsive dystonia
ETC	electron transport chain
Gal-A	α -galactosidase A
GBA	Glucocerebrosidase
GCH1	GTP-cyclohydrolase 1
GCL	glutamyl-cysteine ligase
GD	Gaucher's disease
GPx	glutathione peroxidase
GS	glutathione synthase
GSH	Glutathione
GSSG	glutathione disulphide
H₂O₂	hydrogen peroxide
HD	Huntington Disease
HTT	Huntingtin
HVA	homovanillic acid
iPSCs	induced pluripotent stem cells
LB	Lewy bodies
LMP	lysosomal membrane proteins
LRRK2	leucine-rich repeat kinase 2
LSD	lysosomal storage disorders
MAO	monoamine oxidase
MCS	membrane contact sites
mDNA	mitochondrial DNA
MDV	mitochondrial derived vesicles

MEF	mouse embryonic fibroblasts
MPTP	1-methyl-4-phenyl-1,2,3,6-tetrahydropyridine
NM	Neuromelanin
OXPHOS	oxidative phosphorylation
PD	Parkinson's disease
POLG1	polymerase gamma 1
RA	retinoic acid
ROS	reactive oxygen species
SN	<i>Substantia nigra</i>
SOD1	superoxide dismutase 1
TCA	Citric acid cycle
Tfam	transcription factor A
TFEB	transcription factor EB
TFEB	transcription factor EB
TH	tyrosine hydroxylase
THD	Tyrosine hydroxylase deficiency
TPA	12-O-tetradecanoylphorbol-13-acetate
TPH	tryptophan hydroxylase
v-ATPase	vacuolar-type ATPase
VMAT2	vesicular monoamine transporter protein 2
VPS35	vacuolar sorting protein 35

Declaration of collaborations

I, Haya Alrashidi, carried out all the work described in this thesis, except in Chapters 7 and 8, in which I undertook HPLC-ED monoamine measurements and interpreted the data. The following groups provided the models and prepared the samples:

- ❖ **Chapter 7:** Media from iPSC dopaminergic neurons derived from control and patients with aromatic amino acid decarboxylase deficiency by Dr Giada Rossignoli and Dr Karolin Krämer from Prof Manju Kurian's group (UCL GOS Institute of Child Health)
- ❖ **Chapter 8:** Media and cell lysate from iPSC dopaminergic neurons derived from control and Parkinson's disease patient and carrier by Dr Gurvir Virdi from Prof Sonia Gandhi's group (UCL Queen Square Institute of Neurology, The Francis Crick Institute)

Acknowledgement

Isaac Newton once said, “If I have seen further, is it by standing on the shoulders of giants.” The work undertaken in this thesis wouldn’t have been possible without the guidance and support of my supervisors Professor Simon Heales and Dr Simon Eaton. I am deeply grateful for being given the opportunity to learn first-hand from such greats. Their knowledge, expertise and sheer enthusiasm made this massive undertaking possible and shaped me into the scientist I am today. However, their contributions extend beyond the research level. As someone who suffers greatly from imposter syndrome, I couldn’t have asked for better mentors. They have seen more potential and ability in me than I saw in myself and helped bring it out. Their unwavering belief in me and their never-ending encouragements have been a tremendous reassurance and a massive confidence boost. I sincerely appreciate how they were always at the ready to help me with whatever I needed; however inconvenient it was. For that and much more, I am deeply thankful.

I would also like to extend my thanks to Dr Michael Offord who I was very fortunate to work in the lab alongside for the first 2 years of my PhD journey. His technical expertise and impressive research experience and have been a massive help on the numerous occasions. One of the kindest and most generous people I have met who, despite working on completely different projects and equipment, never failed to take the time to bounce ideas with me.

Next, I would like to thank our research collaborators for giving me the opportunity to be part of more exciting research beyond my own; Dr Serena Barral, Dr Karolin Krämer, Dr Giada Rossignoli, and Professor Majnu Kurian from

UCL Institute of Child Health as well as Dr Gurvir Viridi and Professor Sonia Gandhi from The Francis Crick Institute.

Perhaps unconventional, I would also like to acknowledge all work didn't make it into this thesis. The trials and error, the unsuccessful experiments, and the time spent trouble shooting. They were the necessary stepping-stones without which the protocols and experiments presented this thesis wouldn't have been possible. I believe they are as much part of the scientific method as the published works, and thus should be equally recognised.

Beyond the scope of this research, I would like to take this space to thank my family for their massive support over the years despite me undertaking a journey that is unfamiliar to them. I am also grateful to my friends for their unshakable belief in me, for being by my side throughout, cheering me on despite being separated by time and geography. Finally, I'm forever indebted to my first mentor, Dr Jameela Zamoon (Kuwait University) who have supported and encouraged me during my bachelor's degree and well beyond. Through her guidance, she did more than prepare me academically, but also prepared me for life. I'm grateful for the opportunity to have had such an incredible role model.

Last, but definitely not least, this thesis wouldn't have been possible without the generous contribution of Kuwait University (Kuwait) through funding this work.

Chapter 1. Introduction

1.1. Parkinson's disease:

Parkinson's disease (PD) is a multi-genic, multifactorial, and slowly progressive neurodegenerative disease that affects 1% of people over the age of 60 (Tysnes and Storstein 2017). It was first described by James Parkinson who, in his "Essay on the shaking palsy" in 1817, defined four classical clinical signs of the disease, which are still relevant today. Diagnosis is based on these four classical motor symptoms: resting tremors, bradykinesia, rigidity, and postural instability; collectively defined as parkinsonism (Parkinson 2002). PD occurs predominantly from dopamine deficiency and death of dopaminergic neurons in the *substantia nigra* (SN) area of the brain (Ehringer and Hornykiewicz 1960). The motor symptoms appear as a consequence of dopamine depletion however, patients also experience non-motor related symptoms that manifest more than a decade earlier. These can include mood disorders, sleep problems, gastrointestinal problems, and impaired olfaction (Ziemssen and Reichmann 2007). Most of these non-motor symptoms are directly or indirectly related to a dysregulated serotonin system. Dementia is also prevalent in the late stages of the disease (Kalia and Lang 2015). Currently, there is no cure for PD and available therapies only alleviate the symptoms. These therapies include the dopamine precursor (levodopa; L-3,4-dihydroxyphenylalanine, L-DOPA), dopamine agonists, and inhibitors of dopamine breakdown. They are aimed to replenish the dopamine levels in the brain, the deficiency of which causes the motor symptoms (Sivanandy *et al.* 2022).

Multiple risk factors have been associated with PD. Most of these factors are either genetic or environmental. However, age is the greatest known risk factor for PD (Lee and Gilbert 2016). The majority of PD cases are idiopathic,

meaning the exact cause remains unclear. However, it is hypothesised that PD is a “dual-hit” disease, whereby genetic polymorphism and subsequent exposure to environmental factors cause the cellular pathology leading to PD (Hawkes *et al.* 2007). The first clue to the contribution of environmental factors was recognised in a case of young drug users that injected synthetic heroin that was contaminated by a chemical called 1-methyl-4-phenyl-1,2,3,6-tetrahydropyridine (MPTP). MPTP injection led to development of rapid, severe and irreversible parkinsonism (Ballard *et al.* 1985). It was later discovered that MPTP reaching the brain is metabolically converted to 1-methyl-4-phenylpyridinium (MPP⁺) through the action of monoamine oxidase enzyme residing in astrocytes. Astrocytes then release MPP⁺ which gets taken up specifically by dopaminergic neurons of the SN through the action of the dopamine transporter (Ransom *et al.* 1987). Once in the neurons, MPP⁺ inhibits the mitochondrial electron transport chain (ETC) complex I (Nicklas *et al.* 1987; Langston 2017). Exposure to pesticides, which are chemical agents frequently used in agriculture to control pests, have also been associated with a high risk of developing PD. The first link between pesticide exposure and PD was made in the 1980s when it was observed that there is a high prevalence of PD in areas where there is high pesticide use (Barbeau *et al.* 1987). Since then, several environmental factors have been associated with PD including, but not limited to, rotenone and paraquat (Tanner *et al.* 2011). Interestingly, rotenone shares a similar toxicity mechanism to MPP⁺ where it was found to be a mitochondrial ETC complex I inhibitor (Saravanan *et al.* 2005). Paraquat, on the other hand, was found to induced cellular oxidative stress (Ranjbar *et al.* 2002).

Although most PD cases are idiopathic, genetic predisposition accounts for approximately 15% of PD cases (Domingo and Klein 2018). The first report to uncover the genetic aetiology of PD was made by Polymeropoulos and colleagues in 1997 who for the first time linked a genetic mutation in the gene that codes for the protein α -synuclein, *SNCA*, to autosomal dominant inheritance of PD (Polymeropoulos *et al.* 1997). Since then, an increasing number of genes and mutations have been classified as either causative or risk factor genes (Kalia and Lang 2015). For example, mutations in the gene that codes for leucine-rich repeat kinase 2 (*LRRK2*) and the vacuolar sorting protein 35 (*VPS35*) are considered one of the major causes for monogenic PD, characterised with autosomal dominant inheritance (Zimprich *et al.* 2004; Zimprich *et al.* 2011). Additionally, some gene mutations have been associated with autosomal recessive inheritance of PD. For example, *Parkin* gene mutations are the most common cause for early-onset PD, accounting for approximately 50% of autosomal recessive cases. Mutations in the gene that codes for PTEN-induced kinase 1 (*PINK1*) represent the second most common cause for early-onset PD, whereas mutations in the gene that codes for the protein DJ1 accounts for a rare form of early-onset PD (Koros *et al.* 2017). Interestingly, *Parkin*, *PINK1* and *DJ1* are proteins with functions strongly associated with mitochondria, pointing to the strong association between mitochondrial dysfunction and PD (Borsche *et al.* 2021).

In relevance to risk factor genes, the most common risk factor gene mutations for PD are heterozygous mutations in the gene that codes for the lysosomal glucocerebrosidase (*GBA*) enzyme. The first correlation between *GBA* mutations and PD was made in patients with Gaucher's disease (GD, Machaczka

et al. 1999; Tayebi *et al.* 2001; Tayebi *et al.* 2003). GD is the most common lysosomal storage disease (LSD) where homozygous mutations in the GBA gene hinders the breakdown of glucocerebroside molecules into glucose and ceramide (Baris *et al.* 2014). Consequently, through studies of GD relatives and carriers, the association between GBA heterozygous mutations and PD was made (Goker-Alpan *et al.* 2004; Lwin *et al.* 2004). In a large multicentre association study, it was revealed that PD development is 5-6 times more likely in the presence of GBA mutations (Sidransky 2009). This strong predisposition to PD with heterozygosity for a lysosomal enzyme highlights the involvement of lysosomal dysfunction in PD pathology.

The main pathological hallmarks of PD are dopamine depletion, the death of the majority of dopaminergic neurons in the SN, and the presence of aggregates of unfolded or abnormally folded proteins in the surviving neurons known as Lewy bodies (LB, Dickson 2018). Fritz Heinrich Lewy was the first person to notice these inclusions in the brain in 1910 and thus these aggregates were named after him (Holdorff 2006). LB can be found distributed throughout the central nervous system (CNS), including in astrocytes and microglia. They can be seen when affected tissues are examined under the microscope as eosin-stained dark spherical masses in the cytoplasm. α -synuclein fibrils are the major component of LB, however studies have detected whole organelles as well as more than 90 other molecules present. These include mitochondria, lysosomes as well as LRRK2, DJ1, PINK1, Parkin, GBA and ubiquitin. It is interesting to note that most of these molecules are coded for by genes that have been associated with PD risk (Wakabayashi *et al.* 2013; Wakabayashi *et al.* 1992; Mahul-Mellier *et al.* 2020).

1.2. Dopamine:

Dopamine is a neuromodulatory molecule of the catecholamine family, comprising 80% of the brain catecholamine content. It is a neurotransmitter, a molecule released from one neuron that acts on another neuron, transmitting signals. Dopamine plays vital roles controlling multiple functions, including movement. Movement is the result of the dopamine produced by the midbrain dopaminergic neurons in the SN region of the brain (Berridge 2007). Dopamine was first discovered in the brain by Katharine Montagu and its function as a neurotransmitter was defined by Arvid Carlsson, gaining Carlsson the 2000 Nobel prize in medicine (Montagu *et al.* 1957; Carlsson *et al.* 1957).

Dopamine depletion is considered a central event in PD. This was a result of a landmark discovery by Hornykiewicz and colleagues, who demonstrated a significant decrease of dopamine in post-mortem brain tissue from PD patients (Ehringer and Hornykiewicz 1960). Following this, Seiden and colleagues (1963) discovered that mice given reserpine, an antihypertensive medication that depletes catecholamine stores, have impaired motor function, linking dopamine depletion to motor deficits. They also demonstrated that by giving these mice L-DOPA, they could reverse the motor deficits caused by reserpine (Seiden and Carlsson 1963). Afterwards, Poirier and colleagues (1965) showed that SN injury leads to a depletion of striatal dopamine, providing a clue that ties together the anatomy and physiology of PD (Poirier and Sourkes 1965). Seiden and Poirier's work led Hornykiewicz to postulate the possibility of use of L-DOPA as a treatment for PD, thus he and Walther Birkmayer trialled intravenous treatment of PD patients with L-DOPA. The trial showed dramatic, though transient, motor benefits in patients. Unfortunately, L-DOPA is an emetic substance and, at high

doses, caused undesirable side effects like anorexia, nausea, and vomiting. This has led George Cotzias, in 1967, to develop a new therapeutic approach that employs a slow, gradual increase in the dosage of L-DOPA. This approach produced the same motor benefits but with better side effect tolerability and, in principle, is still used today (Fahn 2008; Cotzias *et al.* 1967).

1.2.1. Dopamine metabolism:

The main pathway for dopamine synthesis in the brain starts when the enzyme tyrosine hydroxylase (TH) converts L-tyrosine to L-DOPA. This step represents the rate limiting step of dopamine synthesis. The reaction requires the presence of tetrahydrobiopterin (BH₄), iron and molecular oxygen and is highly regulated at different levels: during transcription, translation, post-transcriptional modifications and through allosteric modifications. Dopamine is produced through decarboxylation of L-DOPA via the enzyme aromatic amino acid decarboxylase (AADC). L-DOPA, when in excess, can alternatively be converted to 3-methyldopa (3-OMD) by the enzyme catechol-O-methyl transferase (COMT, Meiser *et al.* 2013).

Dopamine is produced in the cytosol of dopaminergic neurons but it is highly unstable at physiological pH and can self-oxidize therefore, it is sequestered and stored in acidic cytoplasmic storage vesicles via the action of a multiprotein complex composed of TH, AADC and vesicular monoamine transporter protein 2 (VMAT2, Cartier *et al.* 2010; Chaudhry *et al.* 2008). Interestingly, Goldstein and colleagues (2013) reported a reduced uptake of dopamine via VMAT2 in post-mortem brain tissue from PD patients possibly leading to increased dopamine oxidation (Goldstein *et al.* 2013). Cytosolic dopamine, not stored in acidic vesicles, can be catabolised to produce more

stable products. Dopamine is metabolised by the sequential action of the enzymes monoamine oxidase (MAO) and aldehyde dehydrogenase (ALDH) to produce 3,4-dihydroxyphenylacetic acid (DOPAC), with 3,4-dihydroxyphenylacetaldehyde (DOPAL) as an intermediate metabolite. Alternatively, dopamine can be first converted to 3-methoxytyramine (3-MT) by COMT. 3-MT is then metabolised by MAO to produce homovanillic acid (HVA). COMT can also metabolise DOPAC to produce HVA. Thus, DOPAC and HVA are commonly used as markers of dopamine metabolism in the brain (Figure 1, Meiser *et al.* 2013). On the basis of this, MAO and COMT inhibitors are used as an adjunctive therapy for PD, taken with L-DOPA, to increase dopamine concentration in the brain (Juárez Olguín *et al.* 2016; Mousseau and Baker 2012).

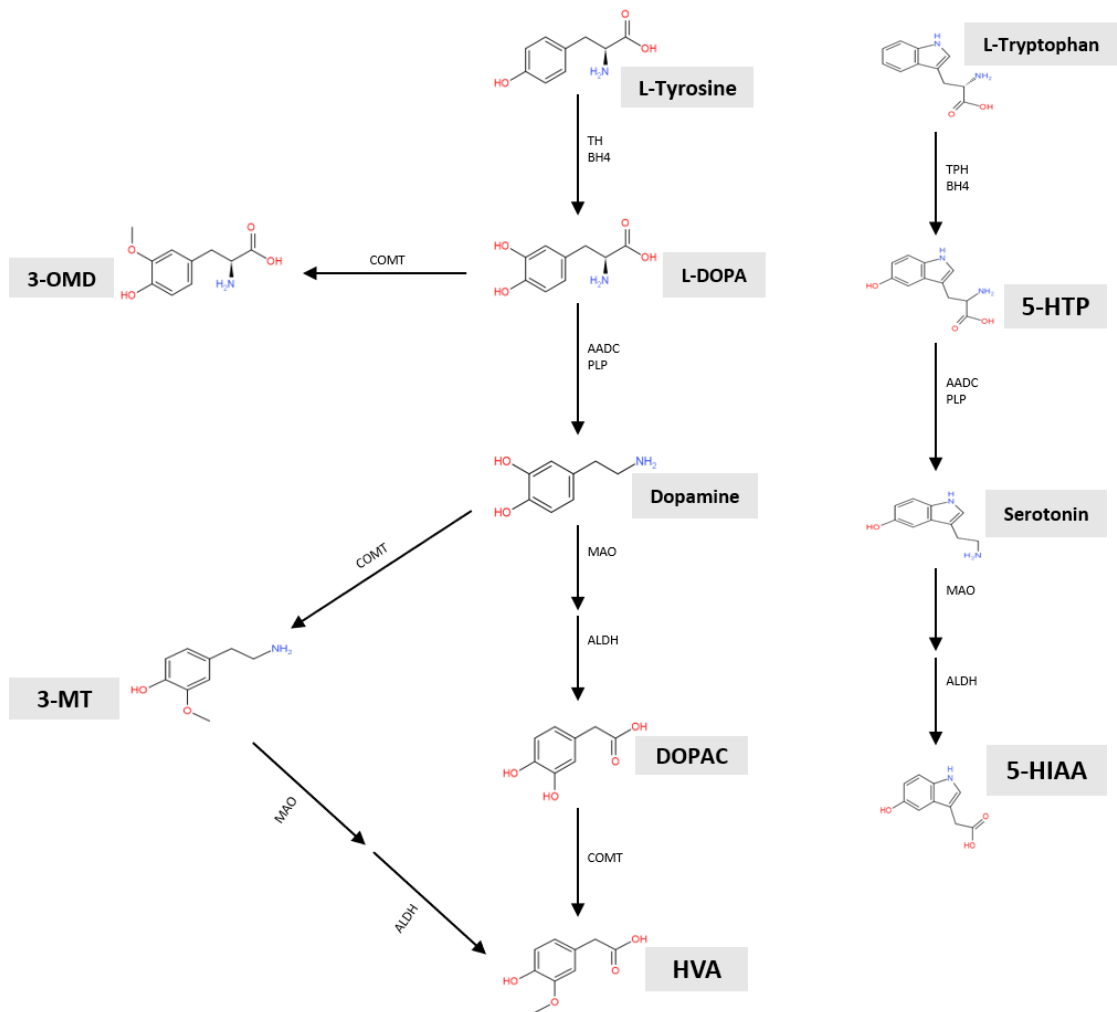


Figure 1 Dopamine and serotonin metabolic pathways. Dopamine synthesis is initiated by the conversion of tyrosine to L-DOPA by tyrosine hydroxylase (TH). L-DOPA is then converted to either dopamine by aromatic amino acid decarboxylase (AADC), or 3-O-methyldopa (3-OMD) by catechol-O-methyltransferase (COMT). Dopamine is metabolised to yield DOPAC by the sequential action of monoamine oxidase (MAO) and aldehyde dehydrogenase (ALDH). Alternatively, it can be metabolised to give homovanillic acid (HVA) by the action of COMT followed by MAO and ALDH. Serotonin synthesis starts with conversion of tryptophan to serotonin by sequential action of tryptophan hydroxylase (TPH) and AADC. The main catabolite of serotonin in the brain

is 5-hydroxyindoleacetic acid (5-HIAA) produced by the sequential action of MAO and ALDH. 5-HTP: 5-hydroxytryptophan, 3-MT: 3-methoxytyramine

1.2.2. Enzymes of the dopamine pathway:

Tyrosine hydroxylase (EC 1.14.16.2, alternatively tyrosine 3-monooxygenase) is the rate limiting enzyme of the dopamine pathway, and as a result, it is often used as a marker of dopaminergic neurons (Verney *et al.* 1982). It was discovered in the 1960s as the enzyme that converts L-tyrosine to L-DOPA (Nagatsu *et al.* 1964). TH function is essential for development and survival and complete loss of TH activity is embryonically lethal (Zhou *et al.* 1995). The human TH is encoded by a single gene that undergoes alternative splicing to produce four TH isozymes (TH1, TH2, TH3 and TH4). TH isoforms assemble to form four different 240 kDa homotetramers, composed of 4 identical 60 kDa monomers (Grima *et al.* 1987; Kobayashi *et al.* 1988). TH activity is tightly regulated through different means because it is the essential enzyme for production of dopamine, the functions of which are imperative for normal physiology. Firstly, TH is regulated at the transcriptional and translational level and through post-translation modification to control the protein expression. Secondly, it is regulated at the enzyme level via availability of its cofactor BH₄, through activation by phosphorylation via protein kinases, and by feedback inhibition via dopamine and other catecholamines. Finally, it is regulated through TH protein degradation via ubiquitination (Tekin *et al.* 2014).

Impaired activity of TH is associated with PD. TH protein and activity was demonstrated to be decreased in PD post-mortem brain tissue compared to control (Lloyd *et al.* 1975; Mogi *et al.* 1988). mRNA levels of the different splice variants of TH were documented to be decreased in post-mortem brain tissue from PD patients compared to control (Ichinose *et al.* 1994). The levels of TH cofactor, BH₄, is documented to be decreased in PD compared to control

(Lovenberg *et al.* 1979). Impaired TH activity was also demonstrated in another disease of dopamine metabolism; rare genetic mutations in TH cause an autosomal recessive form of an inborn error of metabolism known as TH deficiency (THD), first reported by Lüdecke and colleagues (1996). THD can cause infantile parkinsonism, dystonia, delayed motor development and progressive encephalopathy. In addition to genetic sequencing, analysis of the levels of neurotransmitter metabolites in the cerebrospinal fluid (CSF) represent an important diagnostic tool in THD and other neurotransmitter disorders. CSF profiling of THD patients reveals low or undetectable levels of HVA with normal levels of the serotonin metabolite, 5-HIAA. This is indicative of severe impairment of the dopamine pathway, while the serotonin pathway is unaffected. Treatment with the dopamine precursor, L-DOPA, represents the main therapeutic strategy for patients with THD, classifying this disorder as a type of L-DOPA-responsive dystonia (DRD, Willemsen *et al.* 2010; Hoffmann *et al.* 2003).

5,6,7,8-Tetrahydrobiopterin (BH₄) is an important cofactor for TH. It is synthesized by the enzyme GTP-cyclohydrolase 1 (GCH1). Deficiency in GCH1 causes a disorder of inborn error of metabolism called Segawa disease, another type of DRD (Ichinose 2000). Patients with Segawa disease typically present with dystonia in the early years of childhood. Adult onset GCH1 deficiency usually present as L-DOPA-responsive parkinsonism, which mimics PD. Diagnosis of GCH1 deficiency is based on genetic testing, reduced activity of GCH1, and a CSF profile of low levels of BH₄, HVA and 5-HIAA (Wijemanne and Jankovic 2015). As a disorder of dysregulated metabolism of both dopamine and serotonin, supplementation with L-DOPA and 5-hydroxytryptophan (5-HTP, the precursor of serotonin) is an effective treatment in most cases of GCH1 deficiency (Segawa

2011). In addition to Segawa disease, some rare genetic variants in *GCH1* are now considered to be risk factors for PD (Rudakou *et al.* 2019). Furthermore, in the absence of any mutations in *GCH1*, studies have documented reduced activity of *GCH1* and low levels of BH₄ in the CSF and SN post-mortem brain tissue of PD patients (Lovenberg *et al.* 1979; Nagatsu and Nagatsu 2016; Fanet *et al.* 2021).

Aromatic amino acid decarboxylase (AADC, EC 4.1.1.28) is a key enzyme in both dopamine and serotonin synthesis pathways. It is a homodimeric α -decarboxylase that was first identified in 1938 in the kidney as essential for epinephrine synthesis, a product of dopamine (Hornykiewicz 2002). It catalyses the decarboxylation of L-DOPA and 5-HTP to give rise to dopamine and serotonin, respectively, and requires pyridoxal 5'-phosphate as cofactor (Bertoldi 2014). AADC is present in CNS and the peripheral tissues therefore, inhibitors of AADC, such as carbidopa, are used as adjunctive therapies in PD. Carbidopa does not cross the blood brain barrier and therefore, inhibits L-DOPA utilisation in peripheral tissues by peripheral AADC, maximising the level of L-DOPA reaching the brain (Burkhard *et al.* 2001).

Human AADC is the product of the *DDC* gene. Mutations in *DDC* cause another form of inborn error of metabolism known as AADC deficiency (AADCD). AADCD was first described by Clayton and colleagues in 1990s (Hyland and Clayton 1992). AADCD clinical presentation varies widely, possibly as a result of the variability of the type and location of *DDC* gene mutations. The most common AADCD symptoms can include hypotonia, dystonia and developmental delay. Diagnosis of AADCD is based on a CSF analysis of low levels of HVA and 5-HIAA accompanied by high levels of 3-OMD, in addition to reduced enzyme

activity and gene sequencing. Current treatment for AADCDC includes the use of dopamine agonists, MAO inhibitors and pyridoxal 5'-phosphate supplementation however, the response to these medications varies from one patient to another (Himmelreich *et al.* 2019). Generally speaking, AADCDC patients are commonly considered to be L-DOPA-unresponsive (Wassenberg *et al.* 2017).

Monoamine oxidases (MAO, EC 1.4.3.4) are a class of enzymes that function in oxidation of monoamines such as the neurotransmitters dopamine and serotonin (Youdim *et al.* 1988). They are mitochondrial outer membrane proteins present in most cell types. There are two isoforms of MAO, A and B, both of which have the ability to catabolise dopamine. However, the isoforms possess differential substrate affinities where dopamine is predominantly metabolised by MAO-B while serotonin is preferentially metabolised by MAO-A (Garrick and Murphy 1980). In addition to differential substrate affinity, MAO isoforms have differential cellular expression. For example, MAO-A is mainly found in catecholaminergic neurons while MAO-B is expressed by serotonergic neurons and astrocytes (Westlund *et al.* 1985). Because of its central role in breakdown of dopamine, MAO-B inhibitors emerged as an adjunctive therapy in PD, to be given with L-DOPA, aimed at increasing the extracellular availability of dopamine (Birkmayer *et al.* 1975; Jones and Raghanti 2021).

Another important protein in the dopamine pathway is the dopamine transporter (DAT). Following neural transmission, dopamine released into the synapse is sequestered back into the neurons as an important regulatory step. Dopamine re-uptake into neurons is facilitated by DAT, resulting in the termination of the dopamine signal (McHugh and Buckley 2015). DAT is a transmembrane sodium-dependant monoamine transporter that uses the energy

from a sodium gradient to translocate dopamine into the cell (Kristensen *et al.* 2011). It is highly expressed in the presynaptic dopaminergic neurons of the SN and therefore, commonly used as a marker of dopaminergic neurons (Torres *et al.* 2003). Mutations in the gene that code for DAT result in dopamine transporter deficiency syndrome (DTDS), a form of autosomal recessive infantile PD. DTDS results in defective dopamine reuptake and dopamine accumulation in the synapse (Kurian *et al.* 2009). DTDS patients develop characteristic parkinsonism symptoms of resting tremor, rigidity, and bradykinesia. In addition, DTDS patients present with a CSF neurotransmitter profile of increased levels of HVA and dopamine, with normal levels of 5-HIAA (Ng *et al.* 2014).

1.2.3. Dopamine toxicity:

Although neuronal degeneration in PD occurs in many regions of the brain, the SN is the most, and possibly first, region affected. It is hypothesized that the region's specific vulnerability may be a result of its high dopamine content (Hastings and Zigmond 1997; Chen *et al.* 2008). The toxicity of dopamine is supported by both *in vivo* and *in vitro* studies. For example, injection of high concentration of dopamine in the striatum of rats resulted in loss of dopaminergic neurons as early as one week following injection (Filloux and Townsend 1993). In addition, slow and progressive degeneration of the nigrostriatal region was observed in mice engineered to have 5% reduced expression of the gene that codes for VMAT2, a protein that facilitates cytosolic dopamine uptake into acidic vesicles (Caudle *et al.* 2007). Furthermore, in cultured human dopaminergic neurons, Xu and colleagues (2002) have demonstrated that dopamine production is a requirement for the toxic accumulation of α -synuclein protein in the cytosol which results in cell death (Xu *et al.* 2002).

Dopamine is proposed to contribute to cellular toxicity through multiple means. Firstly, dopamine metabolism in the cell is an additional source of reactive oxygen species (ROS). Production of DOPAL by MAO yields hydrogen peroxide (H_2O_2) as a by-product, potentially increasing cellular oxidative stress. (Hermida-Ameijeiras *et al.* 2004; Spina and Cohen 1989; Aluf *et al.* 2013; Mattammal *et al.* 1995). Although a recent study by Graves and colleagues (2019) argues that H_2O_2 produced in this step does not raise cellular oxidative stress. Instead, the electrons produced from this reaction are funnelled into the mitochondrial inner membrane to aid ATP production needed to sustain dopamine neurotransmission by contributing to membrane polarisation (Graves *et al.* 2019). DOPAL itself, was

found to be cytotoxic through its ability to cross-link with cellular proteins, such as α -synuclein, inducing their aggregation (Masato *et al.* 2019). Secondly, cytosolic dopamine can easily oxidize in the presence of enzymes, metals or spontaneously yielding highly reactive molecules known as quinones (Linert *et al.* 1996). Dopamine quinones (DQ) are cytotoxic due to their electron-poor chemical state enabling them to readily react with different cellular components altering their function. For example, DQ have the ability to form adducts with the mitochondrial ETC complexes I, III and VI leading to dysregulated oxidative phosphorylation (Biosa *et al.* 2018). In addition, a study by Huenchuguala and colleagues (2014) demonstrated that DQ derivatives have the ability to form adducts with the lysosomal vacuolar-ATPase (v-ATPase) interfering with lysosomal acidification (Huenchuguala *et al.* 2014). Glutathione, a key antioxidant in the cell, plays a vital role in detoxification of DQ via formation of glutathionyl-dopamine conjugates (Dagnino-Subiabre *et al.* 2000; Bisaglia *et al.* 2010). The catabolic metabolite of glutathionyl-dopamine, cysteinyl-dopamine, can be detected in CSF of PD patients (Badillo-Ramírez *et al.* 2019). Finally, a detrimental consequence to the production of DQ is their ability to spontaneously cyclise giving rise to aminochrome molecules, which are the most stable form of DQ (Sulzer *et al.* 2000). Aminochromes are cytotoxic due to their ability to form adducts with important proteins hindering their function (Figure 2, Herrera *et al.* 2017). Interestingly, aminochrome was used in a study to successfully to create a rodent model of PD. Touchette and colleagues (2017) directly injected aminochrome into the SN *pars compacta* region of rats' brains. Following injection, degeneration of TH⁺ neurons in the region was observed and the appearance of a dark pigment that could potentially be neuromelanin (NM) was

noted (Touchette, Breckenridge and Wilken 2017). Aminochrome is the precursor of NM, which is a complex brain pigment, characteristic of dopaminergic neurons of the SN. NM is largely composed of dopamine derivatives and can be found within the cytoplasm, enclosed in double membrane organelles. The function of NM is not yet clear, but it may serve as a mean to sequester excess dopamine and toxic dopamine products and derivatives from the cytosol as a neuroprotective measure (Fedorow *et al.* 2005; Zecca *et al.* 2003).

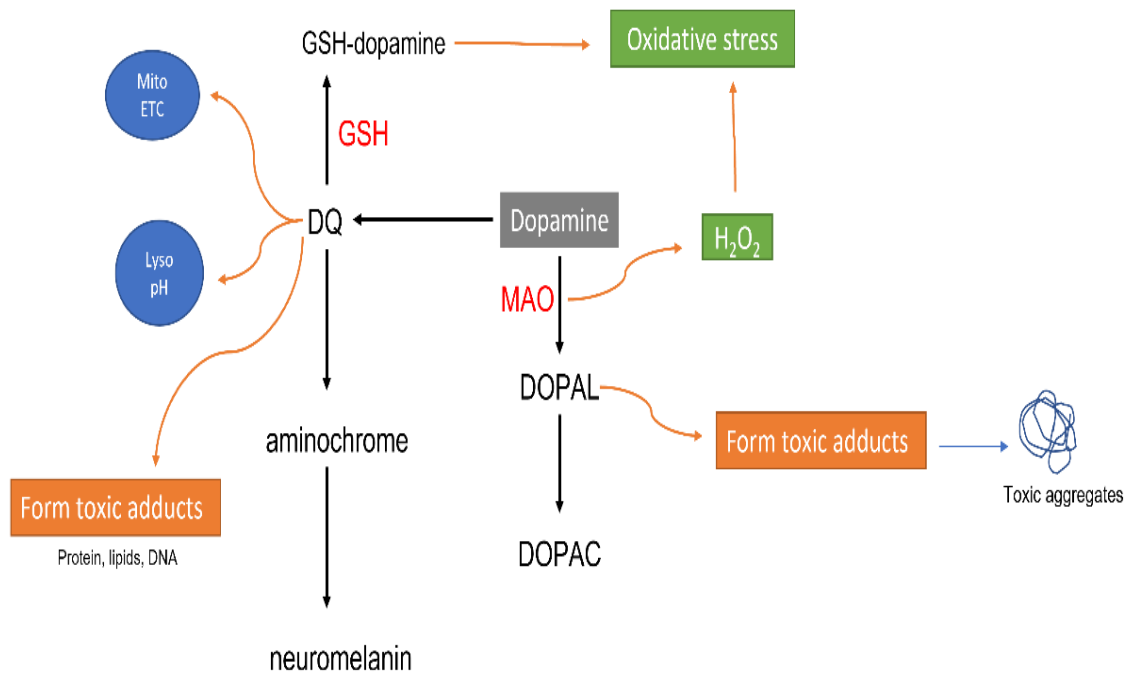


Figure 2 Potential cellular toxicity of dopamine. Production of DOPAL by MAO yields hydrogen peroxide (H₂O₂) as a by-product increasing oxidative stress. DOPAL can cross-link with cellular proteins, inducing their aggregation. Cytosolic dopamine can easily oxidize in the presence of enzymes, metals, or spontaneously yielding dopamine quinones (DQ). DQ can form adducts with the mitochondrial ETC complexes impairing oxidative phosphorylation. DQ derivatives can form adducts with the lysosomal vacuolar-ATPase impairing lysosomal acidification. DQ can readily react with different cellular components altering their function. DQ can form GSH-dopamine conjugates with glutathione (GSH), depleting antioxidant defence. DQ can spontaneously cyclise to form aminochrome molecules, which are cytotoxic. Aminochrome is the precursor of neuromelanin. Mito: mitochondria. Lyso: lysosomes

1.3. Serotonin:

5-hydroxytryptamine, or serotonin, is one of the most widely distributed neurotransmitters with an expression throughout the CNS and extending to the peripheral nervous system. It was first discovered in the 1930s by Vittorio Erspamer, identified as a vasoconstrictor produced by enterochromaffin cells (Erspamer and Asero 1952; Whitaker-Azmitia 1999). Serotonin synthesis starts when tryptophan is converted to 5-hydroxytryptophan (5-HTP) in a reaction that requires tryptophan hydroxylase (TPH, EC 1.14.16.4), BH₄ and molecular oxygen. In a similar manner to dopamine, serotonin is synthesized from 5-HTP by the enzyme AADC. Serotonin catabolism is carried out by the sequential action of MAO and ALDH producing 5-hydroxyindolacetic acid (5-HIAA), the primary metabolites of serotonin (Figure 1, Hyland 2008).

Historically, the dysfunctional dopaminergic system has been considered central to PD pathology, overshadowing the documented perturbation in the serotonergic systems. For example, LB formation has been detected in serotonergic neurons suggesting the possibility of PD pathology extending to serotonergic system (Braak *et al.* 2003). In addition, studies of post-mortem brain tissue from PD patients have revealed loss of serotonergic neurons (Halliday *et al.* 1990). Furthermore, measurement of serotonin in the CSF of PD patients has suggested a correlation between the extent of serotonin loss and the severity of PD motor dysfunction (Tohgi *et al.* 1993). Finally, the level of the serotonin transporter was documented to be decreased in PD patients compared to controls (Politis *et al.* 2010). The serotonin transporter facilitates serotonin reuptake into the neurons following release into the synapse, thereby regulating serotonin neurotransmission (Adnot *et al.* 2013). Interestingly, in a study of

carriers of α -synuclein mutations, one of the established genetic risk factors for PD, reduced level of the serotonin transporter was detected well before the onset of motor symptoms indicative of PD pathology extending to the serotonin system (Wilson *et al.* 2019).

Serotonin governs many functions that include sleep, mood and appetite (Politis *et al.* 2015). Therefore, serotonin depletion in PD presents a good candidate to explain the non-motor symptoms that include sleep disturbances, depression and appetite dysregulation that are common in PD and may even manifest years before clinical presentation. For example, depression is more prevalent in PD patients than in non-PD population and it is attributed to a dysregulated serotonin system (Politis *et al.* 2015; Cummings and Masterman 1999). Furthermore, weight loss was found to be up to 50% more likely in PD patients at disease onset, supporting appetite dysregulation (Abbott *et al.* 1992). In addition, following a 6-year long longitudinal study, it was estimated that sleep disturbances occur in almost 75% of PD patients (Goetz *et al.* 2005). Despite the mounting evidence, very little research has been done on serotonin perturbation in PD, compared to dopamine.

1.4. Molecular mechanisms of Parkinson's Disease

1.4.1. Mitochondria

Neurons have high-energy demands, consuming as much as 20% of an organism's daily energy requirement. In addition to housekeeping functions, neurotransmission and its related processes increase cellular energy demands, making neurons more vulnerable to disorders affecting energy homeostasis. Mitochondria are the main energy source in neurons, producing ATP by oxidative phosphorylation (OXPHOS) via the electron transport chain however, they also carry other roles that support proper neuronal function (Princz *et al.* 2018). Mitochondria are the major source of reactive oxygen species (ROS) in the cell (Murphy 2009). Although ROS are harmful molecules that are implicated in pathogenesis of several neurodegenerative disorders, they play important roles as secondary messengers. For example, hydrogen peroxide (H₂O₂), produced as a by-product of OXPHOS, regulates neuronal excitability through its action on H₂O₂-sensitive ion channels in dopaminergic neurons (Lee *et al.* 2015). Furthermore, mitochondria take part in biosynthesis of several molecules. 13 proteins that are essential for OXPHOS are encoded for by the mitochondrial DNA (Christian and Spremulli 2012). Mitochondria also provide precursors for synthesis of neurotransmitters such as GABA and glutamate and synthesize the majority of the mitochondrial-specific phospholipid, cardiolipin (Tatsuta *et al.* 2014). Mitochondria are a major site for regulation of cellular calcium (Ca²⁺), this regulation is specifically relevant to neurons as Ca²⁺ is a major modulator of neurotransmission and synaptic plasticity (Granatiero *et al.* 2017). Additionally, several studies support the notion that mitochondria contribute to proper myelination of neuronal axons, which accelerates action potentials travelling across, increasing the efficiency of conductance (Ino and Iino 2017). This view is

supported by the observation that disorders that induce axon demyelination in the central and peripheral nervous systems are also associated with mutations in genes affecting mitochondrial function (Niemann *et al.* 2014). Finally, mitochondria play an important role in programmed cell death pathways (Jeong and Seol 2008). Apoptosis can be initiated through mitochondrial release of the mitochondrial cytochrome c into the cytosol, which is the first step in initiating a cascade of cell signalling that results in cell death (Zamzami *et al.* 1996; Yang and Cortopassi 1998)

Mitochondria are dynamic organelles that can adapt to changes in the environment by changing their location, shape, and size, contributing to cellular viability, energy demands and apoptosis. They are trafficked to areas of higher energy needs, which is particularly important in neurons due to their unique, polarised morphology. Neuronal synapses are located on their dendritic and axonal extensions, which can reach up to a meter in length therefore, require the trafficking of mitochondria between distant regions (Schwarz 2013). It was shown that mitochondrial translocation and distribution to the dendrites is imperative for proper neuronal development and function (Li *et al.* 2004). Mitochondria can change their shape and size by undergoing fusion or fission. Fusion redistributes mitochondrial components, sharing proteins and RNA among different mitochondria to compensate for deficits. Fission, on the other hand, facilitates recycling of damaged mitochondria and prevents accumulation of harmful components in the cell through mitophagy (Nasrallah and Horvath 2014). Mitophagy is the specific removal of mitochondria by autophagosomes which fuse with lysosomes to be degraded (Xue *et al.* 2001). This process is of great importance specifically in neurons due to their post-mitotic nature (Fivenson *et al.*

2017). Mitophagy can be initiated via different pathways depending on type of trigger. Receptor-mediated mitophagy is triggered by increased expression of mitochondrial outer membrane receptors, such as Nix. In ubiquitin mediated mitophagy, PINK1 accumulation on mitochondrial surface triggers the recruitment of Parkin or other ubiquitin ligases initiating mitochondrial degradation. Mitophagy can also be triggered by a mechanism that involves translocation of the mitochondrial lipid, cardiolipin, from the inner to the outer mitochondrial membrane, where it interacts with microtubule-associated protein I light chain 3 (LC3) to initiate degradation (Chu 2018).

1.4.1.1. Mitochondrial citric acid cycle

Oxidation of acetyl-CoA, the common final catabolic product of carbohydrates, proteins, and lipids, takes place in the mitochondrial matrix through the citric acid (TCA/Krebs) cycle. Although the main function of the TCA cycle is to break down acetyl-CoA, the pathway also provides substrates for different biosynthetic pathways such as synthesis of amino acids and cholesterol. The first step of the TCA cycle is the condensation of acetyl-CoA and oxaloacetate to form citrate. This reaction is catalysed by citrate synthase (CS, EC 2.3.3.1) enzyme and comprises the rate limiting reaction of the TCA cycle (Akram 2014). CS is homodimer enzyme that is synthesized in the cytosol and translocated into the mitochondrial matrix. Although CS is encoded for by nuclear DNA it is found, almost exclusively, in the mitochondria (Wiegand and Remington 1986). For this reason, CS is commonly used as a marker for mitochondrial content (Larsen *et al.* 2012). Following formation of citrate, a sequence of 7 enzymatic reactions results in the reformation of oxaloacetate which then can be used to convert new acetyl-CoA molecules into citrate. The stepwise reaction of

the TCA cycle results, for each acetyl-CoA molecule, in the formation of three NADH molecules, and one FADH₂, which then participate in the electron transport chain (Figure 3, Akram 2014).

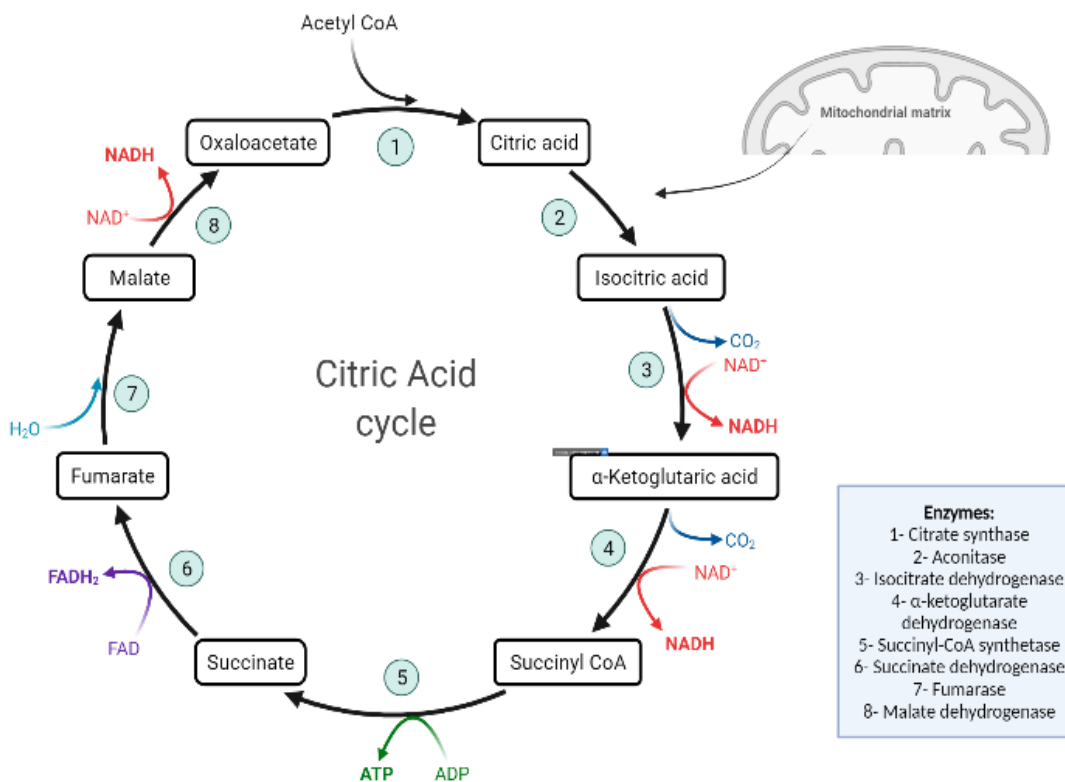


Figure 3 The citric acid cycle. The first step of the TCA cycle is the condensation of acetyl-CoA and oxaloacetate to form citrate by the enzyme citrate synthase. This is then followed by a sequence of 7 enzymatic reactions resulting in the reformation of oxaloacetate which then can be used to convert new acetyl-CoA molecules into citrate. The stepwise reaction of the TCA cycle results, for each acetyl-CoA molecule, in the formation of three NADH molecules and one FADH₂.

1.4.1.2. Mitochondrial electron transport chain

Mitochondria are the powerhouses of the cell. They supply most of the cellular energy demands in the form of ATP through OXPHOS catalysed by the electron transport chain (ETC) complexes. OXPHOS is of added importance in neurons specifically due to their preferential dependency on ATP produced through ETC to sustain their energy demands, making them more susceptible to ETC dysfunction compared to other cell types (Pinto *et al.* 2012; Ngo *et al.* 2015; Bolaños 2016). OXPHOS is the process of harnessing the power of electrons found on electron carriers (NADH and FADH₂) to create a proton motive force that can be used to synthesize ATP molecules. These electron carriers are the products of TCA cycle as well as other enzymatic reaction such as those catalysed by acyl-CoA dehydrogenase, glycerol-3-phosphate dehydrogenase, and choline dehydrogenase. ETC is composed of 5 transmembrane complexes embedded on the inner mitochondrial membrane. In addition to the 5 complexes, the function of ETC is supported by two electron carriers, ubiquinone (coenzyme Q) and cytochrome c. Ubiquinone is a small lipid-soluble molecule that can freely move in and out and diffuse through the inner mitochondrial membrane whereas cytochrome c is a water-soluble protein that is associated with the cristae of the inner mitochondrial membrane (Figure 4, Zhao *et al.* 2019).

The first and rate limiting enzyme of the ETC is NADH-ubiquinone oxidoreductase or complex I (EC 7.1.1.2). Complex I catalyses the oxidation of NADH (produced from the conversion of pyruvate to acetyl-co A by pyruvate dehydrogenase as well as from the TCA cycle) to generate protons that are pumped into the mitochondrial intermembrane space (Sazanov 2014). This reaction results in the reduction of ubiquinone to ubiquinol. Complex I is the

largest ETC complex at a molecular weight of about 1 MDa, composed of 45 subunits, 7 of which are encoded by mitochondrial DNA (Vinothkumar *et al.* 2014). Complex I activity represent the biggest source of mitochondrial ROS, in the form of superoxide anions (Hirst *et al.* 2008; Turrens and Boveris 1980). In PD, there's mitochondrial complex I dysfunction in the form of decreased enzyme activity and increased ROS production, however the exact causal mechanism remains unclear (Valsecchi *et al.* 2010). It is proposed that the decreased activity of complex I seen in PD is a result of oxidative damage to the different complex I subunits (Keeney *et al.* 2006).

Succinate-ubiquinone oxidoreductase is the ETC complex II (EC 1.3.5.1). It catalyses the oxidation of succinate and the transfer of electrons to ubiquinone. This results in the formation of fumarate and ubiquinol. Complex II is unique because, in addition to being a component of ETC, it is also an enzyme that functions in the TCA cycle. Moreover, it is the smallest of all ETC complexes, composed of only four subunits which are encoded for entirely by nuclear DNA. Finally, the oxidation/reduction reaction catalysed by complex II does not result in any protons transferred into the intermembrane space (Cecchini 2003).

Ubiquinol is oxidised by ubiquinol-cytochrome c oxidoreductase, or complex III (EC 1.10.2.2). Complex III transfers the electrons to soluble cytochrome c, pumping protons into the intermembrane space. It is composed of 11 subunits, encoded for by both mitochondrial and nuclear DNA (Schägger *et al.* 1986). Complex III is another important site of mitochondrial superoxide generation, generating ROS both into the mitochondrial matrix and into the cytoplasm (Muller *et al.* 2004; Han *et al.* 2003). Complex III participates in the ubiquinone cycle, otherwise known as Q-cycle. In the Q-cycle, ubiquinone

molecules are reduced to ubiquinol through the complex I and II catalysed reactions. Complex III functions in oxidising ubiquinol back to ubiquinone, through the transfer of its electrons to cytochrome c molecules, thereby restoring ubiquinone electron carrier function in the ETC (Rich 1986). The Q-cycle has been shown to contribute to complex III ROS production through the generation of the electron-deficient intermediate, ubisemiquinone (Sun and Trumpower 2003; Turrens *et al.* 1985). Complex III interacts with complex I and IV to form what are known as respiratory supercomplexes. The organisation into supercomplexes functions to stabilise the different complexes and decrease ROS production (Enríquez 2016; Maranzana *et al.* 2013; Lopez-Fabuel *et al.* 2016). Several studies point to a close association between complex I and III, the disruption of which potentially takes place in PD pathology. For example, it was demonstrated that complex III deficiency disrupted the activity of complex I and that ablation of complex III induced the degradation of complex I (Acín-Pérez *et al.* 2004; Lamantea *et al.* 2002). Another study demonstrated that the formation of complex I, III and IV supercomplex is required for proper complex I and IV biogenesis and assembly (Protasoni *et al.* 2020).

Reduced cytochrome c is oxidised by cytochrome c oxidase, or complex IV (EC 1.9.3.1). The electrons from cytochrome c are transferred to molecular oxygen resulting in formation of H₂O and protons that are pumped into the intermembrane space. Complex IV is composed of 14 subunits, 3 of which are encoded for by mitochondrial DNA (Timón-Gómez *et al.* 2018). Complex IV also function as a site of regulation of the mitochondrial ETC activity through feedback inhibition by ATP (Arnold and Kadenbach 1997). Oxidases are enzymes that reduce molecular oxygen to water, and their catalytic mechanism is often

accompanied by formation of ROS. Regulation of complex IV function through feedback inhibition allows the control of ROS production (Ramzan *et al.* 2020). Complex IV activity has been found to be decreased in fibroblasts, SN neurons, and the frontal cortex of post-mortem brain tissue from PD patients (Holper *et al.* 2019; Lee *et al.* 2018; Reeve *et al.* 2018). Interestingly, it was shown that complex IV protein expression decreases in correlation with increasing α -synuclein aggregation in SN neurons during disease progression of PD (Lang *et al.* 2021). Both wildtype and mutant α -synuclein molecules were shown to form specific protein-protein interactions with complex IV (Elkon *et al.* 2002).

The proton gradient generated from the electron transfer through complex I, III and IV drives the proton motive force required to synthesise ATP via the ATP synthase, or complex V (EC 7.1.2.2). Complex V is composed of 2 domains, F_0 and F_1 . Complex V serves as an ion channel on the inner mitochondrial membrane where protons pass through F_0 domain from the intermembrane space into the mitochondrial matrix, and the energy of this process derives a conformational change in the F_1 domain allowing the synthesis of ATP from ADP and inorganic phosphate (Jonckheere *et al.* 2012).

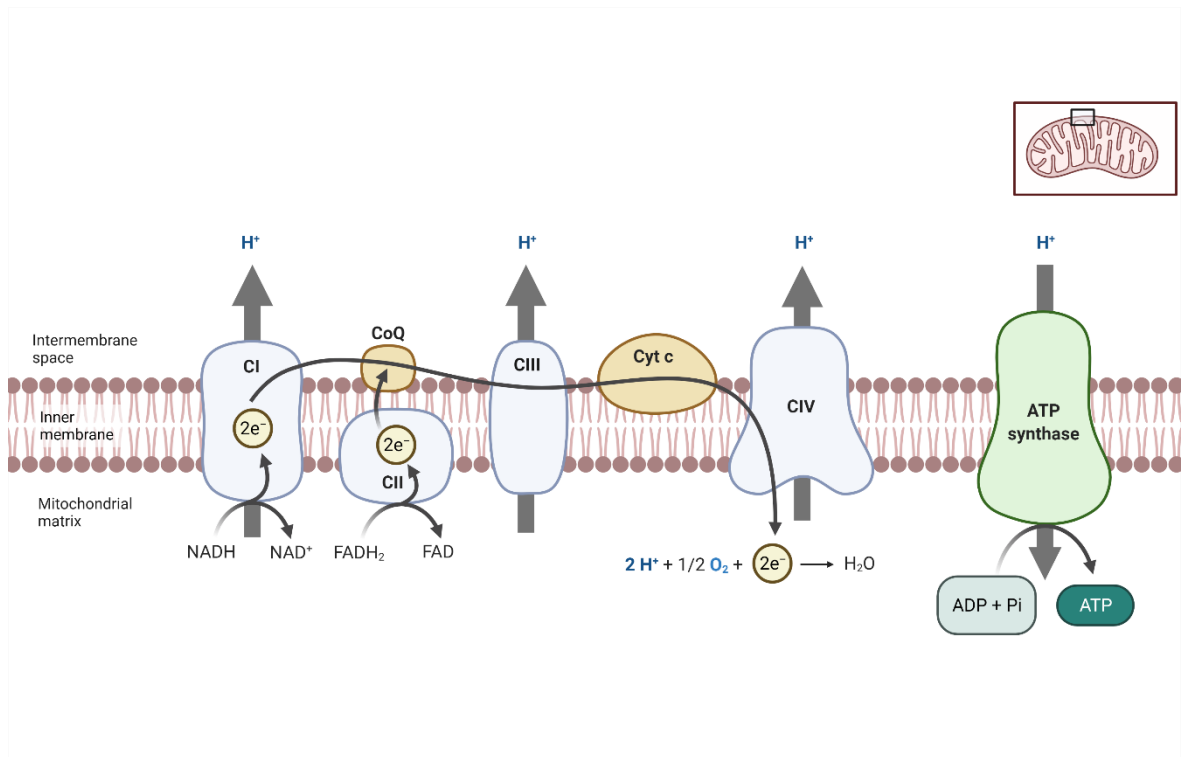


Figure 4 The mitochondrial electron transport chain. The ETC is a series of 5 protein complexes that facilitate the transport of electrons from electron donors to electron acceptors (CI-IV) via redox reactions resulting in the oxidation of molecular oxygen to water and the formation of ATP, the principal form of energy in the cells. Cyt c: cytochrome c. CoQ: coenzyme Q.

1.4.1.3. Mitochondrial impairment in PD

Mitochondrial impairment in PD has been considered a key factor in the pathology following the discovery of a case of drug abusers who rapidly developed parkinsonian symptoms after injection of an illegal substance contaminated with 1-methyl-4-phenyl-1,2,3,6-tetrahydropyridine (MPTP, Langston 2017; Langston *et al.* 1984). MPTP is metabolised by MAO-B to 1-methyl-4-phenylpyridinium (MPP⁺) which is then taken up by dopaminergic neurons specifically via the dopamine transporter (DAT, Gainetdinov *et al.* 1997; Heikkila *et al.* 1984). In dopaminergic neurons, MPP⁺ impairs OXPHOS by inhibiting the transfer of electrons from complex I to ubiquinone. The exact mechanism remains unclear but it is thought to bind at a hydrophobic pocket in a location close to the ubiquinone binding site, preventing its reduction (Nicklas *et al.* 1985; Fendel *et al.* 2008; Krueger *et al.* 1993). This finding has inspired an area of research linking mitochondrial impairment to PD that included landmark studies demonstrating decreased activity of mitochondrial complex I in in the SN of post-mortem brain tissue from PD patients (Schapira *et al.* 1990; Parker *et al.* 1989). Subsequently, mitochondrial complex I activity has been documented to be decreased in brain tissue, platelets, fibroblasts and muscle cells of patients with PD (Lezi and Swerdlow 2012). Interestingly, inhibition of mitochondrial complex I by rotenone was shown to induce dopamine and serotonin turnover. Using the neuronal cell line SH-SY5Y, de la Fuente and colleagues (2017) documented increased extracellular media concentration of DOPAC and 5-HIAA following inhibition of complex I using rotenone. This finding suggests a mechanism through which complex I inhibition may result in the depletion of dopamine and serotonin observed in PD. Because dopamine and serotonin

degradative pathways share similar enzymes to produce DOPAC and 5-HIAA (MAO and ALDH), the mechanism of induction might involve increased MAO enzyme activity. MAO activity produces H₂O₂ as a by-product therefore, increased MAO activity might explain increased oxidative stress and dopamine and serotonin depletion observed in PD (de la Fuente et al. 2017). Several studies associate environmental exposure to toxins such as rotenone and paraquat to PD. Interestingly, both rotenone and paraquat are demonstrated to inhibit mitochondrial complex I (Day *et al.* 1999; Betarbet *et al.* 2000). Following this, studies in specimens from PD patient also presented evidence for the impairment of the other mitochondrial ETC complexes (II-IV, Lin *et al.* 2020; Lopez-Fabuel *et al.* 2017). For example, studies in fibroblasts from PD patients with *PINK1* mutations, complex IV protein expression was demonstrated to be significantly decreased in these cells compared to controls (Lopez-Fabuel *et al.* 2017). In addition, a recent study by Chen and colleagues (2021) demonstrated that mitochondrial ETC dysfunction in PD is potentially more widespread than previously thought, where reduced protein expression of all 5 complexes in post-mortem midbrain tissue from PD patients was documented (Chen *et al.* 2021a).

Evidence for the contribution of mitochondrial impairment to PD pathology is further enforced by evidence from studies of the genetic forms of PD. Many genetic mutations that are associated with either disease incidence or increased disease risk are mutations in genes coding for proteins involved directly or indirectly in mitochondrial function (Ammal Kaidery and Thomas 2018). For example, a recent study has uncovered a causative effect of a rare genetic mutation in a gene coding for one of the complex III subunits for a form of autosomal recessive PD (Lin *et al.* 2020). In mammalian ETC, most ETC

complexes exist as part of a supercomplex. With regard to complex I, it is rarely found free and often associated in a supercomplex with complex III. This finding demonstrate the potential cascade of events following loss of complex III in the presence of mutations, leading to a reduction in complex I (Lopez-Fabuel *et al.* 2017; Acín-Pérez *et al.* 2004). In addition, mutations in the gene that codes for Parkin, an E3 ubiquitin ligase with mitochondrial localisation, cause an autosomal recessive juvenile form of PD (Kitada *et al.* 1998). To date, *Parkin* mutations account for the most prevalent form of autosomal recessive PD (Koros *et al.* 2017). Parkin facilitates ubiquitination of mitochondrial proteins prior to initiation of mitophagy (Schapira 2011). Studies of patient fibroblasts expressing mutant Parkin documented decreased complex I activity and ATP production as well as perturbed mitochondrial morphology (Mortiboys *et al.* 2008). PTEN-induced putative kinase, or PINK1, is a ubiquitously expressed protein harbouring a mitochondrial targeting sequence. Like Parkin, it is involved in the process of mitophagy, where it is recruited to the mitochondrial membrane and becomes ubiquitinated by Parkin, triggering mitophagy (Narendra *et al.* 2010). Mutations in *PINK1* are linked to another form of autosomal recessive PD (Schapira 2011; Valente *et al.* 2004). In addition to its roles in facilitating mitophagy, patient fibroblasts and neurons carrying mutations in *PINK1* showed diminished activity of complex I that is believed to be secondary to loss of function of PINK1 (Morais *et al.* 2014). DJ1 is a protein that can be found in the mitochondrial intermembrane space and matrix. The exact function of DJ1 is still unclear however, research indicates that it carries antioxidant functions (Wilson 2011; Andreeva *et al.* 2019). Mutations in DJ1 have been associated with an autosomal recessive form of PD (Bonifati *et al.* 2003). In dopaminergic neuronal models

possessing homozygous mutations in *DJ1*, loss of function triggered an increase in mitochondrial oxidative stress, accompanied by decreased basal respiration and altered ETC complex integrity, strengthening the evidence for the role of DJ1 in mitochondrial function (Burbulla *et al.* 2017; Heo *et al.* 2012). The effect of loss of DJ1 on mitochondrial function could potentially be due to a role of DJ1 in regulating complex I activity, as DJ1 was found to co-localise with complex I and the loss of which resulted in reduced complex I activity (Hayashi *et al.* 2009). Mutations in α -synuclein were the first mutations to be associated with an autosomal dominant inheritance of PD (Polymeropoulos *et al.* 1997a). Although α -synuclein is normally present in the cytoplasm, a fraction of α -synuclein can also be found in the mitochondria (Li *et al.* 2007). Studies have demonstrated that α -synuclein could interact and inhibit mitochondrial protein import machinery leading to excessive ROS production. It was also shown that α -synuclein can accumulate in the mitochondrial matrix and interfere with complex I function, triggering mitophagy (Di Maio *et al.* 2016; Chinta *et al.* 2010; Devi *et al.* 2008). Mutations in the gene that codes for the mitochondrial polymerase gamma 1 (POLG1) have been associated with an increased risk of PD. PLOG1 is a protein that is targeted into the mitochondria and functions to control mitochondrial DNA synthesis, replication and repair (Hudson *et al.* 2007).

Mitochondrial impairment is not unique to PD, several studies also demonstrated the involvement of mitochondrial impairment in the pathology of other neurodegenerative disorders (Lezi and Swerdlow 2012). Alzheimer's disease (AD) is the most common neurodegenerative disorder. It is caused by extracellular aggregation of amyloid β proteins and the formation intracellular tau protein tangles that lead to neuronal cell death and neurodegeneration (Antuono

and Beyer 1999). Studies suggest that amyloid β aggregates have a role in disrupting mitochondrial respiration and redox state, mitochondrial DNA maintenance and protein import. In addition, tau tangles have been shown to influence mitochondrial dynamics and quality control. They can trigger mitochondria morphological changes, disrupt mitochondrial fusion and fission, and decrease mitochondrial metabolism (Briston and Hicks 2018). In addition, studies have documented decreased activity of several mitochondrial enzymes including complex IV, α -ketoglutarate dehydrogenase and pyruvate dehydrogenase in AD (Swerdlow and Kish 2002).

Amyotrophic lateral sclerosis (ALS) is a neurodegenerative disorder caused by degeneration of the upper and lower motor neurons. Only 10% of disease cases are familial, and the most common cause of which is believed to be mutations in the gene coding for the enzyme superoxide dismutase 1 (SOD1). SOD1 is a ubiquitous antioxidant enzyme that converts superoxide radicals to H_2O_2 and can be found in the cytoplasm and the mitochondria (Abati *et al.* 2020). Cellular and animal models of ALS expressing mutant form of SOD1 show mitochondrial alterations such as fragmentation and vacuolation, perturbation of the activity of the ETC complexes, depolarised mitochondrial membrane potential and mitochondrial calcium dyshomeostasis (Swerdlow *et al.* 2000).

Huntington's Disease (HD) is an autosomal dominant inherited neurodegenerative disorder caused by a CAG nucleotide repeat expansion in the *Huntingtin* (HTT) gene. The disease is characterized by chorea as a result of defective GABAergic medium spiny striatal neurons (Ghosh and Tabrizi 2018). Impaired ETC complex activity and cellular energy state have been documented in HD well before the discovery of the causative *HTT* gene expansion (Jenkins *et*

al. 1993). Dysfunctional complex II is strongly associated with HD and as a result, complex II inhibitors are used in research to model the disease (Benchoua *et al.* 2006).

1.4.2. Lysosomes:

The lysosomes, first described in the 1950s by Christian De Duve, are spherical cellular organelles that have an acidic lumen and filled with more than 60 different types of hydrolases enclosed in a phospholipid bilayer (De Duve 2005; Straus 1954). Their structure makes them perfectly suited for their main function as the cells' primary site for degradation and recycling of proteins, lipids, and carbohydrates (Zhang *et al.* 2021). The acidic lumen of the lysosomes is maintained mainly through the action of the transmembrane proton pump, vacuolar-type ATPase (v-ATPase). v-ATPase actively transports protons into the lysosomal lumen against a concentration gradient using the energy from ATP hydrolysis (Forgac 2007). Lysosomes are the end point of the endosomal-lysosomal pathway, a pathway that functions to internalise, transport and recycle various cellular molecules (Hu *et al.* 2015). Molecules destined for degradation arrive at the lysosomes either from the extracellular matrix or the cell membrane through the process of endocytosis, or from the cytoplasm through the different types of autophagy (Luzio *et al.* 2009; Mizushima *et al.* 2008). Lysosomes are formed from the fusion of endosomes with vesicles originating from the Golgi network (Saftig and Klumperman 2009). Lysosomal biogenesis is regulated by the transcription factor EB (TFEB) which translocates into the nucleus to induce the transcription of a network of genes involved in lysosomal formation and function known as the coordinated lysosomal expression and regulation network (CLEAR). These genes include genes that code for the v-ATPase, lysosomal enzymes, and proteins (Settembre *et al.* 2012; Palmieri *et al.* 2011).

In addition to their degradative capacity, lysosomes perform other key functions in the cell. For example, lysosomes can sense and react to changes in

cellular nutrient homeostasis through mTOR signalling. For example, starvation inhibits mTOR signalling, increasing autophagosome formation and stimulating lysosomal biogenesis to increase cell degradative capacity and recycling (Zhou *et al.* 2013; Settembre *et al.* 2011). In addition, lysosomes have a role in cellular immunity and defence, where pathogens that enter the cell are engulfed by autophagy and delivered to the lysosomes for degradation (Nakagawa *et al.* 1997). Furthermore, lysosomes play a vital role in maintaining the lipid membrane homeostasis through the sphingolipid pathway. The sphingolipid pathway results in the synthesis of ceramides, an important precursor for synthesis of sphingolipids, which are constituents of lipid membranes and axonal myelin sheath (Quinville *et al.* 2021). Ceramides are synthesized in the lysosomes through the breakdown of glucosylceramides into glucose and ceramides. This reaction is catalysed by the lysosomal enzyme glucocerebrosidase (GBA). Other lysosomal enzymes also function in the sphingolipid pathway like sphingomyelinase, ceramidase, and β -galactosidase. Deficiencies in the lysosomal enzymes cause lysosomal storage disorders (LSD), where undegraded molecules accumulate within the lysosomes. One of the most common LSD is Gaucher disease, where GBA enzyme activity is deficient, resulting in the accumulation of glucosylceramides (Abed Rabbo *et al.* 2021; Baris *et al.* 2014)

Two classes of lysosomal proteins are essential for the proper function of the lysosomes: lysosomal enzymes and lysosomal membrane proteins. Lysosomal enzymes include glycosidases, nucleases, proteases, phosphatases, lipases, and sulfatases. This confers on the lysosomes the ability to degrade an array of cellular molecules. The lysosomal enzymes are synthesized in the

endoplasmic reticulum, then transported through the Golgi network where they are modified and tagged with the lysosomal targeting signalling peptide, mannose-6-phosphate. Once in the acidic lumen of the lysosomes, the mannose-6-phosphate tag is dissociated (Seaman 2004). Lysosomal enzymes are unique because they are acid hydrolases, enzymes that function optimally at acidic pH (pH 4-5) in contrast to most of the cellular enzymes that function optimally at neutral pH (pH 7). This is a protective measure to prevent uncontrolled degradation of cellular components (Mindell 2012).

GBA (EC 3.2.1.45) is a lysosomal enzyme responsible for the production of ceramides from glucosylceramide molecules. Another substrate for GBA is glucosphingosine, which is degraded to glucose and sphingosine. GBA can be found in the lysosomes of all tissues as a membrane associated protein with a pH optimum of 5.5. It is delivered to the lysosomes through a pathway that is thought to be independent from the manose-6-phosphate pathway generally employed to deliver lysosomal proteins into the lysosomes. Instead, it is delivered through binding the lysosomal transporter protein LIMP-2 (Reczek *et al.* 2007). Once in the lysosomes, GBA becomes activated by the protein saposin C (Tamargo *et al.* 2012). GBA can be specifically and irreversibly inhibited by conduritol B epoxide (CBE), a glucose analogue, through the formation of covalent bonds at the active site of the enzyme (Ogawa *et al.* 1999). The first report of GBA mutations being the cause of GD was in 1965 when the enzyme was isolated from the spleen of GD patients (Brady *et al.* 1965). The finding inspired the use of enzyme replacement therapy in treatment of GD, which supplies the cells with a recombinant form of the GBA enzyme (Deegan and Cox 2012).

The functions of the lysosomes are also supported by a number of highly specialised proteins residing in within the lysosomal membrane. The lysosomal membrane proteins (LMP) carry out several functions such as transport across the membrane, motility, fusion, and autophagy (Schwake *et al.* 2013). One example of LMP is v-ATPase. v-ATPase is a multimeric membrane-bound protein complex that is structurally similar to the mitochondrial ETC ATP synthase, comprised of two subunits, the membrane bound V_0 and the cytosolic V_1 . V_1 mediates the binding and the hydrolysis of ATP which provides the needed energy for proton translocation across the membrane through V_0 (Figure 5, Beyenbach and Wieczorek 2006). The activity of v-ATPase is regulated via dissociation of the protein complex into membrane bound V_0 and soluble V_1 . This is a reversible process that inhibits proton translocation across the lysosomal lumen (Kane 1995). v-ATPase activity can also be regulated at the transcriptional level by varying its subunit composition. Mammalian v-ATPase subunits are encoded for by multiple genes, and each subunit has multiple isoforms (Toei *et al.* 2010). Different isoforms of each subunits have preferential expression in different tissues (Smith *et al.* 2005).

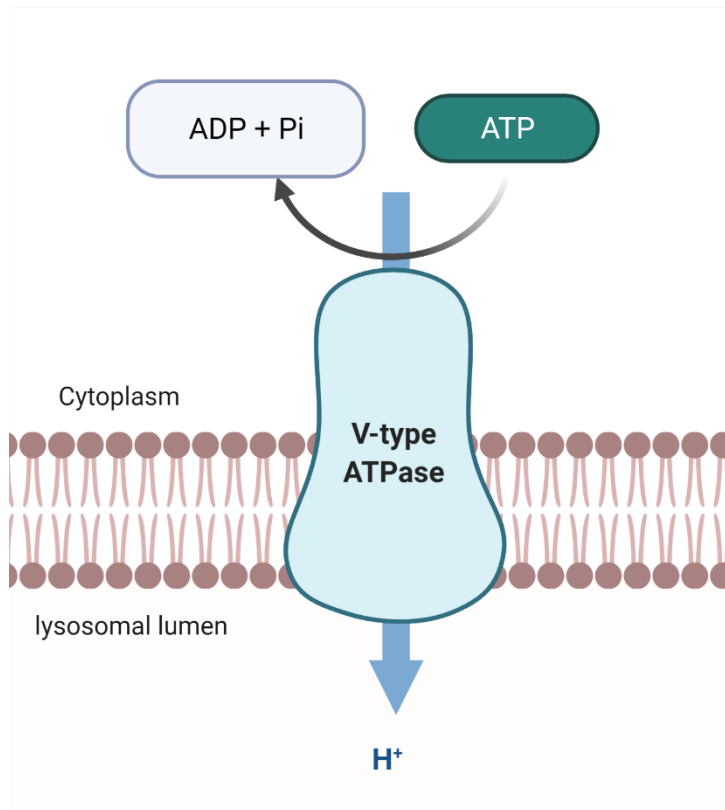


Figure 5 Lysosomal v-ATPase mechanism of action. V-type ATPase uses the energy of ATP dissociation into ADP and inorganic phosphate to translocate protons into the lysosomal lumen against a concentration gradient. Pi: inorganic phosphate

1.4.2.1. Lysosomal impairment in PD

Although mitochondrial impairment has been considered a primary pathogenic event in PD, more and more studies are emerging on lysosomal impairment being another key player in the pathology. Evidence is supported by both genetic and functional studies, with big contributions from studies of LSD (Robak *et al.* 2017). The link between lysosomal impairment and PD initially came from GD patients, an LSD caused by homozygous mutation in the gene that codes for the lysosomal GBA. An increasing number of studies reported that GD patients exhibited both GD and PD phenotypes (Westbroek *et al.* 2011; Sidranskyl 2009; Siebert *et al.* 2014). For example, one study that analysed CSF neurotransmitter metabolites in a GD patient with PD symptoms confirmed perturbed dopamine and serotonin systems (Alonso-Canovas *et al.* 2010). Since then, through studies of GD carriers, heterozygous mutations in *GBA* have been classified as the highest risk factor for PD worldwide (Sidranskyl 2009). The association between *GBA* and PD was also made on the protein level, where Gegg and colleagues (2012) have reported a significant decrease in *GBA* enzyme activity and protein level in post-mortem brain tissue from idiopathic PD patients in the absence of mutations, further supporting the contribution of *GBA* and lysosomes to PD pathology (Gegg *et al.* 2012). Like *GBA*, α -galactosidase A (*Gal-A*) is a lysosomal enzyme involved in the sphingolipid pathway. Deficiency in *Gal-A* results in accumulation of glycosphingolipids causing the LSD, Fabry disease. Following measurement of *Gal-A* enzyme activity in post-mortem brain tissue samples from idiopathic PD patients, Nelson and colleagues (2018) reported a decrease in both enzyme activity and protein level of *Gal-A*. They have also reported a decrease in the lysosomal cathepsin D enzyme activity (Nelson

et al. 2018; Chu *et al.* 2009). Cathepsin D is an aspartyl protease that is highly expressed in the brain and has been shown to play a central role in degradation of α -synuclein (Stoka *et al.* 2016; Aufschnaiter *et al.* 2017). Cathepsin B is another member of the lysosomal cathepsin family of proteases that has been classified as a risk locus for PD by genome wide association studies carried out on a PD cohort of more than 6 thousand subjects (Chang *et al.* 2018).

ATP13A2 is a gene that codes for a lysosomal p-type ATPase enzyme involved in active transport of cations. Mutations that cause loss-of-function result in a rare autosomal recessive type of PD known as Kufor-Rakeb syndrome (Ramirez *et al.* 2006). Loss of function studies in PD patients cells harbouring mutations in *ATP13A2* have documented an increase in lysosomal pH and impaired lysosomal degradation compared to control (Dehay *et al.* 2012). Niemann-Pick type C disease is a form of autosomal recessive LSD caused by homozygous mutations in the *NPC1* gene, leading to accumulation of cholesterol in the lysosomes (Vanier 2013). Like GBA, heterozygous mutations have been associated with a PD risk (Schneider *et al.* 2021).

Lysosomal dysfunction is not unique to PD, it has also been observed in other neurodegenerative diseases. In AD, clearance of amyloid- β tangles mainly takes place through autophagy. Ultrastructural analysis of post-mortem AD brain tissue revealed an accumulation of lysosomes containing autophagic vacuoles due to defects in lysosomal degradative capacity (Nixon *et al.* 2005). Accumulation of autophagic vacuoles in the cytosol was also seen in lymphocytes of HD patients (Nagata *et al.* 2004). Finally, mutations in the gene that codes for the protein Ubiquilin-2 (UBQLN2), are associated with an increased risk for ALS (Ajroud-Driss and Siddique 2015). UBQLN2 appears to facilitate

autophagosome-lysosome fusion, and loss of function was shown to impair lysosomal acidification and degradative capacity (N'Diaye *et al.* 2009; Şentürk *et al.* 2019).

1.4.3. Glutathione

Glutathione (GSH) is the most abundant thiol molecule in the cell. GSH is a tripeptide molecule synthesized from the sequential condensation of glutamate, cysteine, and glycine to form *L*- γ -glutamyl-*L*-cysteinyl-glycine by the enzymes glutamyl-cysteine ligase (GCL) and glutathione synthase (GS), respectively (Lu 2014). GSH is the most important player in the cellular antioxidant defence system, working to maintain cellular redox balance (Gerard-Monnier and Chaudiere 1996). It plays additional roles in detoxification of xenobiotics, regulating apoptosis, cell signalling and presents a reservoir of cysteine (Forman *et al.* 2010). The majority (80-85%) of cellular GSH is present in the cytoplasm, in concentrations of 1-2 mM (Meredith and Reed 1982). GSH is resistant to cellular degradation because of the iso-peptide bond that connects glutamate to cysteine through the γ -carboxyl group instead of the α -carboxyl group. As a result, only one enzyme can break this bond, γ -glutamyl transpeptidase, which is only present on the outer membranes of some cell types (Lu 2014).

As an antioxidant, GSH functions to reduce ROS resulting in the formation of oxidized glutathione, also known as glutathione disulfide (GSSG). The ratio of reduced/oxidized glutathione (GSH/GSSG) is used as a biomarker of cellular oxidative state. This function of GSH to reduce ROS is largely facilitated by glutathione peroxidase (GPx). GPx reduces hydrogen peroxide and lipid peroxide while oxidizing GSH to produce GSSG. GSSG can then be recycled back to GSH by glutathione reductase enzyme. This reaction requires NADPH as a reducing agent, a product of the pentose phosphate pathway and the enzyme action of malate dehydrogenase and isocitrate dehydrogenase (Lu 2009; Minard *et al.* 1998). This process forms the cellular redox cycle through which ROS can be

eliminated and GSH/GSSG ratio maintained. When cells are undergoing severe oxidative stress, this can lead to depletion of cellular GSH levels (Figure 6, Forman *et al.* 2010).

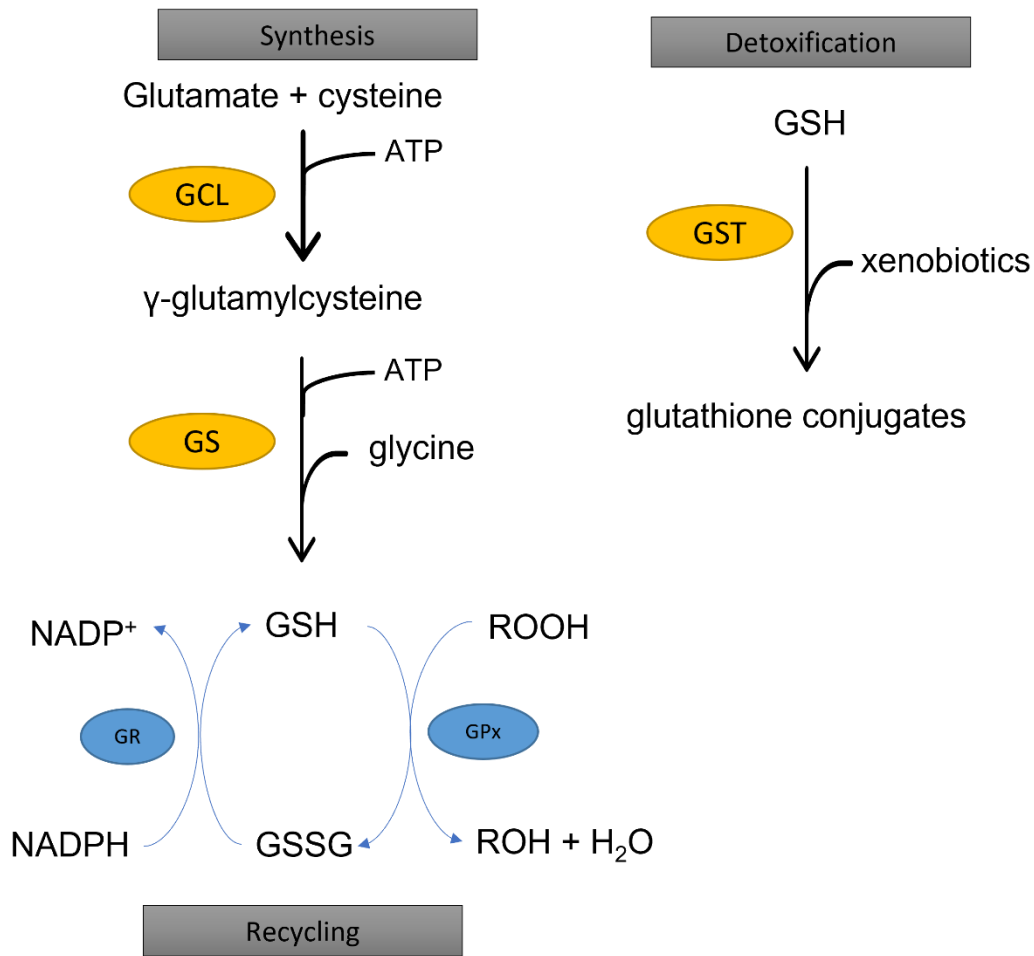


Figure 6 Regulation of glutathione. GSH: glutathione. GCL: glutamylcysteine ligase. GS: glutathione synthase. GSSG: glutathione disulfide. GR: glutathione reductase. GPx: glutathione peroxidase. ROOD: organic peroxides. GST: glutathione S-transferase.

Oxidative stress and ROS production are normal part of metabolism (Apel and Hirt 2004). Neurons are one of the most metabolically active cells in the body, thus maintaining redox balance in neurons is of utmost importance (Cobley *et al.* 2018). GSH function is important in dopaminergic neurons specifically, due to the added burden of H₂O₂ generated from dopamine metabolism in addition to the requirement for detoxification of dopamine quinones (Spina and Cohen 1989). GSH is also important because dopaminergic neurons have high levels of cellular iron where GSH can form several iron complexes like iron(II)glutathione (Sofic *et al.* 1992). This protects iron molecules from taking part in reactions that can increase cellular oxidative stress, like the Fenton reaction (Reichert *et al.* 2020). The importance of GSH for neuronal survival and function has been demonstrated by a number of studies. It was suggested that, in PC12 rat neuronal cells, GSH may play a role in regulation of TH and dopamine transporter activity (Jurma *et al.* 1997). Garrido and colleagues (2011) have shown that down-regulation of glutathione synthase enzyme via RNA silencing in different brain regions of adult rats resulted in progressive degeneration of nigral dopaminergic neurons specifically, while extra-nigral and extra-striatal neurons were less affected (Garrido *et al.* 2011). Using PC12 cells, Jha and colleagues (2000) showed that antisense knockdown of GCL enzyme resulted in 50% decrease of GSH levels. This decrease resulted in increased cellular oxidative stress and impaired mitochondrial function in the form of selective inhibition of complex I, 70% decrease in ATP production and 60% decrease in mitochondrial oxygen consumption rate (Jha *et al.* 2000). siRNA silencing of glutaredoxin, a redox enzyme that uses GSH as a cofactor, has led to 30% reduction in mitochondrial complex I function and an increase in oxidative stress (Lee *et al.* 2009). These

studies demonstrate the importance of maintaining the intricacy of the cellular redox state and the important role GSH plays in preserving the balance.

Dysregulated GSH system is seen in a number of neurodegenerative diseases (Aoyama 2021). In PD specifically, a disease characterised by increased cellular oxidative stress, decreased GSH levels in the SN have been documented (Sofic *et al.* 1992; Jenner *et al.* 2003). Indeed, there are several lines of evidence that point to a dysregulated GSH system in PD. For example, decreased levels of GSH in the SN, putamen, caudate nucleus, globus pallidus, and cerebral cortex areas of the brain have been documented in PD patients (Sian *et al.* 1994; Holmay *et al.* 2013; Pearce *et al.* 1997). GSSG levels are also documented to be decreased (Sian *et al.* 1994). In addition, the activity of GCL, the rate limiting enzyme of GSH synthesis, was found to be significantly lower in PD (Kang *et al.* 1999), and the activity level of GPx, the enzyme responsible for detoxification of H₂O₂, was found to be mildly reduced in PD patients at post-mortem (Kish *et al.* 1985). Furthermore, mutations in the gene that codes for the enzyme glutathione-S-transferase has been associated with PD (Cornetta *et al.* 2013).

Depleted GSH levels have also been documented in other neurodegenerative diseases. In AD, the most common neurodegenerative disorder, abnormal aggregation of amyloid- β results in increased cellular oxidative stress, which plays a central role in pathology (Hodgson *et al.* 2013). Decreased GSH levels have been documented in the frontal cortex of post-mortem brain tissue from AD patients (Mandal *et al.* 2015). Decreased GSH levels were also documented in brain of ALS patients, and was most prominent in the motor cortex (Weiduschat *et al.* 2014). Finally, lower GSH levels were also

documented in plasma of Huntington disease patients and carriers compared to control (Klepac *et al.* 2007).

1.5. Mitochondrial-lysosomal crosstalk

The exact molecular mechanism of PD remains unclear however, there's a growing support for the involvement of both mitochondria and lysosomes in disease pathology. Studies of both causative and risk factor genes for PD revealed that they have either a direct or indirect association with mitochondrial or lysosomal functions. In addition, studies in disease models carrying mutations in genes coding for mitochondrial proteins show lysosomal dysfunction. Similarly, studies in disease models carrying mutations in lysosomal proteins demonstrate compromised mitochondrial function (Plotegher and Duchen 2017). Taken together, this suggest that there exists a dynamic crosstalk between mitochondria and lysosomes, beyond the scope of mitophagy, and the consequence of which potentially play part in PD pathology. This notion is encouraged by a recent study by Kim and colleagues (2021) that demonstrated, for the first time, mitochondrial and lysosomal contacts in neuronal cells. The mechanism of contact was documented to require the activity of the Rab GTPase, RAB7, which is present on lysosomal membranes. In its GTP-bound state, RAB7 facilitates the tethering of mitochondria to lysosomes, and upon hydrolysis of GTP, contact untethering takes place. Furthermore, these contacts appear to depend on functional lysosomal GBA enzyme, whereby loss of function in GBA disrupts contact dynamics (Kim *et al.* 2021). In addition, de La Fuente and colleagues (2017) demonstrated that upon inhibition of mitochondrial complex I using rotenone in SH-SY5Y cells, an increase in dopamine and serotonin turnover was observed, evident by increased extracellular concentration of DOPAC and 5-HIAA. Interestingly, similar results were obtained following inhibition of lysosomal GBA using CBE. The results suggest that both mitochondrial dysfunction and

lysosomal dysfunction may play part in PD pathology. The exact mechanism however, remains unclear (de la Fuente *et al.* 2017).

Another supporting evidence of the interconnectedness of mitochondria and lysosomes was the finding that both mitochondria and lysosomes share an intersected biogenesis machinery. Many lysosomal genes are activated and regulated by the transcription factor EB (TFEB) whereas mitochondrial genes are regulated by the PGC-1 family of co-activators (Settembre *et al.* 2013; Agarwal *et al.* 2017). A study of mitochondrial mitophagy found that following carbonyl cyanide m-chlorophenylhydrazone (CCCP) induction of mitophagy, an increase in the transcription and translation of lysosomal genes, including GBA and cathepsin D, was documented. The mechanism appears to involve activation of TFEB which, interestingly, was found to modulate PGC1 α activity, which is a transcription coactivator of mitochondrial genes. This suggests that TFEB might play a role in the induction of both lysosomal and mitochondrial biogenesis (Figure 7, Ivankovic *et al.* 2016). A similar study by Fernandez-Mosquera and colleagues (2017) supports a connected mitochondrial and lysosomal biogenesis. In response to rotenone or CCCP treatment of mouse embryonic fibroblasts (MEF) and HeLa cells, the transcription of TFEB was rapidly up regulated. This points to a mechanism whereby acute mitochondrial dysfunction, induced activation and nuclear translocation of the lysosomal regulator, TFEB (Fernandez-Mosquera *et al.* 2017). Therefore, TFEB potentially acts as a master regulator of not only lysosomal genes but also mitochondrial genes through modulation of PGC1 α .

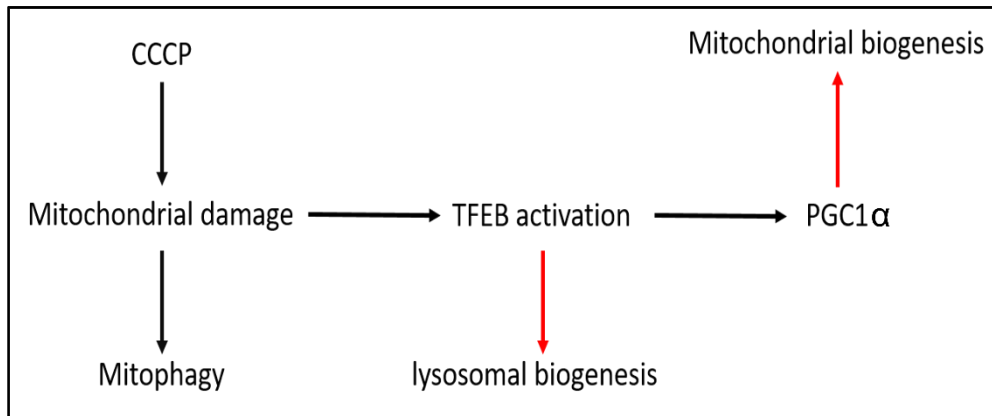


Figure 7 TFEB activation induces mitochondrial and lysosomal biogenesis. Stimulation of mitophagy using carbonyl cyanide m-chlorophenylhydrazone (CCCP) results in nuclear translocation of the transcription factor EB (TFEB). TFEB induces expression of lysosomal proteins and PGC1 α . PGC1 α is a co-activator of mitochondrial protein expression and inducer of mitochondrial biogenesis. (adapted from Ivankovic *et al.* 2016).

1.5.1. Impact of mitochondrial dysfunction on lysosomes

Optimal mitochondrial function appears to be a prerequisite for lysosomal function. This statement is supported by a number of studies investigating the cellular effects of loss of function of mitochondrial proteins. In iPSC dopaminergic neurons derived from PD patient fibroblasts carrying homozygous mutation in the gene coding for mitochondrial DJ1, Burbulla and colleagues (2017) observed increased dopamine oxidation by culture day 70. The formation of neuromelanin plaques was also observed. Interestingly, the activity of lysosomal GBA was found to be decreased and by culture day 180, lysosomal proteolysis was completely diminished. The decreased activity of GBA could potentially be a result of dopamine oxidation as it was found that the metabolites of dopamine oxidation can modify the catalytic site of GBA. The study suggests that the accumulation of oxidized dopamine metabolites following mitochondrial dysfunction contributes to impaired lysosomal function. This hypothesis was supported by the finding that long-term treatment with mitochondrial targeted antioxidants improved lysosomal function (Burbulla *et al.* 2017). In addition to inducing lysosomal dysfunction, depletion of DJ1 appears to play a role in autophagy by initiating the expression of autophagic marker LC3 protein in the neuroblastoma cell line, M17. However, it is still unclear whether the role is direct, or indirect via increased ROS production which was shown to induce autophagy (Thomas *et al.* 2011; Chen and Gibson 2008). PINK1 is a mitochondrial localised kinase that regulates mitochondrial homeostasis and mitophagy. Deletion of PINK1 in mouse embryonic fibroblasts (PINK1 KO MEF) results in mitochondrial fragmentation and loss of ETC complexes' function. Interestingly, PINK1 KO MEF also exhibited large vacuoles in their cytoplasm that

are positive for the lysosomal marker LAMP1, in addition to altered lysosomal function. The mechanism appears to involve increased production of ROS, as antioxidants were able to rescue the lysosomal function. This is also supported by the observation that exogenous H₂O₂ also induces the formation of the large LAMP1 positive vacuoles. However, a decrease in ATP (a consequence of compromised mitochondrial function) may also play a role as neurons put under ATP-deprived conditions also exhibit large vacuole formation (Demers-Lamarche *et al.* 2016). The same study also looked at the effects of loss-of-function of mitochondrial apoptosis-induced factor (AIF) and the mitochondrial GTPase OPA1 on lysosomes. Like PINK1 deletion, mitochondrial fragmentation, loss of ETC complexes' function, in addition to enlarged lysosomal vacuoles were observed (Demers-Lamarche *et al.* 2016). Finally, mutations in the SOD1 results in the accumulation of dysfunctional mitochondria in the axons of motor neurons, triggering axonal degeneration and denervation. A study by Xie and colleagues (2015), demonstrated that mutant SOD1 caused lysosomal defects and interfered with mitophagy. In an adult mice model of ALS carrying mutant SOD1, accumulation of autophagic vacuoles engulfing damaged mitochondria was observed in motor neuron axons (Xie *et al.* 2015).

Effects of impaired mitochondria on lysosomes was also documented upon deletion of the mitochondrial transcription factor A (Tfam). Tfam is an important protein that plays a role in replication and protection of mitochondrial DNA (mtDNA). Tfam protein expression was documented to be decreased in brains of PD patients (Kang *et al.* 2018). Deletion of Tfam in mouse CD⁴⁺ T cells resulted in decreased copy number of mtDNA, reduced mRNA expression of mitochondrial complex I, and loss of fatty acid β oxidation. Notably, these cells

also exhibited enlarged lysosomes with decreased lysosomal cathepsin B enzyme activity, lysosomal Ca^{2+} mobilisation and increased lysosomal pH. Increased nuclear translocation of TFEB was also documented, which is important for activating lysosomal biogenesis. Lipid accumulation was also observed, a phenomenon usually documented in LSD, indicating abnormal lysosomal degradation (Baixauli *et al.* 2015).

1.5.2. Impact of lysosomal dysfunction on mitochondria

The effects of lysosomal impairment on mitochondria are best demonstrated in studies of LSD. Because mitochondrial homeostasis depends on functional lysosomes during the process of mitophagy, secondary defects in mitochondrial function are a major event in LSD. Mitochondrial dysfunction, decreased membrane potential, morphological abnormalities and altered mitochondrial mass are a common pathological phenotype in neurons affected by LSD (Plotegher and Duchen 2017b). For example, in a mouse model of GD, loss of function of GBA resulted in mitochondrial fragmentation, lower membrane potential and decreased activity of ETC complexes I, II and III (Osellame *et al.* 2013). In addition, in primary neurons from a mouse model of NPC, a disease that results in impaired cholesterol trafficking, Yu and colleagues (2005) documented lowered mitochondrial membrane potential, decreases ETC ATP synthase activity and, consequently, lower cellular ATP levels (Yu *et al.* 2005). Similar findings of perturbed mitochondrial energetics were demonstrated in muscle cells from an acid α -glucosidase knockout mouse model of Pompe disease, an LSD that results in glycogen build up in the lysosomes (Lim *et al.* 2015).

1.5.3. Mechanisms of mitochondrial and lysosomal crosstalk

There are a couple of suggested mechanisms for mitochondrial-lysosomal crosstalk. Firstly, through formation of membrane contact sites (MCS). MCS are well established events between ER-mitochondria and ER-lysosomes however, they were only recently demonstrated between mitochondria and lysosomes in human HeLa cells and iPSC derived neurons (Kim *et al.* 2021; Wong *et al.* 2018; Cohen *et al.* 2018). MCS may serve as a hub for exchange of different metabolites like lipids, proteins and ions as well as for regulation of organelle biogenesis, growth and trafficking (Prinz *et al.* 2020). Secondly, mitochondrial-lysosomal crosstalk could commence via mitochondrial derived vesicles (MDV). MDV are relatively uniform membrane vesicles that incorporate specific mitochondrial cargo that bud from mitochondria and are directed towards either lysosomes for degradation or peroxisomes for a function that has yet to be elucidated (Sugiura *et al.* 2014). Cargo destined for lysosomes appears to be an early response to ROS and may include oxidized proteins. The type of proteins included depends on the type of stress the mitochondria are undergoing (Soubannier *et al.* 2012). Finally, the finding that mitochondrial ROS may induce lysosomal dysfunction (see section 1.5.1) points to the possibility of ROS, itself, as a mechanism for mitochondrial-lysosomal crosstalk. A study by Zhang and colleagues (2016) has shown that following inhibition of mitochondrial OXPHOS using CCCP, there was an increase in cellular ROS production. The cellular ROS triggered calcium release from the lysosomes via stimulation of lysosomal calcium membrane channels (Zhang *et al.* 2016). Calcium release from the lumen of the lysosomes triggers autophagy, which can remove damaged mitochondria (Di Paola *et al.* 2018).

1.6. SH-SY5Y cell line in Parkinson's research

Appropriate models are imperative for any scientific study. Due to the selectivity of PD pathogenesis towards dopaminergic neurons, dopaminergic neuronal cell models are necessary for studying the disease mechanism and for development of therapeutics (Alberio *et al.* 2012). The SH-SY5Y cell line is one of the most widely used cell line model for neuroscience research, particularly for PD research (Xicoy *et al.* 2017). It is a neuronal cancer cell line, thrice sub-cloned from the parental SK-N-SH neuroblastoma-like cell population originally obtained from a bone marrow biopsy of a neuroblastoma patient in 1970 (Biedler and Schachner 1978; Biedler *et al.* 1973). The SH-SY5Y subclone is characterised as an N-type cell, which are immature neurons; small and rounded cells with thin neurofilaments, characterised by the high expression of dopamine β -hydroxylase, the enzyme that converts dopamine to norepinephrine (Campos Cogo *et al.* 2020; Walton *et al.* 2004; Ross *et al.* 2015).

Despite the wide use of SH-SY5Y cell line in the proliferative state as a model for dopaminergic neurons, the literature is not clear on their suitability, or whether differentiation into a more mature neuronal-like phenotype is necessary (Xicoy *et al.* 2017). For example, Biedler and colleagues (1978), who generated the SH-SY5Y cell subclone, reported that the cells do not produce detectable levels of norepinephrine, a downstream product of dopamine, concluding they are dopaminergic in nature (Biedler and Schachner 1978). A more recent study, however, do report norepinephrine production in proliferative cells, concluding that they are adrenergic in nature (Géraldine *et al.* 2010). Another study report that the cells produces neither norepinephrine nor dopamine but that they do have the ability to convert exogenous dopamine to norepinephrine, prompting

them to conclude the cells are more adrenergic in nature (Balasooriya and Wimalasena 2007). Furthermore, Sahin and colleagues (2021) demonstrated that proliferative SH-SY5Y cells possess larger potassium current when compared to differentiated cells which have more pronounced sodium currents. The higher number of potassium channels on proliferative SH-SY5Y cells is characteristic of cancer cells, concluding that differentiated SH-SY5Y cells possesses electrophysiological characteristics that better resemble neurons than proliferative cells (Şahin *et al.* 2021; Felipe *et al.* 2006). In addition, the use of SH-SY5Y cells is based on the assumption of their dopaminergic phenotype, where many studies report detection of TH expression in the proliferative state (Watabe and Nakaki 2008; Xie *et al.* 2014). However, others could not detect TH in proliferative cells, a finding further supported by undetectable dopamine levels under basal conditions (Mazzulli *et al.* 2006; de la Fuente 2018).

The controversy in the literature is further impeded by the fact that proliferative and differentiated SH-SY5Y cells have been used almost interchangeably in PD research. For example, they have both been used to study the cellular toxicity of MPTP (Goksu Erol *et al.* 2022; Chen *et al.* 2021b). Both proliferative and differentiated cells were used to understand the potential interplay between toxic dopamine metabolism and decreased activity of mitochondrial complex I (Brenner-Lavie *et al.* 2009; Aguirre *et al.* 2012). Finally, they were also used to investigate the effect of GBA loss-of-function on α -synuclein aggregation (Kim *et al.* 2018; Dermentzaki *et al.* 2013).

There are arguments for and against the use of both proliferative and differentiated cells. Proliferative SH-SY5Y cells are locked into early-differentiation stage, have an epithelial-like morphology and express low levels

of neuronal markers (Hong-rong *et al.* 2010). Proliferation and low levels of neuronal markers confer some experimental uncertainty, especially when using the cells as a model for mature neurons in the case of PD. Continuous proliferation means that at any time point, the cells are at different phases of the cell cycle, which may not represent a very homogenous cell population. Successive proliferation and DNA replication induces mutations that could result in cells with different phenotypes following long periods of culture (Santillo 2021). Finally, although the cells are reported to express enzymes of the dopamine pathway and the dopamine transporter, their expression level is relatively low (Presgraves *et al.* 2004). Nonetheless, proliferative cells do possess some advantages. Firstly, they are easier to obtain and maintain. Because of their neuronal-like nature, they allow the study of the basic biology of neuronal cells (Kaur and Dufour 2012). Furthermore, most genes involved in the pathological pathways of PD are intact in proliferative SH-SY5Y cells (Krishna *et al.* 2014). In addition, genetic manipulation of proliferative cells is easier than differentiated, which, for example, allows the inhibition or overexpression PD related genes to understand the cellular mechanisms of familial forms (Falkenburger and Schulz 2006). Finally, some biochemical techniques are better suited for proliferative cells, such as fluorescence-activated cell sorting (FACS, Falkenburger and Schulz 2006)

SH-SY5Y cells can be differentiated into a more mature neuronal-like phenotype (Hong-rong *et al.* 2010). Upon differentiation, the cell cycle becomes synchronised, and proliferation reduces dramatically. The cells acquire a more neuronal morphology, with extended neurites and cellular polarity. Differentiation induces the expression of neuronal-specific markers, enzymes and

neurotransmitters, producing cells that better resemble mature neurons (Kovalevich and Langford 2013). The cells' proliferative nature offers the advantage of large-scale expansion of cell population prior to differentiation and its relatively low cost offers advantage over the use of primary neurons. Another advantage is that SH-SY5Y cells can be differentiated into different neuronal phenotypes depending on the agent used. One of the most commonly used differentiation agents is retinoic acid (RA, Xicoy *et al.* 2017). RA is a vitamin A derivative that has strong differentiation-promoting properties (Melino *et al.* 1997). Despite its wide use to differentiate SH-SY5Y cells to be used as a dopaminergic model, RA differentiation promotes SH-SY5Y cells to a more cholinergic phenotypes, with induced expression of acetylcholine receptors and the enzyme choline acetyl transferase (Lopes *et al.* 2010; Presgraves *et al.* 2004). Another commonly used differentiation agent is 12-O-tetradecanoylphorbol-13-acetate (TPA). TPA was found to increase cellular noradrenaline content of SH-SY5Y cells by almost 200 fold, therefore results in differentiated cells with an adrenergic phenotype (Påhlman *et al.* 1984). To bypass this problem, treatment with RA is commonly sequentially followed by treatment with TPA, which is reported to produce cells of dopaminergic phenotype (Brown *et al.* 2006; Wang *et al.* 2007; Påhlman *et al.* 1984; Presgraves *et al.* 2004). Other less commonly used differentiation agents include brain-derived neurotrophic factor (BDNF) and staurosporine (Hong-rong *et al.* 2010)

In relevance to PD, SH-SY5Y cells have been extensively used to understand the molecular mechanism of the disease, both in its proliferative and differentiated states. However, up to this point, some of these the pathways (dopamine and serotonin metabolism, mitochondrial ETC, lysosomal GBA, and

glutathione levels) have not been characterised and compared between proliferative and differentiated to clarify which phenotype would be more suitable.

1.7. Induced pluripotent stem cell neurons in Parkinson's research:

Human induced pluripotent stem cells (iPSCs) derived neurons are another commonly used cell model for PD. iPSCs were developed in 2006 by Takahashi and Yamanaka, who generated a protocol that allows the reprogramming of terminally differentiated fibroblasts into pluripotent stem cells; cells that can differentiate into various cell types (Takahashi and Yamanaka 2006). Differentiation of iPSCs into dopaminergic neurons makes them a highly advantageous cell model for dopaminergic neurons, especially considering the inaccessibility of human primary neurons. iPSC-derived neurons from familial PD patients can help understand the role of gene mutations in the molecular mechanism of the disease. For example, iPSCs developed from patients carrying PINK1 mutations uncovered the potential role of mitophagy in PD disease mechanism (Seibler *et al.* 2011). Another advantage for use of iPSCs is in drug screening to determine the suitability of certain drugs for patients, paving the path for the era of personalised medicine. This is useful for instance for determining which Parkinson's and Parkinson's related disease patients would benefit from L-DOPA treatment, as there is a highly variable response to L-DOPA treatment between different patients presenting with the same disease (Titova and Chaudhuri 2017). Despite the advantages, there are some disadvantages to the use of iPSC derived dopaminergic neuronal cells. Firstly, generating iPSCs derived cells is a laborious and time-consuming task that requires experience. Secondly, because the iPSCs are derived from patients or healthy individuals, there are some ethical concerns involved (Lopes *et al.* 2017a). Thirdly, there are concerns of genetic instability of iPSCs derived cells, specifically when kept in culture long-term (Doss and Sachinidis 2019). Finally, one of the pitfalls of iPSCs

derived dopaminergic neurons is the lack of a standardised protocol for differentiation. This leads to variability in the differentiation efficiency, yield, quality, cell maturity and phenotype. This variability is further highlighted when the same differentiation protocol is used by different researchers and different laboratories. For example, Chung and colleagues (2016) have demonstrated the patient derived iPSCs neurons exhibited different disease phenotypes when differentiated using two different differentiation protocols, despite coming from the same cell source (Heger *et al.* 2021; Chung *et al.* 2016).

1.8. Hypotheses

- (i) Biochemical similarities and differences exist between proliferative and differentiated SH-SY5Y cells. This at the level of dopamine, serotonin, mitochondria, lysosomes, and glutathione metabolism. Such similarities and differences need to be considered when using this cell line as a model for PD.

- (ii) Alterations in dopamine status have a downstream impact on lysosomal and mitochondrial function. Dopamine metabolism has been poorly characterized in SH-SY5Y cells. These cells may display a relative dopamine deficiency, when compared to other neurotransmitters such as serotonin. SH-SY5Y cells may therefore represent a useful cellular model of dopamine deficiency.

- (iii) Lysosomal acidification, a key factor in ensuring optimal lysosomal function, is compromised when mitochondrial complex I or lysosomal GBA activity is compromised.

- (iv) iPSC derived dopaminergic neurons present a valuable model in neuroscience research. It is hypothesized that these neurons have a functional dopamine metabolism making them a good model to study disease pathology and test potential therapeutics.

1.9. Aims

- To characterize and compare the biochemistry of proliferative and differentiated SH-SY5Y cells, specifically dopamine and serotonin metabolism, the activity of mitochondrial electron transport chain complexes, lysosomal glucocerebrosidase activity and glutathione levels.
- To explore the potential downstream effects of dopamine metabolism on the activity of mitochondrial electron transport chain complexes, lysosomal glucocerebrosidase activity and glutathione levels.
- To investigate the effect of loss of function of lysosomal glucocerebrosidase or mitochondrial complex I on lysosomal acidification.
- To validate dopamine metabolism in iPSC derived dopaminergic neuronal models for PD and related inborn error of metabolism.
- To test the feasibility of drug and gene therapy for aromatic amino acid decarboxylase deficiency.

Chapter 2. Materials and Methods

2.1. Materials

The following materials were purchased from Sigma Aldrich (Poole, UK): Dulbecco's phosphate buffered saline (PBS), 3,4-dihydroxyphenylacetic acid (DOPAC), 5-hydroxyindol-3-acetic acid (5-HIAA), homovanillic acid (HVA), dopamine hydrochloride, 3-O-methyldopa (3-OMD), 3,4-dihydroxy-L-phenylalanine (L-DOPA), 1-octanesulfonic acid sodium salt, EDTA disodium, sodium acetate trihydrate, citric acid monohydrate, retinoic acid (RA), rotenone, Tris base, triton X-100, hydrochloric acid (HCl), acetyl-CoA, oxaloacetic acid, 5,5' dithio-bis (2-nitrobenzoic acid) (DTNB), dipotassium hydrogen phosphate trihydrate ($K_2HPO_4 \cdot 3H_2O$), potassium dihydrogen phosphate (KH_2PO_4), magnesium chloride, potassium cyanide, bovine serum albumin (fatty acid free), NADH, Coenzyme Q₁, sodium borohydride, ethanol, EDTA dipotassium salt, cytochrome *c* from equine heart, sodium succinate, antimycin A, potassium ferricyanide, sodium L-ascorbate, anti-TH antibody (#T8700) and anti-rabbit antibody (#A0545).

HPLC grade methanol, 0.25% Trypsin-EDTA, heat inactivated foetal bovine serum (FBS), Gibco™ Dulbecco's modified eagle's medium (DMEM)/Ham's F12 1:1 nutrient mix, GlutaMAX™ Supplement (DMEM/F-12), DMEM/F-12 phenol-red free media, 25 cm² tissue culture cell scraper, 3,4-dihydroxybenzylamine hydrobromide (DHBA), 12-O-tetradecanoylphorbol-13-acetate (TPA), anti-NSE antibody (#PA5-27452) and GlutaMAX™ glutamine solution were purchased from Thermo Fisher Scientific (Dartford, UK).

TC10 cell counting kit, trypan blue, mini-protean TGX stain-free gels 4%-20% polyacrylamide, trans-blot turbo transfer pack (PVDF, 7 x 8.5 cm), Precision

Plus Protein dual colour standards and clarity Western ECL substrate were purchased from Bio Rad Laboratories Ltd (Hemel Hempstead, UK).

PD-10 desalting columns containing Sephadex G-25 resin were purchased from GE Healthcare Life Sciences (UK).

0.3 ml clear HPLC vials and screw caps were purchased from Chromacol (UK). Isoproterenol hydrochloride was purchased from Insight Biotechnology (UK). Conduritol B epoxide and Bafilomycin A1 were purchased from Cambridge Bioscience (Cambridge, UK). Rabbit monoclonal antibody to glyceraldehyde 3-phosphate dehydrogenase (GAPDH) (Horseradish peroxidase conjugated, #14C10) was purchased from New England Biolabs (Hitchin, UK). Anti-NeuN antibody (ab104225) was purchased from Abcam (Cambridge, UK). Figures were created using BioRender.com

2.2. Cell culture

SH-SY5Y cells were purchased from the European Collection of Authenticated Cell Cultures (ECACC, Cat #94030304, Salisbury, UK). Cells were cultured in DMEM/F12 GlutaMAX™ medium supplemented with 10% foetal bovine serum (10% FBS). Cells were incubated at 37° C and 5% CO₂. For passaging, once they were confluent, first the culture medium was aspirated, and cells were washed with PBS. 0.25 % trypsin-EDTA was then added to detach cells and cells were incubated for 1 minute at 37° C. 10 % FBS media was added to quench the activity of trypsin and cells were transferred to a falcon tube. Cells were centrifuged at 500 *g* for 5 minutes at room temperature. Afterward, supernatant was decanted, and cell pellet resuspended in 10 % FBS medium. Cells were counted using an automated cell counter (BioRad Laboratories, UK) and plated as required. Medium was changed every 2 days. Cell passages between 18 and 24 were used throughout this thesis to preserve experimental consistency and based on reports of changes in neuronal characteristics occurring with increasing passage number and culture period (Shipley *et al.* 2016; Constantinescu *et al.* 2007).

2.2.1. Cell storage and recovery:

When cells were first received from the ECACC, they were thawed and plated in a T-75 tissue culture flask. Once the cells reached confluency, they were seeded into multiple flasks then cryopreserved for future use. This ensures the availability of a stock of frozen cells with a relatively low passage number to be used once the growing cells exceed the passage number range used in this thesis.

To cryopreserve cells, cells were collected, palletted, then suspended in 1 ml of freezing medium (10% DMSO in FBS) and aliquoted in cryovials. The cryovials were then transferred to a Mr Frosty™ Freezing Container (Fisher Scientific UK Ltd, Loughborough, UK) and stored for 2 days at -80° C. Afterwards, the cryovials were transferred into liquid nitrogen tanks for long-term storage.

2.2.2. L-DOPA treatment

For L-DOPA treated cells, cells were incubated for 1 or 3 hours in phenol-red free 10% FBS media supplemented with 100 µM L-DOPA. For control cells, cells were incubated for 1- or 3-hours phenol-red free 10% FBS media without L-DOPA.

2.3. SH-SY5Y cell differentiation

The SH-SY5Y cells were differentiated using a protocol adapted from Presgraves et al. (2004). The protocol is based on inducing cellular differentiation through sequential treatment with RA and TPA under reduced serum conditions. RA was used because it plays a key role in cellular differentiation. Once in the cells, RA activates the RA nuclear receptors, which are ligand dependant transcriptional regulators. This results in the activation and regulation of genes implicated in growth arrest, cell development and differentiation (Maden 2007). RA treatment was followed with TPA because TPA was shown to induce 200-fold increase in the concentration of noradrenaline, one of the product of dopamine, driving the cellular phenotype towards dopaminergic lineage (Phhlman *et al.* 1984). Cells were treated with TPA for 3 days because it was shown that 3 days treatment with TPA was sufficient enough to induce neurite outgrowth, which is one of the characteristics of neuronal morphology, and further treatment did not lead to an increase in neurite outgrowth (Ota *et al.* 1989). Differentiation was carried out under low serum conditions, using cell culture media containing 1% FBS, which is different to the normal growth conditions using cell culture media containing 10% FBS. Maintenance of cells under reduced serum conditions were shown to inhibit cells from entering the synthesis phase of the cell cycle, S phase. The synthesis phase is the phase where DNA duplication occurs prior to mitosis. This causes the cells to remain in the non-proliferative phase of the cell cycle, or the G₀ phase, facilitating differentiation (Fang *et al.* 2017; He *et al.* 2011)

The sequential treatment with RA and TPA were shown to induce the highest protein expression level of TH, DAT and VMAT-2, the markers of dopaminergic neuronal phenotype, in comparison to proliferative cells, and to the

more common differentiation treatment using RA alone (Xicoy *et al.* 2017; Presgraves *et al.* 2004; Pennypacker *et al.* 1989; Magalingam *et al.* 2020). The combined treatment with RA and TPA appeared to completely inhibit cell proliferation when compared to RA alone or TPA alone (Phhlman *et al.* 1984). Finally, it was shown that the cellular toxicity of sequential treatment with 10 μ M RA and 80 nM TPA was tolerated in SH-SY5Y cells (Magalingam *et al.* 2020).

2.3.1. Differentiation protocol:

Cells were seeded at a density of 10^5 cells/cm² in 10% FBS medium and were incubated overnight (differentiation day 0). The next day, day 1 of differentiation, cell culture media was aspirated, cells were washed with PBS then reduced serum media (1% FBS) supplemented with 10 μ M RA prepared in DMSO was added. Cells were incubated for 2 days away from direct light source. On day 4, culture media was aspirated, medium was removed, and cells were gently washed with PBS. Fresh 1% FBS media supplemented with 80 nM TPA prepared in DMSO was added and cells were incubated for 2 days away from direct light source. On day 7, experiments were carried out (Figure 8).

To ensure proliferative cells used in the experiment were at the same passage number as the differentiated cells, cells were plated on differentiation day 0 however, cells were seeded at 10^4 cells/cm² tissue culture flask in 10% FBS medium to allow them to become confluent by day 7. Media was changed every 2 days.

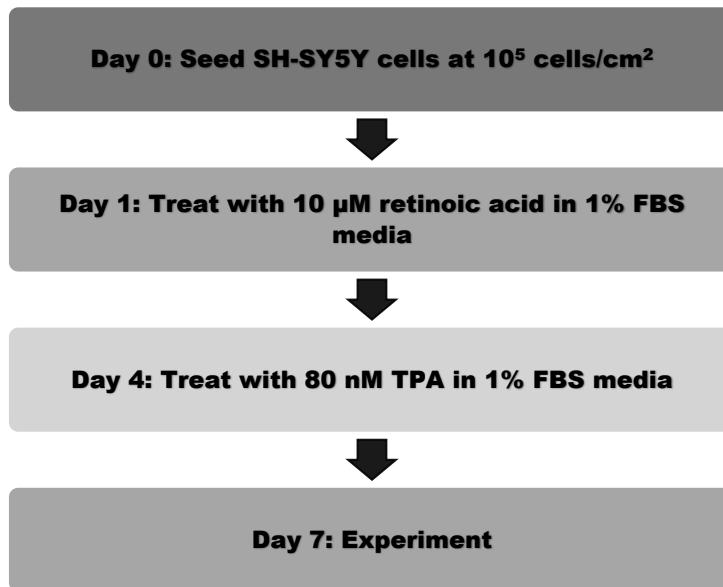


Figure 8 Differentiation protocol for SH-SY5Y cells. RA: retinoic acid; TPA: 12-O-tetradecanoylphorbol-13-acetate.

2.4. Sample preparation:

2.4.1. Bradford protein assay, western blot, and enzyme assays:

Cells were collected and the cell pellet was suspended in PBS. A sample of PBS cell suspension was taken for GBA enzyme assay. Then cells were centrifuged at 500 g, and the pellet was suspended in ice cold lysis buffer (10 mM tris (pH 7.4), 1 mM EDTA, 320 mM sucrose in HPLC grade water). This suspension was aliquoted for Bradford assay, western blot, and each of mitochondrial enzyme assays.

2.4.2. HPLC-ED sample preparation:

2.4.2.1. Extracellular metabolites:

A sample of phenol-red free cell culture media was diluted 1:1 in ice cold 0.8 M perchloric acid (PCA) and incubated on ice in the dark for 10 minutes to precipitate proteins. Sample was then centrifuged at 12000 g for 5 minutes in a 4 °C microfuge. Supernatant then was transferred to an HPLC vial for analysis or stored at -80 °C.

2.4.2.2. Intracellular metabolites:

Cell pellets were suspended in 1 ml ice cold lysis buffer (10 mM tris (pH 7.4), 1 mM EDTA, 320 mM sucrose in HPLC grade water). Cell lysate was diluted 1:1 in ice cold 0.8 M PCA and incubated on ice in the dark for 10 minutes to precipitate protein. Lysate was then centrifuged at 12000 g for 5 minutes in a 4 °C microfuge. Supernatant was then transferred to HPLC vials for analysis or stored at -80 °C. Fraction of cell lysate was taken for protein quantification using Bradford assay.

2.4.3. Glutathione:

Cells were collected and the cell pellet was suspended in PBS. PBS suspension was centrifuged and supernatant decanted. Cell pellet was suspended in 1 ml ice cold lysis buffer (10 mM tris (pH 7.4), 1 mM EDTA, 320 mM sucrose in HPLC grade water). Cell lysate was diluted 1:10 with ice cold 15 mM HPLC grade O-phosphoric acid. Sample was incubated on ice for 10 minutes then centrifuged at 12000 *g* for 5 minutes in a 4 °C microfuge. Supernatant was transferred to HPLC vials for analysis or stored at -80 °C. A fraction of cell lysate was taken for protein quantification using Bradford assay.

2.5. Bradford assay:

Bradford assay is a commonly used assay to determine the protein concentration in a given sample. Protein concentration is a useful normalisation factor when comparing different samples. Bradford is a colorimetric assay developed by Marion M. Bradford in 1976. In principle, the Coomassie brilliant blue G-250 dye binds to the proteins present in a given sample. The binding of the dye to proteins leads to a shift in its colour, from brown to blue. The shift in colour results in a shift in the absorbance of the dye, and correlates with the concentration of proteins in a given sample (Bradford 1976).

In the assay, the unknown protein concentration of a sample is calculated using the linear regression equation from a standard curve created using protein standards of known concentration. To create the protein standard curve, 0-200 $\mu\text{g}/\mu\text{l}$ protein standards were created via serial dilutions of 200 $\mu\text{g}/\mu\text{l}$ stock of bovine serum albumin (BSA) in 25 $\mu\text{g}/\mu\text{l}$ increments. For cell sample, cell lysate was diluted 1:10 in HPLC grade water. 20 μl of each BSA protein standard and each sample were pipetted into 96 well plate in duplicate. 180 μl of Bradford reagent was added to each well in order. The plate was incubated for 1 minute at room temperature before absorbance was measured at 595 nm using Infinite® F200 PRO microplate reader (Tecan, Männedorf, Switzerland). A calibration curve was created by plotting the absorbance of protein standards and their concentrations and the linear regression equation obtained is used to determine the concentration of the samples using their absorbance (Figure 9).

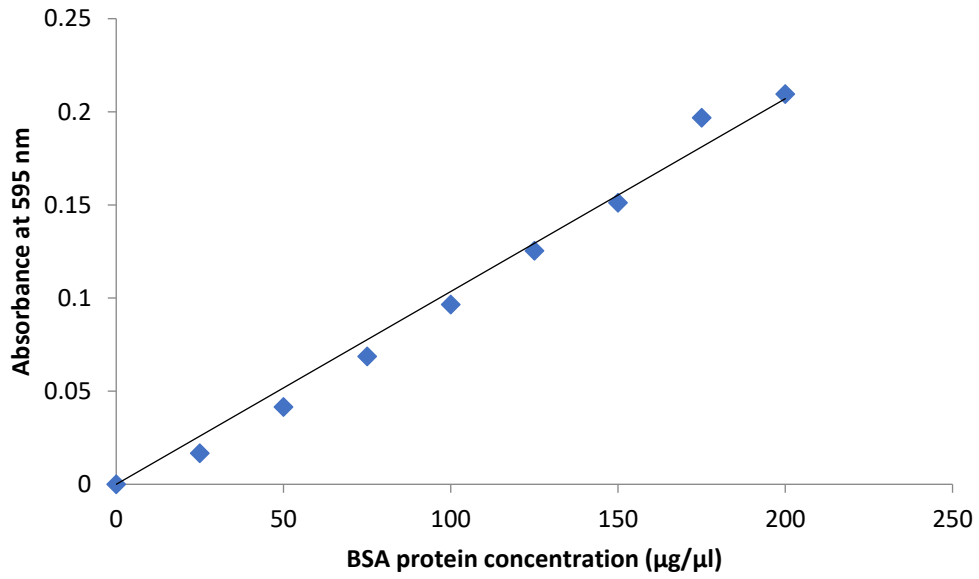


Figure 9 Protein standard curve for Bradford assay. Protein standards were created using bovine serum albumin in concentrations ranging 0-200 µg/µl and their absorbance was read at 595 nm following the addition of Bradford reagent ($R^2 = 0.99$).

2.6. Western blot for protein expression

Western blot is a commonly used technique to separate and identify proteins in a given sample. In principle, the separation is based on the molecular weight of the protein of interest when referenced to a molecular weight ladder that is included in the blot. The proteins are then visualised using specific antibodies that are labelled with a peroxidase label. The amount of protein present can be calculated by measuring the enhanced chemiluminescence of the labelled bands.

After determining the protein concentration of each sample, gel loading samples were prepared according to (Table 1). Samples were mixed and proteins were denatured by boiling the sample at 95 °C for 5 minutes. 20 µl of each sample was pipetted into separate well of a 4–20% polyacrylamide gel and placed in the Bio Rad Mini-PROTEAN® tetra system along with 1X TGS running buffer. 20 µl of molecular weight ladder was added to a separate well. Electrophoresis was carried out for 20 minutes at 300 V, 400 mA. For the protein transfer, a Bio Rad Trans-Blot turbo transfer pack was prepared according to (Figure 10). Transfer was carried out in the Bio Rad Trans-Blot TURBO™ transfer system set at 25 V, 2.5 A for 7 minutes.

Following transfer, membranes were washed with TBST (0.5 L TBS (1 TBS tablets + MilliQ water) + 0.5 ml Tween-20). Membranes were first blocked to prevent unspecific binding by incubation in 5% low fat milk-TBST for 1 hour. Afterwards, membranes were incubated overnight at 4 °C with primary antibody of interest, diluted in 1% milk-TBST at a concentration according to (Table 2). The membrane was then washed for 10 minutes three times with TBST then

incubated with the secondary anti-rabbit antibody diluted in in 1% milk-TBST for 1 hour at room temperature. The membrane was then washed with TBST for 10 minutes three times and visualised using Bio Rad Clarity Western ECL solution and Bio Rad ChemiDOC™ MP imaging system. The bands were quantified using ImageJ software. Protein molecular weight ladder was used to identify the bands and GAPDH expression was used as a loading control and a normalising factor.

Protein sample	10 µg
1:4 Laemmli buffer	2.5 µl
1:5 0.5 M DDT	4 µl
Mili-Q water	Made up to 20 µl

Table 1 Gel electrophoresis loading sample composition.

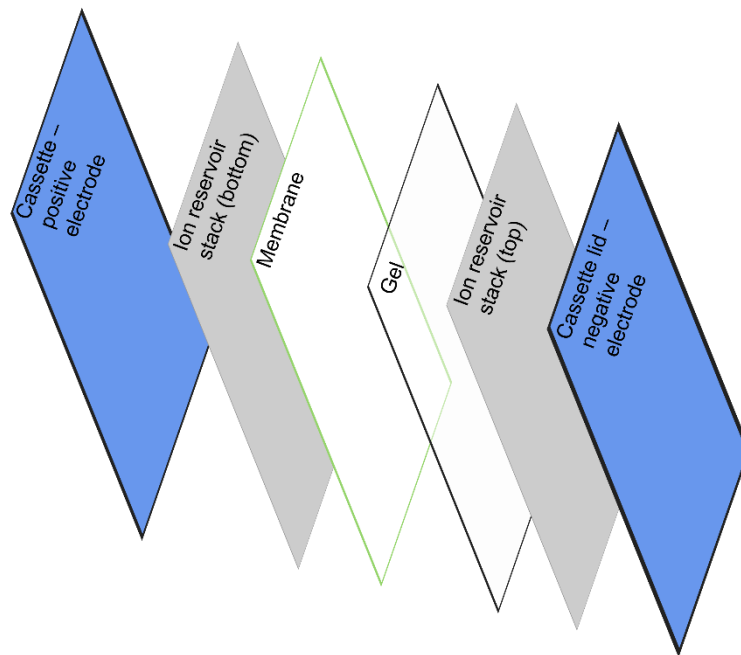


Figure 10 Order of assembly of the Bio Rad Trans-Blot turbo transfer pack. The pack was assembled according to manufacturer instructions. The membrane onto which the proteins will transfer was placed on top of the stack and the positive electrode cassette bottom. The gel is placed on top of the membrane and is covered by another stack and finally the cassette lid to which the negative electrode connects.

Antibody	Dilution
NSE	1/3000
NeuN	1/3000
TH	1/3000
GAPDH	1/3000
Pro-cathepsin D	1/1000
Mature cathepsin D	1/2000
Anti-rabbit	1/3000

Table 2 List of antibodies used and dilutions. Antibodies were diluted in 1 % milk/TBST.

2.7. Enzyme assays:

2.7.1. Citrate synthase assay:

Citrate synthase (CS, EC 4.1.3.7) is the first and rate limiting enzyme in the citric acid (TCA) cycle taking place in the mitochondrial matrix (Marco *et al.* 1974). It catalyses the condensation of oxaloacetic acid and acetyl-CoA to form citrate and free Coenzyme A (Equation 1). Because of its location, CS is commonly used as a measure of mitochondrial content (Larsen *et al.* 2012). In this thesis, CS activity was used as a normalisation factor for the activity of mitochondrial complex I, II-III and IV because the comparison was made between cells that are phenotypically different.

In principle, this is a colorimetric assay to measure the activity of CS based on a method by Shepherd and Garland (1969). The method measures the absorbance of 5-thio-2-nitrobenzoate (TNB), the by-product of the reaction between free Coenzyme A and 5,5'-dithio-bis-(2-nitrobenzoic acid) (DTNB, Ellman's reagent, Equation 1). TNB has an absorbance at 412 nm, which correlates with CS enzyme activity.



Equation 1 Citrate synthase enzyme reaction. CoA: Coenzyme A. DNTB: 5,5'-dithio-bis-(2-nitrobenzoic acid). TNB: 5-thio-2-nitrobenzoate.

Prior to the assay, a stock of 10 mM acetyl-CoA was prepared in Milli-Q water, aliquoted, and stored at -20° C. On the day of the assay, 20 mM DTNB and 20 mM oxaloacetate were freshly prepared in Milli-Q water. 20 µl cell lysate sample was added to a sample cuvette containing 950 µl CS buffer (100 mM Tris/0.1% v/v Triton, pH 8.0), 10 µl of 10 mM acetyl-CoA, 10 µl of 20 mM DTNB. The reaction was started by the addition of 10 µl oxaloacetate and measured for 15 min at 30° C and 412 nm using Uvikon XL spectrophotometer (BioTek Instruments, France). The sample cuvettes were referenced against cuvettes similarly prepared but excluded the addition of oxaloacetate.

The activity of CS was converted to molar concentration using the Beer-Lambert law and DTNB extinction coefficient ($13.6 \times 10^3 \text{ M}^{-1} \text{ cm}^{-1}$). Results were normalised on a protein concentration baseline and expressed as nmol/min/mg protein for each sample:

$$\Delta A = \epsilon \times c \times l$$

ΔA = change in absorbance min^{-1}

ϵ = DTNB extinction coefficient ($13.6 \times 10^3 \text{ M}^{-1} \text{ cm}^{-1}$)

c = enzyme activity in nmol/min/ml

l = path length of cuvette (1 cm)

The linearity of the CS enzyme activity assay was confirmed using an SH-SY5Y cell sample that was serially diluted to give samples of different protein concentrations, and CS activity was measured in each serial dilution. CS activity measured using this assay was found to strongly correlate with protein concentration ($R^2 = 0.988$, Figure 11).

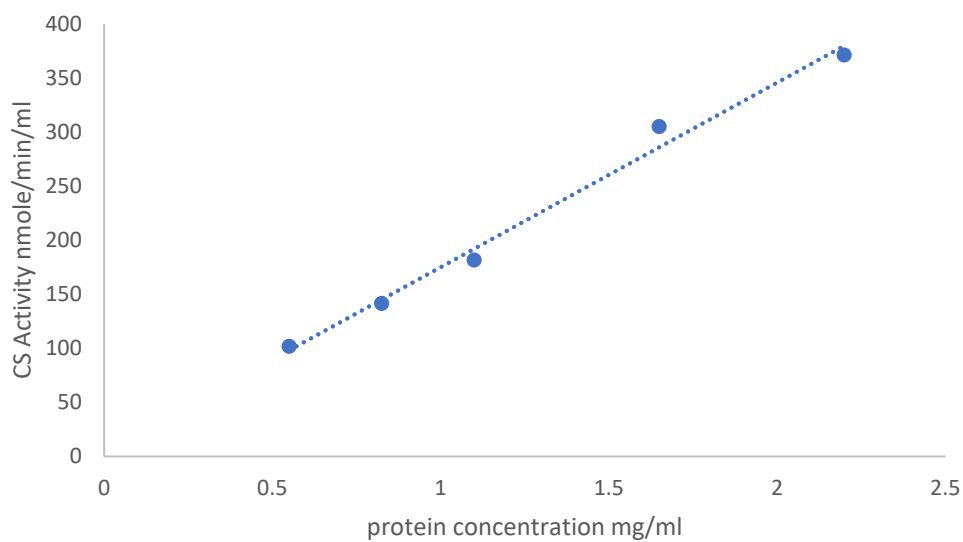


Figure 11 Correlation between citrate synthase (CS) activity and protein concentration in SH-SY5Y cells. A sample of SH-SY5Y cell lysate was serially diluted and CS activity was measured in each dilution sample. Linear regression analysis showed a strong correlation between CS activity and protein concentration of cell lysate ($R^2 = 0.988$).

2.7.2. Mitochondrial NADH-Ubiquinone oxidoreductase (Complex I):

Mitochondrial ETC complex I (EC 7.1.1.2) is the first enzyme complex in the oxidative phosphorylation reaction catalysed by ETC. Complex I catalyses the oxidation of NADH and the transfer of electrons to coenzyme Q (ubiquinone, Equation 2). In this assay, NADH absorbance is measured at 340 nm before and after the addition of the complex I inhibitor, rotenone. The rotenone-sensitive reduction in NADH absorbance is calculated as complex I activity (Reed and Ragan 1987). Coenzyme Q₁ was used as a synthetic substitute for coenzyme Q₁₀ (ubiquinone) due to its higher stability.



Equation 2 Oxidation of NADH by complex I. CoQ: Coenzyme Q.

For the assay, 20 µl of cell sample was mixed with 800 µl of 25 mM potassium phosphate (KH₂PO₄/K₂HPO₄)/10 mM magnesium chloride (MgCl₂·6H₂O) buffer (pH 7.2) and 80 µl of Milli-Q water. Then, 50 µl of 50 mg/ml fatty acid free BSA, 30 µl of 5 mM NADH and 10 µl of 100 mM KCN were added. The reaction was started by the addition of 10 µl of 5 mM CoQ₁ and measured for 6 minutes at 340 nm using Uvikon XL spectrophotometer (BioTek Instruments, France). After 6 minutes, 20 µl of 1 mM rotenone was added and reaction was allowed to run till the end (total run time was 15 minutes).

The activity of complex I was measured by the Beer-Lambert law, where change in absorbance is calculated as absorbance after rotenone addition subtracted from absorbance before rotenone addition to negate the rotenone insensitive rate. Activity was expressed as nmol/min/mg protein after normalisation to protein concentration of each sample:

$$\Delta A = \epsilon \times c \times l$$

$$\Delta A = \Delta A_{0-6} - \Delta A_{10-15} \text{ (change in absorbance min}^{-1} \text{ before rotenone addition} \\ \text{– change in absorbance min}^{-1} \text{ after rotenone addition)}$$

$$\epsilon = \text{extinction coefficient of CoQ}_1 \text{ (} 6.81 \times 10^3 \text{ M}^{-1} \text{ cm}^{-1}\text{)}$$

$$c = \text{concentration of NADH-CoQ}_1$$

$$l = \text{path length of cuvette (1 cm)}$$

The linearity of the complex I enzyme activity assay was confirmed using an SH-SY5Y cell sample that was serially diluted to give samples of different protein concentrations and complex I activity was measured in each serial dilution. Complex I activity measured using this assay was found to strongly correlate with protein concentration ($R^2 = 0.98$, Figure 12)

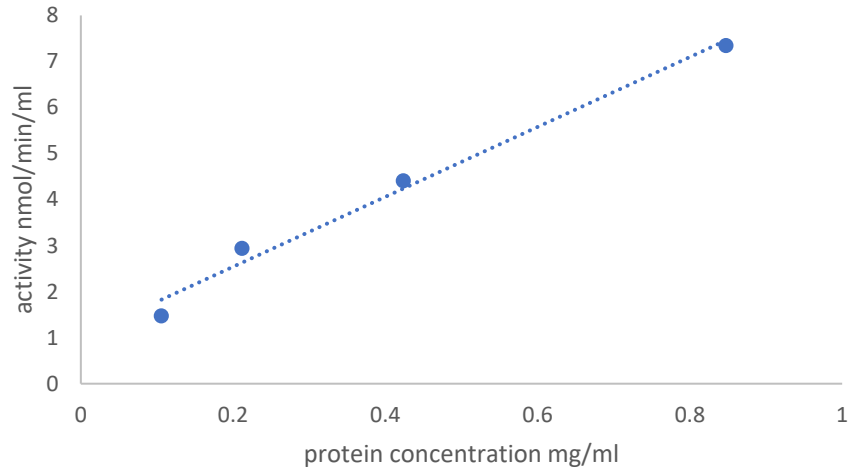


Figure 12 Correlation between mitochondrial complex I activity and protein concentration in SH-SY5Y cells. Complex I enzyme activity was measured in a serial dilution of SH-SY5Y cell lysate and plotted against the protein concentration of each dilution. Complex I activity was found to be linear with an $R^2 = 0.98$.

2.7.3. Mitochondrial succinate dehydrogenase-cytochrome c reductase (complex II-III):

Mitochondrial complex II (EC 1.3.5.1) and III (EC 1.10.2.2) combined enzyme activity results in the oxidation of succinate to fumarate and the reduction of cytochrome c (Equation 3). In this assay, adapted from (King and Howard 1967), reduced cytochrome c has an absorbance at 550 nm. The rate of increase of reduced cytochrome c absorbance corresponds to the combined activity of complex II and III. Antimycin A, a potent complex III inhibitor, is used to separate the specific activity of complex II-III in this assay from other enzymes that may reduce cytochrome c.



Equation 3 The net enzymatic reaction of mitochondrial complex II-III. Complex II catalyses the oxidation of succinate to fumarate while complex III catalyses the reduction of cytochrome c. Cyto c: cytochrome c.

For this assay, 20 µl of cell sample was mixed with 600 µl potassium phosphate buffer (KH₂PO₄/K₂HPO₄, 166 mM, pH 7.4) and 185 µl Milli-Q water. Then, 10 µl of 100 mM KCN, 20 µl of 15 mM EDTA and 125 µl of 0.8 mM cytochrome c was added. The reaction was started by the addition of 40 µl of 0.5 M succinic acid and measured for 6 minutes at 550 nm using Uvikon XL spectrophotometer (BioTek Instruments, France). After 6 minutes, 10 µl of 1 mM antimycin A was added and reaction was allowed to run till the end (total run time was 15 minutes).

The activity of complex II-III was designated as the antimycin A-sensitive increase in reduced cytochrome c levels and was calculated using the Beer-Lambert law and expressed as nmol/min/mg after normalisation to protein concentration of each sample:

$$\Delta A = \epsilon \times c \times l$$

$\Delta A = \Delta A_{0-6} - \Delta A_{10-15}$ (change in absorbance min^{-1} before antimycin A addition – change in absorbance min^{-1} after antimycin addition)

ϵ = extinction coefficient of reduced cytochrome c ($19.2 \times 10^3 \text{ M}^{-1} \text{ cm}^{-1}$)

c = concentration of reduced cytochrome c

l = path length of cuvette (1 cm)

The linearity of the complex II-III enzyme activity assay was confirmed using an SH-SY5Y cell sample that was serially diluted to give samples of different protein concentrations, and the complex II-III activity was measured in each serial dilution. Complex II-III activity measured using this assay was found to strongly correlate with protein concentration ($R^2 = 0.95$, Figure 13)

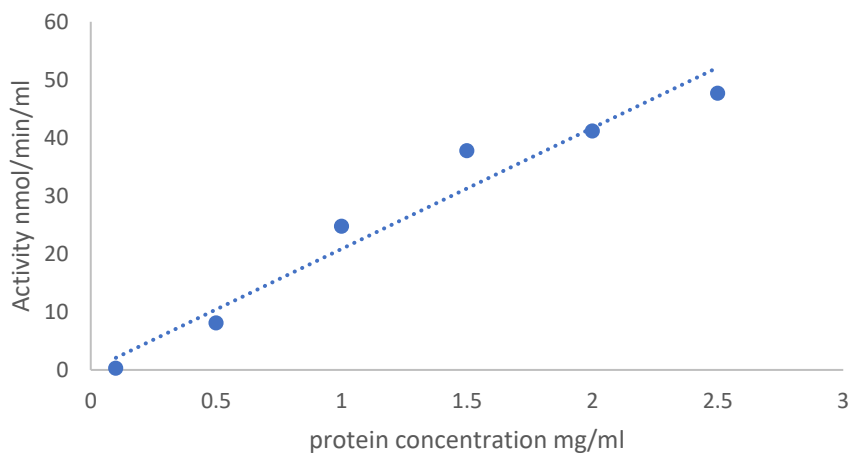


Figure 13 Correlation between mitochondrial complex II-III activity and protein concentration in SH-SY5Y cells. Complex II-III enzyme activity was measured in a serial dilution of SH-SY5Y cell lysates and plotted against the protein concentration of each dilution. Complex II-III activity was found to be linear with an $R^2 = 0.95$.

2.7.4. Mitochondrial cytochrome c oxidase (complex IV):

Mitochondrial complex IV (EC 1.9.3.1) catalyses the oxidation of cytochrome c by molecular oxygen, generating water (Equation 4). This assay was adapted from Wharton & Tzagoloff (1967) and it measures the decrease in absorbance of reduced cytochrome c at 550 nm and relates it to complex IV enzyme activity.



Equation 4 Mitochondrial complex IV enzyme reaction. Cyto c: cytochrome c.

Prior to starting the assay, cytochrome c was reduced by dissolving 10 mg in 1 ml of 0.2mg/ml sodium ascorbate. The mixture was incubated on ice for 10 minutes before removal of sodium ascorbate using a PD-10 desalting column equilibrated with 1:10 dilution of 166 mM potassium phosphate buffer (KH₂PO₄/K₂HPO₄, pH 7.2). The concentration of reduced cytochrome c was determined by preparing two cuvettes, one sample and one reference, containing 50 µl reduced cytochrome c and 950 µl Milli-Q water. The sample cuvette was then blanked against the reference cuvette at 550 nm using Uvikon XL spectrophotometer (BioTek Instruments, France). Afterwards, 10 µl of 100 mM potassium ferricyanide was added to reference cuvette to oxidize cytochrome c. After 1 minute, the absorbance was recorded. The Beer-Lambert law was applied using the reduced cytochrome c extinction coefficient (19.2 x 10³ M⁻¹ cm⁻¹) to determine the concentration of reduced cytochrome c.

For this assay, a cuvette was prepared containing 100 μ l potassium phosphate assay buffer (100 mM, pH 7.0), 50 μ M reduced cytochrome c and Milli-Q water for a total volume of 980 μ l. Reference cuvette was prepared by addition of 10 μ l of 100 mM potassium ferricyanide to the aforementioned mixture. The cuvettes were measured for 2 minutes at 550 nm. Afterwards, 20 μ l of cell sample lysate was added and reaction was measured for a further 6 minutes. Complex IV enzyme activity is defined as a first-order rate constant (k) which is calculated by plotting the natural log of absorbance against time and determining the slope as k/min/ml. Activity was divided by protein concentration (mg/ml) to be expressed as k/min/mg protein.

The linearity of the complex IV enzyme activity assay was confirmed using an SH-SY5Y cell sample that was serially diluted to give samples of different protein concentrations, and the complex IV activity was measured in each serial dilution. Complex IV activity measured using this assay was found to strongly correlate with protein concentration ($R^2 = 0.97$, Figure 14)

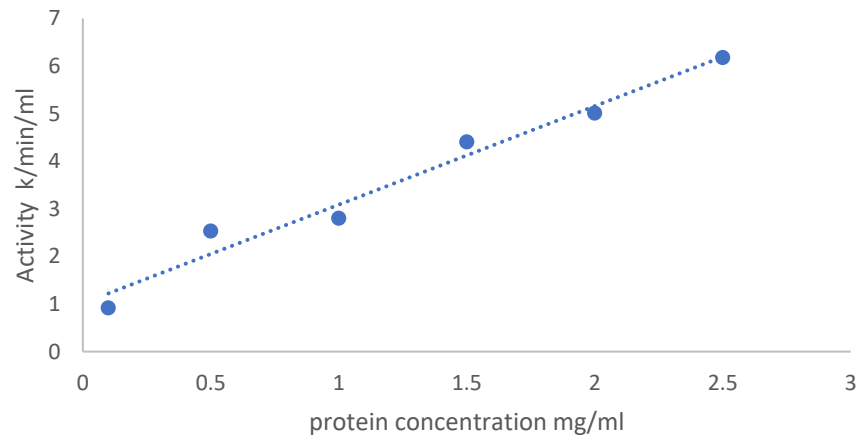


Figure 14 Correlation between mitochondrial complex IV activity and protein concentration in SH-SY5Y cells. Complex IV enzyme activity was measured in a serial dilution of SH-SY5Y cell lysates and plotted against the protein concentration of each dilution. Complex IV activity was found to be linear with an $R^2 = 0.97$

2.7.5. Lysosomal glucocerebrosidase (GBA):

GBA activity assay was adapted from a UV spectrophotometer method by Gegg and colleagues (2012) to be used with a plate reader. At acidic pH, GBA catalyses the hydrolysis of 4-methylumbelliferyl- β -D-glucopyranoside (4-MUG) to give 4-methylumbelliferone (4-MU) and glucose. The addition of an alkaline buffer (pH 10.4) stops the reaction and allows 4-MU to fluoresce. 4-MU fluorescence is measured and correlates with the activity of GBA. In this assay, sodium taurocholate is added to inhibit the activity of the cytosolic β -glucosidase enzyme which also has the ability to breakdown 4-MUG.

In a 96 well plate, duplicate wells were set up with 10 μ l sample, 15 μ l of 148.8 mM sodium taurocholate and 25 μ l of McIlvaine citrate-phosphate buffer, pH 5.4 (MV 5.4, 88 ml 0.1 M citrate + 112 ml 0.2 M Na₂HPO₄, pH 5.4). Duplicate blank wells were also set up with 10 μ l water instead of sample. At timed intervals, 50 μ l of 10 mM 4-MUG (substrate) was added to all wells and mixed. The plate was then incubated at 37° C for 1 hour then 110 μ l of 2.5 M glycine/NaOH (pH 10.4) was added to stop the reaction. In separate wells, 200 μ l of 5 μ M 4-MU and 100 μ l of 2.5 M glycine/NaOH was added to act as a standard. The plate was read at 340 nm excitation and 465 nm emission using Infinite® F200 PRO microplate reader (Tecan, Männedorf, Switzerland). GBA enzyme activity was calculated as nmol/hr/mg using the following equation:

$$\frac{\text{Average test reading} - \text{Average blank reading}}{\text{average standard reading}} \times \frac{60}{\text{incubation time (min)}} \times \frac{1000}{\frac{\text{mg}}{\text{ml}} \text{protein}}$$

The linearity of the GBA enzyme activity assay was confirmed using an SH-SY5Y cell sample that was serially diluted to give samples of different protein concentrations, and the GBA activity was measured in each serial dilution. GBA activity measured using this assay was found to strongly correlate with protein concentration ($R^2 = 0.97$, Figure 15). A standard calibration curve was also created to confirm the linearity between the concentration of 4-M and its fluorescence intensity ($R^2 = 0.99$, Figure 16).

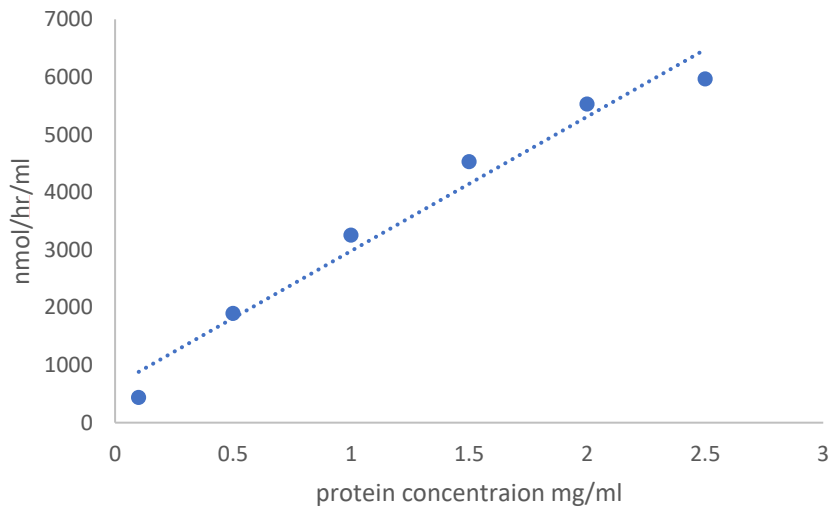


Figure 15 Correlation between GBA activity and protein concentration in SH-SY5Y cells. GBA enzyme activity was measured in a serial dilution of SH-SY5Y celli lysates and plotted against the protein concentration of each dilution. GBA activity was found to be linear with an $R^2 = 0.97$.

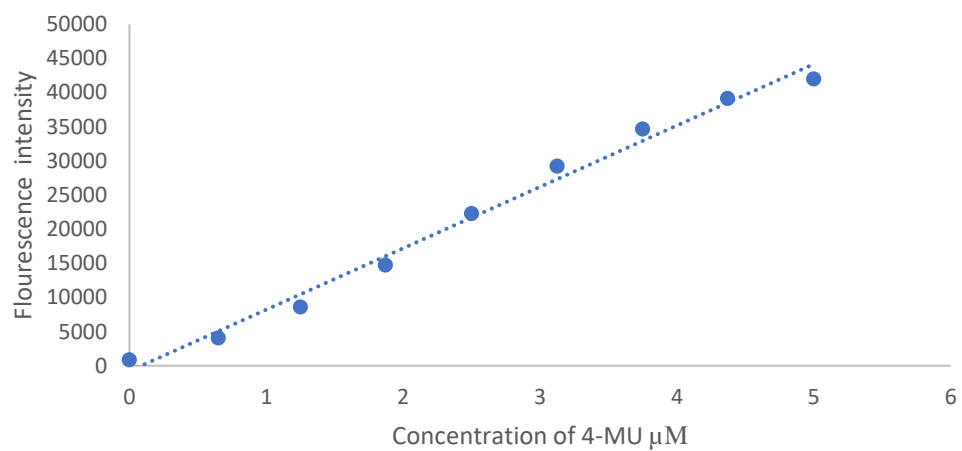


Figure 16 Fluorescence intensity calibration curve for 4-methylumbelliferone (4-MU). The fluorescence intensity of different concentrations of 4-MU (0-5 μM) diluted in 2.5 M glycine/NaOH was measured at 340 nm excitation and 465 nm emission and plotted against the concentration. $R^2 = 0.99$.

2.8. Measurement of glutathione using HPLC-ED:

2.8.1. Equipment:

The HPLC components were the following: PU-980 intelligent HPLC pump (JASCO Ltd, UK), DG-980-50 3-line degasser (Jasco Ltd, UK), AS-1555 intelligent autosampler pump (JASCO Ltd, UK), CO-965 column oven (Jasco Ltd, UK), C18HS column 150 mm × 4.5 mm, 100 Å pore size and 5 µm particle size (Kromatek, UK), Coulochem II electrochemical detector and ESA analytical cell (model 5011A, Thermo Fisher Scientific, UK) coupled to a computer with EZChrom Elite chromatography system V3.1.7 (JASCO Ltd, UK).

2.8.2. Method:

An isocratic, reverse-phase HPLC coupled to an electrochemical detector method, adapted from Allen et al. (2013), was used to measure GSH levels in cell lysate. 15 mM HPLC grade *o*-phosphoric acid was used as the mobile phase with a flow rate of 0.5 ml/min. The column was used as a stationary phase and the column temperature was maintained at 35 °C. The injection volume was kept at 50 µl. The upstream electrode (E1) was set at 50 mV and the downstream electrode (E2) was set at 550 mV. The detection voltage was chosen based on running a cyclic voltammogram to determine the optimal voltage for detection while maintaining specificity of the method (Figure 17). 550 mV was chosen because higher voltages (i.e. 600 mV) reduced detection specificity by detecting an unknown overlapping peak in the sample (Figure 19). GSH concentration was determined by referencing peak area to an external standard of 5 µM GSH. Linearity of the method was confirmed by running a standard curve of different GSH concentrations (1-5 µM, Figure 18)

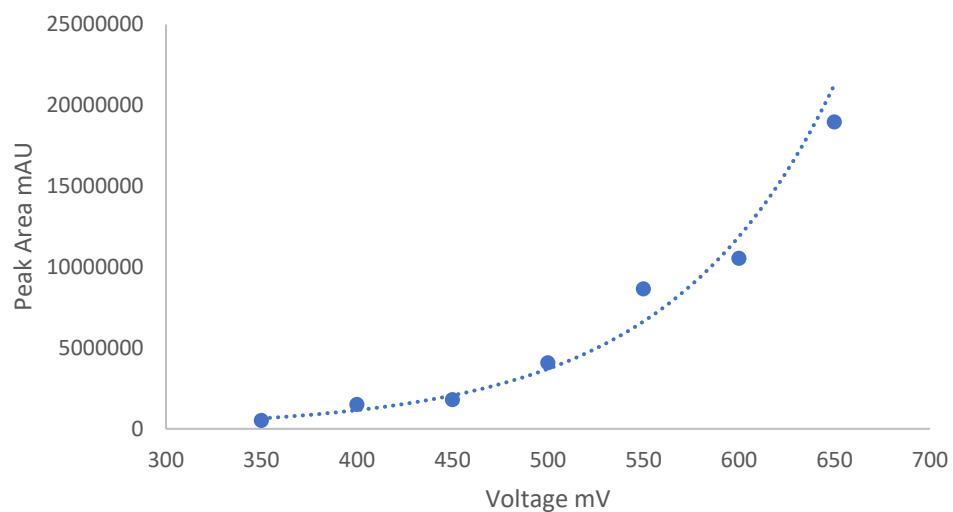


Figure 17 Cyclic voltammogram for glutathione. 5 μ M glutathione prepared in 15 mM O-phosphoric acid run at different working electrode voltages (300 – 650 mV) and plotted against integrated peak area.

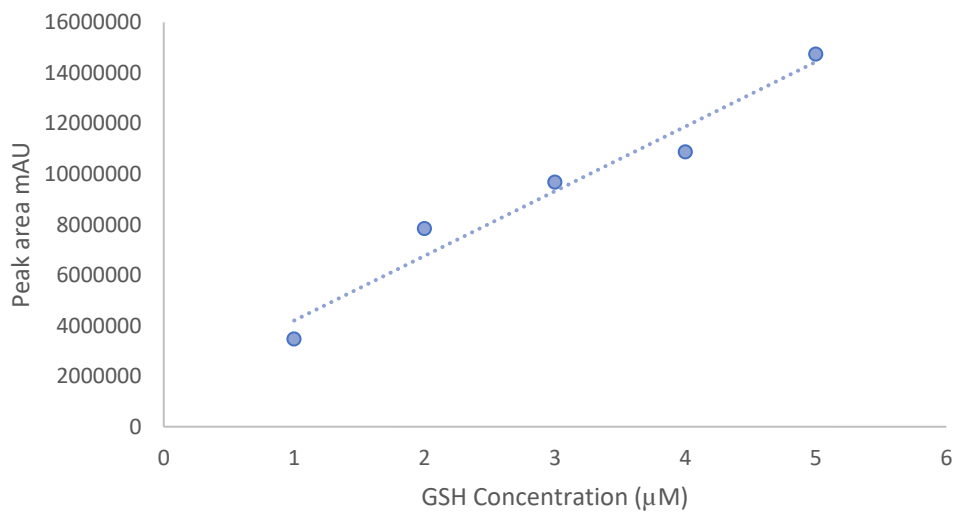


Figure 18 Linear calibration curve for glutathione. Different concentrations of glutathione (1 – 5 µM) were run at a constant detector voltage (550 mV) and area under the curve measured and plotted against concentration to confirm linearity. $R^2 = 0.95$

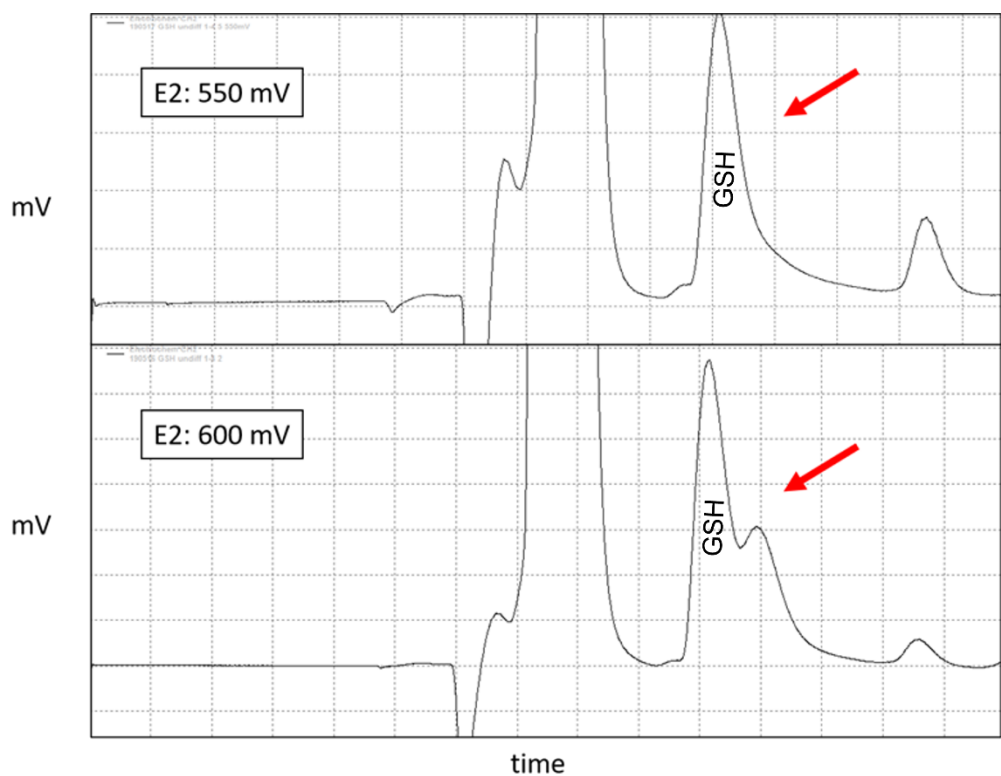


Figure 19 Effect of working electrode voltages on the specificity of HPLC detection. An SH-SY5Y cell sample was run at 550 and 600 mV and the resulting chromatogram analysed. An unknown peak is detected at 600 mV but not at 550 mV (red arrow).

2.9. Statistical Analysis

Results in this thesis presented as mean \pm standard error of mean (SEM) of independent experimental repeats. Test of significance was carried out using unpaired Student's t-test with or without Welch's correction depending on the differences in variance. Differences in variance was tested using an F-test. For multiple comparisons, one-way or two-way ANOVA test was used depending on the number of factors analysed. Statistical analysis was carried out using GraphPad Prism statistical software (Version 9, GraphPad Software INC. San Diego, CA, USA). $p < 0.05$ was considered statistically significant.

Chapter 3. Development of a High-Performance Liquid Chromatography Method for Measurement of Dopamine and Serotonin Metabolites

3.1. Introduction

Chromatography is an analytical technique that allows the separation of a mixture of compounds into the individual constituents. They are separated based on their characteristic relative affinity for a stationary phase and a mobile phase. Liquid chromatography was first developed by Russian botanist Mikhail S. Tswett at the beginning of the 20th century. He devised this analytical technique to purify a mixture of plant pigments. The separation was based on the pigments' interaction with a stationary phase of powdered chalk and alumina packed into a glass column. Pouring the mixture of plant pigments dissolved in a solvent onto the column, he observed that the plant pigments separated as they passed through the column (Weil and Willams 1950). This technique was revolutionized in the 1940s by A. Martin and R. Synge. They employed columns of silica dissolved in water as the stationary phase and used organic solvents as mobile phase. The compounds "partitioned" between the different phases based on their relative solubility, giving rise to partition chromatography; the basis of modern day gas and liquid chromatography (Martin and Synge 1941). The 1960s witnessed the appearance of high-performance liquid chromatography (HPLC) when Csaba Horváth, at Yale University, applied improvements to liquid chromatography by increasing the density of the column packing material and adding a pump to increase the pressure of the applied mobile phase. The result was smaller columns that achieved better separation in less time (Horvath *et al.* 1967).

The core components of an HPLC system are solvent, sample injector, column, pump, detector, and a data integration software. The solvent is the mobile phase, and the column comprises the stationary phase of the HPLC. There are different types of HPLC separation that differ according to the chemical

nature of mobile phase and the column, where compounds separate based on their relative affinities to the packing material of the column, and the mobile phase. For example, in normal-phase HPLC, compounds are separated according to their polarity. The mobile phase is usually nonpolar while the stationary phase is polar. In reverse-phase HPLC, the method used throughout this thesis, the mobile phase is polar while the stationary phase is non-polar. In ion-exchange HPLC, the compounds are separated based on their chemical charge, where the ions in the mobile phase bind the charged stationary phase, and same charge ions in the mobile phase are excluded.

The column is commonly placed inside a temperature-controlled compartment (oven) to ensure reproducibility of the analytical run by maintaining the stationary and mobile phase at a specific temperature. The mobile phase used in a method can be isocratic, which means the composition remains constant throughout the experimental run, or it can be gradient, where the composition changes throughout the run. The pump constitutes the high-performance part of this liquid chromatography technique. It applies high pressure as the mobile phase and sample enter the column, maintaining the flow rate, and reducing separation or elution time. The separated compounds are detected on the detector. HPLC can be coupled to different types of detectors depending on the inherent nature of the compounds of interest. Detection can be based on their fluorescence at a specific wavelength (fluorescence detector), their absorption of UV or visible light (UV-vis detector) or their electrochemistry (electrochemical detector). Electrochemical detectors (ED) detect readily oxidizable/reducible compounds with great selectivity and sensitivity (Meyer 2010).

The HPLC method in this thesis is based on detection using ED. ED offers ultra-sensitive detection power, detecting at as low as picomole levels. A sample is injected into the HPLC, and molecules are separated while passing through the column. Separated molecules enter an ED cell where they undergo oxidation/reduction reaction at electrochemical electrodes producing electrical currents. These electrochemical electrodes are the upstream electrode (E1), where a small voltage is applied to oxidise molecules that have low electrochemical potential, which decreases the signal to noise ratio of the resulting electrochemical chromatogram. The other electrode, the downstream electrode (E2), applies a voltage that oxidises/reduces the molecules of interest as they pass through the ED cell. There are two categories of ED cell, coulometric and amperometry. In coulometric detection, E2 electrode is porous and has a large surface area. When an appropriate voltage is applied, it allows the complete oxidation/reduction of the compounds of interest, and thus the resulting current is directly proportional to the total amount of compound present. In amperometric detection on the other hand, the E2 electrode is smooth and has a small surface area, allowing only a fraction of the compound to be oxidised/reduced. The method used in this thesis employs coulometric detection.

The voltage used determines the sensitivity and specificity of the HPLC method. It is chosen based on its ability to fully oxidize or reduce the molecules of interest, where it is high enough to detect these specific molecules but low enough to not detect other molecules present in the sample analysed. Therefore, voltage applied dictates the number of electrons transferred from the molecules to the electrode or vice-versa, which directly influences the strength of the resulting electrical current. The result of the electrochemical reactions is

presented as a graph, a chromatogram, of electrical currents as a function of time integrated in a special data software. Ultimately, this corresponds to the concentration of molecules present in a given sample (Kilpatrick *et al.* 1986).

HPLC-ED can be used to measure monoamines such as catecholamine neurotransmitters. The detection and quantification of catecholamine metabolites in human CSF is an important diagnostic tool for many diseases (Hyland and Clayton 1992; Batllori *et al.* 2017; Willemsen *et al.* 2010). Extracellular and intracellular measurement of these metabolites in cellular models of diseases can be analogous to CSF neurotransmitter measurement and a great asset in assessing the suitability of these models, understanding disease pathology and development of therapeutics. In this thesis, the detection and quantification of dopamine and serotonin metabolites was enabled by developing the HPLC-ED method in this chapter.

Therefore, the **aim** of the work presented in this chapter was:

- To develop a reproducible, reverse-phase isocratic HPLC-ED method to quantify intracellular and extracellular dopamine and serotonin monoamine metabolites in cellular neuronal models

3.2. Method development:

3.2.1. Equipment:

The HPLC components were the following: PU-1580 intelligent HPLC pump, DG-980-50 3-line degasser, AS-1555 intelligent cooled autosampler, CO-1560 intelligent column thermostat (JASCO UK Ltd), C18HS column 250 mm × 4.5 mm, 100 Å pore size and 5 µm particle size (Kromatek), Coulochem II electrochemical detector and ESA analytical cell (model 5010A and 5011, ThermoFisher Scientific, UK) coupled to a computer with EZChrom Elite chromatography system (V3.1.7, JASCO Ltd, UK). Components were arranged as demonstrated in (Figure 20).

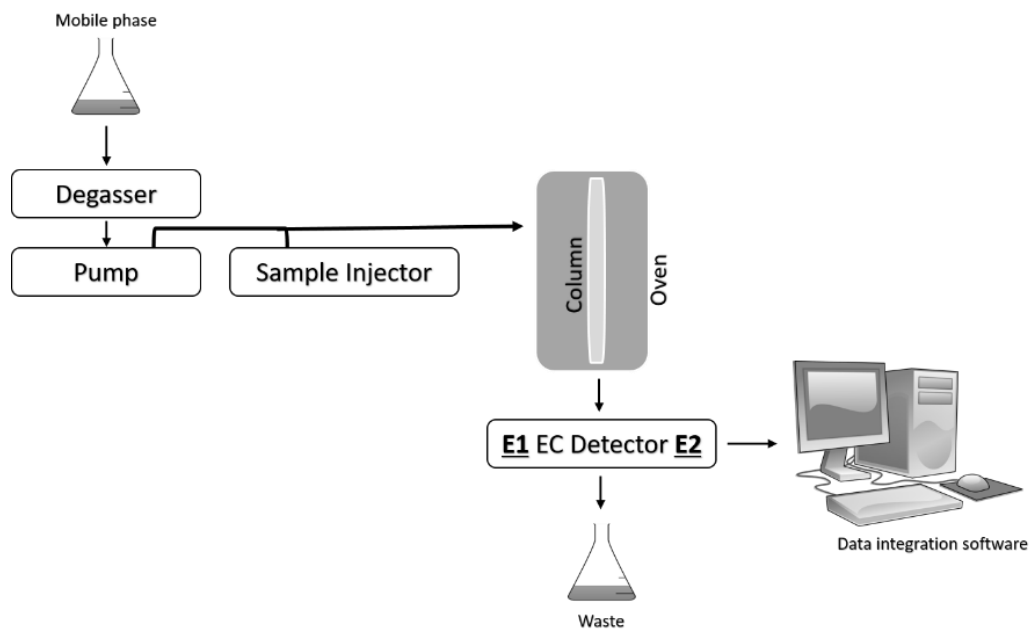


Figure 20 HPLC instrumentation. Mobile phase is de-gassed first before being mixed with the sample and injected into the column. Sample components are separated by the column, then oxidised/reduced in the detector cell. The reaction is then plotted as current against time by the integration software. EC: electrochemical

3.2.2. Method conditions:

This method, adapted from de la Fuente (2017), is a reverse-phase HPLC method, where an aqueous, polar mobile phase passes through a non-polar stationary phase, a column of silica coupled to C18 chains. The difference in polarity allows the separations of the sample molecules injected into the mobile phase on the basis of their polarity. Highly non-polar molecules will bind more strongly to the stationary phase and as a result, elute later in the run. More polar molecules will have a weaker affinity to the stationary phase and elute with the mobile phase earlier in the run (Flanagan et al., 2008) .

This method uses an isocratic mobile phase, where the composition of the mobile phase remains constant throughout the experimental run. The mobile phase was prepared in HPLC grade water to the following composition (Table 3):

Component:	Concentration:
Sodium acetate trihydrate	20 mM
Citric acid monohydrate	12.5 mM
EDTA disodium	0.1 mM
1-octanesulfonic acid	3.35 mM
Methanol	16%
pH	3.45

Table 3 HPLC mobile phase composition. (pH adjusted using concentrated HCl)

Sodium acetate trihydrate and citric acid monohydrate create a citrate-acetate buffer and 1-octanesulfonic acid acts as the ion pair. The ion-pair has a non-polar head group that adheres to the C18 carbon chains on the column, and an ionic head group that will interact with the ionised metabolites in the sample facilitating their retention and elution while passing through the column (Dolan 2008). The acidic pH of 3.45 was found to ensure ionisation of metabolites but preserves the proper separation between 3-OMD, DOPAC and 5-HIAA, as 3-OMD is highly sensitive to pH changes (Figure 21 B and C). 16% methanol ensured the best resolution between eluted compounds when coupled to a flow rate of 1.5 ml/min and a column temperature that was maintained at 27 °C (Figure 21 A and C). The volume of injection was kept at 50 µl. Experimental samples were prepared as described in section 2.4.2.

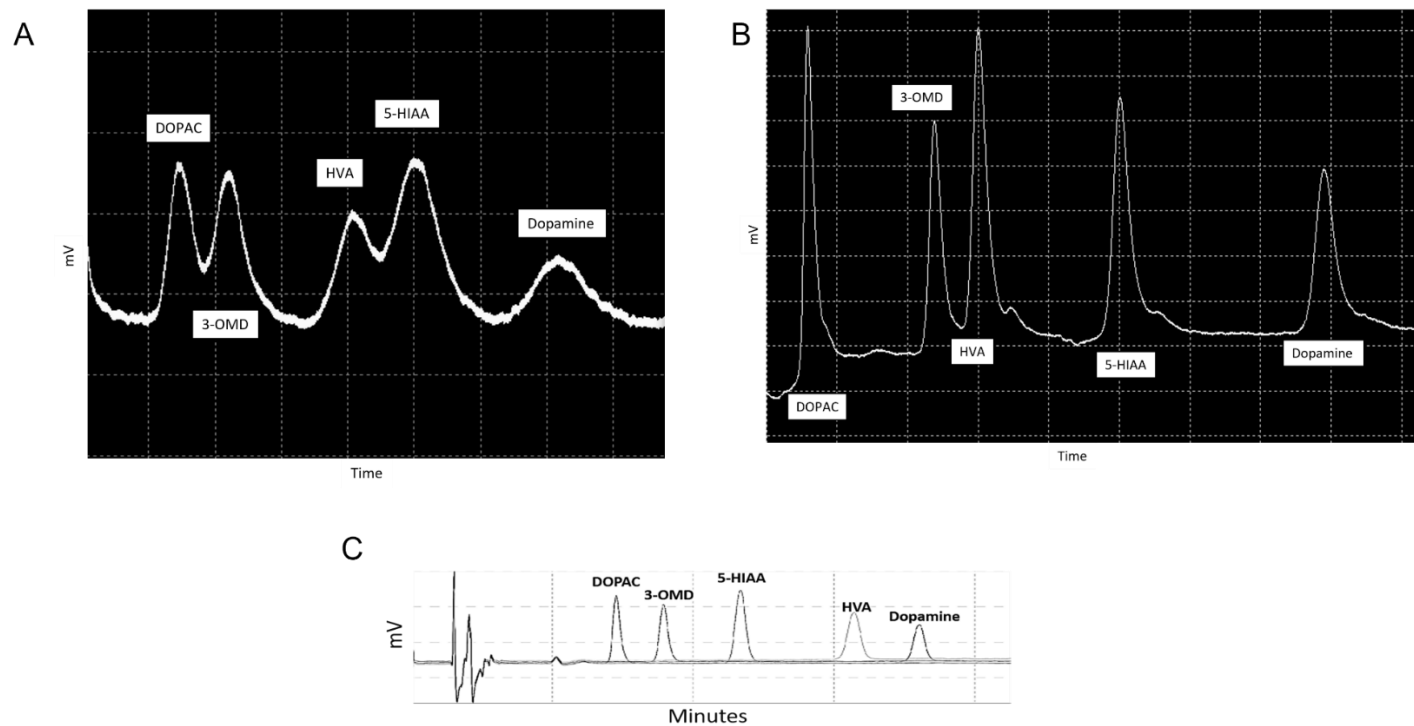


Figure 21 The effect of different method conditions on the resolution of the chromatogram using a sample composed of 500 nM external standard mixture (DOPAC, 3-OMD, 5-HIAA, HVA and dopamine) (A) sample chromatogram run using a mobile phase containing 13 % methanol. (B) sample chromatogram run using a mobile phase at pH 3.3. (C) sample chromatogram using a mobile phase containing 16 % methanol and at pH 3.45.

3.2.3. Method optimisation:

3.2.3.1. Cyclic voltammetry:

Voltammograms are performed to select the optimum voltage at which all compounds of interest are fully oxidized. The redox potential of a molecule is presented as a sigmoidal curve, and the optimum voltage (E2) must be high enough to oxidise a molecule but must be at the minimum value that offers maximum oxidization of compounds while retaining method selectivity by avoiding oxidation of other compounds present in the sample. To perform a cyclic voltammogram to select the optimum voltage (E2), a mixture of the compounds of interest (DOPAC, 3-OMD, 5-HIAA, HVA, and dopamine) was run at a constant concentration (500 nM) and at different voltages of the downstream electrode (E2, 200 – 450 mV). The upstream electrode (E1) was maintained at 50 mV. As a result, the optimum voltage for the downstream electrode (E2) for these experimental conditions and these metabolites was found to be 400 mV. It allowed the maximum oxidation of the compounds of interests while maintaining the specificity of detection to only detect the compound of interest in the sample (Figure 22).

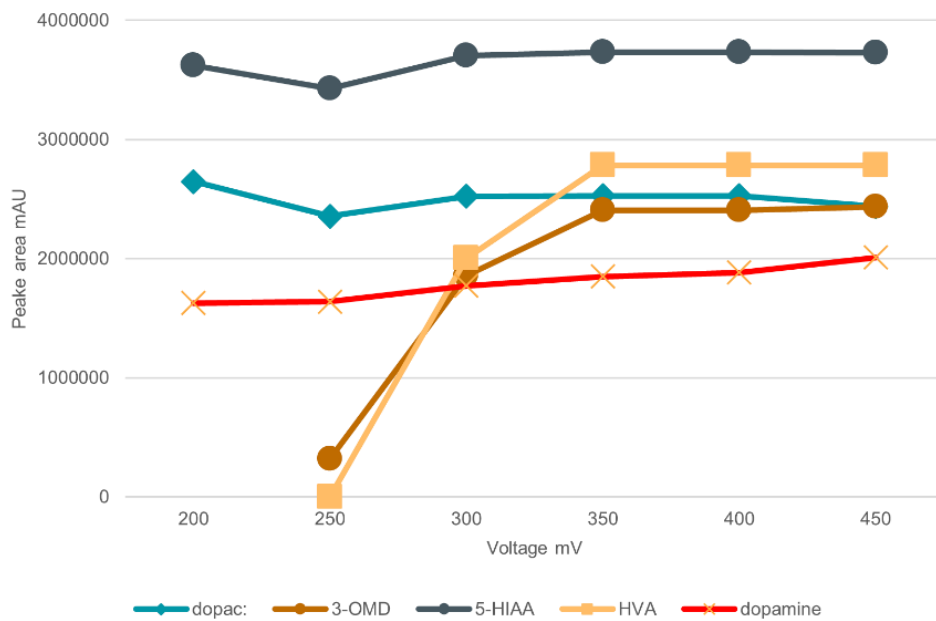


Figure 22 Cyclic voltammograms for dopamine and serotonin metabolites. A 500 nM mixture of DOPAC, 3-OMD, 5-HIAA, HVA and dopamine was run at different voltages of E2 (200-450 mV). The peak area was plotted against the voltage. E2 voltage of 400 mV was the optimum voltage at which all 5 metabolites were at maximum oxidation.

3.2.3.2. Calibration curve:

A linear calibration curve was performed to ensure a linearity of the method developed, that there is a linear correlation relationship between the concentration of metabolites present in the sample and the integrated peak area of the resultant chromatogram. To validate linearity of the method, different concentrations of the metabolites of interest (50 – 500 nM) were injected into the HPLC at a constant voltage (E2, 400 mV) and the integrated peak area of corresponding metabolite was measured and plotted against their concentration (Figure 23).

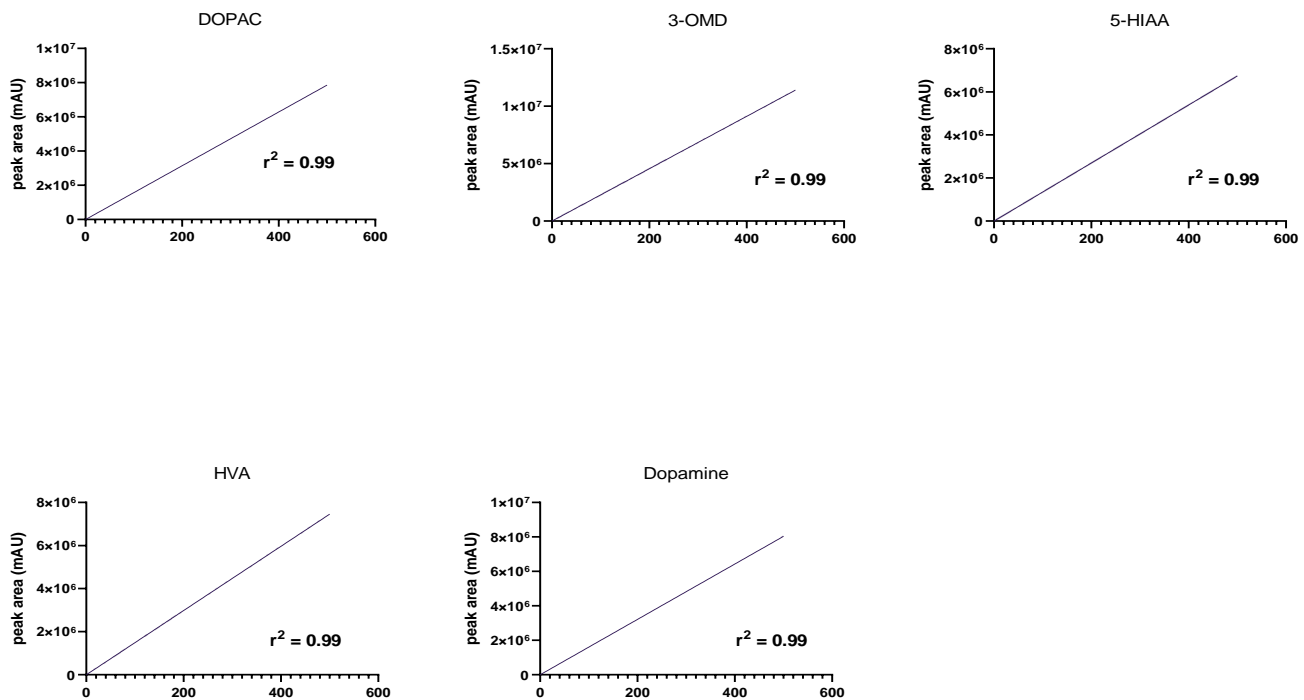


Figure 23 Linear regression curve for dopamine and serotonin metabolites. Different concentrations (50 – 500 nM) of metabolites of interest were run at a constant voltage (400 mV) and the resulting integrated peak area was plotted against the concentration

3.2.3.3. Metabolite temperature sensitivity:

To reduced experimental variability, a number of experimental samples were often run together. Running a set of samples simultaneously on the HPLC-ED can take up to 12 hours at a time depending on the experimental conditions. Therefore, ensuring the stability of the metabolites in the sample over long periods of time is important. To test the temperature stability of metabolites of interest, the metabolites were run at a constant concentration (500 nM) every hour for 12 hours in either a cooled (4°C) or uncooled (room temperature, RT) autosampler HPLC unit. All metabolites showed stability at RT except 5-HIAA. 5-HIAA appeared to be more stable at 4°C as evident from the decreasing integrated peak area over time, which corresponds to its concentration in the sample (Figure 24). Therefore, for this method, a 4°C cooled autosampler unit was used.

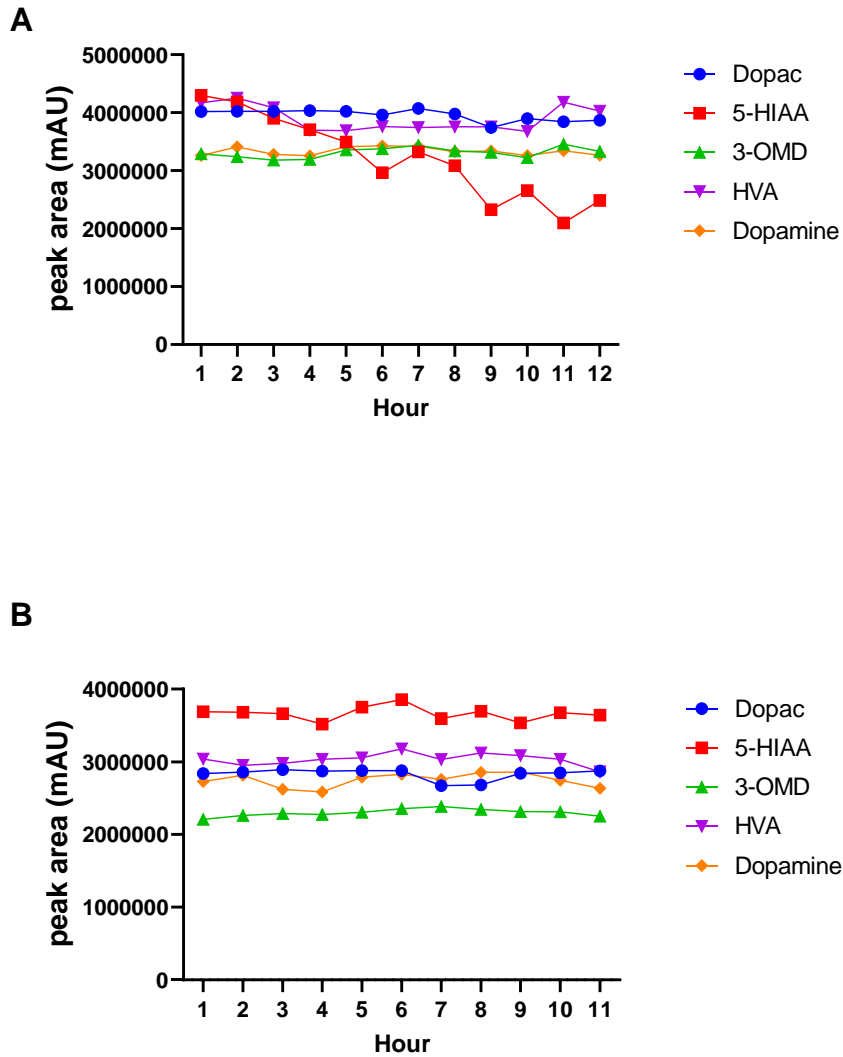


Figure 24 The temperature sensitivity of dopamine and serotonin metabolites. A 500 nM mixture of the metabolites of interest was run for several hours, once every hour in either an (A) uncooled autosampler unit or a (B) 4 °C cooled unit. The integrated peak area (mAU) was calculated and plotted against time.

3.2.3.4. Quality and accuracy of the method:

To ensure quality of each HPLC run, quality control measures were taken as a good tool to inspect the long-term behaviour of the HPLC instrument and method used. In this study, an extracellular sample of L-DOPA treated SH-SY5Y cells (QC) was used to test method reproducibility. Initially, the QC sample was run 12 times during routine work and each time, the integrated peak area of the 5 metabolites of interest was measured. Once a sufficient number of runs was obtained, acceptable performance limits (± 2 SD) were established to use as a statistical control measure of the HPLC-ED method performance (example DOPAC, Figure 25). Thereafter, a QC sample was included in each HPLC-ED run and the integrated peak area of metabolites was calculated to ensure it falls within control limit (± 2 SD). If it does, then the run was classified as in-control. If the values fell outside the control limits, then the run is not “in-control” and any analytical results obtained during the run were disregarded.

The accuracy of an HPLC method is a measure of the nearness between the expected concentration and the concentration calculated from the resulting peak. One method to determine the accuracy of an HPLC method is by calculating the percent recovery, where a known concentration of standard is added to a known concentration of sample, and the concentration of the resulting integrated peak is calculated according to the following equation:

$$\frac{\text{Integrated peak area (sample)}}{\text{Integrated peak area (external standard)}} \times \text{External standard concentration (nM)}$$

The measured concentration is then divided by the expected concentration of the peak to obtain percent recovery (Betz *et al.* 2011). The mean percent recovery of this method was 98.5 ± 0.9 (mean \pm SEM, $n= 4$ each metabolite, DOPAC, 3-OMD, HVA, 5-HIAA and dopamine)

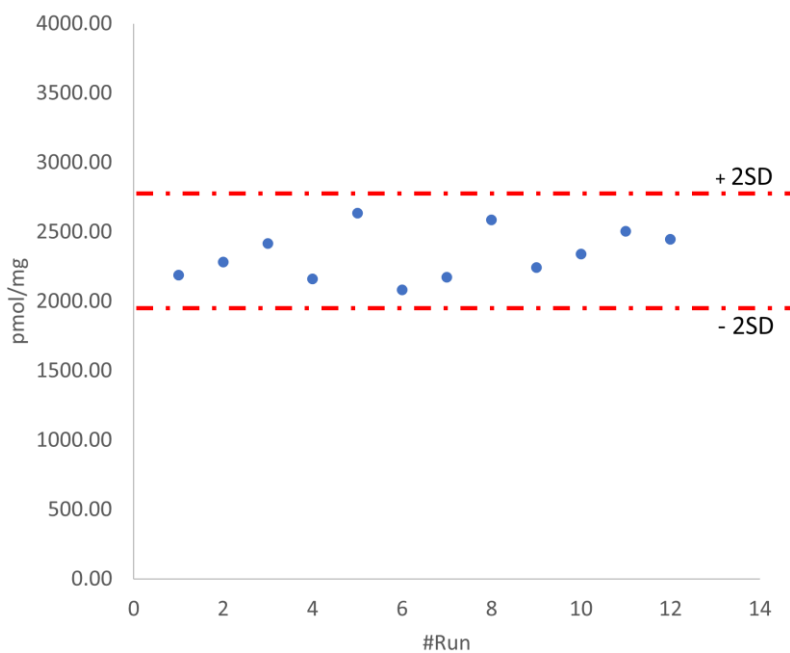


Figure 25 Quality control samples for DOPAC. A QC sample of L-DOPA treated SH-SY5Y cell extracellular sample was obtained and run within routine HPLC-ED runs. After 12 independent runs, mean integrated peak area of DOPAC was calculated and was used to create a control limit ($\pm 2SD$). SD: standard deviation.

3.2.4. Identification and quantification of integrated peaks:

The identification of the metabolites in the experimental sample was enabled by comparing the elution time of the known metabolites in an external standard mixture and the elution times of the metabolites in the sample. First, each metabolite in the external standard mixture (DOPAC, 3-OMD, 5-HIAA, HVA and dopamine) was run separately to determine the elution time at which it will appear in the chromatogram under the conditions of this method. Then the external standard mixture was run to ensure no peak interference occurred between the different metabolites (Figure 26). Once no interference was confirmed, the elution time of the individual molecules in the external standard was used to identify the peaks in the experimental sample, as each metabolite will have a specific elution time (Figure 27).

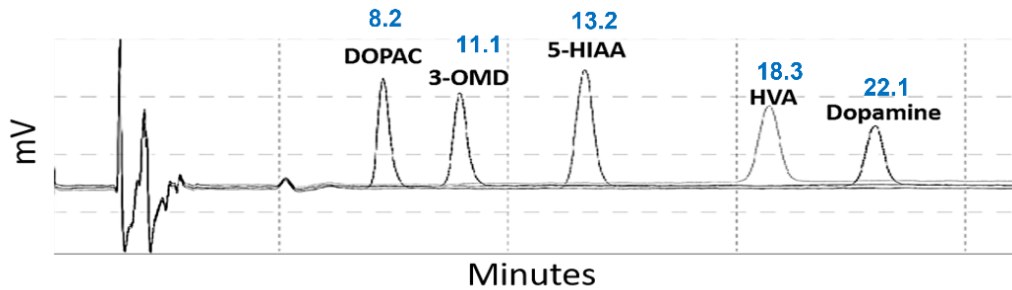


Figure 26 The order and retention times of the external standards. Each metabolite is eluted at a specific time creating a good resolution between the different metabolites and enabling peak identification.

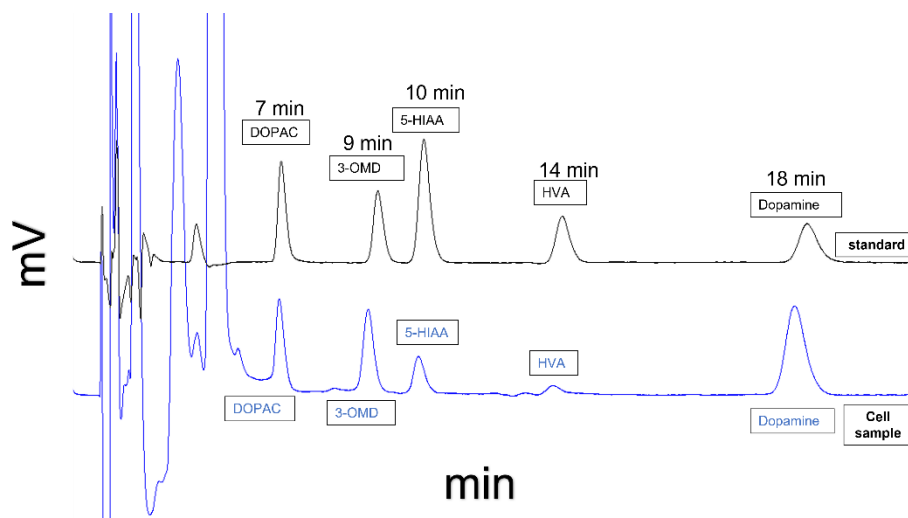


Figure 27 A chromatogram of an experimental sample and external standard. The experimental sample was extracellular media from L-DOPA treated proliferative SH-SY5Y cells, The peaks in external standard (black) are used to identify and quantify the peaks and metabolites of interest in the experimental sample (blue).

The quantification of the concentration of molecules in the experimental sample was enabled by referencing it to an external standard of known concentration. 500 nM external standard containing a mixture of DOPAC, 3-OMD, 5-HIAA, HVA and dopamine was used (Figure 26). The concentration is chosen based on its similarity to the values normally observed in the cells under the experimental conditions of this thesis (de la Fuente *et al.* 2017). This mixture was freshly prepared in HPLC grade water with few drops of concentrated HCl prior to experimental run. The integrated peak areas of standard and sample was used to calculate the unknown concentration of metabolites in samples using the following formula:

$$\frac{\textit{Integrated peak area (sample)}}{\textit{Integrated peak area (external standard)}} \times \textit{External standard concentration (nM)}$$

In summary, the result of this method development is the ability to simultaneously identify and quantify dopamine and serotonin metabolites in cell culture media and cell lysate (Figure 28, Figure 29).

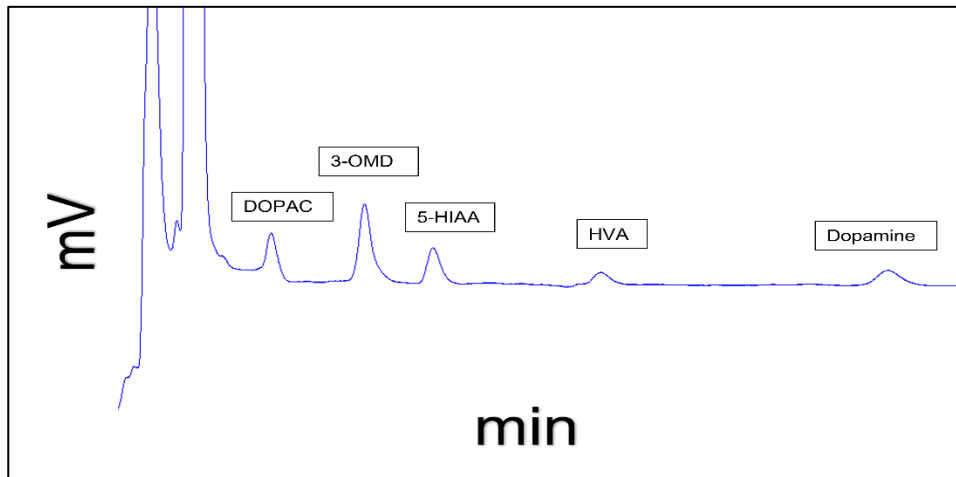


Figure 28 Example of an extracellular neurotransmitter metabolite profile in L-DOPA treated differentiated SH-SY5Y cells.

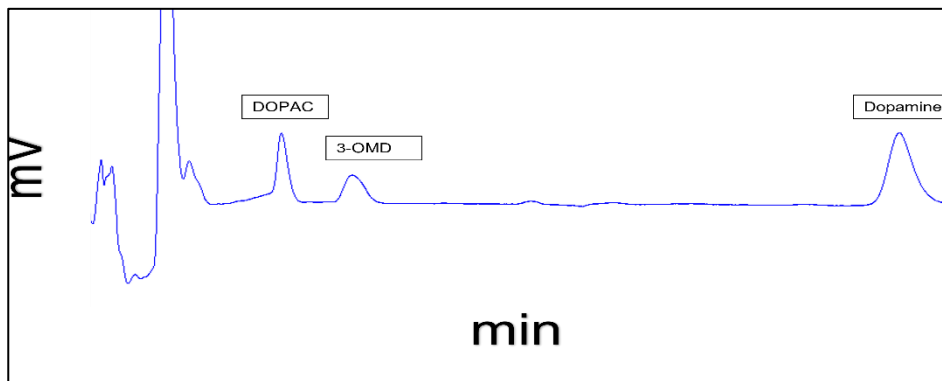


Figure 29 Example of a cell lysate neurotransmitter metabolite profile in L-DOPA treated proliferative SH-SY5Y cells.

3.2.5. Internal standard:

The use of external standards alone is a common way to ensure the accuracy of the HPLC method however, it is also recommended to include an internal standard (IS) in the method.

Including an IS into the external standard and the experimental sample offers a higher degree of accuracy by compensating for any inconsistencies that may occur in volume of injection or any changes in sample pre-treatment, measurement conditions and instrument behaviour. This method was developed with the intention to measure both intracellular and extracellular cell samples therefore, including an IS was explored to improve accuracy, particularly with regards to intracellular samples.

Choosing an IS for a given HPLC method is a complex process that must comply with a set of criteria in order to find the most suitable IS. The IS of choice must not already exist in the external standard mixture or the experimental sample. Additionally, it should have a very similar chemical structure to ensure that it behaves in a similar way to the metabolites of interest under the method conditions (e.g., have a close elution time), however it must form a completely separate peak and not interfere with any of the metabolites of interest. Finally, it must be both chemically stable and easy to obtain.

3,4-Dihydroxybenzylamine (DHBA) is a commonly used IS for measurements of monoamines (He *et al.* 1997; Chan and Ho 2000). It has a chemical structure that is very similar to dopamine. It is a stable molecule as evident by its stability against multiple freeze-thaw cycles (Figure 30). Unfortunately, under the HPLC method conditions used in this thesis, DHBA has

an elution time that is very close to 5-HIAA, one of the key metabolites of interest in both our standards and sample (

Figure 31). This makes DHBA an unsuitable IS for the HPLC method used in this thesis.

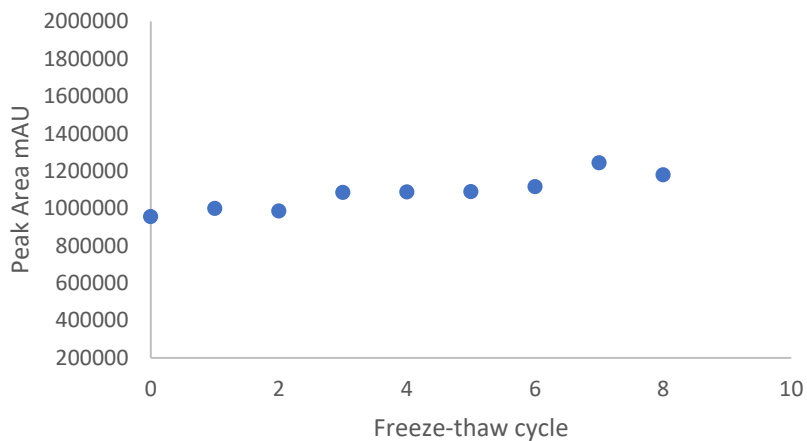


Figure 30 DHBA stability test. DHBA was subjected to multiple freeze and thaw cycles and then analysed on the HPLC. Peak area was plotted against cycle number.

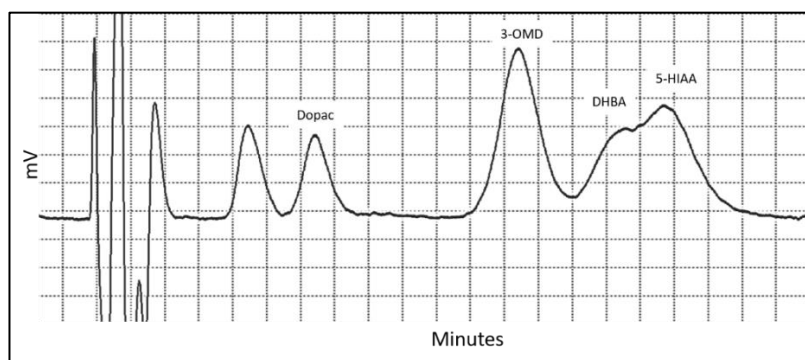


Figure 31 DHBA peak interference with 5-HIAA. Under the method conditions of this thesis, the elution time of DHBA is very close to 5-HIAA.

Isoproterenol was the second choice of IS. It has been used in the literature for monoamine separation (Echizen *et al.* 1989). The choice was based on its structural similarity to our metabolites of interest and the fact that it possesses more methyl groups than DHBA making it more hydrophobic and thus delaying the elution time compared to the metabolites of interest. However, although a good separation between isoproterenol and the external standard metabolites was achieved under the method conditions of this thesis (Figure 32), when included in the experimental samples, isoproterenol had an identical elution time to an unknown compound in the sample, hindering accurate peak quantification as the unknown peak contributed to the peak area of isoproterenol.

Taken together, including an IS in an HPLC method is recommended to increase the accuracy of the method. However, the robustness of the HPLC instrumentation, the use of 5 external standards, the quality control measures taken, and the simple sample preparation process used in this thesis make measurement without an IS sufficient for this thesis.

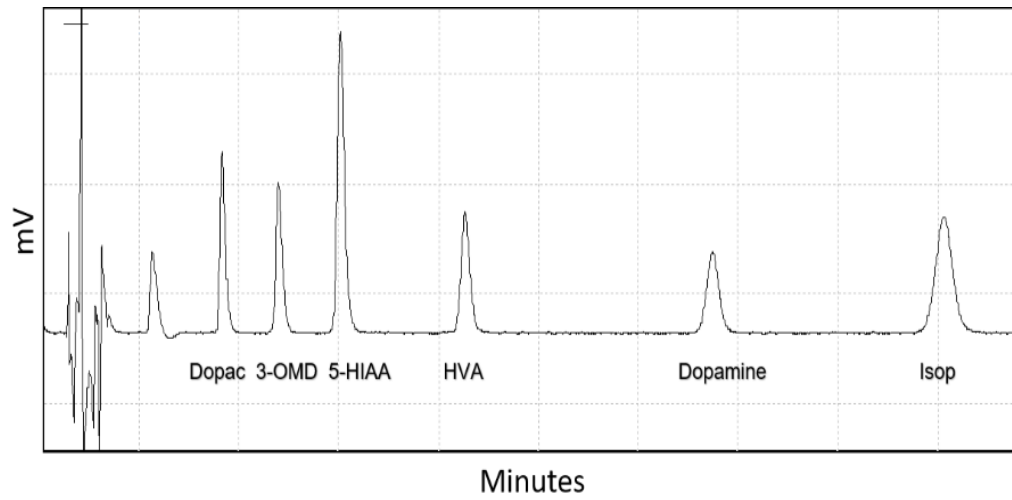


Figure 32 Elution time of external standards and isoproterenol internal standard.

In conclusion, the HPLC-ED protocol developed in this chapter presents a reproducible method for the simultaneous measurements of monoamine metabolites of dopamine and serotonin both from cell culture media and from intracellular lysate of cultured cells.

Chapter 4. Biochemical Comparison Between Proliferative and Differentiated SH-SY5Y Cells as Models for Parkinson's Disease

4.1. Introduction

The use of *in vitro* cancer cell line models has been one of the greatest assets in medical sciences to understand cellular physiology, disease pathology, and to investigate potential therapeutics. The SH-SY5Y human neuroblastoma cell line is one of the most used cell line models in PD research (Xicoy *et al.* 2017). They are a subclone of the parental cell line, SK-N-SH, generated from a bone marrow biopsy in the 1970s (Biedler *et al.* 1973). Their suitability is attributed to their ability to express TH and DAT, both of which are markers of dopaminergic neurons, the neuronal subtype most affected in PD (Michel *et al.* 2016). SH-SY5Y cells have been used to study the key pathological pathways in PD (Xicoy *et al.* 2017). For example, mitochondrial dysfunction is considered central to PD pathology and SH-SY5Y cells have been used to study the effects of the neurotoxins rotenone, 6-hydroxydopamine and 1-methyl-4-phenylpyridinium (MPP⁺) on mitochondrial dynamics and bioenergetics (Wang *et al.* 2011; Giordano *et al.* 2012). SH-SY5Y cells were utilised to understand the effect of mitochondrial dysfunction on dopamine and serotonin metabolism and the effect of dopamine oxidation on mitochondrial function (Biosa *et al.* 2018; de la Fuente *et al.* 2017). In addition to mitochondrial dysfunction, lysosomal dysfunction is another key player in PD pathology. GBA activity is significantly reduced in the presence and absence of gene mutations in brain tissue, monocytes and dried blood spots from patients with PD (Gegg *et al.* 2012; Alcalay *et al.* 2020; Hughes *et al.* 2021). SH-SY5Y cells have been an asset in investigation of the mechanism behind GBA dysregulation. For example, they were used to understand the effect of GBA inhibition on dopamine and serotonin

metabolism, mitochondrial function and oxidative stress (de la Fuente *et al.* 2017; Cleeter *et al.* 2013). In addition, SH-SY5Y cells were used to investigate the effect of heterozygous mutations in GBA on mitochondrial function (Li *et al.* 2019). Finally, PD is a disease of cellular oxidative stress imbalance. SH-SY5Y cells were used to study the effect of dopamine and L-DOPA oxidation and rotenone toxicity on the cellular GSH levels, the major antioxidant in the cell (Allen *et al.* 2013; Watabe and Nakaki 2008).

Despite the wide use of this cell line, the literature is not clear on whether SH-SY5Y cells can be used in their proliferative state or whether differentiation is necessary. Proliferative SH-SY5Y cells form a heterogenous cell population of constantly dividing cells that are non-polarised and have few neuronal processes, making them dissimilar to post-mitotic neurons. In addition, the state of constant proliferation increases the rate of DNA replication error so that higher passage number cells may not perfectly represent the lower passage cells. Despite these concerns, proliferative cells are easy to obtain, grow and maintain. They allow an insight into the basic molecular processes of human cells, including understanding gene function and manipulation of cellular pathways. They permit large scale expansion, which is necessary for example in metabolomics research, and they offer a starting point for drug screening and discovery (Kaur and Dufour 2012). Concerning proliferative SH-SY5Y cells as a PD model specifically, these cells express the dopaminergic neuronal markers TH, DAT and dopamine receptors and whole genomic analysis revealed that most of the genes implicated in PD are intact (Krishna *et al.* 2014; Xicoy *et al.* 2017).

Once differentiated however, SH-SY5Y cells become a more homogenous cell population with a synchronised cell cycle, obtain a more polarised cell morphology and have extended neurites; making them more similar to mature neurons (Xicoy *et al.* 2017). Moreover, differentiation is reported to increase the expression of TH and DAT; key markers of dopaminergic neurons (Ballaz *et al.* 2013; Looyenga *et al.* 2013; Presgraves *et al.* 2004). When compared to proliferative SH-SY5Y cells, differentiated SH-SY5Y cells have been shown to have increased TH expression, higher resistance to the neurotoxin MPP⁺ and are electro-physiologically more similar to mature neurons (Khwanraj *et al.* 2015; Şahin *et al.* 2021). Differentiation of SH-SY5Y cells using sequential treatment with retinoic acid (RA) and the phorbol ester, 12-O-tetradecanoylphorbol-13-acetate (TPA), is reported to drive cellular differentiation into a dopaminergic cell lineage, the type of cells extensively affected in PD (Presgraves *et al.* 2004). Therefore, differentiation of SH-SY5Y cells using RA/TPA could result in a more neuronal-like cells with basal dopamine production, which is reported to be absent in proliferative SH-SY5Y cells (de la Fuente *et al.* 2017).

Thus, the **aims** of this chapter were:

- Develop a reproducible differentiation protocol for differentiation of SH-SY5Y cells into cells that better resemble mature dopaminergic neurons
- Compare the biochemistry of proliferative and differentiated SH-SY5Y cells, focusing on the pathways most affected in PD

4.2. Materials and methods:

4.2.1. Cell culture

SH-SY5Y cells were cultured as described in section 2.2.

4.2.2. SH-SY5Y differentiation

SH-SY5Y cells were differentiated as described in section 2.3.

4.2.3. Western blot for neuronal marker expression

NSE, NeuN and TH protein expression was detected and quantified as described in section 2.6.

4.2.4. L-DOPA treatment

SH-SY5Y cells were treated with 100 μ M L-DOPA in phenol-red free 10% FBS cell culture media for 1 hour as described in section **2.2.2**.

4.2.5. Sample preparation

HPLC-ED extracellular sample was processed as described in section 2.4.2.1 and stored at – 80 °C for analysis. For intracellular sample, cells collected and processed as described in section 2.4.2.2 and stored at – 80 °C for analysis.

Mitochondrial samples and lysosomal GBA samples were prepared as described in section 2.4.1 GSH samples were prepared as described in section 2.4.3.

4.2.1. HPLC-ED analysis

Samples were analysed using the method described in Chapter 3.

4.2.2. Enzyme assays

Mitochondrial CS, complex I, II-III and IV enzyme activity were assayed as described in section 2.7.

Lysosomal GBA enzyme activity was assayed as described in section 2.7.

4.2.3. GSH measurement

GSH levels were determined using HPLC-ED method as described in section 2.8.

4.3. Results

4.3.1. Morphology

Neuronal cells have a unique polarised cell morphology consisting of a cell body with protruding dendrites and a long axon. Proliferative SH-SY5Y cells have a morphology that closely resembles that of mesencephalic cells (Figure 33). Following differentiation by sequential treatment with RA and TPA for 7 days, SH-SY5Y cells acquired a morphology that is more neuronal-like in shape; they became polarised and extended their neurites. In addition, the cells formed clusters. These clusters appeared to be making connections via extension of their neurites between different clusters (Figure 33). In addition, following differentiation, cells appeared to stop proliferating and settle into a more stable population, in contrast to proliferative SH-SY5Y cells which are continuously dividing.

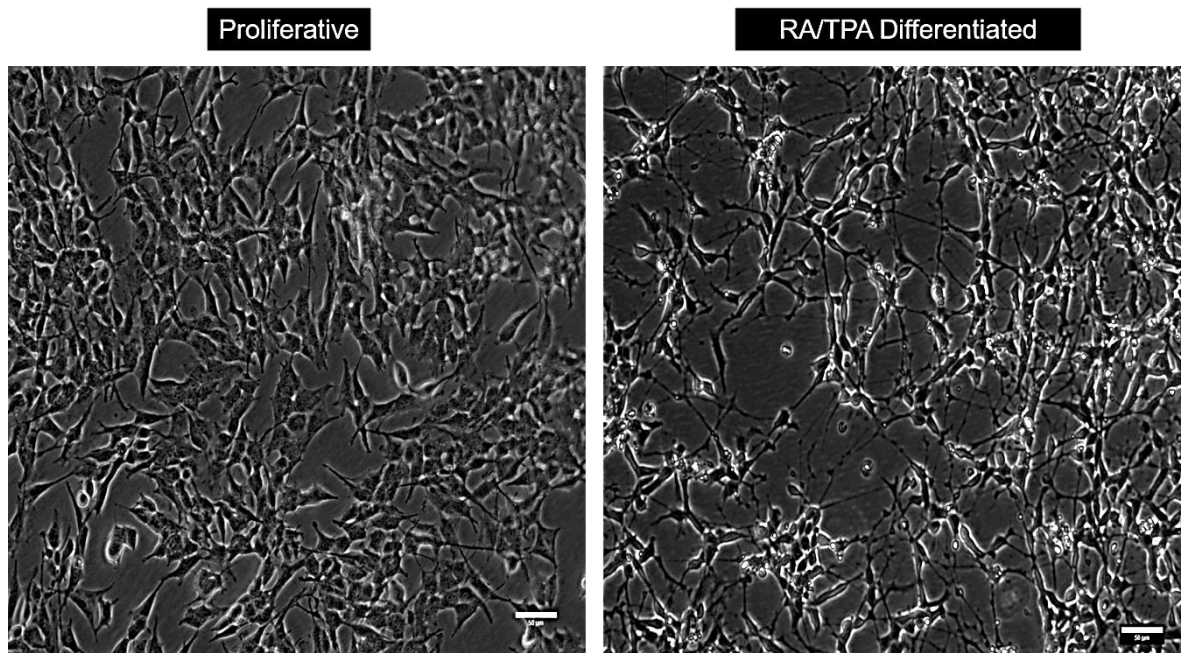


Figure 33 Proliferative and differentiated SH-SY5Y cell morphology as observed under light microscope. Left: proliferative SH-SY5Y cells. Right: differentiated SH-SY5Y cells after 3 days of 10 µM RA treatment followed by 3 days of 80 nM TPA treatment. Scale bar: 50 µm.

4.3.2. Expression of neuronal markers:

Following differentiation of SH-SY5Y cells, confirmation of their neuronal differentiated dopaminergic phenotype was carried out via investigation of protein expression of relevant neuronal markers using western blot. The first marker of interest was the neuronal-specific enolase (NSE). NSE is an isozyme of the enolase family of glycolytic enzymes. NSE expression is specific to neuronal tissue therefore, its presence confirms cells of neuronal origin. It exists a dimer of the γ isozyme of enolase in the cytoplasm of neurons and has a molecular mass of about 45 kDa (Marangos and Schmechel 2003; Isgrò *et al.* 2015). After confirming the band identity using a molecular weight ladder, immunoblotting using an antibody specific against NSE revealed that NSE expression is comparable between proliferative and differentiated SH-SY5Y cells as evidenced by calculation of densitometric band intensity and normalising to the loading control GAPDH. Ratio of band intensity of NSE/GAPDH was 1 for proliferative and 0.97 for differentiated SH-SY5Y cells (Figure 34).

The next neuronal marker of interest was the neuronal nuclei, or NeuN. NeuN is a 48 kDa neuronal nuclear protein, a product of the *Fox-3* gene, and its expression is specific to post-mitotic neurons. As a result, it is widely used as a marker to monitor cellular differentiation as its levels correspond to the withdrawal of cells from the cell cycle and initiation of differentiation. As the cell moves forward through the differentiation process, its levels reciprocally increase (Kim *et al.* 2009). After confirming the band identity using a molecular weight ladder, immunoblotting using an antibody specific against NeuN revealed that NeuN expression increased by almost 2-fold following differentiation of SH-SY5Y cells. This was evidenced by calculation of densitometric band intensity (after

normalising to the loading control GAPDH), NeuN/GAPDH was 0.6 for proliferative and 1 for differentiated SH-SY5Y cells (Figure 35).

TH is the first and rate limiting enzyme of dopamine pathway and a key characteristic of dopaminergic neurons. It is homo-tetramer enzyme composed of 4 identical subunits with a molecular weight of 60 kDa (Szigetvari *et al.* 2019). Using a specific antibody against TH monomer, TH band was detected at a band at approximately 60 kDa in both proliferative and differentiated SH-SY5Y cells. The band identity was confirmed by comparison to TH band from iPSC dopaminergic neurons (Gift from Professor Manju Kurian, UCL, London, UK). TH expression in proliferative and differentiated SH-SY5Y cells was compared using band densitometry after normalising to GAPDH (TH/GAPDH). Levels of TH expression in proliferative was found to be 0.24 and in differentiated 0.23 (Figure 36).

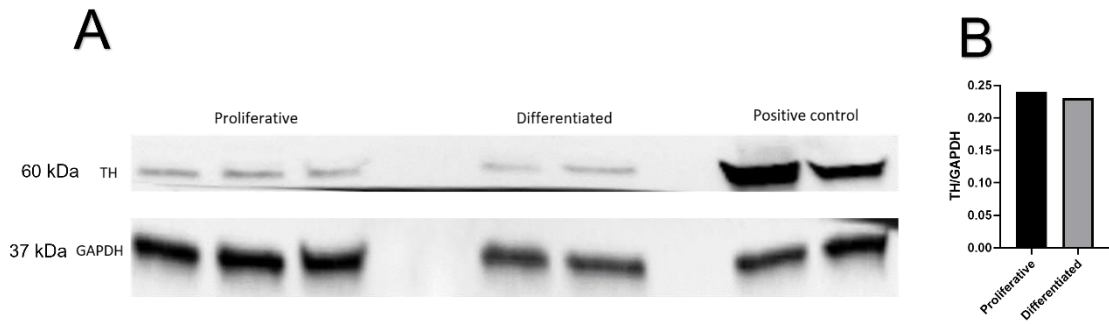


Figure 36 Tyrosine hydroxylase protein expression in proliferative and differentiated SH-SY5Y cells. iPSC dopaminergic neurons were used as a positive control. GAPDH protein expression was used as loading control. A) representative western blot from 2 independent experiments. B) Densitometry of ratio of TH to GAPDH. TH: tyrosine hydroxylase.

4.3.3. Extracellular and intracellular dopamine and serotonin metabolism

Dysregulated dopamine and serotonin metabolism are key pathologies in PD. Therefore, to assess the suitability of any PD model, characterisation of dopamine and serotonin metabolism is important. Despite the wide use of proliferative SH-SY5Y cells as a model for PD, basal dopamine metabolism is reported to be absent in proliferative SH-SY5Y cells (de la Fuente *et al.* 2017). Therefore, a hypothesis was made that given the reports that RA/TPA differentiation derives cells to a more neuronal-like phenotype, differentiation of SH-SY5Y cells would result in measurable basal dopamine metabolism. The analytical method developed in chapter 3 using HPLC-ED was used to measure dopamine and serotonin metabolites in extracellular and intracellular fractions.

Interestingly, under basal conditions, dopamine and its metabolites were undetectable in either proliferative or differentiated SH-SY5Y cells, both intracellularly and extracellularly. In contrast, the main metabolite of serotonin, 5-HIAA, was readily detectable extracellularly. Proliferative and differentiated SH-SY5Y cells showed a similar extracellular basal level of 5-HIAA, 3507 ± 411 pmol/mg and 3561 ± 968 pmol/mg, respectively (Figure 37). Intracellularly however, none of the metabolites were detectable.

The absence of basal dopamine metabolites necessitated the prior incubation of cells with 100 μ M L-DOPA for 1 hour to stimulate the dopamine pathway and bypass the TH rate limiting step. 100 μ M L-DOPA has been previously shown to stimulate dopamine synthesis in proliferative SH-SY5Y cells and iPSC derived dopaminergic neurons (de la Fuente *et al.* 2017; Woodard *et al.* 2014).

Following L-DOPA supplementation, dopamine metabolites were detectable both intracellularly and extracellularly. Measurement of dopamine metabolites revealed a significant difference in the rate of extracellular dopamine turnover between proliferative and differentiated SH-SY5Y cells (as calculated by the ratio of DOPAC and HVA to dopamine). Rate of dopamine turnover was 2.5-fold higher in differentiated compared to proliferative SH-SY5Y cells (0.25 ± 0.04 in proliferative and 0.65 ± 0.08 in differentiated, $p = 0.0012$, Figure 38 B). This was reflected by a significantly higher dopamine level in proliferative than in differentiated (8984 ± 4306 pmol/mg protein and 4046 ± 384 pmol/mg protein, respectively, $p = 0.01$). It was also reflected by a higher level of DOPAC in proliferative compared to differentiated (4363 ± 1856 pmol/mg protein and 1582 ± 293 pmol/mg protein, respectively, $p = 0.11$). However, levels of 3-OMD and HVA were similar between the two cellular phenotypes (3-OMD was 10169 ± 2048 pmol/mg protein in proliferative and 10275 ± 1590 pmol/mg protein in differentiated, $p = 0.96$. HVA was 890 ± 330 pmol/mg protein in proliferative and 1178 ± 307 pmol/mg protein in differentiated, $p = 0.53$, Figure 38 A).

Looking at the serotonin metabolite, 5-HIAA, its levels remained similar in both phenotypes and were not affected by L-DOPA supplementation (3523 ± 670 pmol/mg protein in proliferative and 3790 ± 818 pmol/mg protein in differentiated, $p = 0.81$, Figure 38 A).

Following analysis of intracellular metabolites in L-DOPA supplemented SH-SY5Y cells, only the dopamine metabolites were detectable. Similar to what was seen extracellularly, dopamine levels were higher in proliferative cells compared to differentiated, although results did not reach statistical significance

(3967 ± 865 pmol/mg protein and 2211 ± 312 pmol/mg protein, respectively, $p = 0.09$). Levels of 3-OMD and DOPAC were lower in differentiated cells, but the results were not statistically significant (DOPAC was 1356 ± 327 pmol/mg protein in proliferative and 823 ± 205 pmol/mg protein in differentiated, $p = 0.17$. 3-OMD was 1379 ± 342 pmol/mg protein in proliferative and 681 ± 165 pmol/mg protein in differentiated, $p = 0.08$). HVA was not detected intracellularly (Figure 38 C). For this reason, to compare intracellular dopamine metabolism, dopamine turnover rate was calculated as a ratio of DOPAC to dopamine. Intracellular dopamine metabolism was found to be comparable between the two phenotypes, in contrast the higher dopamine metabolism extracellularly in differentiated cells (0.32 ± 0.02 in proliferative cells and 0.35 ± 0.04 in differentiated cells, $p = 0.65$, Figure 38 D). Similar to what was seen under basal condition, intracellular levels of 5-HIAA were undetectable following L-DOPA supplementation.

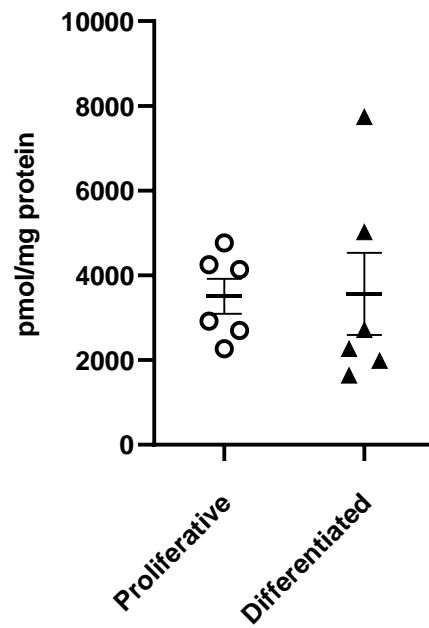


Figure 37 Extracellular level of 5-HIAA under basal conditions. The main serotonin metabolite, 5-HIAA, was detectible in proliferative and differentiated SH-SY5Y cells extracellularly under basal conditions. Results are expressed as ratio to protein concentration and presented as mean \pm SEM of 6 independent cell preparations. Unpaired Student's test was used to test for significance.

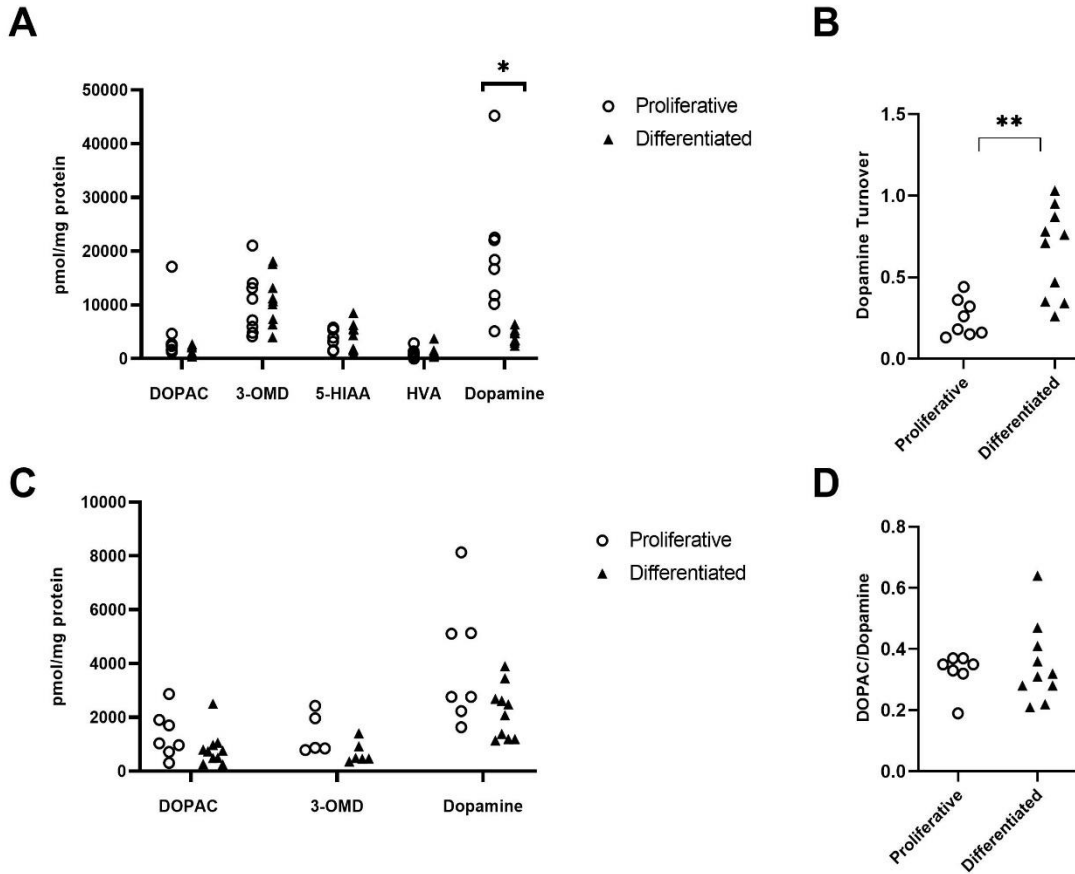


Figure 38 Extracellular and intracellular dopamine and serotonin metabolites in proliferative and differentiated SH-SY5Y cells. A) Extracellular dopamine and serotonin metabolites following 1 hr incubation with 100 μ M L-DOPA. B) Rate of extracellular dopamine turnover, calculated by the ratio of DOPAC and HVA to dopamine. C) Intracellular dopamine and serotonin metabolites following 1 hr incubation with 100 μ M L-DOPA. D) intracellular ratio of DOPAC to dopamine. Results are expressed as ratio to protein concentration and presented as mean \pm SEM of 8-10 independent cell preparations. Unpaired Student's test with or without Welch's correction was used to test for significance. * $p = 0.01$, ** $p = 0.0012$.

4.3.4. Mitochondrial ETC activity

Mitochondrial perturbations are implicated in the pathogenesis of PD. Decreased activity of ETC complexes I and IV have been documented in the SN from PD patients (Holper *et al.* 2019; Schapira 2007). In addition, mitochondrial complex I appears to play a part in the regulation of dopamine and serotonin pathways (de la Fuente *et al.* 2017). Therefore, the activity of the different mitochondrial ETC complexes was characterised in proliferative and differentiated SH-SY5Y cells. Activity was expressed on a protein baseline as well as a ratio to CS enzyme activity. CS is a mitochondrial matrix enzyme that is commonly used as a marker for mitochondrial content, as it showed good correlation (Larsen *et al.* 2012). It has been reported that differentiation was associated with changes in mitochondrial content and CS activity (Schneider *et al.* 2012). Measurement of CS activity revealed a significant 20% decrease following differentiation ($p = 0.04$, Table 4). Therefore, for accurate comparison of ETC complex activity between the two phenotypes, activity was expressed as a ratio to CS to account for changes in mitochondrial content following differentiation.

No significant differences were detected in complex I and II-III activity between the two phenotypes. Complex IV activity, however, was marginally higher in differentiated compared to proliferative, although the increase was not statistically significant (Table 4)

Table 4 Activity of mitochondrial electron transport chain complexes in proliferative and differentiated SH-SY5Y cells. Enzyme activity was measured on a protein baseline and as a ratio to citrate synthase enzyme activity. Results are expressed as ratio to protein concentration and represented as a mean \pm SEM of 9-17 independent cell culture preparations. Unpaired Student's t-test was used to test for significance. ns= not significant

Enzyme	nmol/min/mg protein		Ratio to citrate synthase		
	Proliferative	Differentiated	Proliferative	Differentiated	Significance
Citrate synthase	156.7 \pm 11.1	125.4 \pm 9.1	----	----	p = 0.04
Complex I	11.7 \pm 1.7	9.4 \pm 1.0	0.082 \pm 0.009	0.076 \pm 0.007	ns
Complex II-III	16.2 \pm 2.2	13.4 \pm 2.5	0.096 \pm 0.01	0.093 \pm 0.013	ns
Complex IV**	2.9 \pm 0.5	3.6 \pm 0.8	0.019 \pm 0.003	0.026 \pm 0.005	ns

**Units for complex IV: k/min/mg. For ratio: k/nmol

4.3.5. Lysosomal glucocerebrosidase activity

Heterozygous mutations in GBA are considered the highest risk factor for PD. In addition, GBA expression and activity have been shown to be decreased in SN brain tissue samples, monocytes and dried blood spots from PD patient in the presence and absence of GBA gene mutations (Gegg *et al.* 2012; Alcalay *et al.* 2020; Hughes *et al.* 2021). Therefore, basal GBA activity was characterised in proliferative and differentiated SH-SY5Y cells using an assay specific for lysosomal GBA. This assay includes sodium taurocholate, an inhibitor for non-lysosomal β -glucosidase enzyme that also has the ability to breakdown glucosylceramides. In addition, this assay is carried out at pH 4.5 which is the pH optimum for GBA compared to pH 5.5 which is optimum for β -glucosidase (Derek Burke, PhD thesis, UCL). A significant 1.5-fold increase in mean GBA activity was documented following differentiation compared to proliferative SH-SY5Y cells ($p = 0.01$, Figure 39). Interestingly, there was a greater variability between GBA measurement in individual cell preparations in differentiated compared to proliferative SH-SY5Y cells (35% and 23%, respectively, F-value = 0.02), as evident by calculation of the coefficient of variation using the following formula:

$$\frac{\textit{standard deviation}}{\textit{mean}} \times 100$$

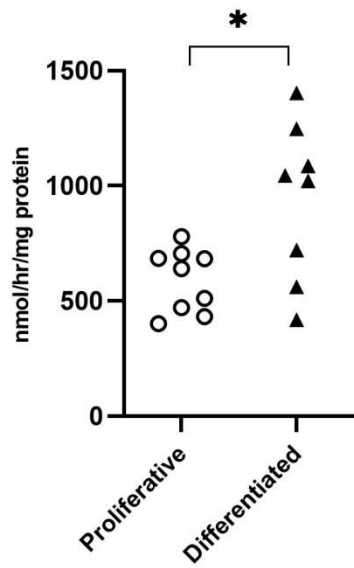


Figure 39 Lysosomal glucocerebrosidase activity in proliferative and differentiated SH-SY5Y cells. GBA activity was 668 ± 36 nmol/hr/mg in proliferative cells while in differentiated 1088 ± 94 nmol/hr/mg ($p = 0.01$). Results are presented as ratio to protein concentration and represent mean \pm SEM of 8–9 independent cell culture preparations. Unpaired student t-test with Welch's correction was used to test for significance.

4.3.6. Glutathione levels

Cellular oxidative stress imbalance is a key player in PD pathology. GSH is an important antioxidant in the cell, protecting against oxidative stress imbalances (Place and Smeyne 2013). There has been a documented decrease in GSH levels in post-mortem brain tissue from PD patients (Riederer *et al.* 1989). Therefore, measurement and comparison of GSH levels in proliferative and differentiated SH-SY5Y cells is an important aspect when considering SH-SY5Y cells for PD research. Using an HPLC-ED method developed to specifically measure reduced GSH, the active species of the antioxidant, levels of cellular GSH were compared between the two phenotypes. Looking at the individual levels of GSH in the two phenotypes there's a notable larger variability between the individual cell preparations measurements in proliferative compared to differentiated by comparing the coefficient of variation. Proliferative SH-SY5Y cells exhibited a 49% percent variability between individual cell preparations. In contrast, the percent variability between the individual measurements in differentiated cell preparations was 16% (f-value = 0.0004, Figure 40).

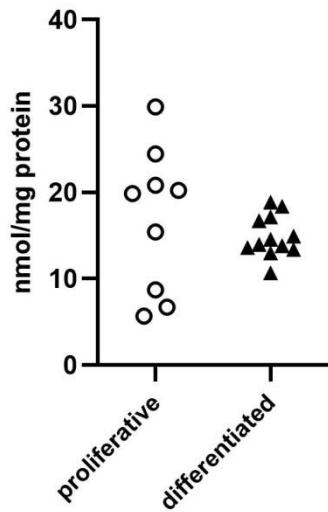


Figure 40 Glutathione level in proliferative and differentiated SH-SY5Y cells. In proliferative cells, GSH was 17 ± 3 nmol/mg protein while in differentiated 15 ± 0.7 nmol/mg protein. Results are expressed as ratio to protein concentration and represent mean \pm SEM of 9–12 independent cell culture preparations. Unpaired student t-test with Welch's correction was used to test for significance.

4.4. Discussion

The neuronal cell line SH-SY5Y is one of the most used cell lines in PD research, due to the assumption of their dopaminergic nature based on expression of TH, the rate limiting enzyme in the dopamine pathway. In this study, basal dopamine was absent in proliferative and differentiated SH-SY5Y cells, an observation that is similar to what has been demonstrated previously by de la Fuente and colleagues (2017). Using proliferative SH-SY5Y cells, they documented the absence of dopamine and its metabolites under basal conditions, necessitating the pre-treatment with L-DOPA. In contrast, Prasuhn and colleagues (2018) have described basal dopamine metabolism in proliferative SH-SY5Y cells, however only following lentiviral transduction to induce ectopic expression of TH gene. Similarly, Ganapathy and colleagues (2016) were able to detect basal dopamine metabolism in proliferative cells but only following stimulation with KCl or ATP. KCl and ATP causes cellular depolarisation and changes in intracellular calcium level, which controls neurotransmitter release thereby inducing dopamine release into the synapse (Prasuhn *et al.* 2018; Ganapathy *et al.* 2016; Südhof 2012). Finally, Magalingam and colleagues (2020) demonstrated basal dopamine level in proliferative SH-SY5Y cells at a concentration of 8 pmol/ml however, only following derivatisation of dopamine through acylation (Magalingam *et al.* 2020). Taken together, this finding suggests the suitability of SH-SY5Y cells as a cell model for PD due to the absence of dopamine under basal conditions, a phenomenon characteristic of the affected dopaminergic neurons in PD. The necessity for pre-treatment with L-DOPA to replenish dopamine metabolism resembles the use of levodopa, the gold standard therapy for PD, to rescue the dopamine deficiency in PD patients.

Because 5-HIAA was readily detectable both under basal conditions and following L-DOPA treatment, it can be assumed that the activity of AADC enzyme is preserved. This leads to the assumption that the absence of dopamine and its metabolites under basal conditions lies with the activity of TH enzyme, the first and rate limiting enzyme of the dopamine pathway. Both cellular phenotypes appear to have comparable expression levels of TH protein as confirmed using western blot (Figure 36). This was also seen following RA differentiation of SH-SY5Y cells by Korecka and colleagues (2013). TH enzyme activity requires the presence of tetrahydrobiopterin (BH₄) as cofactor. The presence of BH₄ can be deduced from a functional serotonin pathway in which TPH also requires BH₄. The enzymatic competition between TH and TPH for BH₄ can be dismissed because the Michaelis constant (K_m) of TPH for BH₄ is 315 ± 37 μM and of TH 5.6 ± 1.0 μM. This means that TH has a higher affinity for BH₄ than TPH (Windahl *et al.* 2009; Briggs *et al.* 2013). Finally, the cell culture medium that the cells are grown in contains L-tyrosine (213 μM) and iron (1.2 mM), components that are required for TH function therefore, deficiencies in these can be disregarded. Iron deficiency can also be disregarded because it is also required for TPH activity, which is not affected in these cells. Treatment of cells with additional L-tyrosine did not stimulate dopamine pathway either. Proliferative and differentiated cells were incubated with different concentrations of L-tyrosine (50 – 500 μM) and dopamine and serotonin metabolites were measured. Only 5-HIAA was detected under these conditions, similar to what was seen in untreated proliferative and differentiated cells (Figure 37). There are several possible reasons as to why this is the case. Dopamine could be synthesized under basal conditions however, at a concentration lower than the detection level of the HPLC-ED method used in

this study (< 50 pmol/ml). TH is the first and rate limiting enzyme in the dopamine synthesis pathway. Dopamine regulation is of utmost importance because of the nature of its functions therefore, TH is subjected to tight regulation via phosphorylation/dephosphorylation by several protein kinases and phosphatases such as protein kinase A and C (Dunkley *et al.* 2004). As a result, induction of upstream signalling pathways might be required for activation of TH and stimulation of the dopamine pathway to ensure tight regulation of dopamine levels. Finally, the serotonin metabolite, 5-HIAA, was readily detectable under basal conditions in SH-SY5Y cells, both proliferative and differentiation phenotypes (Figure 37). Therefore, the cells may possess a stronger serotonergic phenotype. It has been shown that rats' raphe RN46A-B14 cells, which are serotonergic neuronal cells, have the ability to produce dopamine following L-DOPA supplementation as a result of AADC enzyme activity, which is involved in both dopamine and serotonin synthesis (Stansley and Yamamoto 2013). The requirement for L-DOPA supplementation for production of dopamine was similarly the case with the SH-SY5Y cells used in this study.

Following L-DOPA supplementation, dopamine and its metabolites were readily detectable. Interestingly, there was a notable difference in the variability between individual extracellular dopamine measurement between proliferative and differentiated SH-SY5Y cell preparations, where the coefficient of variance was 64% for proliferative and 30% for differentiated (f -value = 7.9×10^{-8} , Figure 38 A). In addition, there was a significant increase in extracellular dopamine metabolism in differentiated cells (Figure 38 B). Differentiation is a process that involves the induction of several signalling pathways that function in growth and

survival, resulting in the induction of the enzymes involved in key pathways that are important for the cell type (Hong-rong *et al.* 2010). For example, in neuronal cells, differentiation is needed to induce the enzymes involved in neurotransmitter synthesis and regulation. In dopaminergic neurons, enzymes of the dopamine pathway are important for their function therefore, the increase in turnover rate of the dopamine pathway could be attributed to induction of the enzymes involved following differentiation. It has been shown that an induction of AADC enzyme activity takes place following differentiation of a neuroblastoma cell line using RA (Ikeda *et al.* 1994). In addition, Presgraves and colleagues (2004) have shown that following RA and TPA differentiation of SH-SY5Y cells, there was an increase in protein expression of TH, DAT and dopamine receptors D₂ and D₃; components central to dopamine neurotransmission (Presgraves *et al.* 2004). These findings indicate that differentiated SH-SY5Y cells differ from proliferative in their dopamine pathway regulation.

GBA is an enzyme in the sphingolipid pathway. The sphingolipid pathway provides the structural components of cell membranes and myelin sheath (Rao *et al.* 2013). The observed increase in GBA following differentiation (Figure 39) could be indicative of induction of the sphingolipid pathway. The cellular morphology of SH-SY5Y cells changes significantly following differentiation in the form of polarisation and neurite extension and branching (Figure 33). These changes would require the upregulation of membrane structural components such as ceramide and sphingomyelin. These molecules may enhance the differentiated cell's ability to perform functions that are characteristic of mature neurons, facilitated by axon myelination and neurite branching. In addition, the

dynamic nature of membranes and their inherent fluidity is an important feature, specifically for neurons, to facilitate signal transduction and neurotransmission. Therefore, induction of sphingolipid pathway is important during differentiation (Mencarelli and Martinez-Martinez 2013).

The cellular redox state, represented by a balance between oxidised/reduced GSH molecules, is dysregulated in PD; a disease where oxidative stress is a key factor in pathology. For this reason, GSH levels in models of PD disease must be characterised. In this study, there was a high variability documented between individual measurements of GSH in proliferative compared to differentiated cell preparations (Figure 40). Similar variability was seen in individual measurement of dopamine in proliferative compared to differentiated cell preparations (Figure 38). GSH is an inherently unstable molecule requiring tight regulation of its different states to maintain the redox balance of cells. Proliferative cells are constantly proliferating, resulting in asynchronous cell cycle stages and a non-homogenous cell population. The variability seen between individual measurement could reflect this heterogeneity, which is enhanced following differentiation, where cells assume a more homogenous population and cell proliferation is arrested. Looking back at GBA measurement in individual cell preparations in differentiated SH-SY5Y cells (Figure 39), there appears some variations as well. This variability appears to group differentiated cells into two populations. One reason might be due to incomplete differentiation of all cells in a specific cell preparation. Pahlman and colleagues (1984) have shown that sequential treatment with RA and TPA results in only 55% differentiation of all treated SH-SY5Y cells in a given population (Påhlman *et al.* 1984). Another

reason might be a result of differential response of different proliferative SH-SY5Y cell preparations to the differentiation agents, RA and TPA, specifically on lysosomal enzymes. This could be another reflection of the constant proliferation state that the cell population is in, lacking homogeneity, resulting in differential responses.

CS is a mitochondrial matrix enzyme that is commonly used as a marker of mitochondrial content (Wanet *et al.* 2015). The decrease in CS following differentiation suggests changes in mitochondrial content between the two phenotypes therefore, when comparing mitochondrial bioenergetics between different cell lines/phenotypes it is of importance to express those results as a ratio to CS. Changes in CS activity following differentiation have been documented in SH-SY5Y cells, mesenchymal cells, murine cells, adipose cells and myoblasts (Forni *et al.* 2016; Kraft *et al.* 2006; Murholm *et al.* 2009; Schneider *et al.* 2012; Moyes *et al.* 1997) In contrast to what was seen in the lysosomal enzyme GBA and CS, mitochondrial ETC complex activities were comparable between proliferative and differentiated cells. Schneider and colleagues (2012) demonstrated that following RA differentiation of SH-SY5Y cells no change took place in complex I activity, similar to what was observed in this study (Table 4, Schneider *et al.* 2012).

In conclusion, this study demonstrates that there are similarities as well as significant differences between the biochemistry of proliferative and differentiated phenotypes of SH-SY5Y cells despite being of the same cell line. These similarities and differences are in biochemical pathways that are central to PD pathology (mitochondria, dopamine, lysosomes, GSH); a disease for which SH-

SY5Y cells are commonly used to model. Therefore, when using this cell line to model PD, a choice between the use of the proliferative or the differentiated phenotype should be made based on the pathway of interest. For example, when studying mitochondrial bioenergetics, differentiation might not be necessary. Taken together, care and careful characterisation are important when considering a cell line and/or cell phenotype to model diseases, more specifically concerning SH-SY5Y cell line for modelling PD.

Chapter 5. Biochemical Effects of L-DOPA Treatment on Proliferative and Differentiated SH-SY5Y Cells

5.1. Introduction

Based on the findings of the previous chapter (Chapter 4), dopamine synthesis under basal conditions was undetectable in SH-SY5Y cells. However, they have the ability to synthesize and metabolise dopamine following treatment with L-DOPA. Therefore, they may provide a useful model to study the downstream effects of oxidative dopamine metabolism, post L-DOPA treatment, on key metabolic pathways affected in PD. Oxidative stress is implicated in PD pathology (Blesa *et al.* 2015). The SN area of the brain, where dopaminergic neurons reside, is the most affected area in PD (González-Hernández *et al.* 2010). The reason for the selective regional vulnerability is hypothesized to be due to dopamine metabolism (Hastings and Zigmond 1997). By its nature, dopamine metabolism is highly oxidative, increasing the oxidative stress burden of dopaminergic neurons. Production of DOPAC and HVA from dopamine involves an oxidative deamination step catalysed by MAO. This step produces H₂O₂ as a by-product, which itself can increase oxidative stress. However, in dopaminergic neurons, which are rich in iron, it can also react with iron via the Fenton reaction to produce hydroxyl radicals (Spina and Cohen 1989; Hermida-Ameijeiras *et al.* 2004; Aluf *et al.* 2013). As a protective mechanism, dopamine is sequestered into acidic vesicles to prevent its oxidation (Chaudhry *et al.* 2008). However, when in excess, dopamine, and its precursor, L-DOPA, can readily oxidize in the cytoplasm. The oxidation process can happen spontaneously, enzymatically (via cyclooxygenases or tyrosinases), or in the presence of metal catalysts to form highly reactive quinone species, dopamine-quinones (DQ) and DOPA-quinones. In addition, these reactions can generate superoxide radicals as

by-products (Graham *et al.* 1978; Hastings 1995). Quinones and ROS are highly reactive toxic species, capable of binding to different cellular components like proteins, lipids, glutathione and DNA, interfering with their structure and function (Meiser *et al.* 2013). DQ has also been documented to interfere with TH (Xu *et al.* 1998), DAT (Whitehead *et al.* 2001), mitochondrial complex I (Aguirre *et al.* 2012), complex III, complex V (Biosa *et al.* 2018) and parkin (Lavoie *et al.* 2005). In relevance to mitochondria specifically, Biosa and colleagues (2018) have shown that DQ can penetrate mitochondria, modify their morphology, and decrease the threshold of mitochondrial permeability transition pore opening. DQ were also shown to interact with mitochondrial proteins such as ATP synthase, disrupting ATP synthesis, resulting in increased ROS production (Biosa *et al.* 2018). DQ have also been shown to interfere with lysosomal function. They have been documented to interfere with the lysosomal-autophagy pathway through disruption of lysosomal acidification and microtubule formation, both of which are important for lysosomal degradative functions (Huenchuguala *et al.* 2014; Paris *et al.* 2010). With regards to redox status of the cell, DQ have been shown to modulate GSH levels in the cells. Allen and colleagues (2013) have reported an increase in GSH levels in proliferative SH-SY5Y cells following treatment with both dopamine or L-DOPA through a cellular mechanism that potentially involves DQ formation (Allen *et al.* 2013).

In summary, L-DOPA, the resultant dopamine, and their derivatives can have negative effects on mitochondrial and lysosomal functions as well as the cellular redox state.

Thus, the **aims** of this chapter were:

- To study the effects of the oxidative dopamine metabolism on mitochondrial and lysosomal functions and GSH levels in SH-SY5Y cell line model
- To compare the effects of oxidative dopamine metabolism between proliferative and differentiated SH-SY5Y cells

5.2. Materials and methods:

5.2.1. Cell culture

SH-SY5Y cells were cultured as described in section 2.2.

5.2.2. L-DOPA treatment

SH-SY5Y cells were treated with 100 μ M L-DOPA for 1 or 3 hours as described in section 2.2.2.

5.2.3. Sample preparation

Mitochondrial samples and lysosomal GBA samples were prepared as described in section 2.4.1. GSH samples were prepared as described in section 2.4.3.

5.2.4. Enzyme assays

Mitochondrial CS, complex I, II-III and IV enzyme activity were assayed as described in section 2.7.

Lysosomal GBA enzyme activity was assayed as described in section 2.7.5.

5.2.5. GSH measurement

GSH levels were determined using HPLC-ED method as described in section 2.8.

5.3. Results

5.3.1. Effect of L-DOPA treatment on mitochondrial ETC complex activity:

Giannopoulos and colleagues (2019) have shown that treatment of proliferative SH-SY5Y cells with 200 μ M L-DOPA for 24 hours significantly impaired mitochondrial function. It has led to changes in mitochondrial morphology and mitochondrial fragmentation and a disrupted mitochondrial membrane potential. In addition, basal respiration was reduced by almost 50% and consequently, ATP synthesis was also reduced by almost 50%. (Giannopoulos *et al.* 2019). To understand the effect of L-DOPA and resultant dopamine on mitochondrial bioenergetics, mitochondrial complex I, II-III, IV and CS enzyme activities were measured following L-DOPA treatment. Proliferative and differentiated SH-SY5Y cells were treated with 100 μ M L-DOPA for either 1 or 3 hours, then mitochondrial complex activity was measured as ratio to CS activity.

Following timed L-DOPA treatment, no changes were observed in CS enzyme activity in either proliferative or differentiated SH-SY5Y cells. CS activity in proliferative cells was significantly higher than in differentiated, similar to what was seen previously in chapter 4 (Figure 41). Looking at the ratio of MCI/CS in proliferative cells, there was an apparent 25% decrease in mean enzyme activity following 3 hours L-DOPA treatment however, the result did not reach statistical significance ($p = 0.6$). No changes to MCI/CS activity were observed in differentiated cells (Figure 42 A). In addition, L-DOPA treatment did not result in any significant changes to MCII-III/CS or MCIV/CS in either proliferative or differentiated cells (Figure 42 B & C). Interestingly however, there was greater variability (in the form of larger SEM) in measurements from individual cell

preparations across all complexes analysed in proliferative cells, despite being taken under the same experimental conditions, compared to differentiated cells (Figure 42, Table 5).

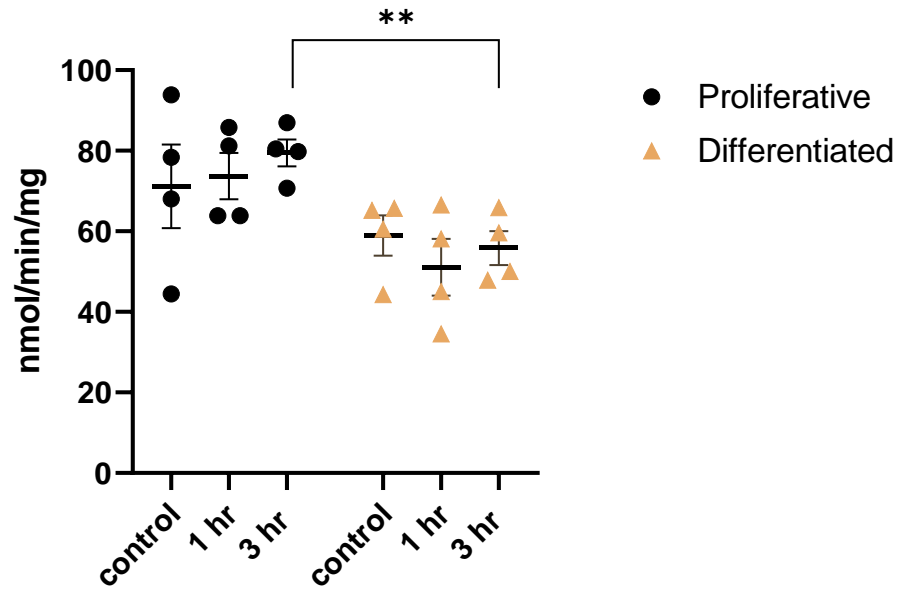


Figure 41 Effect of L-DOPA on citrate synthase enzyme activity. Proliferative and differentiated SH-SY5Y cells were incubated with 100 μ M L-DOPA for 1 or 3 hours and CS enzyme activity was measured and expressed as nmol/min/mg protein. Results are presented as mean \pm SEM of 4 independent cell culture preparations. A two-way ANOVA with a Tukey's multiple comparisons test was used to test for significance. (** $p = 0.005$)

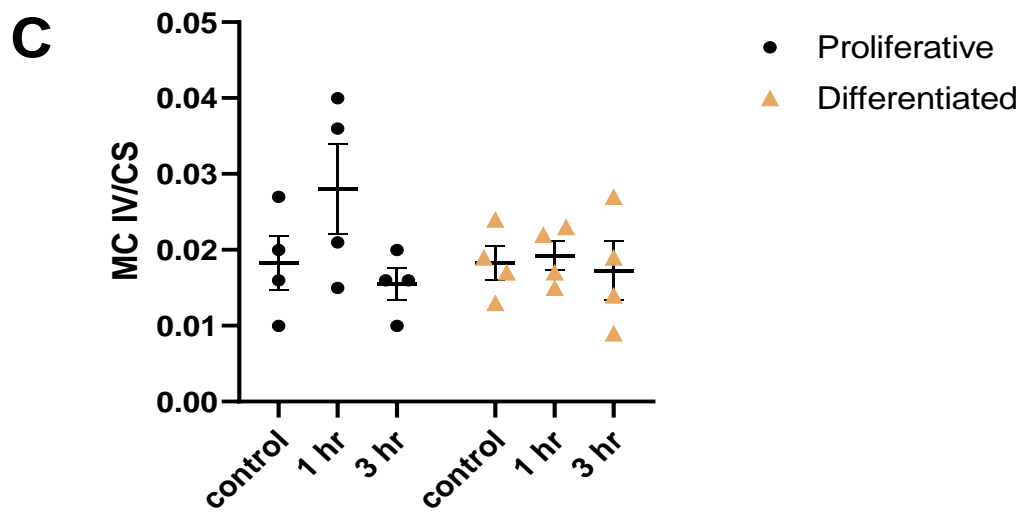
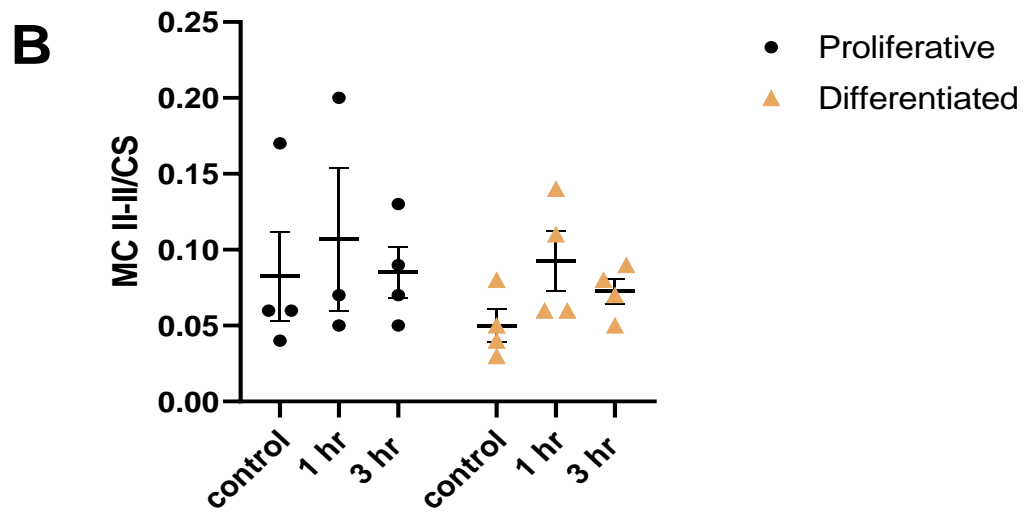
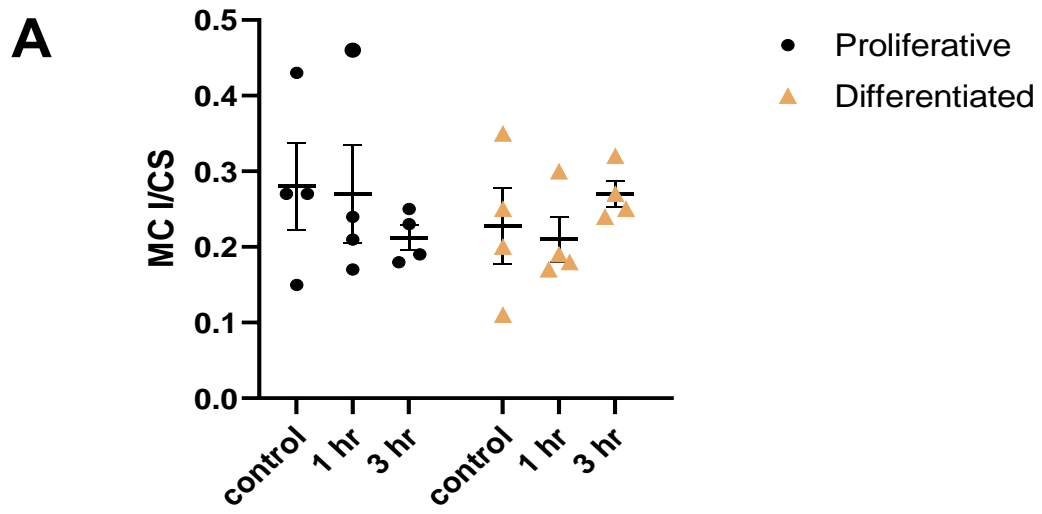


Figure 42 The effect of L-DOPA on mitochondrial complex I, II-III and IV activity. Proliferative and differentiated SH-SY5Y cells were treated with 100 μ M L-DOPA for 1 or 3 hours then MC I, II-III and IV enzyme activities were measured and expressed as ratio to CS enzyme activity. Results are presented as mean \pm SEM of 4 independent cell culture preparations. A two-way ANOVA with a Tukey's multiple comparisons test was used to test for significance. Rout outlier method was used to test for outliers.

5.3.2. Lysosomal GBA enzyme activity

Research by Burbulla and colleagues (2017) have demonstrated that increased cellular oxidative stress, resulting from dopamine oxidation, leads to decreased activity of GBA in iPSC-derived dopaminergic neurons. Through recombinant enzyme studies, they have shown that DQ have the ability to modify cysteine residues in the catalytic site of recombinant GBA resulting in reduced enzyme activity thereby presenting a potential mechanism through which dopamine oxidation can affect GBA activity (Burbulla *et al.* 2017). Therefore, in this experiment I looked at the effect of treatment of proliferative and differentiated SH-SY5Y cells with 100 μ M L-DOPA on GBA enzyme activity. No significant changes were observed in the activity of GBA in either proliferative cells or differentiated cells following L-DOPA treatment (Figure 43).

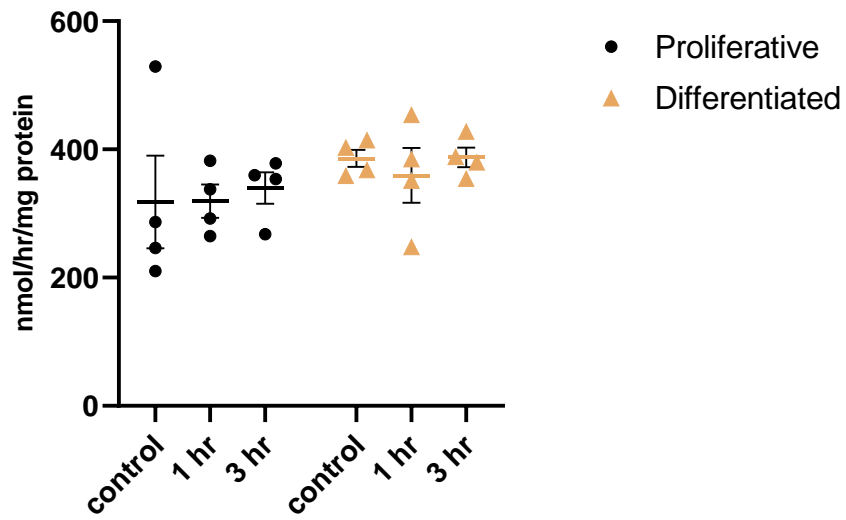


Figure 43 Effect of L-DOPA on glucocerebrosidase enzyme activity. Following 100 μ M L-DOPA treatment for 1 or 3 hours, GBA enzyme activity was measured in proliferative and differentiated SH-SY5Y cells. Results represent mean \pm SEM of 4 independent cell culture preparations. A two-way ANOVA followed by a Tukey's multiple comparisons test was used to test for significance.

5.3.3. GSH levels

It is understood that generation of ROS is one of the mechanisms of inducing cellular toxicity following L-DOPA and dopamine oxidation (Meiser *et al.* 2013). To assess the effects of L-DOPA on cellular oxidative status, GSH levels were measured in proliferative and differentiated SH-SY5Y cells following L-DOPA treatment. There were no statistically significant changes observed in the levels of GSH following L-DOPA treatment neither in proliferative nor in differentiated cells. However, following L-DOPA treatment, GSH levels in individual cell preparations in proliferative cells exhibited greater variation compared to differentiation; an average of 80% coefficient of variation in the different treatment conditions in proliferative compared to 50% in differentiated (Figure 44).

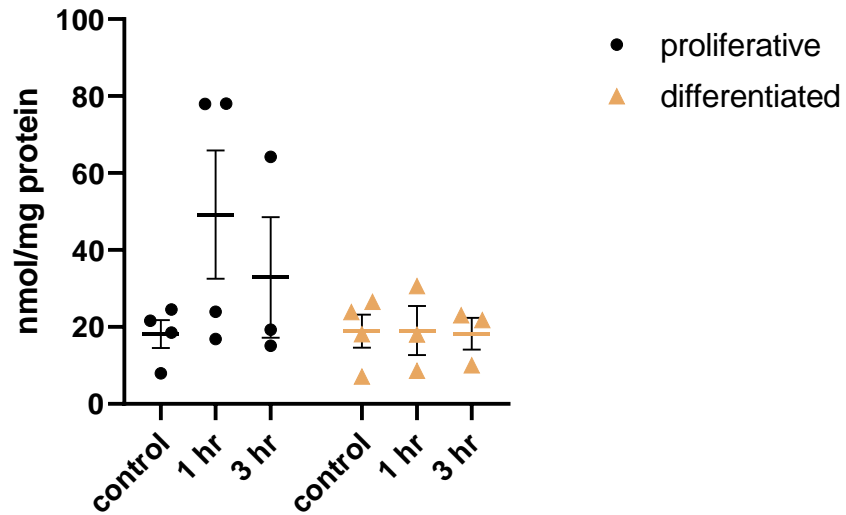


Figure 44 Effect of L-DOPA on glutathione levels. Following 100 μ M L-DOPA treatment for 1 or 3 hours, glutathione levels were measured in proliferative and differentiated SH-SY5Y cells. Results are presented as mean \pm SEM of 3-4 independent cell culture preparations. A two-way ANOVA followed by a Tukey's multiple comparisons test was used to test for significance. Rout outlier test was used to test for outlier.

	Proliferative SH-SY5Y cells			Differentiated SH-SY5Y cells		
L-DOPA treatment	0	1 hour	3 hours	0	1 hour	3 hours
CS	71 ± 10	67 ± 11	79 ± 3 **	59 ± 5	51 ± 7	56 ± 4 **
MCI/CS	0.28 ± 0.06	0.36 ± 0.15	0.21 ± 0.02	0.23 ± 0.05	0.21 ± 0.03	0.27 ± 0.02
MCII-III/CS	0.083 ± 0.030	0.107 ± 0.047	0.085 ± 0.017	0.05 ± 0.011	0.093 ± 0.020	0.073 ± 0.009
MCIV/CS	0.018 ± 0.004	0.028 ± 0.006	0.016 ± 0.002	0.018 ± 0.002	0.019 ± 0.002	0.017 ± 0.004
GBA	318 ± 72	319 ± 26	340 ± 25	386 ± 13	359 ± 42	388 ± 15
GSH	18 ± 7	49 ± 17	33 ± 16	19 ± 4	19 ± 6	18 ± 4

Table 5 The effect of L-DOPA on proliferative and differentiated SH-SY5Y cell biochemistry. Following treatment with 100 μ M L-DOPA for 1 or 3 hours, different parameters of proliferative and differentiated SH-SY5Y biochemistry were assessed. CS and GBA enzyme activity are expressed as nmol/min/mg protein and nmol/hr/mg protein, respectively. GSH is expressed as nmol/mg protein. CS; citrate synthase, MC; mitochondrial complex, GBA; glucocerebrosidase, GSH; glutathione. (** $p = 0.005$)

5.4. Discussion

Oxidative stress is a well-established event in PD pathology (Blesa *et al.* 2015). Dopamine metabolism is considered a key culprit in increasing the oxidative stress burden in dopaminergic neurons (Hastings and Zigmond 1997). Increased oxidative stress can lead to mitochondrial dysfunction (Keeney *et al.* 2006). Dopamine and DQ have been documented to induce changes in mitochondrial respiration and lead to opening of the permeability transition pore (Berman and Hastings 1999). In this study, L-DOPA treatment of proliferative and differentiated SH-SY5Y cells did not result in significant changes in the activity of mitochondrial complex I, II-III and IV or CS activity (Figure 41 and Figure 42). In addition, no significant changes were noted in GBA activity or GSH levels (Figure 43 and Figure 44). With regards to GSH levels, similar conclusions were made by Allen and colleagues (2013) following 1 and 4 hour treatment of proliferative SH-SY5Y cells with both L-DOPA and dopamine (Allen *et al.* 2013). However, focusing on measurements from individual cell preparations, greater variability in individual measurements was observed in proliferative cells compared to differentiated cells, taken under the same experimental conditions. This was evident by larger SEM values in proliferative cell preparation measurements compared to differentiated (

Table 5). These findings are similar to what was observed in Chapter 4, where greater measurement variability was seen in dopamine and GSH levels, despite being taken under the same experimental conditions. Furthermore, the variability, particularly in GSH levels, appeared to be exacerbated by L-DOPA treatment (Figure 44). Similar variability in experimental measurements were documented by Santillo and colleagues (2014). Following whole cell recording in proliferative SH-SY5Y cells, they documented greater variability in the individual cell's responses to a depolarizing stimulus despite belonging to the same cell population (Santillo *et al.* 2014). Proliferative SH-SY5Y cells are, in essence, immature neuroblasts that have the ability to continuously replicate for a long period of time (Presgraves *et al.* 2004; Constantinescu *et al.* 2007). This means that they may not represent a very homogenous cell population and that at any point, different cells are at a different stage of the cell cycle. The cell cycle is a sequence of events or phases (G_0 , G_1 , S, G_2 , and M) that prepare the cell for mitosis and the production of two new daughter cells (Schafer 1998). This has been demonstrated by Rigolio and colleagues (2005) using flow cytometry analysis of proliferative SH-SY5Y cells. They demonstrated that within the same cell population of proliferative SH-SY5Y cells, individual cells exist at different stages of the cell cycle (Rigolio *et al.* 2005). Markovic and colleagues (2004) have demonstrated that GSH can be recruited into the nucleus during proliferation and may play a role in cell division therefore cells at different stages of the cell cycle may have different concentrations of GSH (Markovic *et al.* 2007).

To conclude, this study expands on the findings in chapter 4, where measurements using proliferative SH-SY5Y cells display greater variability and

inconsistencies, highlighting one of the key concerns over the use of constantly proliferating tumour cell lines in research. This variability presents an even greater challenge when using proliferative cells to assess their response to different toxins and treatments.

Chapter 6. Cathepsin D as an Indicator of Lysosomal Acidification

6.1. Introduction

Lysosomal dysfunction is proposed to play a key role in the pathogenesis of a number of neurodegenerative diseases, particularly PD (Dehay *et al.* 2016). Lysosomes are dynamic, acidic (pH 4.2 – 5.3) organelles. The acidic environment of lysosomes is essential to its degradative function as the majority of lysosomal hydrolases function optimally at acidic pH. In addition, the acidity of the lysosomes is essential for the maturation and the proteolytic activation of the immature pro-forms of lysosomal hydrolases (Colacurcio and Nixon 2016).

The acidic environment of the lysosomes is maintained by the action of the vacuolar-type proton ATPase (v-ATPase, Mindell 2012). v-ATPase is a ubiquitous proton pump involved in maintaining the pH homeostasis of the lysosomal lumen. It is composed of two domains, V0 and V1. V0 is involved in proton translocation and is composed of 6 different subunits. V1 on the other hand, catalyses ATP hydrolysis and is composed of 8 subunits. The activity of the v-ATPase is dependent on cytosolic ATP for the translocation of protons into the lysosomal lumen against a concentration gradient (Beyenbach and Wieczorek 2006). The diversity of the different v-ATPase subunits isoforms allows extensive regulation and adaptation to different cellular environments and states (Toei *et al.* 2010).

Increased lysosomal pH has been implicated in PD. Mutations in the gene that codes for the protein ATP13A2 are linked to some forms of juvenile and young onset PD as well as to an autosomal recessive form of PD known as Kufor-Rakeb syndrome (Ramirez *et al.* 2006; Fonzo *et al.* 2007). ATP13A2 is a lysosomal p-type ATPase that appears to function as a polyamine exporter (van

Veen *et al.* 2020). Increased lysosomal pH was demonstrated in both fibroblasts from PD patients carrying mutations in the gene that codes for ATP13A2, as well primary neurons where ATP13A2 gene was knocked down (Dehay *et al.* 2012; Usenovic *et al.* 2012; Bourdenx *et al.* 2016). Furthermore, patients' fibroblasts carrying mutations in *GBA* gene, the most common risk factor for PD, exhibited an increase in lysosomal pH (Bourdenx *et al.* 2016). In addition, overexpression of wildtype or mutant α -synuclein were found to increase lysosomal pH in proliferative SH-SY5Y cells (Nascimento *et al.* 2020). Missense mutations in the gene that codes for the leucine-rich repeat kinase 2, LRRK2, cause late onset PD. Mouse primary neurons carrying missense mutations in *LRRK2* show evidence of elevated lysosomal pH (Schapansky *et al.* 2018). Finally, mutations in the gene coding for v-ATPase accessory protein 2 (*ATP6AP2*) are associated with X-linked parkinsonism with spasticity (XPDS, Korvatska *et al.* 2013; Gupta *et al.* 2015).

The literature demonstrate that lysosomal pH can be considered a key player in PD pathology. The exact mechanism and whether it is a cause, or a consequence remains to be elucidated. One of the methods to investigate lysosomal pH is via the use of fluorescent acidotropic dyes that locate specifically to the lysosomes (Zhou *et al.* 2013; Heaton *et al.* 2020; Nascimento *et al.* 2020; Coffey *et al.* 2014). LysoSensor™ pH indicators are fluorescent dyes that partition and accumulate into acidic compartments and their fluorescent intensity is pH-dependent allowing the measurement of the lysosomal pH by comparing the fluorescence intensity to a pH calibration curve. LysoSensor™ Yellow/Blue DND-160 has predominantly yellow fluorescence in acidic compartment and blue

fluorescence in less acidic organelles and therefore exhibit a dual-emission that is pH-dependent in living cells. LysoSensor™ Blue DND-167 is fluorescent dye that is largely non-fluorescent at neutral pH so can also be used to assess lysosomal pH (Ma *et al.* 2017).

Another commonly used lysosomal pH probe is LysoTracker® (Zhou *et al.* 2013; Colacurcio and Nixon 2016; Chakrama *et al.* 2010). LysoTracker is a selective acidotropic probe that accumulates in acidic compartments and fluoresces at acidic pH and therefore allows the location and tracking of lysosomes (Chazotte 2011). However, the fluorescence intensity of LysoTracker is pH-independent therefore, makes it less useful to monitor small changes in lysosomal pH.

Cathepsin D (CTSD, EC 3.4.23.5) is a lysosomal aspartyl endopeptidase. It is the most ubiquitously expressed lysosomal enzyme and can be found in all cells and tissues except erythrocytes. It breaks down proteins into polypeptide fragments that can be further digested by other lysosomal enzymes and has a pH optimum of 3.5-5.5 (Minarowska *et al.* 2008; Conner and Richo 1992). CTSD is the principal enzyme responsible for digesting α -synuclein, a presynaptic neuronal protein that is both genetically and pathologically implicated in PD (Sevlever *et al.* 2008; Stefanis 2012).

CTSD is first synthesized as pre-proCTSD in the rough endoplasmic reticulum. Pre-proCTSD comprises a pro-form of the enzyme and a signal peptide. The signal peptide gets cleaved as it travels through the ER, giving rise to the pro-form of CTSD (proCTSD, 52 kDa). ProCTSD is then transported to Golgi complex where it is tagged with a lysosomal targeting sequence, mannose-

6-phosphate. Once in the acidic environment of the lysosomes (pH 4-5), proCTSD is proteolytically processed by removal of the pro-peptide to eventually generate the mature form of CTSD (mCTSD, 28 kDa). This step is mediated by the activity of cathepsin B and cathepsin L and first involves the generation of an intermediate proCTSD protein (48 kDa, Laurent-Matha *et al.* 2006). 48 kDa proCTSD is then cleaved to generate mature CTSD which is comprised of a heavy chain (34 kDa) and a light chain (14 kDa). The 34 kDa heavy chain is further processed to give rise to the 28 kDa chain mCTSD (Figure 45, Zaidi *et al.* 2008; Mijanovic *et al.* 2021). One of the ways CTSD activity is regulated is through activation via catalytic cleavage wherein proCTSD is converted to mCTSD. This process is pH-dependent and occurs at acidic pH (pH 3.8-4.2, Hasilik *et al.* 1982). Thus, the maturation (occurs at pH 3-4) and the activity (pH optimum 4-5) of CTSD could be used as a tool to indirectly monitor lysosomal acidification and alkalinisation.

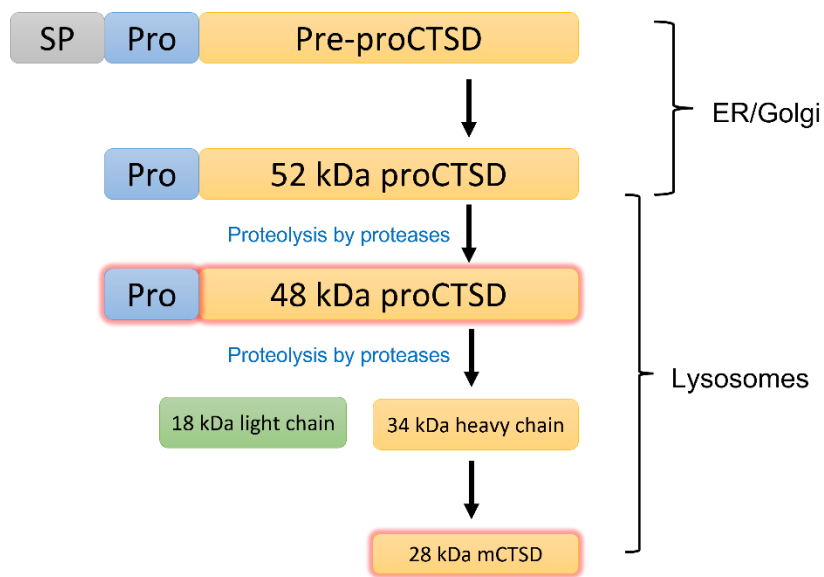


Figure 45 Cathepsin D synthesis pathway. CTSD: cathepsin D. SP: signalling peptide. mCTSD: mature CTSD. proCTSD: pro-form of CTSD enzyme.

CTSD expression and activity is increasingly recognised as a biomarker for PD (Xicoy *et al.* 2019). For example, CTSD protein immunoreactivity was found to be significantly reduced in dopaminergic neurons from post-mortem brain tissue from PD patients (Chu *et al.* 2009). In addition, secreted CTSD levels were documented to be significantly reduced in plasma from PD patients (Kang *et al.* 2021). Furthermore, it has been documented that there is a decrease in the activity of CTSD in CSF and brain tissue of patients with PD (Parnetti *et al.* 2017; Nelson *et al.* 2018). Interestingly, the decrease in activity was found to correlate with a decrease in GBA activity in PD patients with or without mutation in their *GBA* gene (Moors *et al.* 2019). In addition, Yang and colleagues (2020) have documented a significant reduction in CTSD activity in dopaminergic neurons differentiated from patients carrying mutations in their *GBA* gene. They have demonstrated that the decrease in activity is attributed to a decrease in CTSD maturation compared to control. They also demonstrated that by rescuing GBA activity either by the addition of the recombinant enzyme, Cerezyme, or by treatment with Ambroxol, an established GBA activator, they were able to restore CTSD maturation and activity (Yang *et al.* 2020).

Therefore, the **aims** of this chapter were:

- To establish a protocol to measure lysosomal pH in proliferative and differentiated SH-SY5Y cells using LysoSensor dyes
- To demonstrate the feasibility of monitoring the maturation and activity of CTSD as an indirect readout of the state of the lysosomal pH
- To investigate the effect of loss of function of GBA on lysosomal pH

- To investigate the effect of inhibition of mitochondrial complex I activity on lysosomal pH

6.2. Materials and methods:

6.2.1. Materials:

Anti-pro-cathepsin D (ab134169) and anti-cathepsin D (ab75852) monoclonal recombinant antibodies were purchased from Abcam (Cambridge, UK). Cathepsin D activity assay kit was purchased from RayBiotech, Inc. (GA, USA). Conduritol B epoxide (CBE; GBA inhibitor) and bafilomycin A1 (baf; v-ATPase inhibitor) were purchased from Cambridge Bioscience (Cambridge, UK).

6.2.2. Cell culture and differentiation:

Cell culture and differentiation protocol were as described in section 2.2 and section 2.3.

Cells culture medium used in this study included the addition of the commonly used cell culture antibiotic Penicillin/Streptomycin (100 U/ml) due to the presence of recurrent infections of unknown origins during the attempt of this study, greatly delaying the progress of this experiment.

6.2.3. Cell treatment:

6.2.3.1. Bafilomycin A1:

Proliferative and differentiated cells were incubated with a final concentration of 500 nM baf prepared in cell culture media for 16 hours prior to harvesting. Control cells were incubated in normal cell culture media.

6.2.3.2. Conduritol B epoxide:

Proliferative and differentiated cells were incubated with a final concentration of 100 μ M CBE prepared in cell culture medium for 3 days prior to harvesting. Fresh CBE media was added every day. Control cells were incubated in normal cell culture media.

6.2.3.3. Rotenone:

Proliferative and differentiated cells were incubated in cell culture medium containing a final concentration of 100 nM rotenone prepared in ethanol for 24 hours prior to harvesting. Control cells were incubated with the same amount of ethanol, 0.01 v/v%, in cell culture medium and incubated for 24 hours.

6.2.4. Cathepsin D enzyme activity assay:

The enzyme activity of CTSD was determined using a fluorometric assay kit following the manufacturer instructions. This assay utilises a synthetic peptide substrate for CTSD that is labelled with the fluorophore, 7-methoxycoumarin-4-acetic acid (MCA). Active CTSD enzyme will cleave the synthetic substrate releasing the MCA which emits a fluorescence at excitation/emission wavelength of 340/465 nm. The fluorescence intensity can be measured with a fluorescence plate reader and is proportional to enzyme activity.

Briefly, cell pellets were lysed in the provided lysis buffer. Cell suspension was incubated on ice for 10 minutes then centrifuged at 120000 g for 5 minutes and supernatant was taken. 20 µl cell supernatant was added to a black 96 well plate and to it, 30 µl of the provided reaction buffer was added. The substrate solution was prepared by mixing 2 µl substrate to 50 µl reaction buffer and added to each sample well. The plate was mixed and incubated for 1 hour at 37 °C then read at 340 nm excitation and 465 emission. The fluorescent reading was normalised to protein concentration to give RFU/mg/ml, where RFU is relative fluorescence unit.

The linearity of the CTSD enzyme activity assay used was confirmed using an SH-SY5Y cell sample that was serially diluted to give samples of different

protein concentrations, and CTSD activity was measured in each serial dilution. CTSD activity measured using this assay was found to strongly correlate with protein concentration ($R^2 = 0.99$, Figure 46).

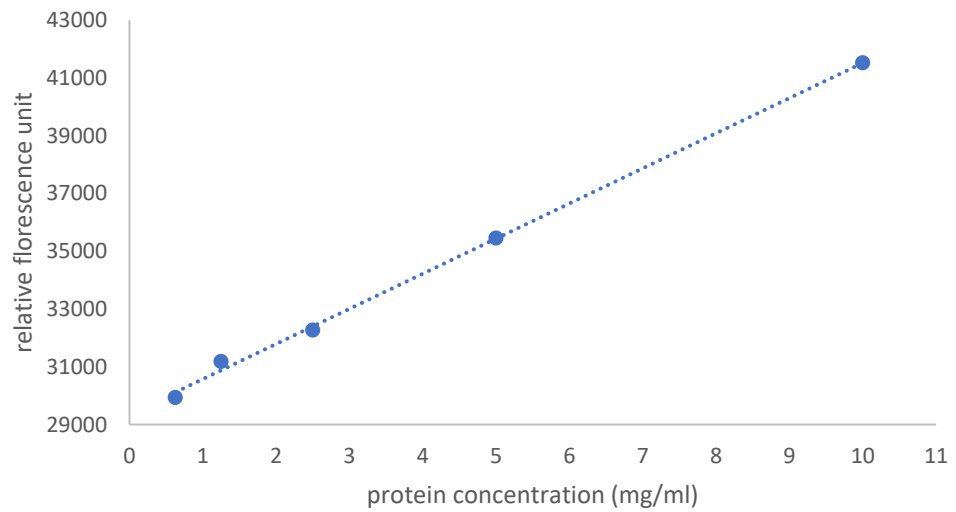


Figure 46 Correlation between cathepsin D enzyme activity and protein concentration in SH-SY5Y cells. A sample of SH-SY5Y cell lysate was serially diluted and CTSD activity was measured in each dilution sample. Linear regression analysis showed a strong correlation between CTSD activity and protein concentration of cell lysate ($R^2 = 0.99$).

6.2.5. Western blot for proCTSD and mCTSD:

Western blot detection of protein expression was carried out as described in section 2.6. In this study, I have focused on the 48 kDa intermediate proCTSD and the 28 kDa mCTSD, as they were the two CTSD species for which very specific monoclonal antibodies against were available.

6.3. Results:

6.3.1. Creating a pH calibration curve using LysoSensor dyes:

The basis of the measurement of lysosomal pH using LysoSensor dyes is the comparison of the fluorescence intensity of the LysoSensor dye incubated with cells to a pH calibration curve established by incubating the dye in different pH buffers and plotting fluorescence intensity against the pH. The first LysoSensor dye used was LysoSensor™ Yellow/Blue DND-160. It is a dual excitation dye where the fluorescence intensity is calculated by taking the ratio of fluorescence at 340/535 nm and 386/535 nm. The intensity of DND-160 was found to increase with the increase in pH when the dye was incubated with pH buffers (3.5-8). The intensity plateaus at pH 7 as this dye only works at acidic pH.

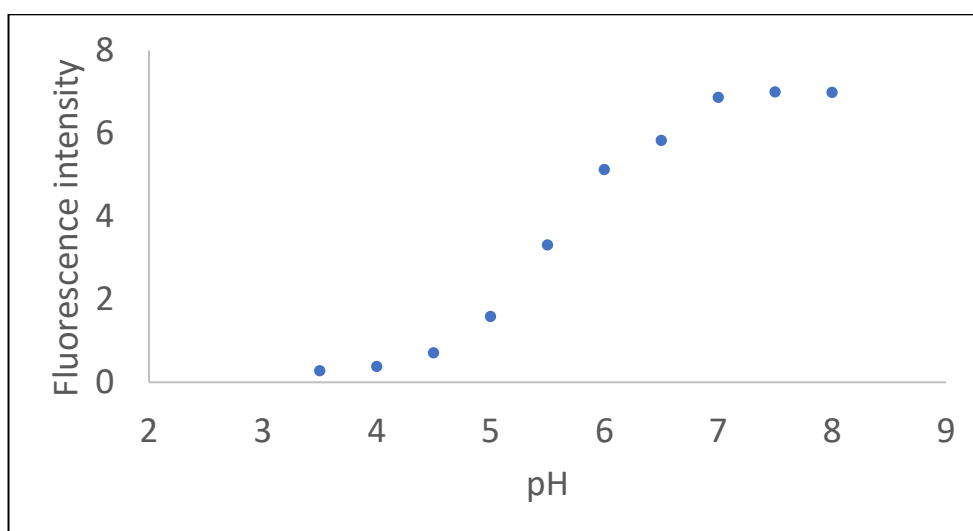


Figure 47 A pH calibration curve of the LysoSensor™ Yellow/Blue DND-160. DND-160 dye was incubated in different pH buffers (3.5-8) and the fluorescent intensity was measured plotted against the pH.

After establishing the calibration curve with the dye and buffers (Figure 47), I attempted to establish a calibration curve using proliferative SH-SY5Y cells by incubating the cells with the DND-160. Unfortunately, incubating the cells with the dye led the cells to detach from the cell culture plate which resulted in massive cell loss during the preparation of the experiment. As a result, establishing a calibration curve wasn't possible. In order to overcome this problem, I first used different types of treated cell culture plates (gas, collagen, laminin) which work to increase cell adherence to the plate, however this did not help cells to adhere more (Figure 48).

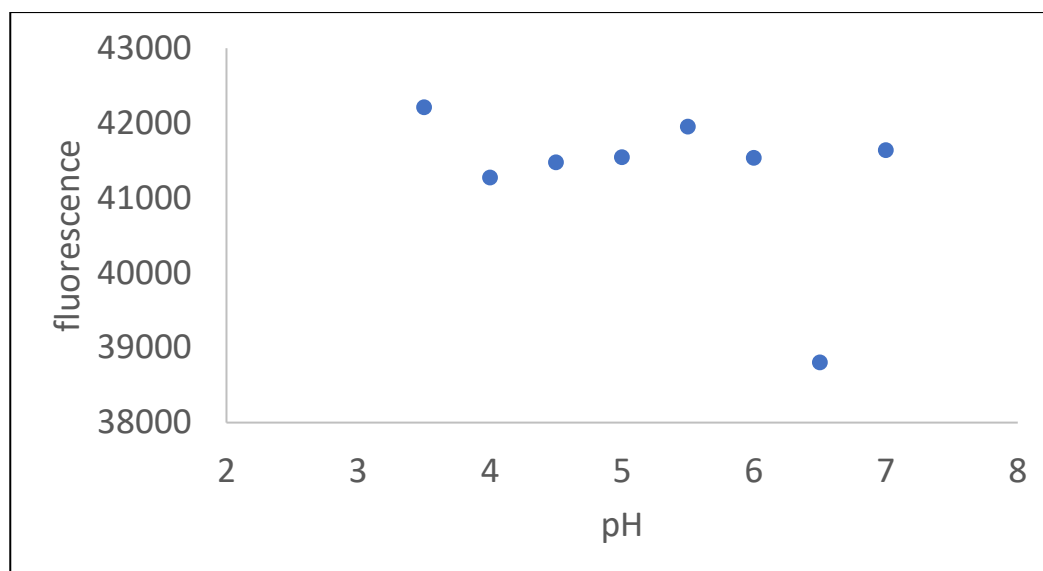


Figure 48 A pH calibration curve of proliferative SH-SY5Y cells incubated with the LysoSensor™ Yellow/Blue DND-160. Proliferative SH-SY5Y cells were incubated with DND-160 dye and different pH buffers (3.5-8) and the fluorescent intensity was measured and plotted against the pH.

Next, I assumed the problem was intrinsic to the dye itself, so I trialled a different dye, LysoSensor™ Blue DND-167. Establishing a pH calibration curve using the DND-167 dye and pH buffers alone was successful, where the fluorescence intensity decreased with increasing pH and plateaued at pH 7 when measured at 370 nm excitation and 435 nm emission (Figure 49). Unfortunately, I faced similar cell adherence issue as I had done with the DND-160.

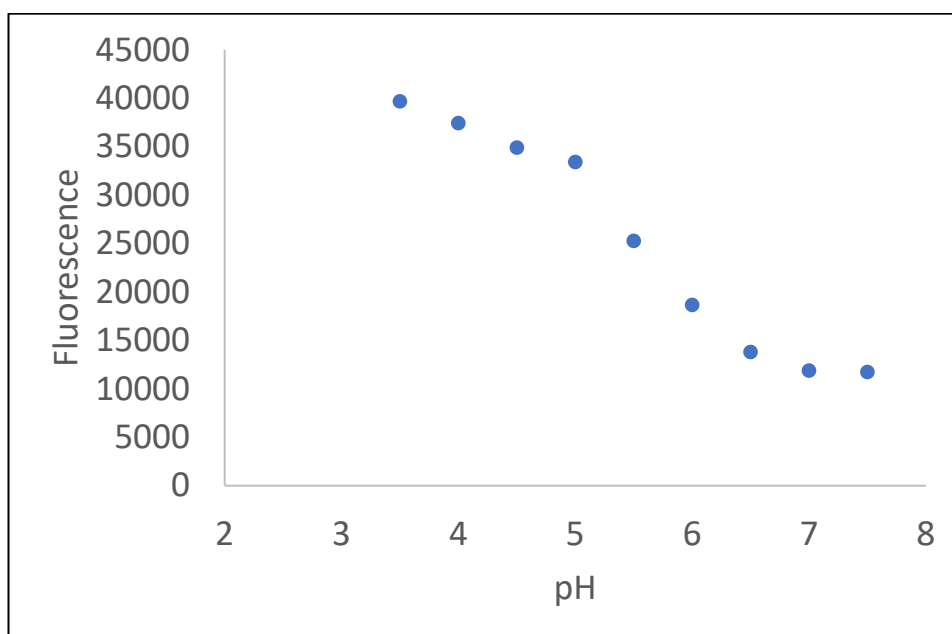


Figure 49 A pH calibration curve of the LysoSensor™ Blue DND-167. DND-167 dye was incubated in different pH buffers (3.5-8) and the fluorescent intensity was measured and plotted against the pH.

Next, I assumed the problem may lay with the cell line itself, so I have used both dyes with a different type of cells, fibroblast cells. Unfortunately, similar cell adherence issues to SH-SY5Y cells were faced with fibroblasts as well (for example Figure 50).

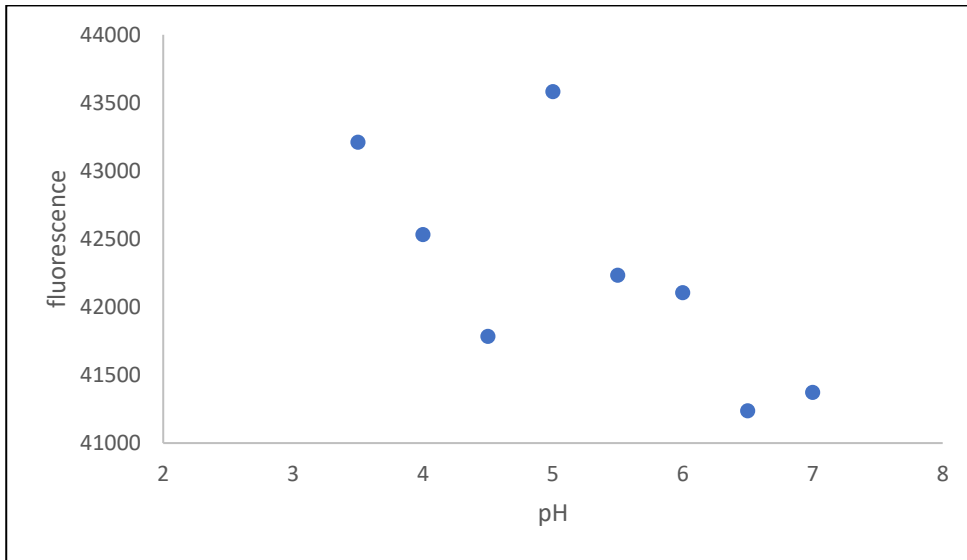


Figure 50 A pH calibration curve of fibroblast cells incubated with the LysoSensor™ Blue DND-167. Fibroblast cells were incubated with DND-167 dye and different pH buffers (3.5-8) and the fluorescent intensity was measured and plotted against the pH.

Following months of trial and error and due to time constrains, I made the decision to devise a different method to help me gain insight on the state of lysosomal pH in proliferative and differentiated SH-SY5Y cells.

6.3.2. Choice of CTSD antibody:

During the process of maturation and activation of CTSD, the proCTSD species is converted to mCTSD (Mijanovic *et al.* 2021). Therefore, to monitor the maturation of CTSD, quantifying the ratio of the proCTSD species to the mCTSD species allows to follow and assess the maturation process. Therefore, I sought to find antibodies that would allow the detection of both species of CTSD. The first antibody tested was a polyclonal anti-CTSD from cell signalling #2284. The antibody was cited to react with both proCTSD and mCTSD on the same blot, which would be a cost and time effective way to reduce experimental variability as I was interested in the ratio of proCTSD/mCTSD. Unfortunately, under my experimental conditions, the antibody reacted strongly to an unknown band at approximately 60 kDa in both proliferative and differentiated SH-SY5Y cells (Figure 51 A). For this reason, I opted to use Abcam recombinant monoclonal antibodies against proCTSD and mCTSD (#ab134169 and # ab75852). These antibodies were found to be very specific to the proteins of interest and permitted the ability to blot the same gel with both antibodies at the same time to minimise loading variability between different gels and the unwanted, though minimal, loss of proteins in the case of stripping the blots (Figure 51 B).

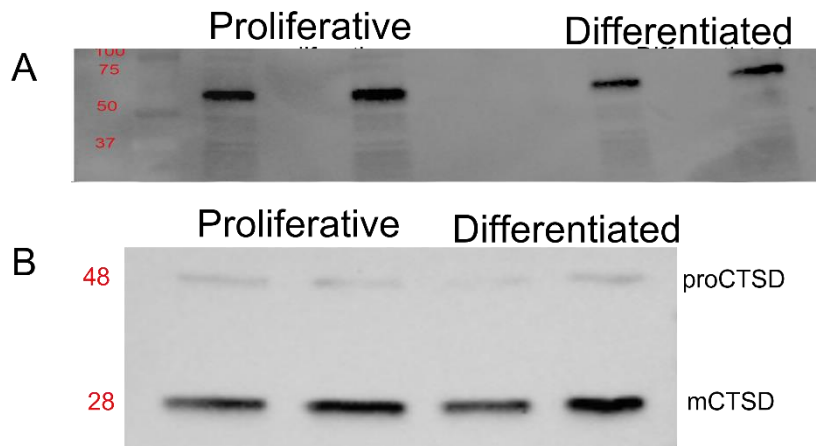


Figure 51 A representative western blot blotted with (A) anti-cathepsin D polyclonal antibody (Cell Signalling #2284) and (B) anti-proCTSD and anti-mCTSD monoclonal antibodies (Abcam #ab134169 and #ab75852) in proliferative and differentiated SH-SY5Y cells. Red: molecular weight in kDa

6.3.3. Effect of bafilomycin A1 on CTSD maturation and activity:

Bafilomycin A1 (baf) is a macrolide antibiotic isolated from *Streptomyces* sp. that is well recognised as a selective inhibitor of v-ATPase (Werner *et al.* 1984; Bowman *et al.* 1988; Yoshimori *et al.* 1991). Baf facilitates the inhibition of v-ATPase by blocking proton translocation through binding the V₀ subunit of v-ATPase. The degree of inhibition is concentration-dependent with complete inhibition achieved at concentrations in the nano molar range therefore, it is one of the most commonly used inhibitors of lysosomal acidification (Wang *et al.* 2021). Baf has been demonstrated to increase lysosomal pH in human proliferative and RA differentiated SH-SY5Y cells, HeLa cells, a lung cancer cell line, an epidermoid cancer cell line and in fibroblasts (Chin *et al.* 2021; Shen *et al.* 2015; Yoshimori *et al.* 1991; Wang *et al.* 2020a; Coffey *et al.* 2014). Treatment of RA differentiated SH-SY5Y cells with 500 nM baf for 16 hours has been shown to not affect lysosomal-mediated proteolysis of long-lived proteins nor alter the lysosomal degradation pathways as it had no effect of LC3 I to II conversion or p62 levels, both of which are markers of autophagy (macroautophagy and chaperon-mediated autophagy, Dermentzaki *et al.* 2013). This might indicate that the cells possess compensatory mechanisms against acute v-ATPase inhibition following exposure to Baf (16 hours) as there were no visible signs of overt cellular toxicity.

In this study, baf was used as a positive control to investigate the effect of lysosomal alkalinisation in CTSD maturation and activity. Therefore, proliferative and differentiated SH-SY5Y cells were incubated with 500 nM baf for 16 hours then the protein expression of proCTSD and mCTSD as well as CTSD enzyme activity were analysed.

Following baf inhibition of v-ATPase, there was, as expected, a significant decrease in the level of mCTSD protein expression in both proliferative and differentiated SH-SY5Y cells as evident by an increase in the densitometry of proCTSD/mCTSD in baf treated cells compared to control (Figure 52 A and B, Table 6). This decrease in CTSD maturation was confirmed by a significant decrease in CTSD enzyme activity (Figure 53, Table 7). Interestingly, the sensitivity to baf inhibition of lysosomal acidification appeared to differ between proliferative and differentiated cells, whereby the degree of alteration in CTSD maturation was significantly different between proliferative and differentiated SH-SY5Y cells (Figure 52 C). This was also confirmed on the enzyme activity level, where the decrease in enzyme activity following baf inhibition differed between proliferative and differentiated SH-SY5Y cells (69% and 90%, respectively, Figure 53 and Table 7).

Taken together, the results of this experiment demonstrate that the v-ATPase inhibitor, baf, affects CTSD maturation and activity. Therefore, any deviation from the optimal pH, in particular an increase in pH, would be reflected on CTSD. Thus, CTSD can be used as an indirect indicator of the state of the lysosomal pH.

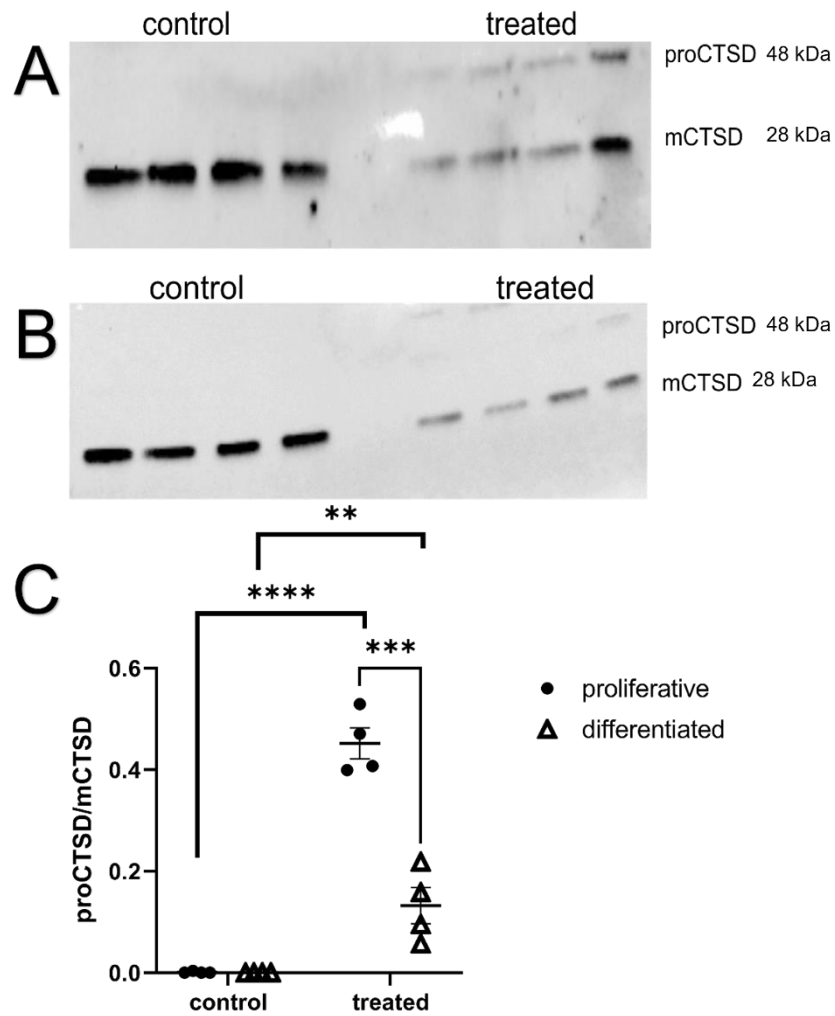


Figure 52 Effect of baf treatment on CTSD maturation. Proliferative (A) and differentiated (B) SH-SY5Y cells were treated with 500 nM bafilomycin A1 for 16 hours then proCTSD and mCTSD protein expression was analysed by western blot. (C) Densitometry of proCTSD and mCTSD expression presented as a ratio of proCTSD/mCTSD. Blot representative of $n = 4$ independent cell culture preparations. A two-way ANOVA was used to compare the means. ** $p = 0.003$, *** $p = 0.0001$, **** $p = < 0.0001$.

	Proliferative	Differentiated	p-value
--	---------------	----------------	---------

Control	0.0009 ± 0.009	0	ns
Treated	0.45 ± 0.03	0.132 ± 0.035	0.0001
p-value	<0.0001	0.0035	

Table 6 Ratio of proCTSD/mCTSD protein expression in control and bafilomycin A1 treated proliferative and differentiated SH-SY5Y cells. Values are presented as mean ± SEM of ratio of proCTSD/mCTSD densitometry of n = 4 independent cell preparations. A two-way ANOVA with multiple comparisons was used to compare the means. ns: not significant

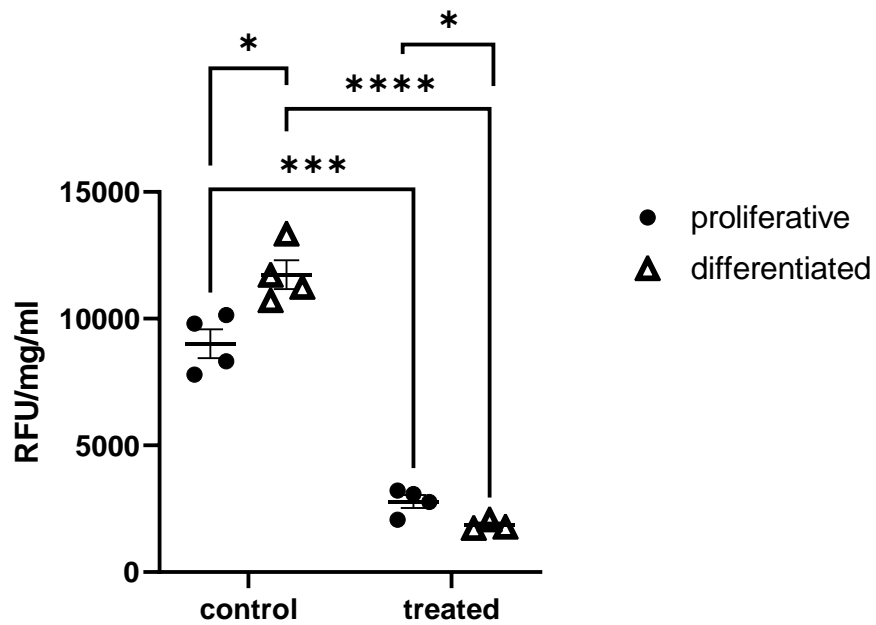


Figure 53 Effect of baf treatment on CTSD enzyme activity. Proliferative and differentiated SH-SY5Y cells were treated with 500 nM bafilomycin A1 for 16 hours then CTSD enzyme activity was assayed. Results were normalised to a protein baseline and represent mean \pm SEM of $n = 4$ independent cell preparations. A two-way ANOVA was used to compare the means. RFU: relative fluorescence unit. * $p < 0.05$, *** $p = 0.0001$, **** $p < 0.0001$

	Proliferative	Differentiated	p-value
Control	9014 ± 570	11739 ± 567	0.029
treated	2786 ± 255	1185 ± 106	0.03
p-value	0.0001	<0.0001	
% Reduction	69	90	

Table 7 CTSD enzyme activity in control and bafilomycin A1 treated SH-SY5Y cells.

Values are presented as mean ± SEM RFU/mg/ml of n= 4 independent experiments. A two-way ANOVA was used to compare the means.

6.3.4. The effect of inhibition of lysosomal GBA on CTSD maturation and activity:

Bourdenx and colleagues (2016) have documented an increase in lysosomal pH in fibroblasts from PD patients carrying mutations in their *GBA* gene (Bourdenx *et al.* 2016). Therefore, to assess the effect of GBA loss-of-function on lysosomal pH, proliferative and differentiated SH-SY5Y cells were treated with conduritol B epoxide (CBE), the selective and irreversible inhibitor of GBA. After treatment, the maturation and activity of CTSD were assessed as an indirect indicator of lysosomal pH. Treatment with 100 μ M CBE for 72 hours has been shown to be sufficient to diminish GBA activity by almost 95% in RA differentiated SH-SY5Y cells (Dermentzaki *et al.* 2013).

Following GBA inhibition, a significant decrease in CTSD maturation was evident by an increase in the ratio of proCTSD/mCTSD protein expression, both in proliferative and differentiated SH-SY5Y cells (Figure 54, Table 8). This decrease was further confirmed by a significant decrease in CTSD activity in both proliferative and differentiated SH-SY5Y cells (Figure 55, Table 9). Interestingly, the degree of reduction in CTSD enzyme activity differed significantly between proliferative and differentiated SH-SY5Y cells, 88% and 51%, respectively (Figure 55, Table 9).

These findings suggest that the increase in lysosomal pH seen in PD patients carrying mutation in their *GBA* gene could be in part due to loss of function of GBA. The findings also demonstrate that CTSD enzyme activity can confirm and reflect the degree of maturation of the enzyme.

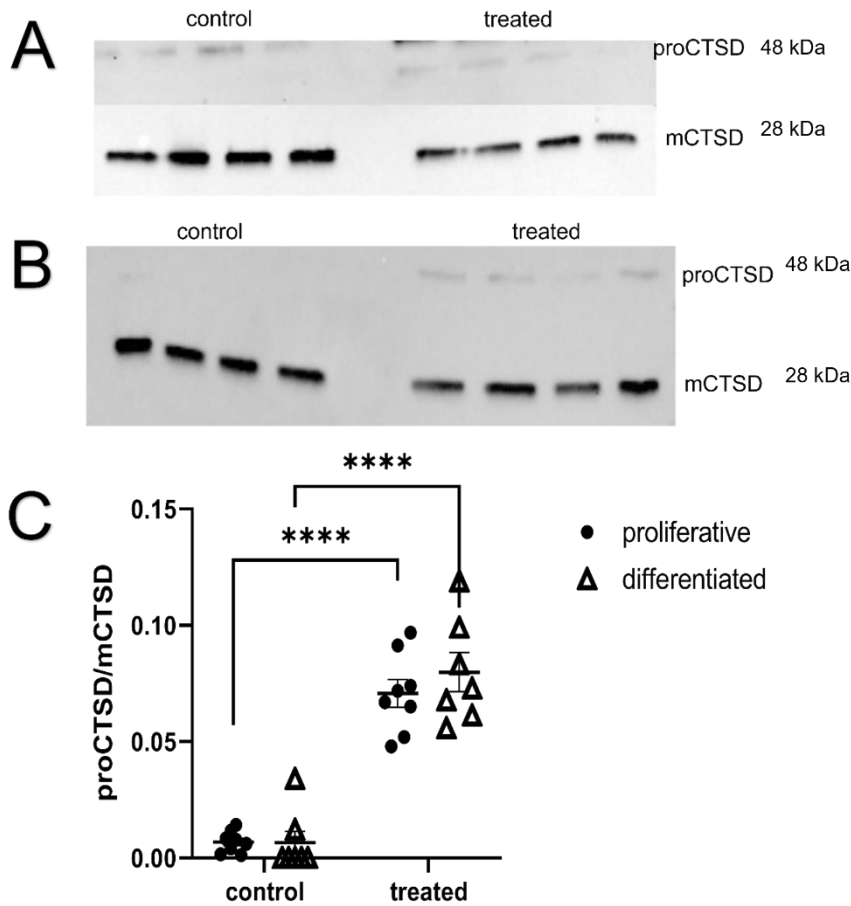


Figure 54 Effect of GBA inhibition on CTSD maturation. Proliferative (A) and differentiated (B) SH-SY5Y cells were treated with 100 μ M CBE for 72 hours then proCTSD and mCTSD protein expression was analysed by western blot. (C) Densitometry of proCTSD and mCTSD expression presented as a ratio of proCTSD/mCTSD. Blot representative of n= 8 independent cell culture preparations. A two-way ANOVA was used to compare the means. **** p = < 0.0001

	Proliferative	Differentiated	p-value
Control	0.007 \pm 0.002	0.004 \pm 0.006	ns

treated	0.071 ± 0.006	0.08 ± 0.008	ns
p-value	<0.0001	<0.0001	

Table 8 Ratio of proCTSD/mCTSD protein expression in control and CBE treated SH-SY5Y cells. Values are presented as mean ± SEM of ratio of proCTSD/mCTSD densitometry of n = 8 independent cell preparations. A two-way ANOVA was used to compare the means. ns: not significant

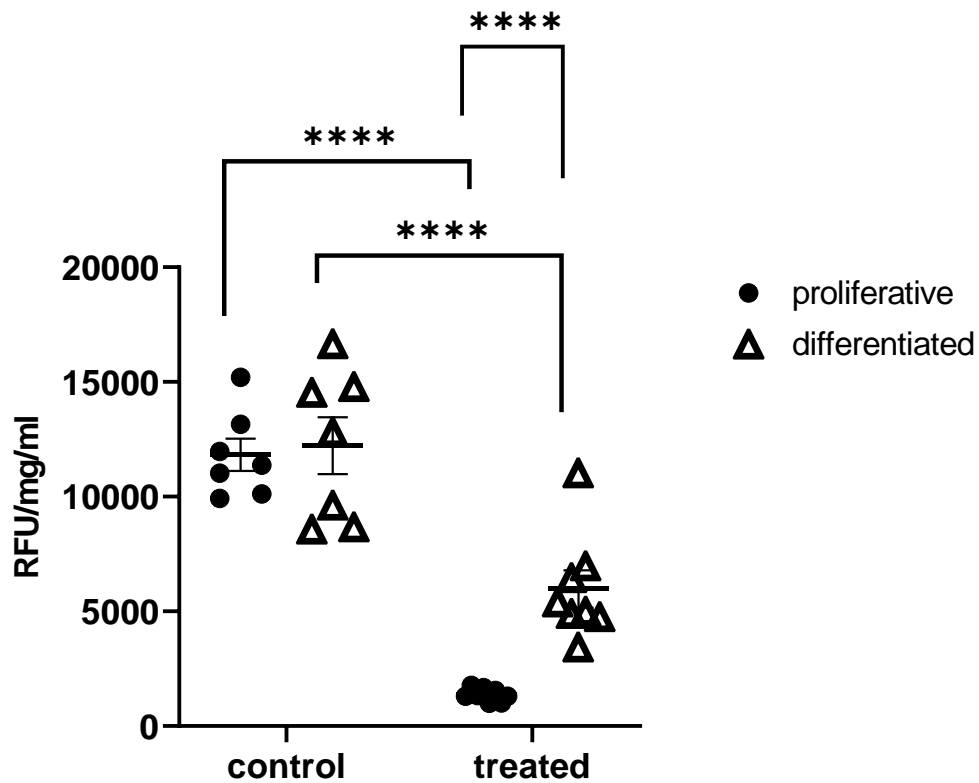


Figure 55 Effect of inhibition of GBA activity on CTSD enzyme activity. Proliferative and differentiated SH-SY5Y cells were treated with 100 μ M CBE for 72 hours then CTSD enzyme activity was measured. Results were normalised on a protein baseline and represent mean \pm SEM of n = 8 independent experiments. A two-way ANOVA was used to compare the means. RFU: relative fluorescence unit. **** p= < 0.0001

6.3.5. The effect of inhibition of mitochondrial complex I on CTSD activity:

The results of the previous experiment prompted the question of whether perturbations in other pathways implicated in PD could also lead to alterations in lysosomal pH. One of these pathways involves the mitochondrial ETC complex I. A decrease in the activity of the mitochondrial complex I is strongly associated with PD pathology (Schapira *et al.* 1990). In addition, a growing number of studies are pointing to an ongoing crosstalk between mitochondria and lysosomes and as a consequence, perturbations in mitochondrial function affect lysosomes (Burbulla *et al.* 2017; Thomas *et al.* 2011; Demers-Lamarche *et al.* 2016; Xie *et al.* 2015) Thus, I investigated whether inhibition of mitochondrial complex I could have any effect on lysosomal CTSD. Proliferative and differentiated SH-SY5Y cells were treated with rotenone, one of the most commonly used neurotoxins to create animal and cellular models of PD (Radad *et al.* 2019). Rotenone is an irreversible inhibitor of mitochondrial complex I, and at a concentration of 100 nM, was demonstrated to reduce complex I activity by more than 50% while preserving cell viability in SH-SY5Y cells (Aylett *et al.* 2013; Mader *et al.* 2012; de la Fuente *et al.* 2017). Following treatment with 100 nM rotenone for 24 hours, a significant decrease in CTSD activity was observed in both proliferative and differentiated SH-SY5Y cells (Figure 56, Table 9). Similar to what was seen following CBE and baf inhibition, the degree of reduction in CTSD enzyme activity significantly differed between proliferative and differentiated SH-SY5Y cells, 25% and 81%, respectively (Figure 56, Table 9).

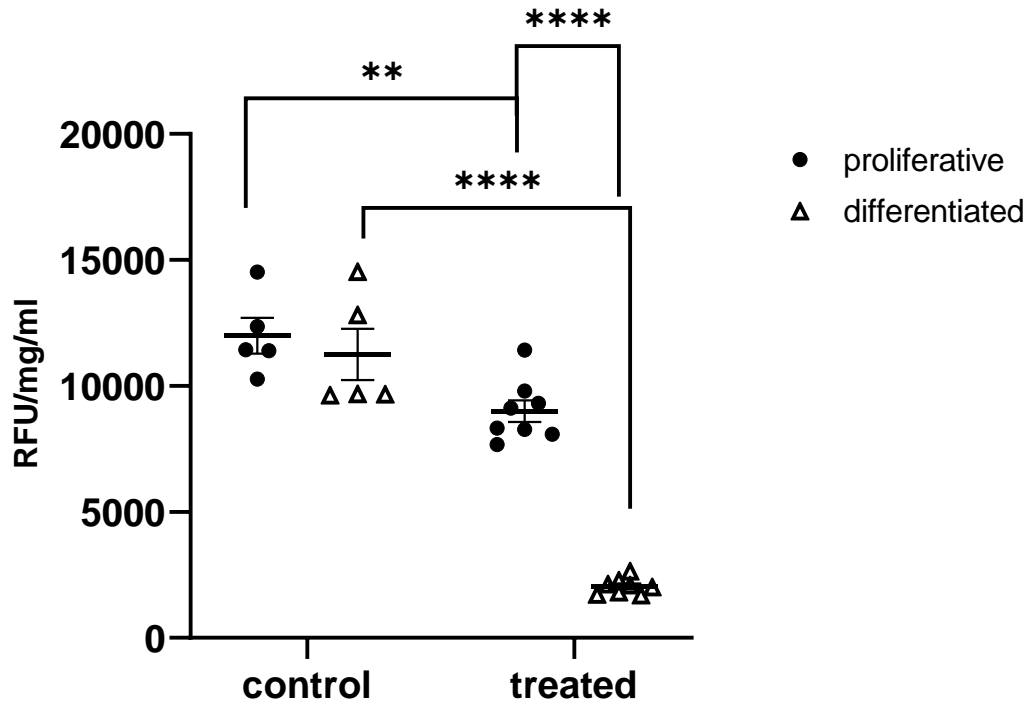


Figure 56 Effect of inhibition of complex I activity on CTSD enzyme activity. Proliferative and differentiated SH-SY5Y cells were treated with 100 nM rotenone for 24 hours then CTSD enzyme activity was measured. Results were normalised on a protein baseline and represent mean \pm SEM of $n = 5-8$ independent experiments. A two-way ANOVA was used to compare the means. ** $p = 0.019$, **** $p = < 0.0001$. RFU: relative fluorescence unit.

	Proliferative	Differentiated	p-value
CBE Treatment			
Control	11822 ± 701	12223 ± 1239	ns
CBE treated	1368 ± 102	5978 ± 814	0.00025
p-value	<0.0001	<0.0001	
% Reduction	88	51	
Rotenone treatment			
Control	11993 ± 712	11294 ± 1021	ns
Rotenone treated	8998 ± 426	2038 ± 112	<0.0001
p-value	0.019	<0.0001	
% Reduction	25	81	

Table 9 CTSD enzyme activity in control, CBE and rotenone treated SH-SY5Y cells.

Values are presented as mean ± SEM RFU/mg/ml of n = 5-8 independent experiments.

To test for significance, A two-way ANOVA was used to compare the means. ns: not significant

6.4. Discussion:

Disruption of mitochondrial and lysosomal function in PD are well established events. There is a growing number of studies pointing to an increase in lysosomal pH in neurodegenerative diseases, particularly PD (Bourdenx *et al.* 2016; Choi *et al.* 2015; Kurzawa-Akanbi *et al.* 2012; Nixon 2020). One of the recently established methods to measure lysosomal pH uses the LysoSensor dyes (Heaton *et al.* 2020). Unfortunately, under the experimental conditions of this study, using these dyes with SH-SY5Y cells was not possible due to the tendency for the cells to detach following incubation with the dyes.

CTSD maturation, from proCTSD to mCTSD, and its activity are pH-dependent processes, requiring the acidic pH range of 4-5 (Laurent-Matha *et al.* 2006) These processes take place within the acidic lumen of the lysosome, which has a normal physiological pH of 4-5 (Pillay *et al.* 2002). This study provides evidence for the use of the ratio of proCTSD/mCTSD and CTSD activity as indirect tools to assess the state of lysosomal pH. This is confirmed by their susceptibility to lysosomal alkalinisation via baf inhibition of v-ATPase (Figure 52, Figure 53). However, the inclusion of a loading control protein during assessment of proCTSD/mCTSD ratio would be useful to assess that the reduction in levels is specific to CTSD maturation. In addition, the increase in lysosomal pH is likely to affect other lysosomal acid hydrolases, that depend on acidic pH for their function. Therefore, assessing other lysosomal enzyme function (e. g. GBA, β -Gal) might be beneficial to confirm lysosomal alkalinisation.

In this study, there was a significant difference in the sensitivity of proliferative and RA/TPA differentiated SH-SY5Y cells to baf treatment, as

evident by the effect on CTSD (Figure 52 and Figure 53). This difference in sensitivity to baf was similarly demonstrated by Chin and colleagues (2012) between proliferative and RA differentiated SH-SY5Y cells. Following treatment with 100 nM Baf, a larger increase in lysosomal pH was observed in proliferative compared to RA differentiated SH-SY5Y cells (Chin *et al.* 2021). One potential reason behind the difference could be due to differences in v-ATPase regulation between the two phenotypes. The expression, assembly, and activity of v-ATPase is suggested to be regulated by differentiation (Toei *et al.* 2010; McGuire *et al.* 2017). For example, during chondrocytes hypertrophy, a process that contribute to normal bone development, Ayodele and colleagues (2017) have shown that proliferative chondrocyte have lower protein expression levels of the V0 subunit, D2, than mature chondrocytes (Ayodele *et al.* 2017). In addition, during osteoclast cell differentiation, it was shown in osteoclast precursor cells, the A3 subunit of v-ATPase is located on the lysosomal membrane. However, following differentiation, the A3 subunit-containing v-ATPase locates to the plasma membrane instead. This is important for the function of osteoclasts that require an acidic extracellular space (Toyomura *et al.* 2003).

The finding that loss of GBA activity impedes CTSD maturation and therefore activity in a similar trend to inhibition of lysosomal acidification by baf (Figure 54 and Figure 56) supports the idea that loss of GBA results in an increased lysosomal pH. Although no direct measurement of lysosomal pH was taken, the increase in pH can be deduced from the dysregulation of two processes that strongly depend on acidic pH (proCTSD to mCTSD maturation and CTSD enzyme activity). Similar findings are supported by a number of studies. In GBA

gene knockout RA differentiated SH-SY5Y cell line model for PD, loss of function of GBA was shown to cause an increase lysosomal pH (Bae *et al.* 2015). In addition, in cell line models with disrupted ATP13A2 expression, Bourdenx and colleagues (2016) demonstrated that proCTSD expression was higher both in fibroblasts from PD patients with ATP13A2 mutation and in a dopaminergic cell line model where ATP13A2 expression was knocked down. This was a result of higher lysosomal pH in these cells. The finding was further confirmed by a reduced CTSD activity in both cell models. Decreasing lysosomal pH using acidic particles that are designed to sequester into the lysosomes reducing the pH of its lumen, resorted the balance in CTSD expression and activity. Similar findings were observed in fibroblasts from patients carrying point mutations in *GBA* gene. Acidifying the lysosomes rescued CTSD expression and activity in *GBA* mutant fibroblasts (Bourdenx *et al.* 2016). Yang and colleagues (2020) demonstrated that a normal function of GBA is required for normal CTSD expression and activity. In dopaminergic neuronal model developed from PD patients carrying *GBA* mutations, rescuing GBA activity either via enzyme replacement or treatment with the GBA enhancer, Ambroxol, successfully restored CTSD expression and activity (Yang *et al.* 2020).

The relationship between GBA, lysosomal pH and CTSD is not exclusive to PD. Post-mortem brain tissue homogenates from patients with Lewy body dementia carrying mutations in *GBA* gene revealed that GBA expression and activity was reduced compared to control (Kurzawa-Akanbi *et al.* 2012). Lewy body dementia is characterised by a build-up of Lewy body plaques in the brain, a phenomenon that represents the hallmark of PD (Sanford 2018). Interestingly,

brain tissue homogenate analysis also revealed that the reduction in GBA expression and activity was accompanied by a reduced expression of CTSD (Kurzawa-Akanbi *et al.* 2012).

There are a couple of hypotheses that suggest a mechanism behind how loss of function in GBA affects CTSD maturation and function. Heterozygous mutations in GBA are the most common risk factor for PD (Migdalska-Richards and Schapira 2016). Homozygous mutations, however, cause one of the most common LSD, Gaucher disease (Platt *et al.* 2018). In a cellular model for Krabbe disease, another type of LSD, Folts and colleagues (2016) have shown that treatment with galactosphingosine, the lipid that accumulates as a result of loss of function in the enzyme galactosylceramidase, caused a significant increase in lysosomal pH in oligodendrocyte precursor cells. This effect was found to be as potent as the effect of treating the cells with baf. Intriguingly, one possible explanation behind galactosphingosine ability to increase lysosomal pH could be due to its possession of a free amine group. Folts and colleagues (2016) have shown that blocking the free amine by derivatisation with an acetyl group blocks the ability of galactosphingosine to increase lysosomal pH. Interestingly, in relevance to Gaucher's disease, the lipids that accumulate are glucocerebroside, not containing a free amine group, and glucosylsphingosine, which possess a free amine group. Folts and colleagues (2016) have shown that glucosylsphingosine, but not glucocerebroside, increased the lysosomal pH of oligodendrocyte precursor cells (Folts *et al.* 2016). In patients with Gaucher's disease, the levels of glucosylsphingosine were found to be drastically higher than the control group (Hein *et al.* 2007). In a zebrafish model for Gaucher's

disease, where formation of glucosylsphingosine was interrupted through acid ceramidase enzyme gene knockout, Lelieveld and colleagues (2022) show that these zebrafish display ameliorated disease course than zebrafish with excessive glucosylsphingosine (Lelieveld *et al.* 2022).

In a mouse primary neuronal cell model for Alzheimer disease (AD), where cells are treated with synthetic oligomers of amyloid- β , which accumulation represents the hallmark of AD, Choi and colleagues (2015) demonstrated a decrease in the protein expression and enzyme activity of both GBA and CTSD. This decrease was also accompanied by an increase in lysosomal pH, as revealed by a decrease in LysoTracker fluorescence, a fluorescence probe that is selective for acidic compartments. The increase in lysosomal pH and decrease in CTSD expression and activity were both attenuated by overexpression of GBA via lentivirus transfection (Choi *et al.* 2015). One possible explanation could be the disruption of lysosomal membrane permeabilization (LMP), as maintenance of lipid homeostasis is imperative for preventing LMP (Serrano-Puebla and Boya 2016). Loss of function in GBA disrupts lipid homeostasis because of its role in the sphingolipid pathway, a pathway important for preserving lipid membrane integrity and homeostasis (Hein *et al.* 2007). Disruption of LMP could result in proton leak from the lysosomal lumen leading to increase in lysosomal pH.

CBE treatment of proliferative and differentiated SH-SY5Y cells also revealed differences in the response of the phenotypes to GBA inhibition where differentiated cells appeared significantly more resistant to the consequence of GBA inhibition on CTSD activity (Figure 55). This could be a result of the

significantly higher activity of GBA found in differentiated SH-SY5Y cells as seen in Chapter 4.

Rotenone is a neurotoxin that is associated with development of PD and degeneration of dopaminergic neurons of the SN (Betarbet *et al.* 2000). In this study, rotenone treatment resulted in reduced activity of CTSD (Figure 56). Rotenone has been shown to decrease cellular production of ATP by almost 50% as early as 6 hours following exposure in RA differentiated SH-SY5Y cells. In addition, it has been demonstrated to lead to a decrease in the fluorescence of the acidic pH fluorescent dye, LysoTracker, indicative of an increase in lysosomal pH (Mader *et al.* 2012). This increase in lysosomal pH could be a result of decrease in ATP production which is required for the active proton transport into the lumen of the lysosomes via V-ATPase. MPTP is a neurotoxin that is also associated with development of PD (Langston *et al.* 1984). The metabolite of MPTP, MPP⁺, was shown to be a selective inhibitor of the SN mitochondrial complex I, similar to rotenone (Nicklas *et al.* 1987). MPTP injection into the SN of wildtype mice has been shown to similarly decrease the activity of CTSD (Bourdenx *et al.* 2016).

The differential response of proliferative and differentiated SH-SY5Y cells to baf and CBE treatments was also apparent following rotenone treatment in this study. The activity of CTSD in differentiated SH-SY5Y cells appeared significantly more sensitive to rotenone treatment (Figure 56). This is in line with several studies concluding that differentiated SH-SY5Y cells are more susceptible to neurotoxins (MPP⁺, 6-hydroxydopamine, rotenone) compared to proliferative SH-

SY5Y cells (Presgraves *et al.* 2004; Lopes *et al.* 2017b; Lopes *et al.* 2010; Simões *et al.* 2021).

To conclude, this study demonstrated the feasibility of use of CTSD as an indirect indicator of the state of lysosomal pH in cells, which is gaining attention for its involvement in disease pathology, particularly in PD. It also brings into attention lysosomal pH as a potential key event in PD pathology and a consequence of loss of function of both lysosomal GBA and mitochondrial complex I. This study further shines the light on the theme of this thesis that demonstrate the existence of similarities as well as significant differences in the biochemistry of proliferative and differentiated SH-SY5Y cells, as well as in their response to different treatments. Therefore, care should be taken when considered as a model for PD and related disease.

**Chapter 7. Investigation of Potential Therapies for Treatment of
Aromatic Amino Acid Decarboxylase Deficiency**

7.1. Introduction

Aromatic amino acid decarboxylase, or AADC (E.C. 4.1.1.28, also known as DOPA decarboxylase), is an enzyme involved in the final step of dopamine and serotonin biosynthesis. It catalyses the conversion of L-DOPA and 5-hydroxytryptophan to dopamine and serotonin, respectively. AADC deficiency (AADCD) is a type of inborn error of metabolism that is caused by rare autosomal recessive genetic mutations in the *DDC* gene, coding for AADC enzyme. Clinical presentation of AADCD varies in symptoms and severity between patients but includes neurodevelopmental delay, oculogyric crisis, and complex movement disorders. The clinical diagnosis of AADCD is based on a CSF neurometabolite profile of low levels of HVA and 5-HIAA, accompanied by high levels of 3-OMD and 5-HTP. These levels reflect the metabolic block imposed on dopamine and serotonin biosynthesis as a result of AADC deficiency. HVA and 5-HIAA are the catabolic products of dopamine and serotonin, respectively. Their levels are diminished as a consequence of loss of dopamine and serotonin. 3-OMD is formed as a result of accumulation of L-DOPA, the precursor of dopamine. When in excess, L-DOPA is converted to 3-OMD via the enzyme COMT. 5-HTP is a substrate of AADC and the precursor of serotonin, and as a result of AADC deficiency, it accumulates (Figure 1, Hyland and Clayton 1992).

The current therapeutic regimens for AADCD vary between patients. This is not only a result of the difficulty to correct primary biochemical defects but also because patients exhibit variable responses to different medications. Treatment can include L-DOPA, dopamine agonists, and MAO inhibitors with the aim to increase dopamine levels (Swoboda *et al.* 2003). Treatment can also include pyridoxal phosphate, the cofactor for AADC (Arnoux *et al.* 2013). Anticholinergic

agents are also used to correct the potential imbalance between the dopaminergic and cholinergic pathways (Wassenberg *et al.* 2017). In addition, the increased conversion of L-DOPA to 3-OMD could potentially deplete the methyl donor pool, 3-methyltetrahydrofolate and s-adenosylmethionine, resulting in secondary cerebral folate deficiency, so folinic acid is also supplemented (Bräutigam *et al.* 2000). Therefore, it is currently difficult to predict the suitable treatment regimen for each patient, requiring laborious and difficult period of trial and error (Wassenberg *et al.* 2017).

It has been proposed that the variability in response to different treatment might be, in part, due to the genetic variability seen in the mutations that cause AADC (Montioli *et al.* 2021). Different genetic mutations can alter different aspects of an enzyme. Mutations can result in decreased transcription, decreased translation, or misfolding of the tertiary structure of an enzyme. Mutations can also interfere with co-factor binding or influence the catalytic activity and efficiency of an enzyme. Therefore, uncovering the effect of genetic mutation on enzymatic function is important to understand the pathology of inborn error of metabolism and exploring potential therapeutics (Cellini 2012; Montioli *et al.* 2014). An enzyme catalytic efficiency is defined as how well an enzyme convert its substrates into products. It is calculated as the ratio of an enzyme's catalytic constant (K_{cat}) to its Michaelis constant (k_m) towards a specific substrate (K_{cat}/k_m , Hammes-Schiffer 2012). Bioinformatic studies of different genetic mutations causing AADC revealed that some mutations can decrease the catalytic efficiency of AADC towards L-DOPA but does not diminish the enzyme activity completely. This is important because it can help decide which patients, based

on the type of mutations they carry, may benefit the most from L-DOPA supplementation (Montioli *et al.* 2020; Longo *et al.* 2021; Montioli *et al.* 2021).

In addition to medications, gene therapy is a rapidly progressing field of medicine that involves the introduction of genetic material into cells to rescue defective gene expression. It is one of the most hopeful therapies for diseases of inborn errors of metabolism, such as AADCDC, to restore a defective or missing enzyme. One of the most common techniques is the insertion of recombinant DNA carrying a functional gene into a viral vector, such as that of a lentivirus (Cotrim and Baum 2008). Because of the monogenetic nature of AADCDC, replacing the defective gene with a functional gene using ectopic expression is a promising therapeutic avenue.

In this study, iPSC dopaminergic neurons derived from two AADCDC patients carrying different mutations on their *DDC* gene were utilised to explore the effect of these mutations on dopamine metabolism and their response to potential AADCDC therapies, namely L-DOPA and lentivirus gene rescue. It is hypothesized that patient-derived dopaminergic neurons have a dopamine metabolism profile that resembles that seen in the CSF of patients. This makes them a good model to study disease pathology and test potential therapeutics.

Thus, the **aims** of this chapter were:

- To investigate the suitability of patient-derived iPSC dopaminergic neurons as a cellular model for AADCDC
- To test the effect of lentivirus gene rescue of *DDC* gene on dopamine metabolism

- To test the use of L-DOPA as therapy for AADC deficiency based on the result of recombinant enzyme studies

7.2. Materials and methods:

7.2.1. Generation of iPSC-derived dopaminergic neuronal model for AADC:

In this chapter, iPSC-derived dopaminergic neurons from two AADC patients and an age-matched healthy control were generated and maintained by the collaborator, Dr Giada Rossignoli and Dr Karolin Krämer, as described in Rossignoli *et al.* 2021. Patient 1 carried homozygous missense mutation in *DDC* gene (c.1039C>G, p.R347G) and presents with neurodevelopmental delay, oculogyric crises and early hypotonia. Patient 2 carries compound heterozygous mutations in *DDC* gene (c.19C>T, p.Arg7*; c.299G>C, p.C100S) and presents with severe global developmental delay, oculogyric crises and hypoglycaemia.

7.2.2. Lentivirus gene rescue of AADC mutant iPSC derived dopaminergic neurons:

The AADC expressing plasmid generation, lentivirus production and cell transfection was carried out by the collaborator, Dr Karolin Krämer, as described in (Kramer 2019, PhD thesis, UCL and Rossignoli *et al.* 2021). Briefly, a lentiviral expression plasmid (pCCL-hSYN1-DDC-IRES-EGFP) was developed by insertion of *DDC* gene coding sequence into a previously developed plasmid (L). A control plasmid CCL-hSYN1-GFP was also produced (M). Plasmid sequences were verified by Sanger sequencing. Lentiviral expression plasmid was validated by transducing HEK 293T cells and Western blotting for AADC protein. Lentiviral vectors were produced using a packaging system and vector titres were quantified by qPCR. Patient-derived dopaminergic neurons were differentiated for 24 days before transduction with lentiviral vectors at 0.5 multiplicity of infection for 24 hours, then differentiated to day 65. On day 65 of differentiation, the iPSC

derived dopaminergic neurons incubated in phenol red-free medium for 24 hours. The medium was then removed, processed, and stored at -80 °C as described in section 2.4.2.1.

7.2.3. L-DOPA treatment and HPLC sample preparation:

After incubating the cells with different concentrations of L-DOPA (40-100 μ M) and analysing cellular viability and dopamine metabolism, 80 μ M L-DOPA was found to be the concentration that is sufficient to stimulate dopamine pathway in iPSC derived dopaminergic neurons while avoiding increased cellular toxicity (Rossignoli *et al.* 2021; Park *et al.* 2016). Thus, on day 65 of differentiation, the iPSC derived dopaminergic neurons were treated with 80 μ M L-DOPA in phenol red-free medium for 24 hours. Untreated cells were incubated in the same medium without L-DOPA for 24 hours. The medium was then removed, processed, and stored at -80 °C as described in section 2.4.2.1.

7.2.4. HPLC-ED measurement of extracellular dopamine metabolites

Samples were analysed as described in Chapter 3.

7.3. Results

7.3.1. Confirmation of AADC deficiency phenotype

CSF analysis of patients carrying mutations in their *DDC* gene have a signature profile of high 3-OMD and low/absent dopamine, HVA and DOPAC. Therefore, to assess the suitability of the AADC deficiency dopaminergic neuronal model generated, extracellular dopamine metabolites were measured using HPLC-ED.

Dopamine was detectable only in dopaminergic neurons derived from control at a level of 157 ± 21 pmol/mg protein. Dopamine was absent in patient-derived neurons (Figure 57 A). Similarly, HVA was only detectable in control neurons, with mean level of 130 ± 120 pmol/mg protein (Figure 57 C). DOPAC levels were highest in control neurons, with mean level of 445 ± 72 pmol/mg. Patient 1 and 2 derived neurons had comparable levels of DOPAC (109 ± 22 and 111 ± 8 pmol/mg protein, respectively, Figure 57 B). 3-OMD was only detectable in patient 1 and 2 derived neurons, with concentrations of 566 ± 165 and 557 ± 162 pmol/mg protein, respectively. 3-OMD was absent in control neurons (Figure 57 D). Taken together, these dopaminergic neurons derived from AADC deficiency patients have a dopamine pathway profile that recapitulates what is seen in the CSF profile of AADC deficiency patients, where there's a high level of 3-OMD and low/absent dopamine, HVA and DOPAC.

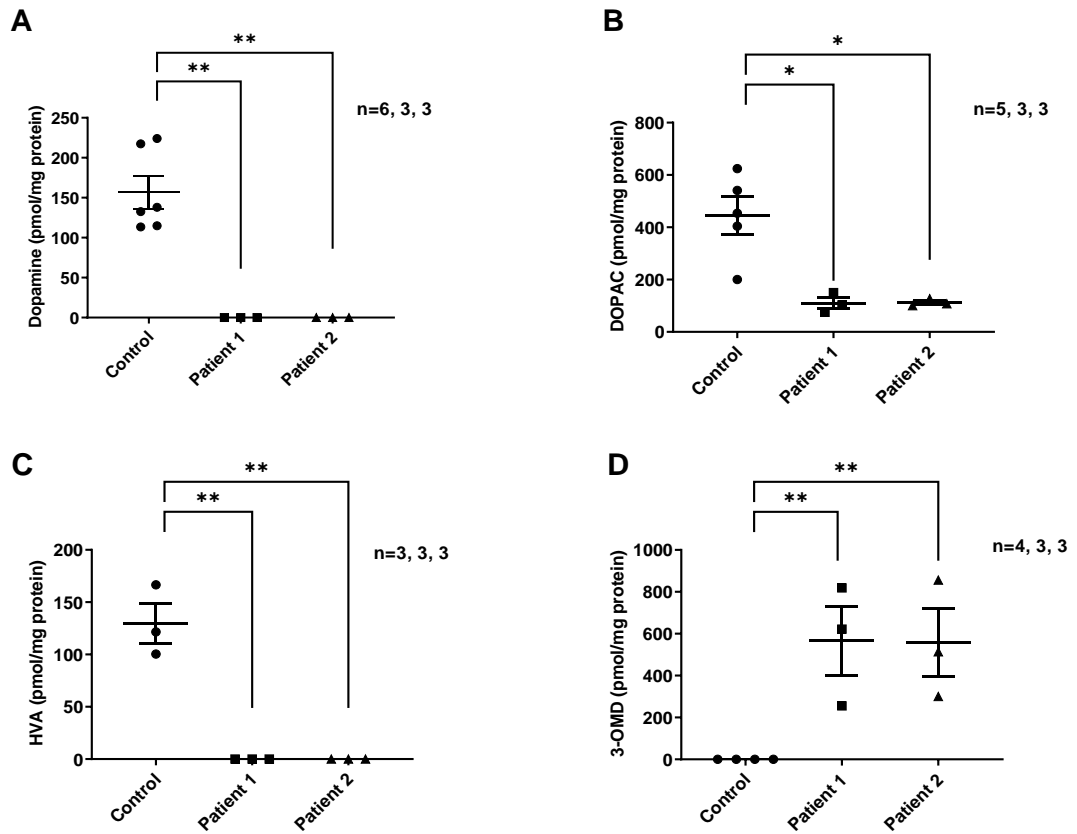


Figure 57 Dopamine metabolites in AADCD patient-derived dopaminergic neurons. Dopamine, DOPAC, HVA and 3-OMD were measured in extracellular cell culture media from AADCD patient-derived iPSC dopaminergic neurons and compared to iPSC dopaminergic neurons carrying functional DDC gene. Data are normalised to protein concentration and expressed as mean \pm SEM. A one-way ANOVA was used to compare the means. n = number of experimental repeats. * $p < 0.05$. ** $p < 0.01$

7.3.2. Lentivirus gene rescue of *DDC* gene

In this preliminary experiment, a lentivirus vector carrying the gene for AADC enzyme was used to rescue *DDC* gene expression in the iPSC dopaminergic neurons analysed above, derived from two AADC patients, patient 1 and 2. The lentivirus constructs were generated, validated, and transduced by the collaborators and increased activity of AADC was confirmed in *DDC* lentivirus treated patients' neurons (Krämer, 2019, PhD thesis, UCL). In this experiment, the patient-derived dopaminergic neurons were treated with either a lentivirus vector not carrying *DDC* gene insert (mock, M) or a lentivirus carrying a copy of the *DDC* gene (lentivirus, L). Following transduction, extracellular dopamine metabolites were analysed using HPLC-ED to assess the effect of ectopic expression of *DDC* gene. When the resulting HPLC-ED chromatograms were analysed, DOPAC and 3-OMD represented the most distinct integrated peaks, therefore the analysis in this section was restricted to comparing DOPAC and 3-OMD.

The patient-derived neurons showed a pattern of dysregulated dopamine metabolism that is characteristic of AADC, with low levels of DOPAC and high levels of 3-OMD compared to control neurons (Figure 57). When treated with mock (M) lentivirus, the patient derived neurons exhibited the characteristic AADC profile of low levels of DOPAC and high levels of 3-OMD when compared to control dopaminergic neurons (Figure 58). This finding confirms that the lentivirus construct did not interfere with the characteristic AADC disease phenotype.

Following transduction with the lentivirus carrying a copy of the *DDC* gene (lentivirus, L), both lines of patient-derived dopaminergic neurons showed an

increase in the mean level of DOPAC however, the increase was not statistically significant (patient 1: $M= 148 \pm 18$ pmol/mg, $L= 252 \pm 74$ pmol/mg. Patient 2: $M= 93 \pm 30$ pmol/mg, $L= 140 \pm 54$ pmol/mg. Figure 58 A). In contrast, there was a mean decrease in 3-OMD levels in both patient-derived dopaminergic neurons following *DDC* gene expression however, the decrease was only statistically significant for patient 1 (patient 1: $M= 1109 \pm 124$ pmol/mg $L= 392 \pm 106$ pmol/mg, $p = 0.001$. Patient 2: $M= 530 \pm 187$ pmol/mg $L= 257 \pm 63$ pmol/mg. Figure 58 B).

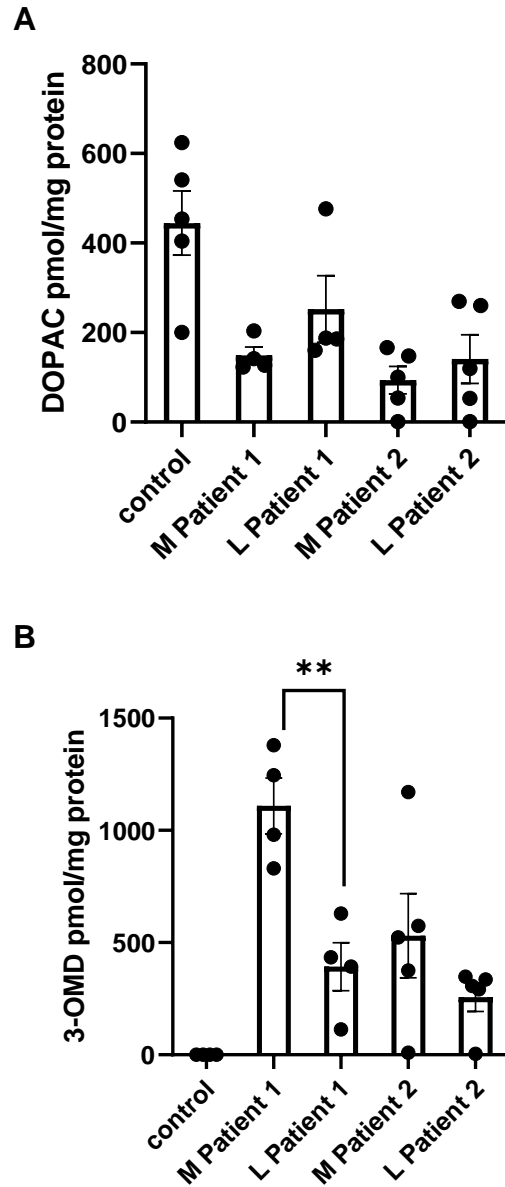


Figure 58 *DDC* gene rescue of AADCDD dopaminergic neurons. Extracellular (A) DOPAC and (B) 3-OMD levels in dopaminergic neurons derived from 2 AADCDD patients following transduction with a lentivirus carrying either *DDC* gene or a mock gene. The results are compared to dopaminergic neurons not carrying any mutations in the *DDC* gene. Results are expressed as ratio to protein concentration and presented as mean \pm SEM of $n = 5$ experimental repeats. An unpaired Student's t-test was used to test for significance. M= mock gene. L = *DDC* gene. ** $p = 0.001$.

7.3.3. L-DOPA as potential therapy for AADC

AADC patients are generally considered to be L-DOPA-unresponsive, as they do not respond well to treatment with the dopamine precursor, L-DOPA. Patients 1 and 2 carry different mutations on the *DDC* gene. The homozygous missense mutations (Arg347Gly) in patient 1 appear to cause a loss-of-function in AADC. Patient 2 however, carries a compound heterozygous mutation on *DDC*, with one allele carrying a missense mutation (Cys100Ser) and the other carrying a nonsense mutation (Arg7*), resulting in an early stop codon. The Cys100Ser mutation in patient 2 changes a -SH functional group for an -OH. This means that the AADC enzyme may still retain the activity, at least partially, given the similar chemical properties of these two functional groups. Thus, through recombinant enzymology studies, patient 2 AADC appeared to retain some residual activity for its substrate, L-DOPA, as evident from a catalytic efficiency (K_{cat}/K_m) of 16 (compared to wild-type catalytic efficiency for L-DOPA of 69, Rossignoli *et al.* 2021). This prompted the question of whether dopamine synthesis in patient 2 could be rescued with L-DOPA supplementation. Therefore, dopaminergic neurons derived from control, patient 1 and patient 2 were treated with 80 μ M L-DOPA and extracellular levels of HVA, a key dopamine metabolite, was measured. The analysis was focused on HVA because it represented the most distinct integrated chromatographic peak from the HPLC-ED analysis for this experiment.

Under basal conditions, mean level of HVA in control-derived dopaminergic neurons was 202 ± 30 pmol/mg protein. Following L-DOPA

treatment, a 10-fold increase was observed in control-derived dopaminergic neurons (2484 ± 364 pmol/mg protein, $p = <0.0001$, Figure 59). For patient 1-derived dopaminergic neurons, which had negligible recombinant AADC enzyme activity, HVA was undetectable both under basal conditions and following L-DOPA treatment. Interestingly however, in patient 2-derived neurons, which retained residual recombinant AADC enzyme activity, and under basal conditions had no detectable HVA levels, following L-DOPA treatment HVA was detected (927 ± 67 pmol/mg, $p = 0.0002$, Figure 59).

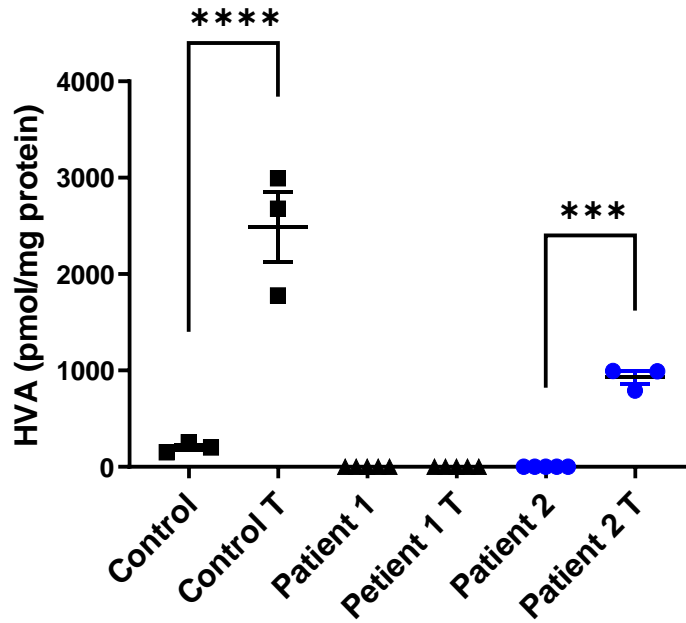


Figure 59 Dopamine metabolites in L-DOPA treated AADC⁰ dopaminergic neurons. Extracellular HVA was measured in iPSC dopaminergic neurons derived from two patients carrying different DDC gene mutations and compared to control iPSC dopaminergic neurons carrying functional DDC gene. Data expressed as ratio to protein concentration and represent mean \pm SEM (n=3, 3, 5, 5, 4, 4 experimental repeats, respectively). An unpaired Student's t-test was used to test for significance. ****p = <0.0001. *** p = 0.0002.

7.4. Discussion

The suitability of any disease model is dependent on its ability to recapitulate what is seen in disease pathology. In AADC_D, clinical diagnosis is based on CSF profile of low/absent dopamine and its metabolites HVA and DOPAC, and serotonin and its metabolite 5-HIAA. Patients also exhibit high levels of 3-OMD, L-DOPA and 5-HTP. Patient-derived iPSC dopaminergic neurons developed in this study exhibited impaired dopamine metabolism as evident by an extracellular neurotransmitter profile (often used as an analogue to CSF profiling) of absent dopamine and HVA, low levels of DOPAC and significantly higher levels of 3-OMD (Figure 57). In addition, extracellular 5-HIAA was undetectable in these cells, the main serotonin metabolite. Therefore, these cells present a suitable dopaminergic neuronal model for AADC_D, as they possess a defective dopamine metabolism reflecting that seen in AADC_D patient CSF profile.

Because of the monogenic nature of AADC_D, gene therapy presents a hopeful therapeutic approach. One of the ways the success of gene therapy is evaluated is through analysis of CSF neurotransmitter profile. Analysis of neurotransmitter profile of extracellular cell culture medium of iPSC-derived neurons can be used as an analogue. High levels of 3-OMD are characteristic of AADC_D phenotype, a result of the block on L-DOPA conversion to dopamine. Therefore, excess L-DOPA is alternatively converted to 3-OMD. In patient 1-derived dopaminergic neurons, there was a significant decrease in 3-OMD levels following lentiviral transfection with *DDC* gene, pointing to a degree of restoration of AADC enzyme activity (Figure 58 B). Patient 2 however, showed a decrease in

3-OMD however the results did not reach statistical significance. The differences in response to gene transfection between patients 1 and 2 were also seen between patients in different AADC gene therapy trials. The first gene therapy clinical trial for AADC took place in Taiwan in 2012. The trials involved infusing four patients with confirmed AADC with an adeno-virus associated gene vector. Following gene therapy, 3 of the 4 patients CSF profile exhibited an increase in HVA (Hwu *et al.* 2012). Chien and colleagues (2017) conducted another gene therapy trial on 10 AADC paediatric patients using adeno-virus associated gene vector. Following 12 months, 8 of the patients experienced an increase in CSF HVA levels. No change was observed in 3-OMD levels and only two patients exhibited mild increase in 5-HIAA (Chien *et al.* 2017). Another adeno-virus vector based gene therapy trial was conducted in Japan in 2019 by Kojima and colleagues. This study included 6 AADC patients and following 1 month after gene therapy, only 3 patients showed mild elevations in HVA (Kojima *et al.* 2019). Although the work presented in this experiment requires further validation, the results obtained demonstrate a successful pilot study for the feasibility of ectopic expression of *DDC* to rescue AADC function in iPSC dopaminergic neurons derived from AADC patients.

L-DOPA as a treatment for AADC is only effective for a very small fraction of AADC patients therefore, it is generally considered that AADC patients are L-DOPA-unresponsive (Wassenberg *et al.* 2017). Recombinant enzyme studies revealed that patient 2 AADC enzyme retained some catalytic activity, approximately one-quarter of the catalytic efficiency of the wild-type enzyme. It was therefore hypothesised that incubation of patient 2 cells with

exogenous L-DOPA would result in increased dopamine metabolism. This resulted in restoration of dopamine metabolism in patient 2-derived neurons, reflected by increased HVA level, demonstrating the importance of understanding the consequence of the different gene mutations on the enzyme activity (Figure 59).

To conclude, this study demonstrates the usefulness of generation of patient-derived dopaminergic neurons as a tool for exploring disease mechanisms and potential therapeutics. Furthermore, it demonstrates a proof of concept for the potential use of lentiviral gene rescue in AADC. Finally, this study establishes a personalised approach for decoding which AADC patient may benefit from L-DOPA therapy, further confirming the importance of understanding the effects of specific mutations on enzyme activity to decide the benefit of certain therapeutics in inborn error of metabolism.

**Chapter 8. Assessing Dopamine Metabolism in an iPSC Dopaminergic
Neuronal Model for Parkinson's Disease**

8.1. Introduction

The use of human induced pluripotent stem cells (iPSC) in research has become a great asset in understanding cellular physiology and pathology. This has led to the development of several methodologies to differentiate iPSC into different types of cells, including mature dopaminergic neurons (Takahashi and Yamanaka 2006; Liu *et al.* 2020). The current dopaminergic neuronal differentiation protocols are expensive, time consuming and offer a low efficiency of dopaminergic neuron generation (10-70%, Marton and Ioannidis 2019). Dr Gurvir Viridi and colleagues (The Francis Crick Institute, London, UK) have developed a new protocol for iPSC differentiation into dopaminergic neurons based on a protocol by Kriks *et al.* (2011). This protocol differs from previous protocols in the omission of the use of recombinant brain-derived neurotrophic factors (BDNF) and glial cell-derived neurotrophic factors (GDNF), which facilitates cell differentiation. The use of these factors to differentiate cells into dopaminergic neurons increases the differentiation period and is economically costly. The newly developed protocol resulted in more than 80% enrichment of TH⁺ cells, a marker of dopaminergic neurons, in a relatively short period of time and was more economically favourable. The resultant dopaminergic neurons express voltage-gated calcium channels, can spontaneously oscillate calcium, and have the electrophysiology of mature neurons. They also express the dopamine transporter, another characteristic of dopaminergic neurons (Dr Gurvir Viridi and colleagues, The Francis Crick Institute, London, UK). Functional dopamine metabolism is also a key characteristic of dopaminergic neurons. A condition for any dopaminergic neuronal model is the ability to synthesize and metabolise dopamine (Chinta and Andersen 2005). Therefore, assessing

dopamine metabolism in the iPSC dopaminergic neurons developed by Dr Viridi and colleagues (The Francis Crick Institute, London, UK) is an important step to further verify their suitability as a dopaminergic neuronal model and their use in PD research.

The development of iPSC dopaminergic neurons derived from PD patient can be a great asset in understanding the mechanism of disease. About 15% of PD cases are familial, meaning they are linked to genetic mutations. Developing dopaminergic neurons from familial PD patients can offer an insight into the consequences of these mutations and give clues to disease mechanism. Mutations in PTEN-induced kinase 1 (PINK1) are considered one of the most common causes of familial PD (Balestrino and Schapira 2020; Valente *et al.* 2004). PINK1 functions in mitochondrial quality control pathways by tagging and identifying damaged/dysfunctional mitochondria. This allows the removal of these mitochondria by lysosomes (Ge *et al.* 2020). However, studies of PINK1 mutations in cellular and animal models suggest that it may also have functions in regulation of the dopamine pathway (Lu *et al.* 2018; Maynard *et al.* 2020). The mechanistic consequence of PINK1 mutations on cellular pathology, specifically dopamine metabolism, is still unclear.

Thus, the **aims** of this preliminary study were

- To compare dopamine metabolism at two differentiation time points of a novel protocol for differentiation of iPSC into dopaminergic neurons
- To assess the cells' response to L-DOPA stimulation
- To gain insight into the mechanism of PD cellular pathology by analyzing dopamine metabolism in iPSC dopaminergic neurons

derived from PD patients carrying different mutations in the *PINK1* gene

8.2. Methods

8.2.1. Generation of iPSC dopaminergic neuronal model

The dopaminergic neuronal model used in this study were generated and maintained by the collaborator, Dr Gurvir Virdi (The Francis Crick Institute, London, UK). In brief, the dopaminergic neurons were derived from three independent control iPSC lines and differentiated for three and four weeks. Differentiation was triggered by incubating the iPSC in a chemically defined growth medium composed of DMEM/F12, N2 supplement, neurobasal, B27 supplement, L-glutamine, non-essential amino acids, penicillin-streptomycin, β -mercaptoethanol and insulin. After 2 days, the media was supplemented with the small molecules SB431542, dorsomorphin, CHIR99021 and purmorphamine. SB431542 is a transforming growth factor- β (TGF- β) inhibitor which suppresses cellular proliferation. Dorsomorphin is an inhibitor of AMP kinase which promotes neural induction of human stem cells. CHIR99021 is an inhibitor of glycogen synthase kinase 3 (GSK-3) that promotes reprogramming of somatic cells to iPSCs. Purmorphamine is an activator of the hedgehog pathway which promotes neuronal differentiation.

On day 8, CHIR99021, and SB431542 were removed. On day 19, cells were either cryopreserved or on day 20 they were terminally differentiated using N2B27 medium supplemented with compound E and Y-27632 dihydrochloride. Compound E accelerates the differentiation of neuronal stem cells and Y-27632 dihydrochloride improves survival of stem cells during initiation of differentiation. The cells were then maintained in the same media.

For patient-derived dopaminergic neuronal model, iPSCs were derived from 3 separate sources. The first source was an early-onset PD patient with a homozygous mutation in the *PINK1* gene (W90L). This mutation is in exon 1 and causes a frameshift mutation which leads to a premature stop codon. This patient also carries a heterozygous mutation in the gene *Parkin* (R275W). The second source of iPSC was the parent of the PD patient, who is unaffected, and is a heterozygote for the same mutation in the *PINK1* gene (W90L). The third source of iPSC is a commercial iPSC *PINK1* mutation line carrying homozygous point mutation in *PINK1* (I368N, Ando *et al.* 2017).

8.2.2. HPLC sample preparation

The dopaminergic neurons were incubated in phenol-free “N2B27” medium for 24 hours with or without the presence of 80 μ M L-DOPA. The choice for the use of 80 μ M concentration of L-DOPA was made by the collaborators based on the assumption that this was a sufficient concentration to stimulate dopamine metabolism in iPSC dopaminergic neurons without inducing cellular toxicity (Rossignoli *et al.* 2021).

After 24 hours, media was processed as described in section 2.4.2.1 and stored at -80 °C until analysis. For intracellular sample, cells were collected and processed as described in section 2.4.2.2 and stored at -80 °C for analysis.

8.2.3. HPLC-ED analysis

Samples were analysed using the method described in Chapter 3.

8.3. Results

8.3.1. Comparison of basal dopamine metabolism between 3 and 4-weeks differentiated dopaminergic neurons:

Using the HPLC-ED method developed in chapter 3, dopamine and its metabolites were compared at two different differentiation time points (3 and 4-weeks), both intracellularly and extracellularly. In this experiment, the comparisons were made with the assumption of similar cell count in each cell preparation as the cells in each condition were grown and differentiated under the same experimental conditions. Therefore, the results in this chapter are expressed as nmol/L due to the lack of protein measurement and/or cell count.

Under basal conditions, only the main dopamine metabolite, DOPAC, was detectable in the extracellular media and intracellular lysate of control iPSC dopaminergic neurons at both differentiation time points. Compared to 4-weeks differentiated, 3-weeks differentiated dopaminergic neurons had significantly lower levels of DOPAC, both intracellularly and extracellularly (Extracellularly: 3-weeks = 1072 ± 24 nmol/L, 4-weeks = 2212 ± 56 nmol/L, $p = <0.0001$ and intracellularly: 3-weeks = 86.5 ± 9 nmol/L, 4-weeks = 212.6 ± 13 nmol/L, $p = 0.0012$, Figure 60).

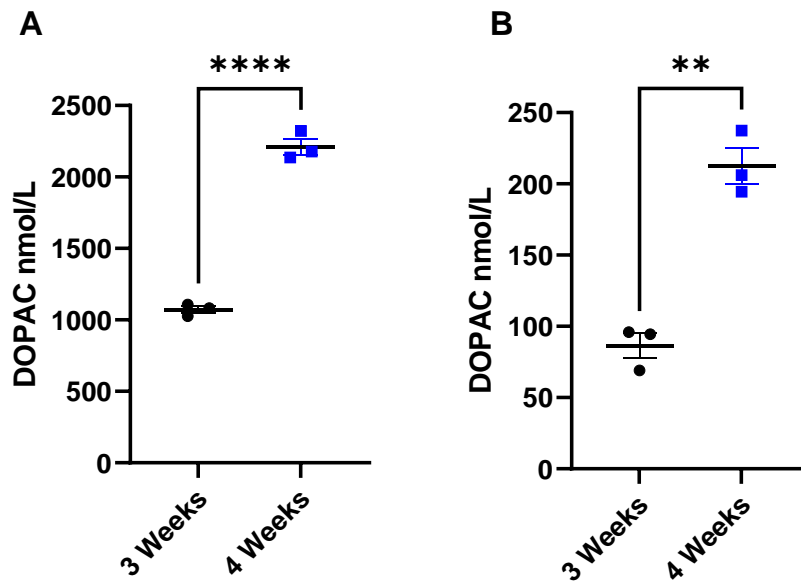


Figure 60 Basal dopamine metabolism at different differentiation time points.

(A) Extracellular and (B) intracellular DOPAC was measured in iPSC dopaminergic neurons differentiated for 3-weeks and 4-weeks. Results represent mean \pm SEM of 3 independent control iPSC lines. Unpaired Student's t-test was used to test for significance. **** $p < 0.0001$, ** $p = 0.001$

8.3.2. Effect of L-DOPA stimulation on 3- and 4-week differentiated dopaminergic neurons:

The dopamine precursor L-DOPA, commercially known as levodopa, is the gold standard treatment in PD. It functions to stimulate dopamine synthesis. For a cellular model to correctly model PD, its response to L-DOPA should be investigated. Therefore, the cells were treated with 80 μ M L-DOPA for 24 hours then dopamine metabolism was analysed at different time points of the differentiation protocol.

The levels of dopamine were comparable both extracellularly and intracellularly between 3- and 4-week differentiated dopaminergic neurons (Figure 61 A and B, Table 10 and Table 11). The levels of extracellular DOPAC and HVA were highest in the 4-week differentiated dopaminergic neurons (Figure 61 A, Table 10) In addition, intracellular DOPAC levels were also higher in 4-week differentiated dopaminergic neurons however, HVA levels were similar (Figure 61 B, Table 11).

Dopamine turnover can be used to compare the rate of dopamine metabolism between the two differentiation time points. It is calculated as the ratio of dopamine metabolites to dopamine (DOPAC+HVA/dopamine). This can offer a more accurate comparison as it was not possible to normalise the results to a cell count or a protein baseline. The mean rate of dopamine turnover was higher in 4-week cells compared to 3-week, both extracellularly and intracellularly. However, the results reached statistical significance only in intracellular fractions (Figure 62, Table 12).

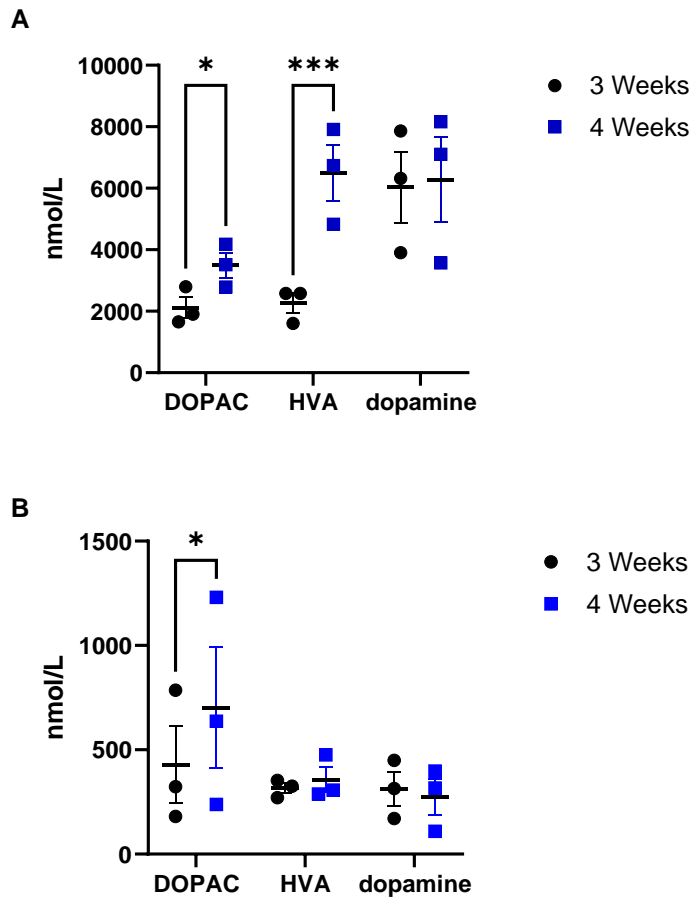


Figure 61 Dopamine metabolism following L-DOPA stimulation at different dopaminergic differentiation time points. (A) Extracellular and (B) intracellular dopamine metabolites measured in dopaminergic neurons differentiated for 3- and 4-weeks, then treated with 80 μ M L-DOPA for 24 hours. Results represent mean \pm SEM of 3 independent control iPSC lines. An unpaired Student's t-test was used to test for significance. Extracellular * $p = 0.04$, *** $p = 0.0001$. Intracellular * $p = 0.02$

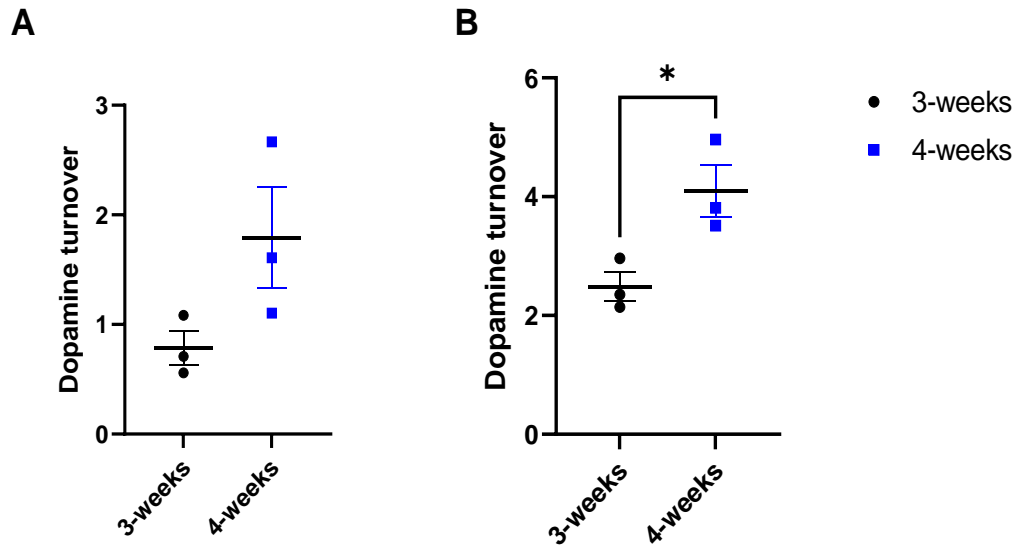


Figure 62 Dopamine turnover following L-DOPA stimulation at different dopaminergic differentiation time points. Rate of (A) extracellular and (B) intracellular dopamine turnover in dopaminergic neurons differentiated for 3- and 4-weeks treated with 80 μ M L-DOPA for 24 hours. Results represent mean \pm SEM of 3 independent control iPSC lines. An unpaired Student's t-test was used to test for significance. * $p = 0.03$

<i>Extracellular</i>	<i>3-weeks</i>	<i>4-weeks</i>	<i>p-value</i>
<i>DOPAC</i>	2116 ± 345	3493 ± 401	0.04
<i>HVA</i>	2253 ± 325	6494 ± 898	0.0001
<i>Dopamine</i>	6029 ± 1153	6277 ± 1387	ns

Table 10 Extracellular dopamine metabolites. Presented as mean ± SEM nmol/L of 3 independent control iPSC lines. An unpaired Student's t-test was used to test for significance. ns: not significant

<i>Intracellular</i>	<i>3-weeks</i>	<i>4-weeks</i>	<i>p-value</i>
<i>DOPAC</i>	429 ± 182	702 ± 288	0.02
<i>HVA</i>	316 ± 24	356 ± 59	ns
<i>Dopamine</i>	312 ± 80	274 ± 12.8	ns

Table 11 Intracellular dopamine metabolites. Presented as mean ± SEM nmol/L of 3 independent control iPSC lines. An unpaired Student's t-test was used to test for significance. ns: not significant

<i>Dopamine turnover</i>	<i>3-weeks</i>	<i>4-weeks</i>	<i>p-value</i>
<i>Extracellular</i>	0.7 ± 0.1	1.8 ± 0.4	ns
<i>Intracellular</i>	2.5 ± 0.2	4.1 ± 0.4	0.033

Table 12 Dopamine turnover. Presented as mean ± SEM nmol/L of 3 independent control iPSC lines. An unpaired Student's t-test was used to test for significance. ns: not significant

8.3.3. Dopamine metabolism in iPSC dopaminergic neuronal model for PD:

Based on the biochemical analysis of the cells, the differentiation protocol established by Dr Viridi and colleagues (The Francis Crick Institute, London, UK) allows the production of mature dopaminergic neurons. Therefore, the protocol can be used to develop a suitable model for PD through differentiation of iPSC dopaminergic neurons derived from patients carrying mutations in genes implicated in PD. Loss-of-function in the *PINK1* gene represents the second most common cause for early onset PD. PINK1 facilitates multiple functions that governs mitochondrial homeostasis, dynamics and regulation of mitophagy (Wang *et al.* 2020b). In order to gain mechanistic insights on the cellular pathology of familial PD, dopaminergic neurons were differentiated for 4-weeks from three independent cell sources carrying mutations in their *PINK1* gene then dopamine metabolism was analysed and compared to control dopaminergic neurons.

Under basal conditions, only DOPAC was detectable in the extracellular media and intracellular lysate of PINK1 patient dopaminergic neurons (Figure 63), consistent with what was seen in control cells (Figure 60). Extracellular DOPAC was significantly higher in PINK1 patient dopaminergic neurons compared to control (control = 2212 ± 56 nmol/L, patient = 3130 ± 22 nmol/L, $p = 0.0001$. Figure 63 A). In contrast, intracellular DOPAC was significantly lower in PINK1 patient dopaminergic neurons compared to control (control = 212 ± 12 nmol/L, patient = 68 ± 6 nmol/L, $p = 0.0006$. Figure 63 B).

The response of the patient derived neurons to L-DOPA was also investigated. Control and PINK1 patient neurons were treated with 80 μ M L-

DOPA for 24 hours then dopamine metabolism was analysed in extracellular media and intracellular lysate. Extracellular mean levels of DOPAC, HVA and dopamine were comparable between control and PINK1 patient neurons. Intracellularly however, the mean level of DOPAC was higher in control compared to PINK1 patient neurons, although the difference did not reach statistical significance. On the other hand, intracellular HVA and dopamine were comparable between control and PINK1 patient neurons (Figure 64, Table 13, Table 14).

To accurately compare dopamine metabolism between control and PINK1 patient neurons, dopamine turnover was calculated following treatment with L-DOPA. The mean rate of extracellular dopamine turnover was similar between control and PINK1 patient neurons. Intracellularly however, the mean rate of dopamine turnover was lower in PINK1 patient neurons, although the result did not reach statistical significance (Figure 65, Table 15).

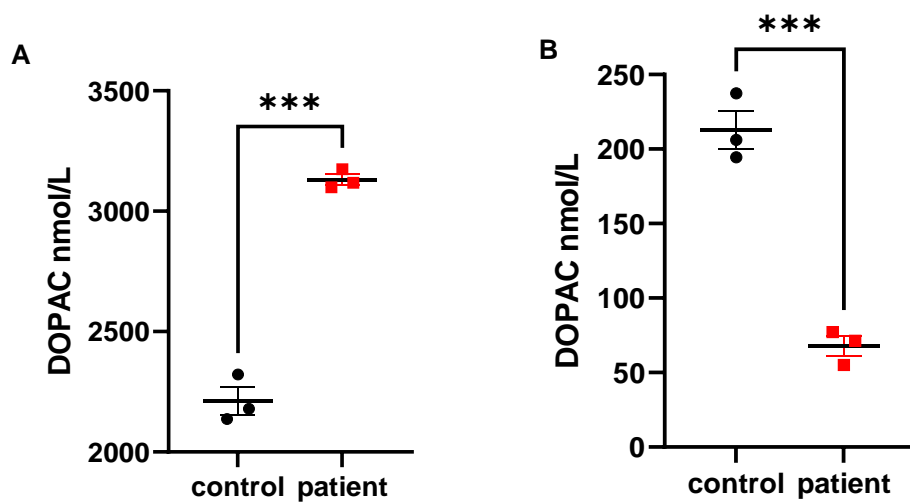


Figure 63 Basal dopamine metabolism in control and PINK1 patient dopaminergic neurons. (A) Extracellular and (B) intracellular DOPAC was measured in dopaminergic neurons derived from patients carrying mutations in their PINK1 gene and matched controls. Results represent mean \pm SEM of 3 independent iPSC lines for control, and 3 independent iPSC lines carrying PINK1 mutations. An unpaired Student's t-test was used to test for significance. A) $p = 0.001$, B) $p = 0.0006$

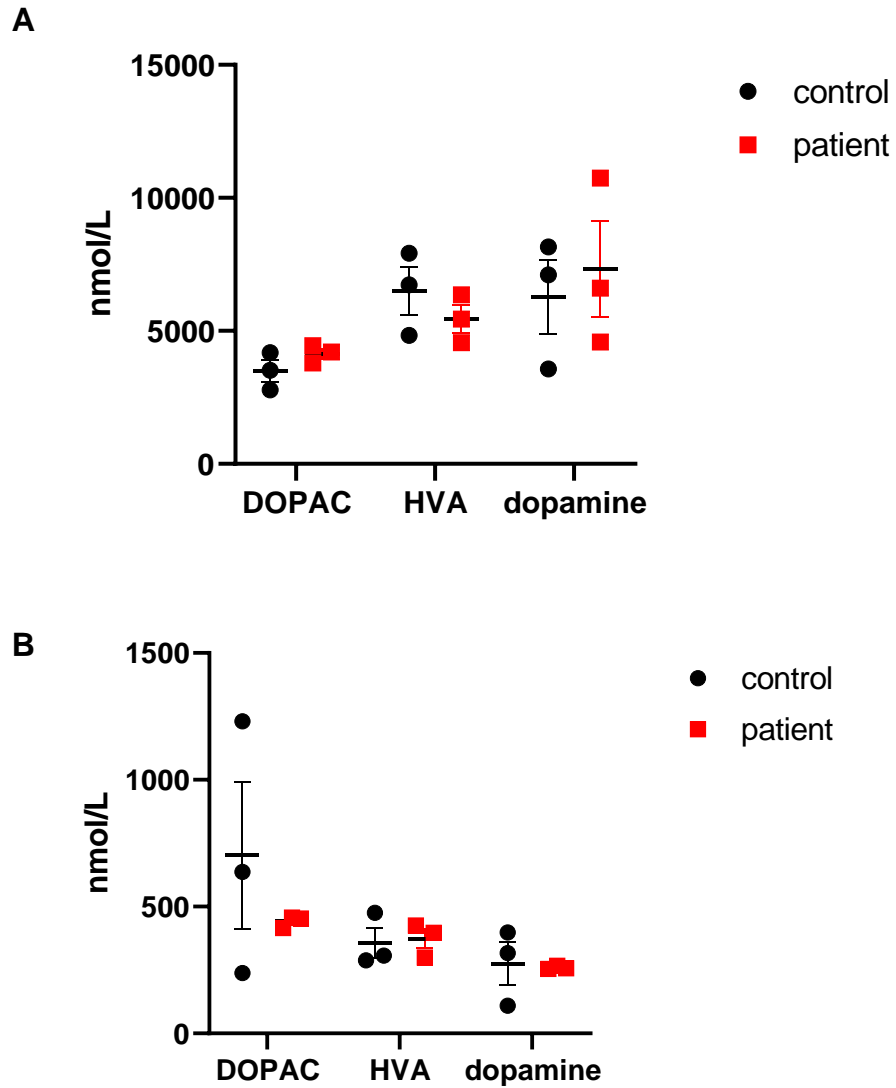


Figure 64 Dopamine metabolism following L-DOPA stimulation in control and PINK1 patient neurons. (A) Extracellular and (B) intracellular dopamine metabolites were measured in dopaminergic neurons from control and PINK1 patients following incubation with 80 μ M L-DOPA for 24 hours. Results represent mean \pm SEM of 3 independent control iPSC lines and 3 independent PINK1 mutation iPSC lines. An unpaired Student's t-test was used to test for significance.

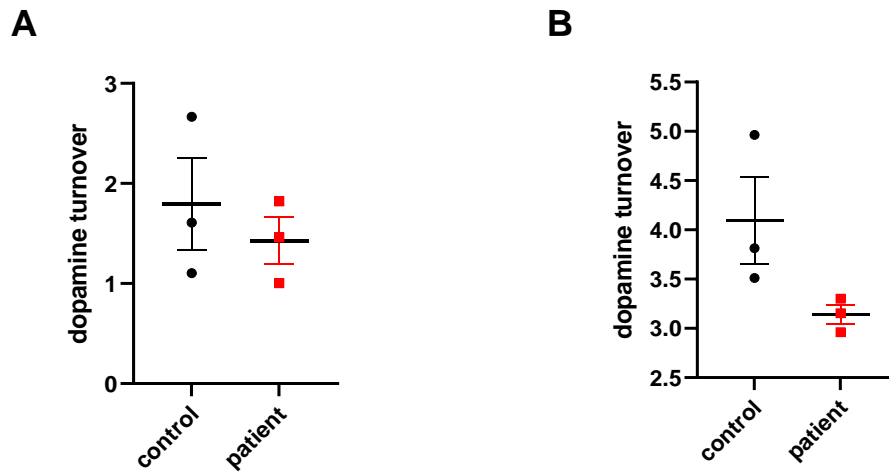


Figure 65 Dopamine turnover in L-DOPA treated dopaminergic neurons. Rate of (A) extracellular and (B) intracellular dopamine turnover in dopaminergic neurons from control and PINK1 patients treated with 80 μ M L-DOPA for 24 hours. Results represent mean \pm SEM of 3 independent control iPSC lines and 3 independent PINK1 mutation iPSC lines. An unpaired Student's t-test was used to test for significance.

<i>Extracellular</i>	<i>control</i>	<i>PINK1 patient</i>	<i>p-value</i>
<i>DOPAC</i>	3492 ± 401	4147 ± 189	ns
<i>HVA</i>	6494 ± 898	5452 ± 518	ns
<i>Dopamine</i>	6276 ± 1387	7313 ± 1813	ns

Table 13 Extracellular dopamine metabolites. Presented as mean ± SEM nmol/L of 3 independent control and 3 independent PINK1 patients iPSC lines. An unpaired Student's t-test was used to test for significance. ns: not significant

<i>Intracellular</i>	<i>control</i>	<i>PINK1 patient</i>	<i>p-value</i>
<i>DOPAC</i>	702 ± 288	441 ± 13	ns
<i>HVA</i>	356 ± 59	374 ± 38	ns
<i>Dopamine</i>	274 ± 85	259 ± 4	ns

Table 14 Intracellular dopamine metabolites. Presented as mean ± SEM nmol/L of 3 independent control and 3 independent PINK1 patients iPSC lines. An unpaired Student's t-test was used to test for significance. ns: not significant

<i>Dopamine turnover</i>	<i>control</i>	<i>PINK1 patient</i>	<i>p-value</i>
<i>Extracellular</i>	1.8 ± 0.46	1.4 ± 0.23	ns
<i>Intracellular</i>	4.1 ± 0.4	3.1 ± 0.1	ns

Table 15 Dopamine turnover. Presented as mean ± SEM nmol/L of 3 independent control and 3 independent PINK1 patients iPSC lines. An unpaired Student's t-test was used to test for significance. ns: not significant

8.4. Discussion:

The work presented in this chapter provides a proof of concept for use of the cells developed by Dr Virdi and colleagues (The Francis Crick Institute, London, UK) as a model for mature dopaminergic neurons, and as a disease model for PD. Functional dopamine metabolism is the hallmark of the dopaminergic neuronal phenotype (Chinta and Andersen 2005). Therefore, for development and use of dopaminergic cellular models, analysis of their dopamine metabolism is important. The results of this study show that the dopaminergic neurons developed by Dr Virdi and colleagues are able to produce and metabolise dopamine both under basal conditions and following stimulation with L-DOPA. In addition, these cells are able to do so as early as 3-weeks of differentiation, although their capacity increases following 4 weeks of differentiation as evident by the significant increase in production of extracellular DOPAC and HVA and intracellular dopamine turnover (Figure 61 A, Figure 62 B). This is a possible indication that the expression of enzymes of the dopamine pathway increases beyond the 3-week mark as a result of continued differentiation, similar to what was seen following differentiation of SH-SY5Y and LUHME cells (Chapter 4, Alrashidi *et al.* 2021; Tüshaus *et al.* 2021; Presgraves *et al.* 2004). Finally, as the main serotonin metabolite, 5-HIAA, was undetectable, this suggests that these cells possess a specific dopaminergic lineage. This was in contrast to the findings in Chapter 4, where SH-SY5Y cells, which are commonly cited and used as a dopaminergic neuronal model, appear to possess a mixed serotonergic and dopaminergic phenotype evident by their basal expression of TH and production of 5-HIAA. Cells exhibiting mixed dopaminergic

and serotonergic phenotypes is also one of the issues facing iPSC dopaminergic differentiation (Arenas *et al.* 2015).

PINK1 mutations are associated with one of the most common forms of familial PD (Wang *et al.* 2020b). Dysregulated dopamine metabolism is one of the key pathologies of PD (Meiser *et al.* 2013). PINK1 is a mitochondrial protein that functions in mitochondrial quality control through the initiation of mitophagy to remove damaged mitochondria (Wang *et al.* 2020b). However, a number of studies suggest that PINK1 may also play a role in regulation of TH expression and consequently, dopamine metabolism. For example, Lu and colleagues (2018) demonstrated that PINK1 knockdown in murine mesencephalic cells (MN9D) reduced dopamine expression and suppressed TH protein expression. On the other hand, PINK1 overexpression in MN9D cells resulted in increased TH protein expression. These findings imply that PINK1 may possess a regulatory function over TH expression (Lu *et al.* 2018). Similar findings were demonstrated by Matsui and colleagues (2010) following analysis of dopamine metabolism in brain tissue of homozygous and heterozygous *PINK1* mutant medaka fish (*Oryzias latipes*). DOPAC levels were found to be decreased in *PINK1* mutant fish compared to control, suggesting that PINK1 might be required for proper dopamine metabolism in medaka fish (Matsui *et al.* 2010). In addition, Maynard and colleagues (2020) have demonstrated reduced protein expression of TH protein in the brain tissue from mice carrying homozygous mutations in *PINK1* (Maynard *et al.* 2020). The protocol developed by Dr Viridi and colleagues allowed the preliminary study of the effect of loss of PINK1 on dopamine metabolism in a disease model generated from PD patients carrying mutations in PINK1. Under

basal condition, significantly lower in intracellular DOPAC in PINK1 patient dopaminergic neurons was documented compared to control (Figure 63). This may potentially be a result of reduced intracellular dopamine turnover in PINK1 patient neurons, although the results did not reach statistical significance (Figure 65). It is of interest to note here that the iPSC derived dopaminergic neurons analysed in this study carried different PINK1 mutations. As demonstrated in section 7.3.3) different gene mutations can have different functional consequences on the enzyme that may result in different pathological mechanisms. Therefore, this should be kept in mind when interpreting the results from this study. However, the result of this preliminary analysis supports the hypothesis that PINK1, although a mitochondrial associated protein, has other cellular functions that may extend to modulation of dopamine metabolism. Interestingly, the loss of function of another mitochondrial protein, respiratory chain complex I, was also shown to affect dopamine metabolism. In proliferative SH-SY5Y cells, it was shown that inhibition of mitochondrial complex I using rotenone led to significant increase in dopamine breakdown (de la Fuente *et al.* 2017). Taken together, this finding further highlights the importance of functional mitochondria for proper dopamine metabolism.

In summary, the iPSC dopaminergic neuronal differentiation protocol developed by Dr Viridi and colleagues (The Francis Crick Institute, London, UK) results in neurons that are functionally dopaminergic with higher efficiency and at a lower cost. The protocol also allows the generation of dopaminergic neuronal models from patients carrying mutations in genes associated with PD risk as a valuable tool that offers insight into the pathological mechanism of disease.

Chapter 9. General Discussion

9.1. Discussion:

Parkinson's disease (PD) is the second most common neurodegenerative disorder; a group of disorders that result from progressive damage to the structure or function of neurons in the brain (Dugger and Dickson 2017). In PD, the dopaminergic neurons residing the SN are the most extensively affected subtype of neurons. These neurons control movement by regulating the dopamine system (Chan *et al.* 2010). For reasons yet to be elucidated, a progressive loss of dopaminergic neurons accompanied by dopamine depletion in surviving neurons occurs, resulting in PD (Michel *et al.* 2016). Through investigation of tissues from PD patients, several pathways have been documented to be perturbed (Balestrino and Schapira 2020). Decreased activity of mitochondrial respiratory chain complex I is proposed to be one of the central events in PD cellular pathology (Schapira *et al.* 1990; Parker *et al.* 1989). However, relatively recently, involvement of lysosomal dysfunction is being recognised as another key event. This was highlighted after several studies demonstrated that heterozygous mutation in lysosomal GBA is the highest risk factor for PD (Sidransky 2009). Lysosomal dysfunction in PD is also supported by the presence of aggregates of unfolded and/or misfolded proteins forming the hallmark of PD, Lewy bodies. Lewy bodies are formed as a result of dysregulated protein degradation machinery through the autophagic-lysosomal pathway. In PD diagnosis, the presence of Lewy bodies is considered a marker for neuronal degeneration (Arotcarena *et al.* 2019; Wakabayashi *et al.* 2013). There are many proposed factors that contribute to the specific vulnerability of dopaminergic neurons in PD. These include the added oxidative stress burden of dopamine metabolism, high cytosolic calcium levels and pace-making activity, and iron

levels (Chan *et al.* 2010; Surmeier *et al.* 2017; Oakley *et al.* 2007; Jenner *et al.* 2003). Oxidative dopamine metabolism, which increases the cellular oxidative stress burden, making them more susceptible to any imbalance in the antioxidant defence machinery (Herrera *et al.* 2017a). Glutathione (GSH) is a major antioxidant in the cell, and its functions in dopaminergic neurons specifically are considerably more important due to the oxidative dopamine metabolism. Lower levels of GSH have been documented in the SN brain tissues from PD patients (Sofic *et al.* 1992). In order to understand how disruption of these pathways results or contributes to the neuronal cell death seen in PD, appropriate models are important, both to investigate disease mechanism and to develop potential therapeutics. SH-SY5Y neuronal cell line is one the most commonly used cell lines in PD research (Xicoy *et al.* 2017). The cells are used almost interchangeably in their proliferative and differentiated states, as it has remained unclear whether proliferative cells are a suitable dopaminergic neuronal model. Most studies employ proliferative SH-SY5Y as a model for dopaminergic neurons based on the basal expression of TH, a marker of dopaminergic neurons, without appropriate analysis of whether the dopamine pathway is functional. The work presented in chapter 4 shows that basal dopamine production is absent in proliferative SH-SY5Y cells, despite detectable TH expression. This was in contrast to the presence of basal production of the serotonin metabolite, 5-HIAA (Figure 37) Interestingly however, the cells do possess the ability to synthesize dopamine, as evident from the ability to utilise L-DOPA, the dopamine precursor (Figure 38). Following retinoic acid/tetradecanoylphorbol acetate (RA/TPA) differentiation, it was interesting to find that differentiated SH-SY5Y cells had similar level of TH expression but still lacked the ability to basally produce

dopamine, requiring L-DOPA supplementation (Figure 36). TH expression was shown to double following RA/TPA sequential treatment, which is the reason this differentiation protocol was chosen (Presgraves *et al.* 2004). However, under the experimental conditions of this thesis, TH expression was comparable between proliferative and RA/TPA differentiated SH-SY5Y cells (Figure 36). One reason behind this discrepancy could be due to different responses of SH-SY5Y cells obtained from different sources. Wang and colleagues (2007) have shown that proliferative SH-SY5Y cells sourced from two different laboratories reacted differently to the same differentiation agents. This was seen at the level of TH protein expression, specifically (Wang *et al.* 2007). Another reason behind the relative dopamine-deficient state of both proliferative and differentiated SH-SY5Y cells in this thesis (Figure 37), and the need for L-DOPA supplementation to simulate the pathway (Figure 38), could be due to the nature of dopamine metabolism itself. Dopamine is an important neurotransmitter with vital functions. This means that its production, release and breakdown require tight regulation. This can be through the regulation of the rate limiting enzyme of dopamine production, TH. TH activity is regulated on the level of protein expression, posttranslational modification, and upstream activation signals (phosphorylation/dephosphorylation, Dunkley and Dickson 2019; Dunkley *et al.* 2004). Therefore, stimulation of upstream pathways might be important to trigger the production of dopamine.

These findings raises the question for the need to differentiate SH-SY5Y cells as a requirement to be used as dopaminergic neuronal model (Hong-rong *et al.* 2010). Although the cells are proliferative, they express the neuronal

markers NSE and NeuN, and the specific dopaminergic neuronal marker, TH (Figure 34, Figure 35, Figure 36). The cells also possess the ability to metabolise dopamine (Figure 38). In addition, the finding that under basal conditions, both proliferative and differentiated SH-SY5Y cells were able to produce similar levels of the serotonin metabolite, 5-HIAA, brings forth the question of the true dopaminergic nature of the cells. This is supported by the documentation of the expression of subtypes of the serotonin receptor, 5-HT_{1A} and 5-HT₇, in SH-SY5Y cells (Adeosun *et al.* 2012; Tempio *et al.* 2020; Li *et al.* 2020).

Despite the aforementioned similarities, differentiated SH-SY5Y cells were able to metabolise dopamine at significantly greater rate than proliferative cells (Figure 38). Due to the nature and functions of the dopamine system, the requirement for efficient handling through reuptake, recycle or breakdown is an important feature of mature dopaminergic neurons (Chinta and Andersen 2005). This part of the study concludes that the dopamine system appears more mature in differentiated SH-SY5Y cells and thus, for studies of the dopamine pathway, differentiated SH-SY5Y cells are perhaps better suited. In addition, the lack of basal dopamine production may provide a useful model to study dopamine deficiency states and the evaluation of therapeutic agents, including L-DOPA. Toxic dopamine metabolism is hypothesized to play a role in the selective PD vulnerability towards dopaminergic neurons (Herrera *et al.* 2017a). In chapter 5, incubating proliferative and differentiated SH-SY5Y cells with L-DOPA did not result in any significant changes to mitochondrial respiratory chain activity, lysosomal GBA activity or levels of GSH (Table 5). In this study, cells were exposed to L-DOPA for a relatively short period of time (1 and 3 hours) which

may not have been sufficient to be detrimental to the cells. Allen and colleagues (2013) have shown that 50 μ M L-DOPA increased GSH levels but only after 24 hours (Allen *et al.* 2013). Similar findings were documented in rat PC12 neuronal cells, where cellular toxicity of L-DOPA was documented only after 24-48 hours (Jin *et al.* 2008). However, 100 μ M L-DOPA was shown to be a non-toxic concentration in SH-SY5Y cells (de la Fuente *et al.* 2017). In view of these findings, a number of factors may need to be considered with regards to cellular toxicity to L-DOPA. These may include time of exposure, concentration of the drug and cell type.

In addition to the apparent differences in dopamine metabolism, GBA activity was significantly higher in differentiated SH-SY5Y cells (Figure 39). This could potentially be a result of an induced sphingolipid pathway. Differentiated cell morphology is far more polarised with extended neurites and extensive branching (Figure 33). This may require increased synthesis of cell membrane components, such as ceramides, which are products of the sphingolipid pathway. However, considering the growing number of studies demonstrating a unique, yet still ambiguous, role for GBA in neuronal physiology, the upregulation of GBA activity in differentiated cells may serve another role that is unique to mature neurons. This notion is encouraged by the finding that GBA can modulate the dynamics of mitochondria and lysosomal physical contacts in neurons (Kim *et al.* 2021) and affect lysosomal acidification and cathepsin D (CTSD) maturation (Chapter 6, Yang *et al.* 2020; Bae *et al.* 2015).

One of the major concerns surrounding the use of cell lines is their inherent proliferative, immature nature, which is in contrast to most cells they are used to

model. This issue is further amplified when using proliferative cells to model post-mitotic neurons, which are terminally differentiated early in life and stay this way for decades. This issue is best exemplified when comparing GSH levels in proliferative and differentiated SH-SY5Y cells. GSH is a very unstable molecule requiring tight regulation to maintain its reduced state, which is imperative for its antioxidant and detoxifying functions (Smeyne and Smeyne 2013). When cells are constantly going through different cell cycle stages, it may become difficult to maintain the homeostasis of such unstable molecules. However, once differentiated, the SH-SY5Y cells exhibit better control on GSH levels, as judged by a more consistent GSH level measurements across separate cell preparations (Figure 40).

SH-SY5Y cells, both proliferative and differentiated, are commonly used to study the effects of toxins on cellular physiology (Presgraves et al. 2004; Lopes et al. 2017; Lopes et al. 2010; Simões et al. 2021). However, as demonstrated in chapter 6, there are significant differences in the sensitivity of proliferative and differentiated cells to different toxins (rotenone, bafilomycin A1 and CBE, Table 16). This another example of the differences in the inherent biochemistry of the two cellular phenotypes, despite being of the same cell line. This observation should be highlighted as SH-SY5Y cells are commonly used to create toxin-based models for PD, a disease where environmental toxins are accepted as potential disease trigger (Kalia and Lang 2015; Falkenburger *et al.* 2016).

	Proliferative	Differentiated	p-value
Bafilomycin A1	69	90	0.03
CBE	88	51	0.00025
Rotenone	25	81	<0.0001

Table 16 Percent reduction in CTSD enzyme activity in response to different toxins. Proliferative and differentiated SH-SY5Y cells were treated with either Bafilomycin A1, conduritol B epoxide (CBE) or rotenone then CTSD activity was measured. Results are presented as %reduction relative to control. A Student's t-test was used to compare the means (Chapter 6).

Despite the aforementioned differences, some processes appear to be conserved between proliferative and differentiated SH-SY5Y cells. This is seen in chapter 4 when comparing mitochondrial respiratory chain activity between the two phenotypes. Respiratory chain complex activities appear to be conserved, when normalised to CS activity (Table 4). Li and colleagues (2020) have documented a significant increase in both basal mitochondrial respiration and basal ATP production following RA differentiation of SH-SY5Y cells (Li *et al.* 2020). In addition, Schneider and colleagues (2012) demonstrated a significant increase in basal mitochondrial oxygen capacity rate following RA differentiation of SH-SY5Y cells for 5 days. However, they have also demonstrated that mitochondrial content has not changed following differentiation, as judged by CS activity and mitochondrial DNA level (Schneider *et al.* 2012; Larsen *et al.* 2012). These measurements reflect the activity of the ETC as a single entity, which is in contrast to this study where the activity of the different complexes is measured in isolation under substrate saturation conditions. However, the significant changes in CS activity level seen in this thesis following TPA/RA differentiation of SH-SY5Y cells, should be taken into consideration when expressing and comparing results between different cells, especially between different phenotypes of the same cell type, as it has been shown to change during cellular differentiation (Forni *et al.* 2016; Kraft *et al.* 2006; Murholm *et al.* 2009; Schneider *et al.* 2012; Moyes *et al.* 1997). In spite of this, it should also be noted that the significant decrease in CS activity might be specific to CS activity rather than a change in mitochondrial content itself. In this case, measurement of other mitochondrial content markers, such as cardiolipin, should be considered (Larsen *et al.* 2012).

In spite of the immense number of studies demonstrating the different pathways affected in PD, they still lack a mechanistic insight (Zeng *et al.* 2018). It remains unclear how these affected pathways create a cascade of events that eventually result in dopamine depletion and death of dopaminergic neurons. In addition, which affected pathway is the primary cause and which is a consequence, or a secondary event, is yet to be elucidated. One key paper by de la Fuente and colleagues (2017) demonstrated a possible link. Using proliferative SH-SY5Y cells, they demonstrated that decreased activity of mitochondrial complex I or lysosomal GBA disrupts dopamine and serotonin metabolism, leading to potential decrease in the availability of both neurotransmitters (de la Fuente *et al.* 2017). The findings in chapter 6 build on this link, demonstrating that decreased activity of mitochondrial complex I or lysosomal GBA interfere with proper maturation and activity of CTSD. Although no direct measurement of lysosomal pH was undertaken, the disruption of two processes (maturation and activity of CTSD) that are strongly dependent on lysosomal acidification, suggests that lysosomal acidification was affected in these cells. Yang and colleagues (2020) also demonstrated that loss of function of GBA also affects CTSD maturation and activity. However, they suggest that this is a direct result of reduced ceramide production, which is the product of GBA enzyme activity (Yang *et al.* 2020). Ceramides are a common product of many lysosomal enzymes, produced not only by GBA but also by acid sphingomyelinase and galactosylceramidase enzyme activities (Quinville *et al.* 2021). Therefore, the activity of GBA may not be a limiting factor for production of ceramides in the cell.

The acidic environment of lysosomal lumen is a limiting factor for its function as a major site for degradation and recycling of cellular components, as the activity of the majority of lysosomal enzymes has an acidic pH optimum. This means that degradation of cellular components, including proteins and dysfunctional organelles, requires the acidification of the lysosomal lumen. Therefore, impairment of lysosomal acidification can lead to accumulation of proteins that were otherwise destined to be degraded. This can cause the formation of protein aggregates in the cytoplasm that can impair cellular function. In the case of PD, cytoplasmic aggregates largely composed of α -synuclein proteins form in dopaminergic neurons and represent the hallmark of the disease, Lewy bodies (Wakabayashi *et al.* 2013). CTSD is the major lysosomal enzyme involved in the breakdown of α -synuclein (Sevlever *et al.* 2008). As demonstrated in chapter 6, CTSD activity is sensitive to changes in the pH of the lysosomal lumen (Figure 52, Figure 53). This draws a potential scenario where loss of function in GBA activity can interfere with proper lysosomal acidification which is required for CTSD maturation and function. As a result, loss of CTSD activity may lead to accumulation and aggregation of α -synuclein proteins in the cell, a precursor of Lewy bodies.

In addition to Lewy bodies, impaired mitophagy is another proposed factor involved in PD pathology (Vives-Bauza and Przedborski 2011). Mitophagy is the process of selective removal of dysfunctional mitochondria through autophagy (Rodriguez-Enriquez *et al.* 2006). Impairment of mitophagy is strongly linked to PD as mutation in PINK1 and Parkin, proteins proposed to play a role in initiation of mitophagy, account for the majority of autosomal-recessive PD cases (Lill

2016; Ge *et al.* 2020). During mitophagy, damaged mitochondria are engulfed by autophagosomes to be delivered to the lysosomes for degradation (Onishi *et al.* 2021). The acidic environment of the lysosomes is important for the degradation of the autophagosomes and their cargo, as this process is proposed to be catalysed by cathepsin B and CTSD enzymes, which have an acidic pH optimum (Koike *et al.* 2005). Therefore, impairment of lysosomal acidification might be a contributing factor for cellular accumulation of damaged mitochondria seen in PD. It has been shown that mutations in lysosomal GBA resulted in to disruption of both mitophagy and lysosomal degradation in SH-SY5Y cells and post-mortem brain tissue from PD patients carrying mutations in *GBA* (Li *et al.* 2019). One potential mechanism could be that loss of function of GBA results in disruption of lysosomal acidification, which in turn halts its degradative capacity leading to accumulation of dysfunctional mitochondria in the cell.

The findings in chapter 6 also add to the growing theme in research that highlights the existence of a dynamic crosstalk between mitochondria and lysosomes, beyond the scope of mitophagy, that is important for neuronal cell homeostasis (Deus *et al.* 2020; Plotegher and Duchen 2017b). Kim and colleagues (2021) demonstrated a dynamic and physical contact tethering taking place between mitochondrial and lysosomes in neurons. The dynamics of this contact, interestingly, appears to be require functional GBA (Kim *et al.* 2021). In chapter 6, it was demonstrated that disruption of mitochondrial function, as a consequence of rotenone inhibition of mitochondrial complex I, interfered with the activity of CTSD (Figure 56). This finding proposes the hypothesis that the proximity afforded by mitochondrial-lysosomal tethering, might be important for

the delivery of ATP produced by the mitochondrial respiratory chain to the lysosomal v-ATPase. ATP is required for active transport of protons via v-ATPase into the lysosomal lumen which is necessary to maintain the acidity of the lumen (Figure 66, Mindell 2012). Therefore, disruption of mitochondrial function can result in reduced ATP production and consequently lead to disruption of the active process required for maintaining lysosomal acidification. This can result in accumulation of unfolded/misfolded proteins as well as dysfunctional organelles as a consequence of disruption of the autophagic-lysosomal system.

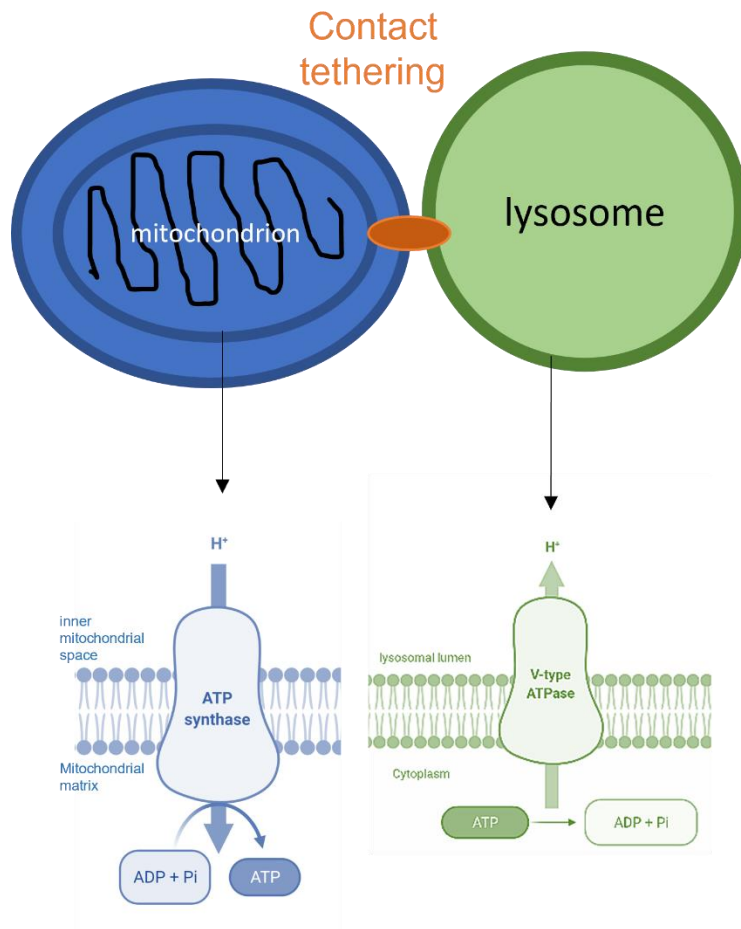


Figure 66 Mitochondrial-lysosomal contact tethering facilitates ATP delivery to lysosomes. The proximity afforded by mitochondrial-lysosomal contact tethering, might be important for the delivery of ATP produced by the mitochondrial respiratory chain ATP synthase to the lysosomal v-ATPase. ATP is required for active transport of protons via v-ATPase into the lysosomal lumen which is necessary to maintain the acidity of the lumen.

When considering the pathogenesis of PD, a wide range of model systems are evaluated (Xicoy *et al.* 2017; Chia *et al.* 2020). In view of the fact that dopamine availability, and to some extent serotonin, is affected in PD, important information may be gained from studying cells derived from patients with primary inherited disorders of monoamine metabolism. Furthermore, such studies are leading to targeted treatments that could be extended to PD. For example in AADC deficiency, gene therapy is a promising treatment to correct the disruption of dopamine metabolism by correcting AADC expression (Hwu *et al.* 2012; Chien *et al.* 2017; Kojima *et al.* 2019). In chapter 7, iPSC dopaminergic neurons derived from AADC deficiency patients were used to test the feasibility of correcting dopamine metabolism via rescuing AADC enzyme function through ectopic expression using viral vectors (Figure 58). This presents AADC as a possible target for PD therapy as well, where patients can benefit from restoration of dopamine levels. Restoration of dopamine levels is the current basis for the gold standard PD therapy, L-DOPA. However, chronic L-DOPA supplementation, although effective, has many undesirable side effects including motor fluctuation, dyskinesia and depression (Hauser 2009). In addition, due to the progressive neuronal loss that occurs in PD, in many patients there's reduced availability of AADC enzyme resulting in reduced efficacy of L-DOPA treatment (Ciesielska *et al.* 2017). Thus, enhancement of AADC enzyme expression or overexpression using viral vectors has been the subject of many preclinical studies and clinical trials. In a recent clinical trial, viral vector based AADC enzyme expression delivered directly to the putamen of moderately advanced PD patients was demonstrated to be safe and well-tolerated (Christine *et al.* 2022). It enhanced motor responses to L-DOPA treatment with all cohort showing either stability or

improvement of motor function during the 3-year trial (Christine *et al.* 2022; Nutt *et al.* 2020).

Creating disease models derived from patients carrying disease-linked genetic mutations can also offer a wealth of information on disease mechanism. Although PD is largely idiopathic, about 15% of disease cases have a genetic link. Mutations in PINK1 are one of the most common genetic mutations associated with PD inheritance (Balestrino and Schapira 2020). PINK1 is a mitochondrial-associated protein, involved in mitochondrial quality control, where its accumulation on the mitochondrial outer membrane identifies and tags damaged mitochondria for removal through mitophagy (Narendra *et al.* 2010). In chapter 8, a preliminary analysis of dopamine metabolism was carried in iPSC dopaminergic neurons derived from PD patients carrying mutations in PINK1. DOPAC levels were found to be significantly lower in the patient-derived cells compared to control cells not carrying any mutations in PINK1 (Figure 63) This finding supports previous findings that suggest PINK1 may have functions involved in regulation of TH and dopamine metabolism (Lu *et al.* 2018; Maynard *et al.* 2020; Matsui *et al.* 2010). Thus, through the use of patient derived cells, new insights into the functions of PINK1, beyond mitochondrial quality control, can be gained to further elucidate the mechanism behind its involvement in PD pathology.

9.2. Conclusion:

In conclusion, this thesis provides a functional comparison between proliferative and differentiated SH-SY5Y cells, two phenotypes of one of the most commonly used cell line in PD research. The two phenotypes are used almost interchangeably without prior biochemical characterisation of the pathways implicated in PD. The work presented here highlights the similarities between the two phenotypes, particularly in mitochondrial respiratory chain activity. However, it also brings to attention multiple significant differences, namely in the regulation of unstable molecules like dopamine and GSH and the response to different toxins. It provides a framework through which the decision to use a specific cell line and/or cell phenotype should be made, which is via careful functional characterisation of the model and pathways of interest. The work also emphasizes the importance of functional biochemical analysis of cellular processes. Despite the common use of SH-SY5Y cells as a dopaminergic neuronal model, primarily based on their protein expression of TH, the rate limiting enzyme of the dopamine pathway, SH-SY5Y cells do not produce any dopamine under basal conditions. This brings forth a number of questions concerning the regulation of dopamine metabolism in these cells and the possible requirement of environmental signals, in addition to the possibility of their dual serotonergic/dopaminergic phenotype. In addition, the work provides evidence to support one of the major concerns surrounding the use of proliferative cell lines, which is experimental variabilities and inconsistencies, that could be reduced following differentiation. Furthermore, this thesis sheds the light on the potential involvement of lysosomal pH in PD pathology as a consequence of loss of function of lysosomal GBA or mitochondrial complex I. This could be a result of

disrupted mitochondrial-lysosomal crosstalk dynamics, providing a potential mechanistic insight. Finally, this thesis demonstrates the value for the use of patient-derived cells as disease models to understand the contribution of genetic mutations for disease mechanisms, particularly the consequence of which on dopamine metabolism, and to investigate potential therapeutics.

9.3. Further work:

To confirm the hypotheses and results presented in this thesis, and to further our understanding of the biochemistry of neuronal cells and the disease mechanism of PD through the use of neuronal cell models, the following can be considered:

- ❖ Evaluate further the the absence of dopamine under basal conditions seen in Chapter 4, i.e. to gain more information on the integrity of the dopamine pathway by measurement of the activity of the dopamine pathway enzymes, TH and AADC, in proliferative and differentiated SH-SY5Y cells, as well as to determine the phosphorylation status of TH and measure the concentration of co-factors.
- ❖ In order to gain further understanding of the bioenergetic differences between proliferative and differentiated SH-SY5Y cells, it would be of interest to assess the following:
 - Measure and compare mitochondrial oxygen consumption rate and supercomplex activity to assess mitochondrial function.
 - Assess and compare glycolytic flux.
 - measure mitochondrial specific phospholipid, cardiolipin, to confirm the apparent change in mitochondrial connect.
- ❖ In chapter 5, GSH levels were analyzed as an insight into the state of oxidative stress in proliferative and differentiated SH-SY5Y cells following L-DOPA treatment. This could be expanded by assessment of NADPH oxidase which is an important source of cellular ROS. Increased expression of NADPH oxidase is documented in PD (Belarbi

et al. 2017). In addition, dopamine was shown to increase the expression of NADPH oxidase (Begieneman *et al.* 2016). Measurement of the enzyme activity under basal and stress conditions can provide an insight into how oxidative stress may contribute to PD. Oxidative stress could also be assessed by measurement of products such as hydrogen peroxide, superoxide, or oxidative stress markers. This, in particular, following treatment of the SH-SY5Y cells with L-DOPA.

- ❖ The results from Chapter 6 suggest that both lysosomal GBA and mitochondrial complex I might be important for maintaining the acidic environment of the lysosome. Thus, to expand on these results,
 - The effect of increased lysosomal pH on dopamine and serotonin metabolism in proliferative and differentiated SH-SY5Y cells could be assessed.
 - Similarly, to further our understanding of the nature of metabolic crosstalk between mitochondria and lysosomes, it would be of interest to investigate the effect of increased lysosomal pH on mitochondrial complex I activity in proliferative and differentiated SH-SY5Y cells.
 - The increase in lysosomal pH can be achieved using either Baf or chloroquine, both of which are shown to increase lysosomal pH however via different mechanisms.
 - Finally, to confirm the changes in lysosomal pH, the following would be advantageous:

- development of flow-cytometer method for direct measurement of lysosomal pH using LysoSensor dyes is important. This to confirm the perturbation of lysosomal acidification following inhibition of mitochondrial complex I and lysosomal GBA.
 - Measure the activity of other lysosomal hydrolases to confirm perturbation of lysosomal pH.
- ❖ The preliminary studies in Chapters 7 and 8 provided a proof of concept for use of patient-derived iPSC dopaminergic neurons to investigate disease mechanisms and assess potential therapies through a translational precision medicine approach. To confirm and expand on the results of cell line-based work presented in this thesis, the use of PD patient-derived iPSC dopaminergic neurons would present an invaluable tool. For example, PINK1 mutations are the second most frequent cause of autosomal recessive PD (Gandhi and Plun-Favreau 2017). In chapter 8, it was demonstrated that mutation in PINK1 has an effect on dopamine metabolism in PD patient-derived dopaminergic neurons. Confirmation of these results as well as assessing the state of the enzymes of the dopamine pathway in these cells would be valuable to gain further insight on the cellular functions of PINK1, beyond the scope of mitochondrial quality control.

Bibliography

- Abati E., Bresolin N., Comi G., Corti S. (2020) Silence superoxide dismutase 1 (SOD1): a promising therapeutic target for amyotrophic lateral sclerosis (ALS). *Expert Opin. Ther. Targets* **24**, 295–310.
- Abbott R. A., Cox M., Markus H., Tomkins A. (1992) Diet, body size and micronutrient status in Parkinson's disease. *Eur. J. Clin. Nutr.* **46**, 879–884.
- Abed Rabbo M., Khodour Y., Kaguni L. S., Stiban J. (2021) Sphingolipid lysosomal storage diseases: from bench to bedside. *Lipids Health Dis.* **20**, 1–29.
- Acín-Pérez R., Bayona-Bafaluy M. P., Fernández-Silva P., Moreno-Loshuertos R., Pérez-Martos A., Bruno C., Moraes C. T., Enríquez J. A. (2004) Respiratory complex III is required to maintain complex I in mammalian mitochondria. *Mol. Cell* **13**, 805–815.
- Adeosun S. O., Albert P. R., Austin M. C., Iyo A. H. (2012) 17 β -estradiol-induced regulation of the novel 5-HT1A-related transcription factors NUDR and Freud-1 in SH SY5Y cells. *Cell. Mol. Neurobiol.* **32**, 517–521.
- Adnot S., Houssaini A., Abid S., Marcos E., Amsellem V. (2013) Serotonin transporter and serotonin receptors. *Handb. Exp. Pharmacol.* **218**, 365–380.
- Agarwal S., Yadav A., Chaturvedi R. K. (2017) Peroxisome proliferator-activated receptors (PPARs) as therapeutic target in neurodegenerative disorders. *Biochem. Biophys. Res. Commun.* **483**, 1166–1177.
- Aguirre P., Urrutia P., Tapia V., Villa M., Paris I., Segura-Aguilar J., Núñez M. T. (2012) The dopamine metabolite aminochrome inhibits mitochondrial complex i and modifies the expression of iron transporters DMT1 and FPN1. *BioMetals* **25**, 795–803.
- Ajrout-Driss S., Siddique T. (2015) Sporadic and hereditary amyotrophic lateral sclerosis (ALS). *Biochim. Biophys. Acta - Mol. Basis Dis.* **1852**, 679–684.
- Akram M. (2014) Citric Acid Cycle and Role of its Intermediates in Metabolism.

Cell Biochem. Biophys. **68**, 475–478.

- Alberio T., Lopiano L., Fasano M. (2012) Cellular models to investigate biochemical pathways in Parkinson's disease. *FEBS J* **279**, 1146–1155.
- Alcalay R. N., Wolf P., Sum M., Chiang R., Helesicova K., Zhang X. K., Merchant K., et al. (2020) Longitudinal Measurements of Glucocerebrosidase activity in Parkinson's patients. *Ann. Clin. Transl. Neurol.* **7**, 1816–1830.
- Allen G. F. G. G., Ullah Y., Hargreaves I. P., Land J. M., Heales S. J. R. R. (2013) Dopamine but not l-dopa stimulates neural glutathione metabolism. Potential implications for Parkinson's and other dopamine deficiency states. *Neurochem. Int.* **62**, 684–694.
- Alonso-Canovas A., Katschnig P., Tucci A., Carecchio M., Wood N. W., Edwards M., Martínez Castrillo J. C., Burke D., Heales S., Bhatia K. P. (2010) Atypical Parkinsonism with apraxia and supranuclear gaze abnormalities in type 1 Gaucher disease. Expanding the spectrum: Case report and literature review. *Mov. Disord.* **25**, 1506–1509.
- Alrashidi H., Eaton S., Heales S. (2021) Biochemical characterization of proliferative and differentiated SH-SY5Y cell line as a model for Parkinson's disease. *Neurochem. Int.* **145**, 105009.
- Aluf Y., Vaya J., Khatib S., Loboda Y., Finberg J. P. M. (2013) Selective inhibition of monoamine oxidase A or B reduces striatal oxidative stress in rats with partial depletion of the nigro-striatal dopaminergic pathway. *Neuropharmacology* **65**, 48–57.
- Ammal Kaidery N., Thomas B. (2018) Current perspective of mitochondrial biology in Parkinson's disease. *Neurochem. Int.* **117**, 91–113.
- Ando M., Fiesel F. C., Hudec R., Caulfield T. R., Ogaki K., Górka-Skoczylas P., Kozirowski D., et al. (2017) The PINK1 p.I368N mutation affects protein stability and ubiquitin kinase activity. *Mol. Neurodegener.* **12**.
- Andreeva A., Bekkhozhin Z., Omertassova N., Baizhumanov T., Yeltay G., Akhmetali M., Toibazar D., Utepbergenov D. (2019) The apparent

- deglycase activity of DJ-1 results from the conversion of free methylglyoxal present in fast equilibrium with hemithioacetals and hemiaminals. *J. Biol. Chem.* **294**, 18863–18872.
- Antuono P., Beyer J. (1999) The burden of dementia. A medical and research perspective. *Theor. Med. Bioeth.* **20**, 3–13.
- Aoyama K. (2021) Glutathione in the Brain. *Int. J. Mol. Sci.* **22**, 22.
- Apel K., Hirt H. (2004) Reactive oxygen species: metabolism, oxidative stress, and signal transduction. *Annu. Rev. Plant Biol.* **55**, 373–399.
- Arenas E., Denham M., Carlos Villaescusa J. (2015) How to make a midbrain dopaminergic neuron.
- Arnold S., Kadenbach B. (1997) Cell respiration is controlled by ATP, an allosteric inhibitor of cytochrome-c oxidase. *Eur. J. Biochem.* **249**, 350–354.
- Arnoux J. B., Damaj L., Napuri S., Serre V., Hubert L., Cadoudal M., Simard G., Ceballos I., Christa L., Lonlay P. De (2013) Aromatic L-amino acid decarboxylase deficiency is a cause of long-fasting hypoglycemia. *J. Clin. Endocrinol. Metab.* **98**, 4279–4284.
- Arotcarena M.-L., Teil M., Dehay B. (2019) Autophagy in Synucleinopathy: The Overwhelmed and Defective Machinery. *Cells* **8**, 565.
- Aufschnaiter A., Kohler V., Buttner S. (2017) Taking out the garbage: cathepsin D and calcineurin in neurodegeneration. *Neural Regen Res* **12**, 1776–1779.
- Aylett S. B., Neergheen V., Hargreaves I. P., Eaton S., Land J. M., Rahman S., Heales S. J. R. (2013) Levels of 5-methyltetrahydrofolate and ascorbic acid in cerebrospinal fluid are correlated: Implications for the accelerated degradation of folate by reactive oxygen species. *Neurochem. Int.* **63**, 750–755.
- Ayodele B. A., Mirams M., Pagel C. N., Mackie E. J. (2017) The vacuolar H⁺ ATPase V0 subunit d2 is associated with chondrocyte hypertrophy and supports chondrocyte differentiation. *Bone reports* **7**, 98–107.

- Badillo-Ramírez I., Saniger J. M., Rivas-Arancibia S. (2019) 5-S-cysteinyl-dopamine, a neurotoxic endogenous metabolite of dopamine: Implications for Parkinson's disease. *Neurochem. Int.* **129**, 104514.
- Bae E. J., Yang N. Y., Lee C., Lee H. J., Kim S., Sardi S. P., Lee S. J. (2015) Loss of glucocerebrosidase 1 activity causes lysosomal dysfunction and α -synuclein aggregation. *Exp. Mol. Med.* **2015 473 47**, e153–e153.
- Baixauli F., Acin-Perez R., Villarroya-Beltri C., Mazzeo C., Nunez-Andrade N., Gabande-Rodriguez E., Ledesma M. D., et al. (2015) Mitochondrial Respiration Controls Lysosomal Function during Inflammatory T Cell Responses. *Cell Metab* **22**, 485–498.
- Balasooriya I., Wimalasena K. (2007) Are SH-SY5Y and MN9D cell lines truly dopaminergic? *FASEB J.* **21**, 25–26.
- Balestrino R., Schapira A. H. V. (2020) *Parkinson disease*. *Eur J Neurol.*
- Ballard P. A., Tetrad J. W., Langston J. W. (1985) Permanent human parkinsonism due to 1-methyl-4-phenyl-1,2,3,6-tetrahydropyridine (MPTP). *Neurology* **35**, 949–949.
- Ballaz S., Morales I., Rodríguez M., Obeso J. A. (2013) Ascorbate prevents cell death from prolonged exposure to glutamate in an in vitro model of human dopaminergic neurons. *J. Neurosci. Res.* **91**, 1609–1617.
- Barbeau A., Roy M., Bernier G., Campanella G., Paris S. (1987) Ecogenetics of Parkinson's disease: prevalence and environmental aspects in rural areas. *Can. J. Neurol. Sci.* **14**, 36–41.
- Baris H. N., Cohen I. J., Mistry P. K. (2014) Gaucher Disease: The Metabolic Defect, Pathophysiology, Phenotypes And Natural History. *Pediatr. Endocrinol. Rev.* **12**, 72.
- Batlloiri M., Molero-Luis M., Ormazabal A., Casado M., Sierra C., García-Cazorla A., Kurian M., Pope S., Heales S. J., Artuch R. (2017) Analysis of human cerebrospinal fluid monoamines and their cofactors by HPLC. *Nat. Protoc.* **12**, 2359–2375.
- Begieneman M. P. V., Horst E. N. ter, Rijvers L., Meinster E., Leen R., Pankras

- J. E., Fritz J., et al. (2016) Dopamine induces lipid accumulation, NADPH oxidase-related oxidative stress, and a proinflammatory status of the plasma membrane in H9c2 cells. *Am. J. Physiol. Heart Circ. Physiol.* **311**, H1097–H1107.
- Belarbi K., Cuvelier E., Destée A., Gressier B., Chartier-Harlin M. C. (2017) NADPH oxidases in Parkinson's disease: a systematic review. *Mol. Neurodegener.* 2017 121 **12**, 1–18.
- Benchoua A., Trioulier Y., Zala D., Gaillard M. C., Lefort N., Dufour N., Saudou F., et al. (2006) Involvement of mitochondrial complex II defects in neuronal death produced by N-terminus fragment of mutated huntingtin. *Mol. Biol. Cell* **17**, 1652–1663.
- Berman S. B., Hastings G. (1999) *Dopamine Oxidation Alters Mitochondrial Respiration and Induces Permeability Transition in Brain Mitochondria: Implications for Parkinson's Disease.*
- Berridge K. C. (2007) *The debate over dopamine's role in reward: The case for incentive salience.*
- Bertoldi M. (2014) Mammalian dopa decarboxylase: Structure, catalytic activity and inhibition. *Arch. Biochem. Biophys.* **546**, 1–7.
- Betarbet R., Sherer T. B., MacKenzie G., Garcia-Osuna M., Panov A. V., Greenamyre J. T. (2000) Chronic systemic pesticide exposure reproduces features of Parkinson's disease. **3**, 1301–1306.
- Betz J. M., Brown P. N., Roman M. C. (2011) Accuracy, Precision, and Reliability of Chemical Measurements in Natural Products Research. *Fitoterapia* **82**, 44.
- Beyenbach K. W., Wieczorek H. (2006) *The V-type H⁺ ATPase: Molecular structure and function, physiological roles and regulation.* J Exp Biol.
- Biedler J. L., Helson L., Spengler B. A. (1973) Morphology and Growth, Tumorigenicity, and Cytogenetics of Human Neuroblastoma Cells in Continuous Culture. *Cancer Res.* **33**, 2643–2652.
- Biedler J. L., Schachner M. (1978) Multiple Neurotransmitter Synthesis by

Human Neuroblastoma Cell Lines and Clones. *Cancer Res.* **38**, 3751–3757.

Biosa A., Arduini I., Soriano M. E., Giorgio V., Bernardi P., Bisaglia M., Bubacco L. (2018) Dopamine oxidation products as mitochondrial endotoxins, a potential molecular mechanism for preferential neurodegeneration in Parkinson Disease. *ACS Chem. Neurosci.* **9**, 2849–2858.

Birkmayer W., Riederer P., Youdim M. B. H., Linauer W. (1975) The potentiation of the anti aknetic effect after L-Dopa treatment by an inhibitor of Mao-B, deprenil. *J. Neural Transm.* 1975 363 **36**, 303–326.

Bisaglia M., Soriano M. E., Arduini I., Mammi S., Bubacco L. (2010) Molecular characterization of dopamine-derived quinones reactivity toward NADH and glutathione: implications for mitochondrial dysfunction in Parkinson disease. *Biochim. Biophys. Acta* **1802**, 699–706.

Blesa J., Trigo-Damas I., Quiroga-Varela A., Jackson-Lewis V. R. (2015) Oxidative stress and Parkinson's disease. *Front. Neuroanat.* **9**.

Bolaños J. P. (2016) Bioenergetics and redox adaptations of astrocytes to neuronal activity. *J. Neurochem.* **139 Suppl 2**, 115–125.

Bonifati V., Rizzu P., Baren M. J. Van, Schaap O., Breedveld G. J., Krieger E., Dekker M. C. J., et al. (2003) Mutations in the DJ-1 gene associated with autosomal recessive early-onset parkinsonism. *Science* **299**, 256–259.

Borsche M., Pereira S. L., Klein C., Grünewald A. (2021) Mitochondria and Parkinson's Disease: Clinical, Molecular, and Translational Aspects. *J. Parkinsons. Dis.* **11**, 45–60.

Bourdenx M., Daniel J., Genin E., Soria F. N., Blanchard-Desce M., Bezdard E., Dehay B. (2016) Nanoparticles restore lysosomal acidification defects: Implications for Parkinson and other lysosomal-related diseases. *Autophagy* **12**, 472.

Bowman E. J., Siebers A., Altendorf K. (1988) Bafilomycins; A class of inhibitors of membrane ATPases from microorganisms, animal cells, and plant cells. *Proc. Natl. Acad. Sci. U. S. A.* **85**, 7972–7976.

- Braak H., Del K., Rüb U., Vos R. A. I. De, Jansen E. N. H., Braak E. (2003) Staging of brain pathology related to sporadic Parkinson's disease.pdf. **24**, 197–211.
- Bradford M. (1976) A Rapid and Sensitive Method for the Quantitation of Microgram Quantities of Protein Utilizing the Principle of Protein-Dye Binding. *Anal. Biochem.* **72**, 248–254.
- Brady R. O., Kanfer J., Shapiro D. (1965) The Metabolism of Glucocerebrosides. *J. Biol. Chem.* **240**, 39–43.
- Bräutigam C., Wevers R. A., Hyland K., Sharma R. K., Knust A., Hoffmann G. F. (2000) The influence of L-dopa on methylation capacity in aromatic L-amino acid decarboxylase deficiency: biochemical findings in two patients. *J. Inherit. Metab. Dis.* **23**, 321–324.
- Brenner-Lavie H., Klein E., Ben-Shachar D. (2009) Mitochondrial complex I as a novel target for intraneuronal DA: Modulation of respiration in intact cells. *Biochem. Pharmacol.* **78**, 85–95.
- Briggs G. D., Nagy G. M., Dickson P. W. (2013) Mechanism of action of salsolinol on tyrosine hydroxylase. *Neurochem. Int.* **63**, 726–731.
- Briston T., Hicks A. R. (2018) *Mitochondrial dysfunction and neurodegenerative proteinopathies: Mechanisms and prospects for therapeutic intervention*. Portland Press Ltd.
- Brown J. M., Gouty S., Iyer V., Rosenberger J., Cox B. M. (2006) Differential protection against MPTP or methamphetamine toxicity in dopamine neurons by deletion of ppN/OFQ expression. *J. Neurochem.* **98**, 495–505.
- Burbulla L. F., Song P., Mazzulli J. R., Zampese E., Wong Y. C., Jeon S., Santos D. P., et al. (2017) Dopamine oxidation mediates mitochondrial and lysosomal dysfunction in Parkinson's disease. *Science (80-.)*. **357**, 1255–1261.
- Burkhard P., Dominici P., Borri-Voltattorni C., Jansonius J. N., Malashkevich V. N. (2001) Structural insight into Parkinson's disease treatment from drug-inhibited DOPA decarboxylase. *Nat. Struct. Biol.* **8**, 963–967.

- Campos Cogo S., Gradowski Farias da Costa do Nascimento T., Almeida Brehm Pinhatti F. de, França Junior N. de, Santos Rodrigues B., Regina Cavalli L., Elifio-Esposito S. (2020) An overview of neuroblastoma cell lineage phenotypes and in vitro models. *Exp. Biol. Med.* **245**.
- Carlsson A., Lindqvist M., Magnusson T. (1957) *3,4-Dihydroxyphenylalanine and 5-hydroxytryptophan as reserpine antagonists [16]*. Nature Publishing Group.
- Cartier E. A., Parra L. A., Baust T. B., Quiroz M., Salazar G., Faundez V., Egaña L., Torres G. E. (2010) A Biochemical and Functional Protein Complex Involving Dopamine Synthesis and Transport into Synaptic Vesicles. *J. Biol. Chem.* **285**, 1957–1966.
- Caudle W. M., Richardson J. R., Wang M. Z., Taylor T. N., Guillot T. S., McCormack A. L., Colebrooke R. E., Monte D. A. Di, Emson P. C., Miller G. W. (2007) Reduced vesicular storage of dopamine causes progressive nigrostriatal neurodegeneration. *J. Neurosci.* **27**, 8138–8148.
- Cecchini G. (2003) Function and Structure of Complex II of the Respiratory Chain. *Annu. Rev. Biochem.* **72**, 77–109.
- Cellini B. (2012) Biochemical and Computational Approaches to Improve the Clinical Treatment of Dopa Decarboxylase-Related Diseases: An Overview. *Open Biochem. J.* **6**, 131–138.
- Chakrama F. Z., Seguin-Py S., Grand J. N. Le, Fraichard A., Delage-Mourroux R., Despouy G., Perez V., Jouvenot M., Boyer-Guittaut M. (2010) GABARAPL1 (GEC1) associates with autophagic vesicles.
- Chan C. S., Gertler T. S., Surmeier D. J. (2010) A molecular basis for the increased vulnerability of substantia nigra dopamine neurons in aging and Parkinson's disease. *Mov. Disord.* **25**, S63–S70.
- Chan E. C. Y., Ho P. C. (2000) High-performance liquid chromatography/atmospheric pressure chemical ionization mass spectrometric method for the analysis of catecholamines and metanephrines in human urine. *Rapid Commun. Mass Spectrom.* **14**,

1959–1964.

- Chang D., Nalls M. A., Hunkapiller J., Brug D., Cai F., Kerchner G. A., Ayalon G., et al. (2018) A meta-analysis of genome-wide association studies identifies 17 new Parkinson's disease risk loci. **49**, 1511–1516.
- Chaudhry F. A., Edwards R. H., Fonnum F. (2008) Vesicular neurotransmitter transporters as targets for endogenous and exogenous toxic substances. *Annu. Rev. Pharmacol. Toxicol.* **48**, 277–301.
- Chazotte B. (2011) Labeling lysosomes in live cells with lysotracker. *Cold Spring Harb. Protoc.* **6**, 210–213.
- Chen C., McDonald D., Blain A., Sachdeva A., Bone L., Smith A. L. M., Warren C., et al. (2021a) Imaging mass cytometry reveals generalised deficiency in OXPHOS complexes in Parkinson's disease. *npj Park. Dis.* **7**.
- Chen H., Teng Y., Liu Z., Geng F., Chen X., Jiang H., Yang J., Zheng M., Wang Z., Yang L. (2021b) Molecular Mechanism of Platelet-Derived Growth Factor (PDGF)-BB-Mediated Protection Against MPP+ Toxicity in SH-SY5Y Cells. *J. Mol. Neurosci.* **71**, 1131–1143.
- Chen L., Ding Y., Cagniard B., Laar A. D. Van, Mortimer A., Chi W., Hastings T. G., Un J. K., Zhuang X. (2008) Unregulated cytosolic dopamine causes neurodegeneration associated with oxidative stress in mice. *J. Neurosci.* **28**, 425–433.
- Chen Y., Gibson S. B. (2008) Is mitochondrial generation of reactive oxygen species a trigger for autophagy? *Autophagy* **4**, 246–248.
- Chia S. J., Tan E.-K., Chao Y.-X. (2020) Historical Perspective: Models of Parkinson's Disease. *Int. J. Mol. Sci.* **21**, 2464.
- Chien Y. H., Lee N. C., Tseng S. H., Tai C. H., Muramatsu S. ichi, Byrne B. J., Hwu W. L. (2017) Efficacy and safety of AAV2 gene therapy in children with aromatic L-amino acid decarboxylase deficiency: an open-label, phase 1/2 trial. *Lancet Child Adolesc. Heal.* **1**, 265–273.
- Chin M. Y., Patwardhan A. R., Ang K.-H., Wang A. L., Alquezar C., Welch M., Nguyen P. T., et al. (2021) Genetically Encoded, pH-Sensitive mTFP1

Biosensor for Probing Lysosomal pH. *ACS Sensors* **6**, 2168.

Chinta S. J., Andersen J. K. (2005) Dopaminergic neurons. *Int. J. Biochem. Cell Biol.* **37**, 942–946.

Chinta S. J., Mallajosyula J. K., Rane A., Andersen J. K. (2010) Mitochondrial α -synuclein accumulation impairs complex I function in dopaminergic neurons and results in increased mitophagy in vivo. *Neurosci. Lett.* **486**, 235–239.

Choi S., Kim D., Kam T. I., Yun S., Kim S., Park H., Hwang H., et al. (2015) Lysosomal Enzyme Glucocerebrosidase Protects against A β 1-42 Oligomer-Induced Neurotoxicity. *PLoS One* **10**, e0143854.

Christian B. E., Spremulli L. L. (2012) Mechanism of protein biosynthesis in mammalian mitochondria. *Biochim Biophys Acta* **1819**, 1035–1054.

Christine C. W., Richardson R. M., Laar A. D. van, Thompson M. E., Fine E. M., Khwaja O. S., Li C., et al. (2022) Safety of AADC Gene Therapy for Moderately Advanced Parkinson Disease. *Neurology* **98**, e40–e50.

Chu C. T. (2018) Multiple pathways for mitophagy: A neurodegenerative conundrum for Parkinson's disease. *Neurosci Lett.*

Chu Y., Dodiya H., Aebischer P., Olanow C. W., Kordower J. H. (2009) Alterations in lysosomal and proteasomal markers in Parkinson's disease: Relationship to alpha-synuclein inclusions. *Neurobiol. Dis.* **35**, 385–398.

Chung S. Y., Kishinevsky S., Mazzulli J. R., Graziotto J., Mrejeru A., Mosharov E. V., Puspita L., et al. (2016) Parkin and PINK1 Patient iPSC-Derived Midbrain Dopamine Neurons Exhibit Mitochondrial Dysfunction and α -Synuclein Accumulation. *Stem cell reports* **7**, 664–677.

Ciesielska A., Samaranch L., San Sebastian W., Dickson D. W., Goldman S., Forsayeth J., Bankiewicz K. S. (2017) Depletion of AADC activity in caudate nucleus and putamen of Parkinson's disease patients; implications for ongoing AAV2-AADC gene therapy trial. *PLoS One* **12**.

Cleeter M. W. J., Chau K. Y., Gluck C., Mehta A., Hughes D. A., Duchon M., Wood N. W., Hardy J., Mark Cooper J., Schapira A. H. (2013) Glucocerebrosidase inhibition causes mitochondrial dysfunction and free

- radical damage. *Neurochem. Int.* **62**, 1–7.
- Cobley J. N., Fiorello M. L., Bailey D. M. (2018) 13 reasons why the brain is susceptible to oxidative stress. *Redox Biol.* **15**, 490.
- Coffey E. E., Beckel J. M., Laties A. M., Mitchell C. H. (2014) Lysosomal alkalization and dysfunction in human fibroblasts with the Alzheimer's disease-linked presenilin 1 A246E mutation can be reversed with cAMP. *Neuroscience* **263**, 111–124.
- Cohen S., Valm A. M., Lippincott-Schwartz J. (2018) *Interacting organelles*. Elsevier Ltd.
- Colacurcio D. J., Nixon R. A. (2016) Disorders of lysosomal acidification—The emerging role of v-ATPase in aging and neurodegenerative disease. *Ageing Res. Rev.* **32**, 75–88.
- Conner G. E., Richo G. (1992) Isolation and characterization of a stable activation intermediate of the lysosomal aspartyl protease cathepsin D. *Biochemistry* **31**, 1142–1147.
- Constantinescu R., Constantinescu A. T., Reichmann H., Janetzky B. (2007) Neuronal differentiation and long-term culture of the human neuroblastoma line SH-SY5Y. *J. Neural Transm. Suppl.* **72**, 17–28.
- Cornetta T., Patrono C., Terrenato I., Nigris F. De, Bentivoglio A. R., Testa A., Palma V., Poggioli T., Padua L., Cozzi R. (2013) Epidemiological, clinical, and molecular study of a cohort of Italian Parkinson disease patients: Association with glutathione-s-transferase and DNA repair gene polymorphisms. *Cell. Mol. Neurobiol.* **33**, 673–680.
- Cotrim A. P., Baum B. J. (2008) Gene therapy: some history, applications, problems, and prospects. *Toxicol. Pathol.* **36**, 97–103.
- Cotzias G. C., Woert M. H. Van, Schiffer L. M. (1967) Aromatic amino acids and modification of parkinsonism. *N. Engl. J. Med.* **276**, 374–379.
- Cummings J. L., Masterman D. L. (1999) Depression in patients with Parkinson's disease. *Int. J. Geriatr. Psychiatry* **14**, 711–718.

- D. Mousseau D., B. Baker G. (2012) Recent Developments in the Regulation of Monoamine Oxidase Form and Function: Is the Current Model Restricting Our Understanding of the Breadth of Contribution of Monoamine Oxidase to Brain [dys]Function? *Curr. Top. Med. Chem.* **12**, 2163–2176.
- Dagnino-Subiabre A., Cassels B. K., Baez S., Johansson A. S., Mannervik B., Segura-Aguilar J. (2000) Glutathione transferase M2-2 catalyzes conjugation of dopamine and dopa o-quinones. *Biochem. Biophys. Res. Commun.* **274**, 32–36.
- Day B. J., Patel M., Calavetta L., Chang L. Y., Stamler J. S. (1999) A mechanism of paraquat toxicity involving nitric oxide synthase. *Proc. Natl. Acad. Sci. U. S. A.* **96**, 12760–12765.
- Deegan P. B., Cox T. M. (2012) Imiglucerase in the treatment of Gaucher disease: a history and perspective. *Drug Des. Devel. Ther.* **6**, 81–106.
- Dehay B., Martinez-Vicente M., Caldwell G. A., Caldwell K. A., Yue Z., Cookson M. R., Klein C., Vila M., Bezdard E. (2016) Lysosomal Impairment in Parkinson's Disease. *Movement Disord.* **28**, 725–732.
- Dehay B., Ramirez A., Martinez-Vicente M., Perier C., Canron M.-H. M. H., Doudnikoff E., Vital A., Vila M., Klein C., Bezdard E. (2012) Loss of P-type ATPase ATP13A2/PARK9 function induces general lysosomal deficiency and leads to Parkinson disease neurodegeneration. *Proc. Natl. Acad. Sci.* **109**, 9611–9616.
- Demers-Lamarche J., Guillebaud G., Tlili M., Todkar K., Belanger N., Grondin M., Nguyen A. P., Michel J., Germain M. (2016) Loss of Mitochondrial Function Impairs Lysosomes. *J Biol Chem* **291**, 10263–10276.
- Dermentzaki G., Dimitriou E., Xilouri M., Michelakakis H., Stefanis L. (2013) Loss of beta-glucocerebrosidase activity does not affect alpha-synuclein levels or lysosomal function in neuronal cells. *PLoS One* **8**, e60674.
- Deus C. M., Yambire K. F., Oliveira P. J., Raimundo N. (2020) Mitochondria–Lysosome Crosstalk: From Physiology to Neurodegeneration. *Trends Mol. Med.* **26**, 71–88.

- Devi L., Raghavendran V., Prabhu B. M., Avadhani N. G., Anandatheerthavarada H. K. (2008) Mitochondrial Import and Accumulation of α -Synuclein Impair Complex I in Human Dopaminergic Neuronal Cultures and Parkinson Disease Brain. *J. Biol. Chem.* **283**, 9089–9100.
- Dickson D. W. (2018) Neuropathology of Parkinson Disease. *Parkinsonism Relat. Disord.* **46**, S30.
- Dolan J. W. (2008) Ion pairing--blessing or curse? Ion-pair chromatography can be your best friend or your worst enemy. *LC-GC North Am.* **26**, 170–173.
- Domingo A., Klein C. (2018) Genetics of Parkinson disease. *Handb. Clin. Neurol.* **147**, 211–227.
- Doss M. X., Sachinidis A. (2019) Current Challenges of iPSC-Based Disease Modeling and Therapeutic Implications. *Cells* **8**, 403.
- Dugger B. N., Dickson D. W. (2017) Pathology of Neurodegenerative Diseases. *Cold Spring Harb. Perspect. Biol.* **9**.
- Dunkley P. R., Bobrovskaya L., Graham M. E., Nagy-Felsobuki E. I. Von, Dickson P. W. (2004) Tyrosine hydroxylase phosphorylation: Regulation and consequences. *J. Neurochem.* **91**, 1025–1043.
- Dunkley P. R., Dickson P. W. (2019) Tyrosine hydroxylase phosphorylation in vivo. *J. Neurochem.* **149**, 706–728.
- Duve C. De (2005) *The lysosome turns fifty.*
- Echizen H., Itoh R., Ishizaki T. (1989) Adenosine and dopamine simultaneously determined in urine by reversed-phase HPLC, with on-line measurement of ultraviolet absorbance and electrochemical detection. *Clin. Chem.* **35**, 64–68.
- Ehringer H., Hornykiewicz O. (1960) Verteilung Von Noradrenalin Und Dopamin (3-Hydroxytyramin) Im Gehirn Des Menschen Und Ihr Verhalten Bei Erkrankungen Des Extrapyramidalen Systems. *Klin. Wochenschr.* **38**, 1236–1239.
- Elkon H., Don J., Melamed E., Ziv I., Shirvan A., Offen D. (2002) Mutant and

wild-type α -synuclein interact with mitochondrial cytochrome C oxidase. *J. Mol. Neurosci.* **18**, 229–238.

Enríquez J. A. (2016) Supramolecular Organization of Respiratory Complexes. <http://dx.doi.org/10.1146/annurev-physiol-021115-105031> **78**, 533–561.

Erspamer V., Asero B. (1952) Identification of Enteramine, the Specific Hormone of the Enterochromaffin Cell System, as 5-Hydroxytryptamine. *Nat.* 1952 1694306 **169**, 800–801.

Fahn S. (2008) The history of dopamine and levodopa in the treatment of Parkinson's disease. *Mov. Disord.* **23**.

Falkenburger B. H., Saridaki T., Dinter E. (2016) Cellular models for Parkinson's disease. *J. Neurochem.* **139**, 121–130.

Falkenburger B. H., Schulz J. B. (2006) Limitations of cellular models in Parkinson's disease research, in *J. Neural Transm. Suppl.*, pp. 261–268. *J. Neural Transm Suppl.*

Fanet H., Capuron L., Castanon N., Calon F., Vancassel S. (2021) Tetrahydrobiopterin (BH4) Pathway: From Metabolism to Neuropsychiatry. *Curr. Neuropharmacol.* **19**, 591.

Fang C. L. C. Y., Wu C. C., Fang C. L. C. Y., Chen W. Y., Chen C. L. (2017) Long-term growth comparison studies of FBS and FBS alternatives in six head and neck cell lines. **12**, e0178960.

Fedorow H., Tribl F., Halliday G., Gerlach M., Riederer P., Double K. L. (2005) Neuromelanin in human dopamine neurons: comparison with peripheral melanins and relevance to Parkinson's disease. *Prog. Neurobiol.* **75**, 109–124.

Felipe A., Vicente R., Villalonga N., Roura-Ferrer M., Martínez-Mármol R., Solé L., Ferreres J. C., Condom E. (2006) Potassium channels: New targets in cancer therapy. *Cancer Detect. Prev.* **30**, 375–385.

Fendel U., Tocilescu M. A., Kerscher S., Brandt U. (2008) Exploring the inhibitor binding pocket of respiratory complex I. *Biochim. Biophys. Acta - Bioenerg.* **1777**, 660–665.

- Fernandez-Mosquera L., Diogo C. V., Yambire K. F., Santos G. L., Luna Sanchez M., Benit P., Rustin P., et al. (2017) Acute and chronic mitochondrial respiratory chain deficiency differentially regulate lysosomal biogenesis. *Sci Rep* **7**, 45076.
- Filloux F., Townsend J. J. (1993) Pre- and postsynaptic neurotoxic effects of dopamine demonstrated by intrastriatal injection. *Exp. Neurol.* **119**, 79–88.
- Fivenson E. M., Lautrup S., Sun N., Scheibye-Knudsen M., Stevnsner T., Nilsen H., Bohr V. A., Fang E. F. (2017) Mitophagy in neurodegeneration and aging. *Neurochem. Int.* **109**, 202.
- Flanagan, Robert J. Perrett, David Whelpton R. (2007) *Electrochemical Detection in HPLC*, RSC Chromatography Monographs. Royal Society of Chemistry, Cambridge.
- Folts C. J., Scott-Hewitt N., Prö C., Mayer-Prö M., Noble M. (2016) Lysosomal Re-acidification Prevents Lysosphingolipid-Induced Lysosomal Impairment and Cellular Toxicity.
- Fonzo A. Di, Chien H. F., Socal M., Giraudo S., Tassorelli B. C., Iliceto G., Fabbrini G., et al. (2007) *ATP13A2 missense mutations in juvenile parkinsonism and young onset Parkinson disease*.
- Forgac M. (2007) *Vacuolar ATPases: Rotary proton pumps in physiology and pathophysiology*.
- Forman H. J., Zhang H., Rinna A. (2010) Glutathione: Overview of its protective roles, measurement, and biosynthesis. **30**, 1–12.
- Forni M. F., Peloggia J., Trudeau K., Shirihai O., Kowaltowski A. J. (2016) Murine mesenchymal stem cell commitment to differentiation is regulated by mitochondrial dynamics. *Stem Cells* **34**, 743–755.
- G W., H H., H D., A B., H Z. (1984) Metabolic products of microorganisms. 224. Bafilomycins, a new group of macrolide antibiotics. Production, isolation, chemical structure and biological activity. *J. Antibiot. (Tokyo)*. **37**, 110–117.
- Gainetdinov R. R., Fumagalli F., Jones S. R., Caron M. G. (1997) Dopamine transporter is required for in vivo MPTP neurotoxicity: evidence from mice

lacking the transporter. *J. Neurochem.* **69**, 1322–1325.

- Ganapathy K., Datta I., Sowmithra S., Joshi P., Bhonde R. (2016) Influence of 6-Hydroxydopamine Toxicity on α -Synuclein Phosphorylation, Resting Vesicle Expression, and Vesicular Dopamine Release. *J. Cell. Biochem.*, 2719–2736.
- Gandhi S., Plun-Favreau H. (2017) Mutations and mechanism: how PINK1 may contribute to risk of sporadic Parkinson's disease. *Brain* **140**, 2–5.
- Garrick N. A., Murphy D. L. (1980) Species differences in the deamination of dopamine and other substrates for monoamine oxidase in brain. *Psychopharmacol.* 1980 721 **72**, 27–33.
- Garrido M., Tereshchenko Y., Zhevtsova Z., Taschenberger G., Bähr M., Kügler S. (2011) Glutathione depletion and overproduction both initiate degeneration of nigral dopaminergic neurons. *Acta Neuropathol.* **121**, 475.
- Ge P., Dawson V. L., Dawson T. M. (2020) PINK1 and Parkin mitochondrial quality control: a source of regional vulnerability in Parkinson's disease. *Mol. Neurodegener.* **15**, 20.
- Gegg M. E., Burke D., Heales S. J. R., Cooper J. M., Hardy J., Wood N. W., Schapira A. H. V. (2012) Glucocerebrosidase deficiency in substantia nigra of parkinson disease brains. *Ann. Neurol.* **72**, 455–463.
- Géraldine M., Stéphanie D., Bénédicte L., Isabelle D., Monique L., Sylvie V. (2010) DHA enhances the noradrenaline release by SH-SY5Y cells. *Neurochem. Int.* **56**, 94–100.
- Gerard-Monnier D., Chaudiere J. (1996) [Metabolism and antioxidant function of glutathione]. *Pathol. Biol. (Paris)*. **44**, 77–85.
- Ghosh R., Tabrizi S. J. (2018) Clinical Features of Huntington's Disease. *Adv. Exp. Med. Biol.* **1049**, 1–28.
- Giannopoulos S., Samardzic K., Raymond B. B. A. A., Djordjevic S. P., Rodgers K. J. (2019) L-DOPA causes mitochondrial dysfunction in vitro : A novel mechanism of L- DOPA toxicity uncovered. *Int. J. Biochem. Cell Biol.* **117**, 105624.

- Giordano S., Lee J., Darley-USmar V. M., Zhang J. (2012) Distinct Effects of Rotenone, 1-methyl-4-phenylpyridinium and 6-hydroxydopamine on Cellular Bioenergetics and Cell Death. *PLoS One* **7**, e44610.
- Goetz C. G., Wu J., Curgian L. M., Leurgans S. (2005) Hallucinations and sleep disorders in PD: Six-year prospective longitudinal study. *Neurology* **64**, 81–86.
- Goker-Alpan O., Schiffmann R., LaMarca M. E., Nussbaum R. L., McInerney-Leo A., Sidransky E. (2004) Parkinsonism among Gaucher disease carriers. *J. Med. Genet.* **41**, 937–940.
- Goksu Erol A. Y., Kocanci F. G., Dora D. D., Uysal H. (2022) Additive cell protective and oxidative stress reducing effects of combined treatment with cromolyn sodium and masitinib on MPTP-induced toxicity in SH-SY5Y neuroblastoma cells. *Chem. Biol. Interact.*, 109808.
- Goldstein D. S., Sullivan P., Holmes C., Miller G. W., Alter S., Strong R., Mash D. C., Kopin I. J., Sharabi Y. (2013) Determinants of buildup of the toxic dopamine metabolite DOPAL in Parkinson's disease. *J. Neurochem.* **126**, 591–603.
- González-Hernández T., Cruz-Muros I., Afonso-Oramas D., Salas-Hernandez J., Castro-Hernandez J. (2010) Vulnerability of Mesostriatal Dopaminergic Neurons in Parkinson's Disease. *Front. Neuroanat.* **4**.
- Graham D. G., Tiffany S. M., Bell W. R., Gutknecht W. F. (1978) Autoxidation versus Covalent Binding of Quinones as the Mechanism of Toxicity of Dopamine, 6-Hydroxydopamine, and Related Compounds toward CI 300 Neuroblastoma Cells in Vitro. *Mol. Pharmacol.* **14**, 644–653.
- Granatiero V., Stefani D. De, Rizzuto R. (2017) Mitochondrial Calcium Handling in Physiology and Disease. *Adv. Exp. Med. Biol.* **982**, 25–47.
- Graves S. M., Xie Z., Stout K. A., Zampese E., Burbulla L. F., Shih J. C., Kondapalli J., et al. (2019) Dopamine metabolism by a monoamine oxidase mitochondrial shuttle activates the electron transport chain. *Nat. Neurosci.* **2019 231 23**, 15–20.

- Grima B., Lamouroux A., Boni C., Julien J. F., Javoy-agid F., Mallet J. (1987) A single human gene encoding multiple tyrosine hydroxylases with different predicted functional characteristics. *Nature* **326**, 707–711.
- Gupta H. V., Vengoechea J., Sahaya K., Virmani T. (2015) A splice site mutation in *ATP6AP2* causes X-linked intellectual disability, epilepsy, and parkinsonism. *Parkinsonism Relat Disord.*
- Halliday G. M., Blumbergs P. C., Cotton R. G. H., Blessing W. W., Geffen L. B. (1990) Loss of brainstem serotonin- and substance P-containing neurons in Parkinson's disease. *Brain Res.* **510**, 104–107.
- Hammes-Schiffer S. (2012) Catalytic Efficiency of Enzymes: A Theoretical Analysis. *Biochemistry* **52**, 2012–2020.
- Han D., Antunes F., Canali R., Rettori D., Cadenas E. (2003) Voltage-dependent anion channels control the release of the superoxide anion from mitochondria to cytosol. *J. Biol. Chem.* **278**, 5557–5563.
- Hasilik A., Figura K. von, Conzelmann E., Nehr Korn H., Sandhoff K. (1982) Lysosomal enzyme precursors in human fibroblasts. Activation of cathepsin D precursor in vitro and activity of beta-hexosaminidase A precursor towards ganglioside GM2. *Eur. J. Biochem.* **125**, 317–21.
- Hastings T. G. (1995) Enzymatic oxidation of dopamine: the role of prostaglandin H synthase. *J. Neurochem.* **64**, 919–924.
- Hastings T. G., Zigmond M. J. (1997) Loss of dopaminergic neurons in parkinsonism: possible role of reactive dopamine metabolites. *J. Neural Transm. Suppl.* **49**, 103–110.
- Hauser R. A. (2009) Levodopa: Past, Present, and Future. *Eur. Neurol.* **62**, 1–8.
- Hawkes C. H., Tredici K. Del, Braak H. (2007) Parkinson's disease: a dual-hit hypothesis. *Neuropathol. Appl. Neurobiol.* **33**, 599–614.
- Hayashi T., Ishimori C., Takahashi-Niki K., Taira T., Kim Y. chul, Maita H., Maita C., Ariga H., Iguchi-Ariga S. M. M. (2009) DJ-1 binds to mitochondrial complex I and maintains its activity. *Biochem. Biophys. Res. Commun.* **390**, 667–672.

- He H., Stein C. M., Christman B., Wood A. J. J. (1997) Determination of catecholamines in sheep plasma by high-performance liquid chromatography with electrochemical detection: Comparison of deoxyepinephrine and 3,4-dihydroxybenzylamine as internal standard. *J. Chromatogr. B Biomed. Appl.* **701**, 115–119.
- He Y., Zhang W.-Y. Y., Gong M., Huang J.-Y. Y., Tang N., Feng T., Wei G.-H. H., He T.-C. C., Bi Y. (2011) Low serum concentration facilitates the differentiation of hepatic progenitor cells. *Saudi Med. J.* **32**, 128–34.
- Heaton R. A., Heales S., Rahman K., Sexton D. W., Hargreaves I. (2020) The Effect of Cellular Coenzyme Q10 Deficiency on Lysosomal Acidification. *J. Clin. Med.* **9**, 1923.
- Heger L. M., Wise R. M., Hees J. T., Harbauer A. B., Burbulla L. F. (2021) Mitochondrial Phenotypes in Parkinson's Diseases—A Focus on Human iPSC-Derived Dopaminergic Neurons. *Cells* **10**, 3436.
- Heikkila R. E., Manzino L., Cabbat F. S., Duvoisin R. C. (1984) Protection against the dopaminergic neurotoxicity of 1-methyl-4-phenyl-1,2,5,6-tetrahydropyridine by monoamine oxidase inhibitors. *Nat.* 1984 3115985 **311**, 467–469.
- Hein L. K., Meikle P. J., Hopwood J. J., Fuller M. (2007) Secondary sphingolipid accumulation in a macrophage model of Gaucher disease. *Mol. Genet. Metab.* **92**, 336–345.
- Heo J. Y., Park J. H., Kim S. J., Seo K. S., Han J. S., Lee S. H., Kim J. M., et al. (2012) DJ-1 Null Dopaminergic Neuronal Cells Exhibit Defects in Mitochondrial Function and Structure: Involvement of Mitochondrial Complex I Assembly. *PLoS One* **7**, 32629.
- Hermida-Ameijeiras Á., Méndez-Álvarez E., Sánchez-Iglesias S., Sanmartín-Suárez C., Soto-Otero R. (2004) Autoxidation and MAO-mediated metabolism of dopamine as a potential cause of oxidative stress: role of ferrous and ferric ions. *Neurochem. Int.* **45**, 103–116.
- Herrera A., Munoz P., Steinbusch H. W. M., Segura-Aguilar J. (2017a) Are

Dopamine Oxidation Metabolites Involved in the Loss of Dopaminergic Neurons in the Nigrostriatal System in Parkinson's Disease? *ACS Chem Neurosci* **8**, 702–711.

Herrera A., Muñoz P., Steinbusch H. W. M., Segura-Aguilar J. (2017b) Are Dopamine Oxidation Metabolites Involved in the Loss of Dopaminergic Neurons in the Nigrostriatal System in Parkinson's Disease? *ACS Chem. Neurosci.* **8**, 702–711.

Himmelreich N., Montioli R., Bertoldi M., Carducci C., Leuzzi V., Gemperle C., Berner T., et al. (2019) Aromatic amino acid decarboxylase deficiency: Molecular and metabolic basis and therapeutic outlook. *Mol. Genet. Metab.* **127**, 12–22.

Hirst J., King M. S., Pryde K. R. (2008) The production of reactive oxygen species by complex I ROS (reactive oxygen species) production by complex I in the cell. *Biochem. Soc. Trans.* **36**.

Hodgson N., Trivedi M., Muratore C., Li S., Deth R. (2013) Soluble oligomers of amyloid- β cause changes in redox state, DNA methylation, and gene transcription by inhibiting EAAT3 mediated cysteine uptake. *J. Alzheimers. Dis.* **36**, 197–209.

Hoffmann G. F., Assmann B., Bräutigam C., Dionisi-Vici C., Häussler M., Klerk J. B. C. De, Naumann M., Steenbergen-Spanjers G. C. H., Strassburg H. M., Wevers R. A. (2003) Tyrosine hydroxylase deficiency causes progressive encephalopathy and dopa-nonresponsive dystonia. *Ann. Neurol.* **54**, S56–S65.

Holdorff B. (2006) Fritz Heinrich Lewy (1885-1950). *J. Neurol.* **253**, 677–678.

Holmay M. J., Terpstra M., Coles L. D., Mishra U., Ahlskog M., Öz G., Cloyd J. C., Tuite P. J. (2013) N-acetylcysteine Boosts Brain and Blood Glutathione in Gaucher and Parkinson's Diseases. *Clin. Neuropharmacol.* **36**, 103.

Holper L., Ben-Shachar D., Mann J. J. (2019) Multivariate meta-analyses of mitochondrial complex I and IV in major depressive disorder, bipolar disorder, schizophrenia, Alzheimer disease, and Parkinson disease.

Neuropsychopharmacology **44**, 837–849.

Hong-rong X., Lin-sen H., Guo-yi L. (2010) SH-SY5Y human neuroblastoma cell line: in vitro cell model of dopaminergic neurons in Parkinson's disease. *Chin. Med. J. (Engl)*. **123**, 1086–1092.

Hornykiewicz O. (2002) Dopamine miracle: From brain homogenate to dopamine replacement. *Mov. Disord.* **17**, 501–508.

Horvath C. G., Preiss B. A., Lipsky S. R. (1967) Fast Liquid Chromatography: An Investigation of Operating Parameters and the Separation of Nucleotides on Pellicular Ion Exchangers. *Anal. Chem.*

Hu Y. B., Dammer E. B., Ren R. J., Wang G. (2015) The endosomal-lysosomal system: From acidification and cargo sorting to neurodegeneration. *Transl. Neurodegener.* **4**, 1–10.

Hudson G., Schaefer A. M., Taylor R. W., Tiangyou W., Gibson A., Venables G., Griffiths P., Burn D. J., Turnbull D. M., Chinnery P. F. (2007) Mutation of the Linker Region of the Polymerase γ -1 (POLG1 Gene Associated With Progressive External Ophthalmoplegia and Parkinsonism. *Arch. Neurol.* **64**, 553–557.

Huenchuguala S., Muñoz P., Zavala P., Villa M. M. M., Cuevas C., Ahumada U., Graumann R., et al. (2014) Glutathione transferase mu 2 protects glioblastoma cells against aminochrome toxicity by preventing autophagy and lysosome dysfunction. *Autophagy* **10**, 618–630.

Hughes L. P., Pereira M. M. M., Hammond D. A., Kwok J. B., Halliday G. M., Lewis S. J. G., Dzamko N. (2021) Glucocerebrosidase Activity is Reduced in Cryopreserved Parkinson's Disease Patient Monocytes and Inversely Correlates with Motor Severity. *J. Parkinsons. Dis.*, 1–9.

Hwu W. L., Muramatsu S. I., Tseng S. H., Tzen K. Y., Lee N. C., Chien Y. H., Snyder R. O., Byrne B. J., Tai C. H., Wu R. M. (2012) Gene therapy for aromatic L-amino acid decarboxylase deficiency. *Sci. Transl. Med.* **4**.

Hyland K. (2008) Clinical utility of monoamine neurotransmitter metabolite analysis in cerebrospinal fluid. *Clin. Chem.* **54**, 633–641.

- Hyland K., Clayton P. T. (1992) Aromatic L-amino acid decarboxylase deficiency: Diagnostic methodology. *Clin. Chem.* **38**, 2405–2410.
- Ichinose H. (2000) [Segawa's disease]. *Rinsho Shinkeigaku* **40**, 1284–1286.
- Ichinose H., Ohye T., Fujita K., Pantucek F., Lange K., Riederer P., Nagatsu T. (1994) Quantification of mRNA of tyrosine hydroxylase and aromatic L-amino acid decarboxylase in the substantia nigra in Parkinson's disease and schizophrenia. *J. Neural Transm. Park. Dis. Dement. Sect.* **8**, 149–158.
- Ikeda H., Ikegaki N., Kennett R. H., Wilson D. F. (1994) Retinoic Acid Induced Differentiation in Human Neuroblastoma. **19**, 1487–1494.
- Ino D., Iino M. (2017) Schwann cell mitochondria as key regulators in the development and maintenance of peripheral nerve axons. *Cell. Mol. Life Sci.* **74**, 827–835.
- Isgrò M. A., Bottoni P., Scatena R. (2015) Neuron-specific enolase as a biomarker: Biochemical and clinical aspects, in *Adv. Exp. Med. Biol.*, Vol. 867, pp. 125–143. Springer, Dordrecht.
- Ivankovic D., Chau K. Y., Schapira A. H., Gegg M. E., D'I., KY C., AH S., et al. (2016) Mitochondrial and lysosomal biogenesis are activated following PINK1/parkin-mediated mitophagy. *J Neurochem* **136**, 388–402.
- Jenkins B. G., Koroshetz W. J., Beal M. F., Rosen B. R. (1993) Evidence for impairment of energy metabolism in vivo in Huntington's disease using localized ¹H NMR spectroscopy. *Neurology* **43**, 2689–2695.
- Jenner P., Hunot, Olanow, Beal, Kordower, Tatton, Schapira (2003) *Oxidative stress in Parkinson's disease*. *Ann Neurol*.
- Jeong S. Y., Seol D. W. (2008) The role of mitochondria in apoptosis. *BMB Rep.* **41**, 11–22.
- Jha N., Jurma O., Lalli G., Liu Y., Pettus E. H., Greenamyre J. T., Liu R. M., Forman H. J., Andersen J. K. (2000) Glutathione Depletion in PC12 Results in Selective Inhibition of Mitochondrial Complex I Activity: IMPLICATIONS FOR PARKINSON'S DISEASE. *J. Biol. Chem.* **275**, 26096–26101.

- Jillienne C. Touchette, Julie M. Breckenridge, Gerald H. Wilken and H. M. (2017) Direct intranigral injection of dopaminochrome causes degeneration of dopamine neurons. *55*, 9557–9561.
- Jin C. M., Yang Y. J., Huang H. S., Lim S. C., Kai M., Lee M. K. (2008) Induction of dopamine biosynthesis by L-DOPA in PC12 cells: implications of L-DOPA influx and cyclic AMP. *Eur. J. Pharmacol.* **591**, 88–95.
- Jonckheere A. I., Smeitink J. A. M., Rodenburg R. J. T. (2012) Mitochondrial ATP synthase: architecture, function and pathology. *J. Inherit. Metab. Dis.* **35**, 211–225.
- Jones D. N., Raghanti M. A. (2021) The role of monoamine oxidase enzymes in the pathophysiology of neurological disorders. *J. Chem. Neuroanat.* **114**, 101957.
- Juárez Olguín H., Calderón Guzmán D., Hernández García E., Barragán Mejía G. (2016) The Role of Dopamine and Its Dysfunction as a Consequence of Oxidative Stress. *Oxid. Med. Cell. Longev.* **2016**, 1–13.
- Jurma O. P., Hom D. G., Andersen J. K. (1997) Decreased Glutathione Results in Calcium-Mediated Cell Death in PC12. *Free Radic. Biol. Med.* **23**, 1055–1066.
- Kalia L. V., Lang A. E. (2015) Parkinson's disease. *Lancet* **386**, 896–912.
- Kane P. M. (1995) Disassembly and reassembly of the yeast vacuolar H⁺-ATPase in vivo. *J. Biol. Chem.* **270**, 17025–17032.
- Kang I., Chu C. T., Kaufman B. A. (2018) *The mitochondrial transcription factor TFAM in neurodegeneration: emerging evidence and mechanisms*. Wiley Blackwell.
- Kang J., Kim J. W., Heo H., Lee J., Park K. Y., Yoon J. H., Chang J. (2021) Identification of BAG2 and Cathepsin D as Plasma Biomarkers for Parkinson's Disease. *Clin. Transl. Sci.* **14**, 606–616.
- Kang Y., Viswanath V., Jha N., Qiao X., Mo J. Q., Andersen J. K. (1999) Brain γ -glutamyl cysteine synthetase (GCS) mRNA expression patterns correlate with regional-specific enzyme activities and glutathione levels. *J. Neurosci.*

Res. **58**, 436–441.

- Kaur G., Dufour J. M. (2012) Cell lines: Valuable tools or useless artifacts. *Spermatogenesis* **2**, 1.
- Keeney P. M., Xie J., Capaldi R. A., Bennett J. P. (2006) Parkinson's disease brain mitochondrial complex I has oxidatively damaged subunits and is functionally impaired and misassembled. *J. Neurosci.* **26**, 5256–5264.
- Khwanraj K., Phruksaniyom C., Madlah S., Dharmasaroja P. (2015) Differential Expression of Tyrosine Hydroxylase Protein and Apoptosis-Related Genes in Differentiated and Undifferentiated SH-SY5Y Neuroblastoma Cells Treated with MPP+. *Neurol. Res. Int.* **2015**.
- Kilpatrick I. C., Jones M. W., Phillipson O. T. (1986) A Semiautomated Analysis Method for Catecholamines, Indoleamines, and Some Prominent Metabolites in Microdissected Regions of the Nervous System: An Isocratic HPLC Technique Employing Coulometric Detection and Minimal Sample Preparation. *J. Neurochem.* **46**, 1865–1876.
- Kim K. K., Adelstein R. S., Kawamoto S. (2009) Identification of Neuronal Nuclei (NeuN) as Fox-3, a New Member of the Fox-1 Gene Family of Splicing Factors. *J. Biol. Chem.* **284**, 31052–31061.
- Kim S., Wong Y. C., Gao F., Krainc D. (2021) Dysregulation of mitochondria-lysosome contacts by GBA1 dysfunction in dopaminergic neuronal models of Parkinson's disease. *Nat. Commun.* **12**.
- Kim S., Yun S. P., Lee S., Umanah G. E., Bandaru V. V. R., Yin X., Rhee P., et al. (2018) GBA1 deficiency negatively affects physiological α -synuclein tetramers and related multimers. *Proc. Natl. Acad. Sci. U. S. A.* **115**, 798–803.
- King T. E., Howard R. L. (1967) [52] Preparations and properties of soluble NADH dehydrogenases from cardiac muscle. *Methods Enzymol.* **10**, 275–294.
- Kish S. J., Morito C., Hornykiewicz O. (1985) Glutathione peroxidase activity in Parkinson's disease brain. *Neurosci. Lett.* **58**, 343–346.

- Kitada T., Asakawa S., Hattori N., Matsumine H., Yamamura Y., Minoshima S., Yokochi M., Mizuno Y., Shimizu N. (1998) Mutations in the parkin gene cause autosomal recessive juvenile parkinsonism. *Nat.* 1998 3926676 **392**, 605–608.
- Klepac N., Relja M., Klepac R., Hećimović S., Babić T., Trkulja V. (2007) Oxidative stress parameters in plasma of Huntington's disease patients, asymptomatic Huntington's disease gene carriers and healthy subjects. *J. Neurol.* 2007 25412 **254**, 1676–1683.
- Kobayashi K., Kaneda N., Ichinose H., Kishi F., Nakazawa A., Kurosawa Y., Fujita K., Nagatsu T. (1988) Structure of the human tyrosine hydroxylase gene: alternative splicing from a single gene accounts for generation of four mRNA types. *J. Biochem.* **103**, 907–912.
- Koike M., Shibata M., Waguri S., Yoshimura K., Tanida I., Kominami E., Gotow T., et al. (2005) Participation of autophagy in storage of lysosomes in neurons from mouse models of neuronal ceroid-lipofuscinoses (Batten disease). *Am. J. Pathol.* **167**, 1713–1728.
- Kojima K., Nakajima T., Taga N., Miyauchi A., Kato M., Matsumoto A., Ikeda T., et al. (2019) Gene therapy improves motor and mental function of aromatic l-amino acid decarboxylase deficiency. *Brain* **142**, 322–333.
- Korecka J. A., Kesteren R. E. van, Blaas E., Spitzer S. O., Kamstra J. H., Smit A. B., Swaab D. F., Verhaagen J., Bossers K. (2013) Phenotypic characterization of retinoic acid differentiated SH-SY5Y cells by transcriptional profiling. *PLoS One* **8**, e63862.
- Koros C., Simitsi A., Stefanis L. (2017) Genetics of Parkinson's Disease: Genotype–Phenotype Correlations. *Int. Rev. Neurobiol.* **132**, 197–231.
- Korvatska O., Strand N. S., Berndt J. D., Strovast T., Chen D. H., Leverenz J. B., Kikianitsa K., et al. (2013) Altered splicing of ATP6AP2 causes X-linked parkinsonism with spasticity (XPDS). *Hum. Mol. Genet.* **22**, 3259–3268.
- Kovalevich J., Langford D. (2013) Considerations for the use of SH-SY5Y neuroblastoma cells in neurobiology. *Methods Mol Biol* **1078**, 9–21.

- Kraft C. S., Lemoine C. M. R., Lyons C. N., Michaud D., Mueller C. R., Moyes C. D. (2006) Control of mitochondrial biogenesis during myogenesis. *Am J Physiol Cell Physiol* **290**, 1119–1127.
- Kriks S., Shim J.-W., Piao J., Ganat Y. M., Wakeman D. R., Xie Z., Carrillo-Reid L., et al. (2011) Dopamine neurons derived from human ES cells efficiently engraft in animal models of Parkinson's disease.
- Krishna A., Biryukov M., Trefois C., Antony P. M. A. A., Hussong R., Lin J., Heinäniemi M., et al. (2014) Systems genomics evaluation of the SH-SY5Y neuroblastoma cell line as a model for Parkinson's disease. *BMC Genomics* **15**, 1–21.
- Kristensen A. S., Andersen J., Jorgensen T. N., Sorensen L., Eriksen J., Loland C. J., Stromgaard K., Gether U. (2011) SLC6 Neurotransmitter Transporters: Structure, Function, and Regulation. *Pharmacol. Rev.* **63**, 585–640.
- Krueger M. J., Sablin S. O., Ramsay R., Singer T. P. (1993) Reactivation of NADH dehydrogenase (complex I) inhibited by 1-methyl-4-(4'-alkylphenyl)pyridinium analogues: a clue to the nature of the inhibition site. *J. Neurochem.* **61**, 1546–1548.
- Kurian M. A., Zhen J., Cheng S. Y., Li Y., Mordekar S. R., Jardine P., Morgan N. V., et al. (2009) Homozygous loss-of-function mutations in the gene encoding the dopamine transporter are associated with infantile parkinsonism-dystonia. *J. Clin. Invest.* **119**, 1595–1603.
- Kurzawa-Akanbi M., Hanson P. S., Blain P. G., Lett D. J., McKeith I. G., Chinnery P. F., Morris C. M. (2012) Glucocerebrosidase Mutations alter the endoplasmic reticulum and lysosomes in Lewy body disease. *J. Neurochem.* **123**, 298.
- la Fuente C. de (2018) *Dopamine and Serotonin Metabolism in Parkinson's Models*. UCL.
- la Fuente C. de, Burke D. G., Eaton S., Heales S. J. R. R. (2017) Inhibition of neuronal mitochondrial complex I or lysosomal glucocerebrosidase is

associated with increased dopamine and serotonin turnover. *Neurochem. Int.* **109**, 94–100.

Lamantea E., Carrara F., Mariotti C., Morandi L., Tiranti V., Zeviani M. (2002) A novel nonsense mutation (Q352X) in the mitochondrial cytochrome b gene associated with a combined deficiency of complexes I and III. *Neuromuscul. Disord.* **12**, 49–52.

Lang A., Dassler E., Milenkovic I., Lutz M. I., Kovacs G. G. (2021) Variable expression of mitochondrial complex IV in the course of nigral intracellular accumulation of α -synuclein. *Park. Relat. Disord.* **90**, 57–61.

Langston J. W. (2017) The MPTP story. *J. Parkinsons. Dis.* **7**, S11–S19.

Langston J. W., Irwin I., Langston E. B., Forno L. S. (1984) 1-Methyl-4-phenylpyridinium ion (MPP⁺): identification of a metabolite of MPTP, a toxin selective to the substantia nigra. *Neurosci. Lett.* **48**, 87–92.

Larsen S., Nielsen J., Hansen C. N., Nielsen L. B., Wibrand F., Stride N., Schroder H. D., et al. (2012) Biomarkers of mitochondrial content in skeletal muscle of healthy young human subjects. *J. Physiol.* **590**, 3349–3360.

Laurent-Matha V., Derocq D., Prébois C., Katunuma N., Liaudet-Coopman E. (2006) Processing of human cathepsin D is independent of its catalytic function and auto-activation: Involvement of cathepsins L and B. *J. Biochem.* **139**, 363–371.

Lavoie M. J., Ostaszewski B. L., Weihofen A., Schlossmacher M. G., Selkoe D. J. (2005) Dopamine covalently modifies and functionally inactivates parkin. **11**.

Lee A., Gilbert R. M. (2016) Epidemiology of Parkinson Disease. *Neurol. Clin.* **34**, 955–965.

Lee C. R., Patel J. C., O'Neill B., Rice M. E. (2015) Inhibitory and excitatory neuromodulation by hydrogen peroxide: translating energetics to information. *J Physiol* **593**, 3431–3446.

Lee D. W., Kaur D., Chinta S. J., Rajagopalan S., Andersen J. K. (2009) A

Disruption in Iron-Sulfur Center Biogenesis via Inhibition of Mitochondrial Dithiol Glutaredoxin 2 May Contribute to Mitochondrial and Cellular Iron Dysregulation in Mammalian Glutathione-Depleted Dopaminergic Cells: Implications for Parkinson's Disease. *Antioxid. Redox Signal.* **11**, 2083.

Lee R. G., Sedghi M., Salari M., Shearwood A.-M. J., Stentenbach M., Kariminejad A., Goullee H., et al. (2018) Early-onset Parkinson disease caused by a mutation in CHCHD2 and mitochondrial dysfunction. *Neurol. Genet.* **4**, e276.

Lelieveld L. T., Gerhardt S., Maas S., Zwiers K. C., Wit C. de, Beijk E. H., Ferraz M. J., et al. (2022) Consequences of excessive glucosylsphingosine in glucocerebrosidase-deficient zebrafish. *J. Lipid Res.* **63**, 100199.

Lezi E., Swerdlow R. H. (2012) Mitochondria in neurodegeneration. *Adv. Exp. Med. Biol.* **942**, 269–286.

Li D., Ding Z., Gui M., Hou Y., Xie K. (2020) Metabolic Enhancement of Glycolysis and Mitochondrial Respiration Are Essential for Neuronal Differentiation. *Cell. Reprogram.* **22**, 291–299.

Li H., Ham A., Ma T. C., Kuo S.-H. H., Kanter E., Kim D., Ko H. S., et al. (2019) Mitochondrial dysfunction and mitophagy defect triggered by heterozygous GBA mutations. *Autophagy* **15**, 113–130.

Li W. W., Yang R., Guo J. C., Ren H. M., Zha X. L., Cheng J. S., Cai D. F. (2007) Localization of α -synuclein to mitochondria within midbrain of mice. *Neuroreport* **18**, 1543–1546.

Li Z., Okamoto K. I., Hayashi Y., Sheng M. (2004) The importance of dendritic mitochondria in the morphogenesis and plasticity of spines and synapses. *Cell* **119**, 873–887.

Lill C. M. (2016) Genetics of Parkinson's disease. *Mol. Cell. Probes* **30**, 386–396.

Lim J. A., Li L., Kakhlon O., Myerowitz R., Raben N. (2015) Defects in calcium homeostasis and mitochondria can be reversed in Pompe disease. *Autophagy* **11**, 385–402.

- Lin C. H., Tsai P. I., Lin H. Y., Hattori N., Funayama M., Jeon B., Sato K., et al. (2020) Mitochondrial UQCRC1 mutations cause autosomal dominant parkinsonism with polyneuropathy. *Brain* **143**, 3352–3373.
- Linert W., Herlinger E., Jameson R. F., Kienzl E., Jellinger K., Youdim M. B. H. (1996) Dopamine, 6-hydroxydopamine, iron, and dioxygen--their mutual interactions and possible implication in the development of Parkinson's disease. *Biochim. Biophys. Acta* **1316**, 160–168.
- Liu G., David B. T., Trawczynski M., Fessler R. G. (2020) Advances in Pluripotent Stem Cells: History, Mechanisms, Technologies, and Applications. *Stem cell Rev. reports* **16**, 3–32.
- Lloyd K. G., Davidson L., Hornykiewicz O. (1975) The neurochemistry of Parkinson's disease: effect of L-dopa therapy. *J. Pharmacol. Exp. Ther.* **195**.
- Longo C., Montioli R., Bisello G., Palazzi L., Mastrangelo M., Brennenstuhl H., Laureto P. P. de, Opladen T., Leuzzi V., Bertoldi M. (2021) Compound heterozygosis in AADC deficiency: A complex phenotype dissected through comparison among heterodimeric and homodimeric AADC proteins. *Mol. Genet. Metab.* **134**, 147–155.
- Looyenga B. D., Resau J., MacKeigan J. P. (2013) Cytokine Receptor-Like Factor 1 (CRLF1) Protects against 6-Hydroxydopamine Toxicity Independent of the gp130/JAK Signaling Pathway. *PLoS One* **8**.
- Lopes F. M., Bristot I. J., Motta L. L. da, Parsons R. B., Klamt F. (2017a) Mimicking Parkinson's Disease in a Dish: Merits and Pitfalls of the Most Commonly used Dopaminergic In Vitro Models. *NeuroMolecular Med.* 2017 **19**, 241–255.
- Lopes F. M., Motta L. L. da, Bastiani M. A. De, Pfaffenseller B., Aguiar B. W., Souza L. F. de, Zanatta G., et al. (2017b) RA Differentiation Enhances Dopaminergic Features, Changes Redox Parameters, and Increases Dopamine Transporter Dependency in 6-Hydroxydopamine-Induced Neurotoxicity in SH-SY5Y Cells. *Neurotox Res* **31**, 545–559.

- Lopes F. M., Schroder R., Frota Jr. M. L. da, Zanotto-Filho A., Muller C. B., Pires A. S., Meurer R. T., et al. (2010) Comparison between proliferative and neuron-like SH-SY5Y cells as an in vitro model for Parkinson disease studies. *Brain Res* **1337**, 85–94.
- Lopez-Fabuel I., Douce J. Le, Logan A., James A. M., Bonvento G., Murphy M. P., Almeida A., Bolaños J. P. (2016) Complex I assembly into supercomplexes determines differential mitochondrial ROS production in neurons and astrocytes. *Proc. Natl. Acad. Sci. U. S. A.* **113**, 13063–13068.
- Lopez-Fabuel I., Martin-Martin L., Resch-Beusher M., Azkona G., Sanchez-Pernaute R., Bolaños J. P. (2017) Mitochondrial respiratory chain disorganization in Parkinson's disease-relevant PINK1 and DJ1 mutants. *Neurochem. Int.* **109**, 101–105.
- Lovenberg W., Levine R. A., Robinson D. S., Ebert M., Williams A. C., Calne D. B. (1979) Hydroxylase cofactor activity in cerebrospinal fluid of normal subjects and patients with Parkinson's disease. *Science* **204**, 624–626.
- Lu L., Jia H., Gao G., Duan C., Ren J., Li Y., Yang H. (2018) Pink1 Regulates Tyrosine Hydroxylase Expression and Dopamine Synthesis. *J. Alzheimer's Dis.* **63**, 1361–1371.
- Lu S. C. (2009) REGULATION OF GLUTATHIONE SYNTHESIS. *Mol. Aspects Med.* **30**, 42.
- Lu S. C. (2014) Glutathione Synthesis. *Biochim Biophys Acta.* **1830**, 3143–3153.
- Lüdecke B., Knappskog P. M., Clayton P. T., Surtees R. A. H., Clelland J. D., Heales S. J. R., Brand M. P., Bartholomé K., Flatmark T. (1996) Recessively inherited L-DOPA-responsive parkinsonism in infancy caused by a point mutation (L205P) in the tyrosine hydroxylase gene. *Hum. Mol. Genet.* **5**, 1023–1028.
- Luzio J. P., Parkinson M. D. J., Gray S. R., Bright N. A. (2009) The delivery of endocytosed cargo to lysosomes. *Biochem. Soc. Trans.* **37**, 1019–1021.
- Lwin A., Orvisky E., Goker-Alpan O., LaMarca M. E., Sidransky E. (2004)

- Glucocerebrosidase mutations in subjects with parkinsonism. *Mol. Genet. Metab.* **81**, 70–73.
- Ma L., Ouyang Q., Werthmann G. C., Thompson H. M., Morrow E. M. (2017) Live-cell Microscopy and Fluorescence-based Measurement of Luminal pH in Intracellular Organelles. *Front. Cell Dev. Biol.* **5**, 1–18.
- Machaczka M., ... M. R.-A. journal of, 1999 undefined (1999) Parkinson's syndrome preceding clinical manifestation of Gaucher's disease. *Wiley Online Libr.*
- Maden M. (2007) Retinoic acid in the development, regeneration and maintenance of the nervous system. *Nat. Rev. Neurosci.* 2007 810 **8**, 755–765.
- Mader B. J., Pivtoraiko V. N., Flippo H. M., Klocke B. J., Roth K. A., Mangieri L. R., Shacka J. J. (2012) Rotenone Inhibits Autophagic Flux Prior to Inducing Cell Death.
- Magalingam K. B., Radhakrishnan A. K., Somanath S. D., Md S., Haleagrahara N. (2020) Influence of serum concentration in retinoic acid and phorbol ester induced differentiation of SH-SY5Y human neuroblastoma cell line. *Mol. Biol. Rep.* **47**, 8775–8788.
- Mahul-Mellier A. L., Burtscher J., Maharjan N., Weerens L., Croisier M., Kuttler F., Leleu M., Knott G. W., Lashuel H. A. (2020) The process of Lewy body formation, rather than simply α -synuclein fibrillization, is one of the major drivers of neurodegeneration. *Proc. Natl. Acad. Sci. U. S. A.* **117**, 4971–4982.
- Maio R. Di, Barrett P. J., Hoffman E. K., Barrett C. W., Zharikov A., Borah A., Hu X., et al. (2016) α -Synuclein binds to TOM20 and inhibits mitochondrial protein import in Parkinson's disease. *Sci. Transl. Med.* **8**, 301–330.
- Mandal P. K., Saharan S., Tripathi M., Murari G. (2015) Brain glutathione levels -a novel biomarker for mild cognitive impairment and Alzheimer's disease. *Biol. Psychiatry* **78**, 702–710.
- Maranzana E., Barbero G., Falasca A. I., Lenaz G., Genova M. L. (2013)

Mitochondrial respiratory supercomplex association limits production of reactive oxygen species from complex i. *Antioxidants Redox Signal.* **19**, 1469–1480.

Marco R., Pestaña A., Sebastian J., Sols A. (1974) Oxaloacetate metabolic crossroads in liver. Enzyme compartmentation and regulation of gluconeogenesis. *Mol. Cell. Biochem.* **3**, 53–70.

Markovic J., Borrás C., Ortega Á., Sastre J., Viña J., Pallardó F. V. (2007) Glutathione is recruited into the nucleus in early phases of cell proliferation. *J. Biol. Chem.* **282**, 20416–20424.

Martin A. J. P., Syngé R. L. M. (1941) A new form of chromatogram employing two liquid phases. *Biochem. J.*

Marton R. M., Ioannidis J. P. A. (2019) A Comprehensive Analysis of Protocols for Deriving Dopaminergic Neurons from Human Pluripotent Stem Cells. *Stem Cells Transl. Med.* **8**, 366–374.

Masato A., Plotegher N., Boassa D., Bubacco L. (2019) Impaired dopamine metabolism in Parkinson's disease pathogenesis. *Mol. Neurodegener.* **14**.

Matsui H., Taniguchi Y., Inoue H., Kobayashi Y., Sakaki Y., Toyoda A., Uemura K., Kobayashi D., Takeda S., Takahashi R. (2010) Loss of PINK1 in medaka fish (*Oryzias latipes*) causes late-onset decrease in spontaneous movement. *Neurosci. Res.* **66**, 151–161.

Mattammal M. B., Haring J. H., Chung H. D., Raghu G., Strong R. (1995) An endogenous dopaminergic neurotoxin: implication for Parkinson's disease. *Neurodegeneration* **4**, 271–281.

Maynard M. E., Redell J. B., Kobori N., Underwood E. L., Fischer T. D., Hood K. N., LaRoche V., Waxham M. N., Moore A. N., Dash P. K. (2020) Loss of PTEN-induced kinase 1 (Pink1) reduces hippocampal tyrosine hydroxylase and impairs learning and memory. *Exp. Neurol.* **323**.

Mazzulli J. R., Mishizen A. J., Giasson B. I., Lynch D. R., Thomas S. A., Nakashima A., Nagatsu T., Ota A., Ischiropoulos H. (2006) Cytosolic Catechols Inhibit α -Synuclein Aggregation and Facilitate the Formation of

- Intracellular Soluble Oligomeric Intermediates. *J. Neurosci.* **26**, 10068.
- McGuire C., Stransky L., Cotter K., Forgac M. (2017) Regulation of V-ATPase activity. *Front. Biosci. (Landmark Ed.)* **22**, 609–622.
- McHugh P. C., Buckley D. A. (2015) The Structure and Function of the Dopamine Transporter and its Role in CNS Diseases. *Vitam. Horm.* **98**, 339–369.
- Meiser J., Weindl D., Hiller K. (2013) Complexity of dopamine metabolism. *Cell Commun. Signal.* **11**, 34.
- Melino G., Thiele C. J., Knight R. A., Piacentini M. (1997) Retinoids and the control of growth/death decisions in human neuroblastoma cell lines. *J. Neurooncol.* **31**, 65–83.
- Mencarelli C., Martinez-Martinez P. (2013) Ceramide function in the brain: when a slight tilt is enough. *Cell. Mol. Life Sci.* **70**, 181–203.
- Meredith M. J., Reed D. J. (1982) Status of the mitochondrial pool of glutathione in the isolated hepatocyte. *J. Biol. Chem.* **257**, 3747–3753.
- Meyer V. R. (2010) *Practical High-Performance Liquid Chromatography: Fifth Edition.*
- Michel P. P., Hirsch E. C., Hunot S. (2016) Understanding Dopaminergic Cell Death Pathways in Parkinson Disease. *Neuron* **90**, 675–691.
- Migdalska-Richards A., Schapira A. H. V. V (2016) The relationship between glucocerebrosidase mutations and Parkinson disease. *J. Neurochem.* **139**, 77–90.
- Mijanovic O., Petushkova A. I., Brankovic A., Turk B., Solovieva A. B., Nikitina A. I., Bolevich S., Timashev P. S., Parodi A., Zamyatnin A. A. (2021) *Cathepsin d—managing the delicate balance.* MDPI AG.
- Minard K. I., Jennings G. T., Loftus T. M., Xuan D., McAlister-Henn L. (1998) Sources of NADPH and Expression of Mammalian NADP⁺-specific Isocitrate Dehydrogenases in *Saccharomyces cerevisiae* *.
- Minarowska A., Gacko M., Karwowska A., Minarowski Ł. (2008) Human

- cathepsin D. *Folia Histochem. Cytobiol.* **46**, 23–38.
- Mindell J. A. (2012) Lysosomal Acidification Mechanisms. *Annu. Rev. Physiol.* **74**, 69–86.
- Mizushima N., Levine B., Cuervo A. M., Klionsky D. J. (2008) Autophagy fights disease through cellular self-digestion. *Nature* **451**, 1069.
- Mogi M., Harada M., Kiuchi K., Kojima K., Kondo T., Narabayashi H., Rausch D., Riederer P., Jellinger K., Nagatsu T. (1988) Homospecific activity (activity per enzyme protein) of tyrosine hydroxylase increases in parkinsonian brain. *J. Neural Transm.* **72**, 77–82.
- Montagu K. A., Montagu, A. K. (1957) Catechol Compounds in Rat Tissues and in Brains of Different Animals. *Natur* **180**, 244–245.
- Montioli R., Bisello G., Dindo M., Rossignoli G., Voltattorni C. B., Bertoldi M. (2020) New variants of AADC deficiency expand the knowledge of enzymatic phenotypes. *Arch. Biochem. Biophys.* **682**, 108263.
- Montioli R., Dindo M., Giorgetti A., Piccoli S., Cellini B., Voltattorni C. B. orri (2014) A comprehensive picture of the mutations associated with aromatic amino acid decarboxylase deficiency: from molecular mechanisms to therapy implications. *Hum. Mol. Genet.* **23**, 5429–5440.
- Montioli R., Voltattorni C. B., Giovanni G. Di (2021) *Aromatic amino acid decarboxylase deficiency: The added value of biochemistry*. MDPI AG.
- Moors T. E., Paciotti S., Ingrassia A., Quadri M., Breedveld G., Tasegian A., Chiasserini D., et al. (2019) Characterization of Brain Lysosomal Activities in GBA-Related and Sporadic Parkinson's Disease and Dementia with Lewy Bodies. *Mol. Neurobiol.* **56**, 1344–1355.
- Morais V. A., Haddad D., Craessaerts K., Bock P.-J. De, Swerts J., Vilain S., Aerts L., et al. (2014) PINK1 loss-of-function mutations affect mitochondrial complex I activity via NdufA10 ubiquinone uncoupling. *Science* **344**, 203–7.
- Mortiboys H., Thomas K. J., Koopman W. J. H., Klaffke S., Abou-Sleiman P., Olpin S., Wood N. W., et al. (2008) Mitochondrial function and morphology are impaired in parkin -mutant fibroblasts. *Ann. Neurol.* **64**, 555–565.

- Moyes C. D., Mathieu-Costello O. A., Tsuchiya N., Filburn C., Hansford R. G. (1997) Mitochondrial biogenesis during cellular differentiation. *Am. J. Physiol. - Cell Physiol.* **272**.
- Muller F. L., Liu Y., Remmen H. Van (2004) Complex III releases superoxide to both sides of the inner mitochondrial membrane. *J. Biol. Chem.* **279**, 49064–49073.
- Murholm M., Dixen K., Qvortrup K., Hansen L. H. L., Amri E.-Z., Madsen L., Barbatelli G., Quistorff B., Hansen J. B. (2009) Dynamic Regulation of Genes Involved in Mitochondrial DNA Replication and Transcription during Mouse Brown Fat Cell Differentiation and Recruitment. *PLoS One* **4**, e8458.
- Murphy M. P. (2009) How mitochondria produce reactive oxygen species. *Biochem. J.* **417**, 1–13.
- N'Diaye E. N., Kajihara K. K., Hsieh I., Morisaki H., Debnath J., Brown E. J. (2009) PLIC proteins or ubiquilins regulate autophagy-dependent cell survival during nutrient starvation. *EMBO Rep.* **10**, 173–179.
- Nagata E., Sawa A., Ross C. A., Snyder S. H. (2004) Autophagosome-like vacuole formation in Huntington's disease lymphoblasts. *Neuroreport* **15**, 1325–1328.
- Nagatsu T., Levitt M., Udenfriend S. (1964) Tyrosine Hydroxylase. *J. Biol. Chem.* **239**, 2910–2917.
- Nagatsu T., Nagatsu I. (2016) Tyrosine hydroxylase (TH), its cofactor tetrahydrobiopterin (BH4), other catecholamine-related enzymes, and their human genes in relation to the drug and gene therapies of Parkinson's disease (PD): historical overview and future prospects. *J. Neural Transm.* **123**, 1255–1278.
- Nakagawa I., Amano A., Mizushima N., Yamamoto A., Yamaguchi H., Kamimoto T., Nara A., et al. (1997) Autophagy defends cells against invading group A Streptococcus. *science.sciencemag.org* **15**, 631.
- Narendra D. P., Jin S. M., Tanaka A., Suen D. F., Gautier C. A., Shen J.,

- Cookson M. R., Youle R. J. (2010) PINK1 Is Selectively Stabilized on Impaired Mitochondria to Activate Parkin. *PLoS Biol.* **8**, 1000298.
- Nascimento A. C., Erustes A. G., Reckziegel P., Bincoletto C., Ureshino R. P., Pereira G. J. S., Smaili S. S. (2020) α -Synuclein Overexpression Induces Lysosomal Dysfunction and Autophagy Impairment in Human Neuroblastoma SH-SY5Y. *Neurochem. Res.* **45**, 2749–2761.
- Nasrallah C. M., Horvath T. L. (2014) Mitochondrial dynamics in the central regulation of metabolism. *Nat Rev Endocrinol* **10**, 650–658.
- Nelson M. P., Boutin M., Tse T. E., Lu H., Haley E. D., Ouyang X., Zhang J., Auray-Blais C., Shacka J. J. (2018) The lysosomal enzyme alpha-Galactosidase A is deficient in Parkinson's disease brain in association with the pathologic accumulation of alpha-synuclein. *Neurobiol. Dis.* **110**, 68–81.
- Ng J., Heales S. J. R., Kurian M. A. (2014) Clinical features and pharmacotherapy of childhood monoamine neurotransmitter disorders. *Pediatr. Drugs* **16**, 275–291.
- Ngo D. C., Ververis K., Tortorella S. M., Karagiannis T. C. (2015) *Introduction to the molecular basis of cancer metabolism and the Warburg effect.*
- Nicklas W. J., Youngster S. K., Kindt M. V., Heikkila R. E. (1987) MPTP, MPP+ and mitochondrial function. *Life Sci.* **40**, 721–729.
- Nicklas W. m. do. J., Vyas I., Heikkila R. E. (1985) Inhibition of NADH-linked oxidation in brain mitochondria by 1-methyl-4-phenyl-pyridine, a metabolite of the neurotoxin, 1-methyl-4-phenyl-1,2,5,6-tetrahydropyridine. *Life Sci.* **36**, 2503–2508.
- Niemann A., Huber N., Wagner K. M., Somandin C., Horn M., Lebrun-Julien F., Angst B., et al. (2014) The Gdap1 knockout mouse mechanistically links redox control to Charcot-Marie-Tooth disease. *Brain* **137**, 668–682.
- Nixon R. A. (2020) *The aging lysosome: An essential catalyst for late-onset neurodegenerative diseases.*
- Nixon R. A., Wegiel J., Kumar A., Yu W. H., Peterhoff C., Cataldo A., Cuervo A. M. (2005) Extensive involvement of autophagy in Alzheimer disease: An

immuno-electron microscopy study. *J. Neuropathol. Exp. Neurol.* **64**, 113–122.

- Nutt J. G., Curtze C., Hiller A., Anderson S., Larson P. S., Laar A. D. Van, Richardson R. M., et al. (2020) Aromatic L-Amino Acid Decarboxylase Gene Therapy Enhances Levodopa Response in Parkinson's Disease. *Mov. Disord.* **35**, 851–858.
- Oakley A. E., Collingwood J. F., Dobson J., Love G., Perrott H. R., Edwardson J. A., Elstner M., Morris C. M. (2007) Individual dopaminergic neurons show raised iron levels in Parkinson disease. *Neurology* **68**, 1820–1825.
- Ogawa S., Uetsuki S., Tezuka Y., Morikawa T., Takahashi A., Sato K. (1999) Synthesis and evaluation of glucocerebrosidase inhibitory activity of anhydro deoxyinositols from (+)-epi- and (-)-vibo-quercitols. *Bioorg. Med. Chem. Lett.* **9**, 1493–1498.
- Onishi M., Yamano K., Sato M., Matsuda N., Okamoto K. (2021) Molecular mechanisms and physiological functions of mitophagy. *EMBO J.* **40**.
- Osellame L. D., Rahim A. A., Hargreaves I. P., Gegg M. E., Richard-Londt A., Brandner S., Waddington S. N., Schapira A. H. V, Duchen M. R. (2013) Mitochondria and quality control defects in a mouse model of gaucher disease - Links to parkinson's disease. *Cell Metab.* **17**, 941–953.
- Ota A., Shen-Orr Z., Roberts C. T., Leroith D. (1989) TPA-induced neurite formation in a neuroblastoma cell line (SH-SY5Y) is associated with increased IGF-I receptor mRNA and binding. *Mol. Brain Res.* **6**, 69–76.
- P J Marangos and, Schmechel D. E. (2003) Neuron Specific Enolase, A Clinically Useful Marker for Neurons and Neuroendocrine Cells. <http://dx.doi.org/10.1146/annurev.ne.10.030187.001413> **10**, 269–295.
- Påhlman S., Ruusala A.-I., Abrahamsson L., Mattsson M. E. K., Esscher T. (1984) Retinoic acid-induced differentiation of cultured human neuroblastoma cells: a comparison with phorbol ester-induced differentiation. *Cell Differ.* **14**, 135–144.
- Palmieri M., Impey S., Kang H., Ronza A. di, Pelz C., Sardiello M., Ballabio A.

(2011) Characterization of the CLEAR network reveals an integrated control of cellular clearance pathways. *Hum. Mol. Genet.* **20**, 3852–3866.

Paola S. Di, Scotto-Rosato A., Medina D. L. (2018) *TRPML1: The Ca(2+)retaker of the lysosome*. Elsevier Ltd.

Paris I., Perez-Pastene C., Cardenas S., Iturra P., Muñoz P., Couve E., Caviedes P., Segura-Aguilar J. (2010) Aminochrome induces disruption of actin, alpha-, and beta-tubulin cytoskeleton networks in substantia-nigra-derived cell line. *Neurotox. Res.* **18**, 82–92.

Park K. H., Shin K. S., Zhao T. T., Park H. J., Lee K. E., Lee M. K. (2016) L-DOPA modulates cell viability through the ERK-c-Jun system in PC12 and dopaminergic neuronal cells. *Neuropharmacology* **101**, 87–97.

Parker W. D., Boyson S. J., Parks J. K. (1989) Abnormalities of the electron transport chain in idiopathic parkinson's disease. *Ann. Neurol.* **26**, 719–723.

Parkinson J. (2002) An Essay on the Shaking Palsy. *J. Neuropsychiatry Clin. Neurosci.* **14**, 223–236.

Parnetti L., Paciotti S., Eusebi P., Dardis A., Zampieri S., Chiasserini D., Tasegian A., et al. (2017) Cerebrospinal fluid β -glucocerebrosidase activity is reduced in parkinson's disease patients. *Mov. Disord.* **32**, 1423–1431.

Pearce R. K. B., Owen A., Daniel S., Jenner P., Marsden C. D. (1997) Alterations in the distribution of glutathione in the substantia nigra in Parkinson's disease. *J. Neural Transm.* **104**, 661–77.

Pennypacker K. R., Kuhn D. M., Billingsley M. L. (1989) Changes in expression of tyrosine hydroxylase immunoreactivity in human SMS-KCNR neuroblastoma following retinoic acid or phorbol ester-induced differentiation. *Mol. Brain Res.* **5**, 251–258.

Phhlman S., Ruusala A.-I., Abrahamsson L., Mattsson M. E. K. K., Esscher T., Pählman S., Ruusala A.-I., et al. (1984) Retinoic acid-induced differentiation of cultured human neuroblastoma cells: a comparison with phorbol ester-induced differentiation. *Cell Differ.* **14**, 135–144.

- Pillay C. S., Elliott E., Dennison C. (2002) Endolysosomal proteolysis and its regulation. *Biochem. J.* **363**, 417–429.
- Pinto M., Pickrell A. M., Moraes C. T. (2012) Regional susceptibilities to mitochondrial dysfunctions in the CNS. *Biol. Chem.* **393**, 275–81.
- Place T., Smeyne R. J. (2013) *Glutathione Metabolism and Parkinson's Disease*.
- Platt F. M., d'Azzo A., Davidson B. L., Neufeld E. F., Tiffet C. J. (2018) Lysosomal storage diseases. *Nat. Rev. Dis. Prim.* 2018 **41** **4**, 1–25.
- Plotegher N., Duchen M. R. (2017a) Mitochondrial Dysfunction and Neurodegeneration in Lysosomal Storage Disorders. *Trends Mol Med* **23**, 116–134.
- Plotegher N., Duchen M. R. (2017b) Crosstalk between Lysosomes and Mitochondria in Parkinson's Disease. *Front Cell Dev Biol* **5**, 110.
- Poirier L. J., Sourkes T. L. (1965) INFLUENCE OF THE SUBSTANTIA NIGRA ON THE CATECHOLAMINE CONTENT OF THE STRIATUM. *Brain* **88**, 181–192.
- Politis M., Niccolini F., Fox S. H., Chuang R., Brotchie J. M. (2015) Serotonin in Parkinson's disease. *Behav Brain Res* **277**, 136–145.
- Politis M., Wu K., Loane C., Kiferle L., Molloy S., Brooks D. J., Piccini P. (2010) Staging of serotonergic dysfunction in Parkinson's disease: an in vivo 11C-DASB PET study. *Neurobiol. Dis.* **40**, 216–221.
- Polymeropoulos M. H., Lavedan C., Leroy E., Ide S. E., Dehejia A., Dutra A., Pike B., et al. (1997a) Mutation in the α -Synuclein Gene Identified in Families with Parkinson's Disease. **276**, 2045–2048.
- Polymeropoulos M. H., Lavedan C., Leroy E., Ide S. E., Dehejia A., Dutra A., Pike B., et al. (1997b) Mutation in the α -synuclein gene identified in families with Parkinson's disease. *Science (80-)*. **276**, 2045–2047.
- Prasuhn J., Mårtensson C. U., Krajka V., Klein C., Rakovic A., Martensson C. U., Krajka V., Klein C., Rakovic A. (2018) Genome-Edited, TH-expressing

Neuroblastoma Cells as a Disease Model for Dopamine-Related Disorders: A Proof-of-Concept Study on DJ-1-deficient Parkinsonism. *Front. Cell. Neurosci.* **11**, 1–8.

- Presgraves S. P., Ahmed T., Borwege S., Joyce J. N. (2004) Terminally differentiated SH-SY5Y cells provide a model system for studying neuroprotective effects of dopamine agonists. *Neurotox. Res.* **5**, 579–598.
- Princz A., Kounakis K., Tavernarakis N. (2018) Mitochondrial contributions to neuronal development and function. *Biol Chem.*
- Prinz W. A., Toulmay A., Balla T. (2020) The functional universe of membrane contact sites. *Nat. Rev. Mol. Cell Biol.* **21**, 7–24.
- Protasoni M., Pérez-Pérez R., Lobo-Jarne T., Harbour M. E., Ding S., Peñas A., Diaz F., et al. (2020) Respiratory supercomplexes act as a platform for complex III-mediated maturation of human mitochondrial complexes I and IV. *EMBO J.* **39**, e102817.
- Quinville B. M., Deschenes N. M., Ryckman A. E., Walia J. S. (2021) A Comprehensive Review: Sphingolipid Metabolism and Implications of Disruption in Sphingolipid Homeostasis. *Int. J. Mol. Sci.* **22**, 5793.
- Radad K., Al-Shraim M., Al-Emam A., Wang F., Kranner B., Rausch W. D., Moldzio R. (2019) Rotenone: from modelling to implication in Parkinson's disease. *Folia Neuropathol.* **57**, 317–326.
- Ramirez A., Heimbach A., Gründemann J., Stiller B., Hampshire D., Cid L. P., Goebel I., et al. (2006) Hereditary parkinsonism with dementia is caused by mutations in ATP13A2, encoding a lysosomal type 5 P-type ATPase. *Nat. Genet.* **38**, 1184–1191.
- Ramzan R., Vogt S., Kadenbach B. (2020) Stress-mediated generation of deleterious ROS in healthy individuals - role of cytochrome c oxidase. *J. Mol. Med. (Berl)*. **98**, 651.
- Ranjbar A., Pasalar P., Sedighi A., Abdollahi M. (2002) Induction of oxidative stress in paraquat formulating workers. *Toxicol. Lett.* **131**, 191–194.
- Ransom B. R., Kunis D. M., Irwin I., Langston J. W. (1987) Astrocytes convert

the parkinsonism inducing neurotoxin, MPTP, to its active metabolite, MPP+. *Neurosci. Lett.* **75**, 323–328.

- Rao R. P., Vaidyanathan N., Rengasamy M., Oommen A. M., Somaiya N., Jagannath M. R. (2013) Sphingolipid Metabolic Pathway : An Overview of Major Roles Played in Human Diseases. **2013**.
- Reczek D., Schwake M., Schröder J., Hughes H., Blanz J., Jin X., Brondyk W., Patten S. Van, Edmunds T., Saftig P. (2007) LIMP-2 Is a Receptor for Lysosomal Mannose-6-Phosphate-Independent Targeting of β -Glucocerebrosidase. *Cell* **131**, 770–783.
- Reed J. S., Ragan C. I. (1987) The effect of rate limitation by cytochrome c on the redox state of the ubiquinone pool in reconstituted NADH: cytochrome c reductase. *Biochem. J.* **247**, 657–662.
- Reeve A. K., Grady J. P., Cosgrave E. M., Bennison E., Chen C., Hepplewhite P. D., Morris C. M. (2018) Mitochondrial dysfunction within the synapses of substantia nigra neurons in Parkinson's disease. *npj Park. Dis.* **2018** *4*, 1–10.
- Reichert C. O., Freitas F. A. de, Sampaio-Silva J., Rokita-Rosa L., Barros P. de L., Levy D., Bydlowski S. P. (2020) Ferroptosis Mechanisms Involved in Neurodegenerative Diseases. *Int. J. Mol. Sci.* **21**, 1–27.
- Rich P. R. (1986) A perspective on Q-cycles. *J. Bioenerg. Biomembr.* **18**, 145–156.
- Riederer P., Sofic E., Rausch W. -D, Schmidt B., Reynolds G. P., Jellinger K., Youdim M. B. H. (1989) Transition Metals, Ferritin, Glutathione, and Ascorbic Acid in Parkinsonian Brains. *J. Neurochem.* **52**, 515–520.
- Rigolio R., Miloso M., Nicolini G., Villa D., Scuteri A., Simone M., Tredici G. (2005) Resveratrol interference with the cell cycle protects human neuroblastoma SH-SY5Y cell from paclitaxel-induced apoptosis. *Neurochem. Int.* **46**, 205–211.
- Robak L. A., Jansen I. E., Rooij J. van, Uitterlinden A. G., Kraaij R., Jankovic J., Heutink P., et al. (2017) Excessive burden of lysosomal storage disorder

gene variants in Parkinson's disease. *Brain* **140**, 3191–3203.

Rodriguez-Enriquez S., Kim I., Currin R. T., Lemasters J. J. (2006) Tracker dyes to probe mitochondrial autophagy (mitophagy) in rat hepatocytes. *Autophagy* **2**, 39–46.

Ross R. A., Walton J. D., Han D., Guo H. F., Cheung N. K. V. (2015) A distinct gene expression signature characterizes human neuroblastoma cancer stem cells. *Stem Cell Res.* **15**, 419–426.

Rossignoli G., Krämer K., Lugarà E., Alrashidi H., Pope S., La Fuente Barrigon C. De, Barwick K., et al. (2021) Aromatic l-amino acid decarboxylase deficiency: A patient-derived neuronal model for precision therapies. *Brain* **144**, 2443–2456.

Rudakou U., Ouled Amar Bencheikh B., Ruskey J. A., Krohn L., Laurent S. B., Spiegelman D., Liong C., et al. (2019) Common and rare GCH1 variants are associated with Parkinson's disease. *Neurobiol. Aging* **73**, 231.e1-231.e6.

Saftig P., Klumperman J. (2009) Lysosome biogenesis and lysosomal membrane proteins: trafficking meets function. *Nat. Rev. Mol. Cell Biol.* **2009 109** **10**, 623–635.

Şahin M., Öncü G., Yılmaz M. A., Özkan D., Saybaşılı H. (2021) Transformation of SH-SY5Y cell line into neuron-like cells: Investigation of electrophysiological and biomechanical changes. *Neurosci. Lett.* **745**, 135628.

Sanford A. M. (2018) Lewy Body Dementia. *Clin. Geriatr. Med.* **34**, 603–615.

Santillo S. (2021) Changes in Biophysical Properties of Undifferentiated SH-SY5Y Cells During Long-Term Cultures. *Neuroscience*.

Santillo S., Moriello A. S., Maio V. Di (2014) Electrophysiological variability in the SH-SY5Y cellular line. *Gen. Physiol. Biophys* **33**, 121–129.

Saravanan K. S., Sindhu K. M., Mohanakumar K. P. (2005) Acute intranigral infusion of rotenone in rats causes progressive biochemical lesions in the striatum similar to Parkinson's disease. *Brain Res.* **1049**, 147–155.

- Sazanov L. A. (2014) The mechanism of coupling between electron transfer and proton translocation in respiratory complex I. *J. Bioenerg. Biomembr.* **46**, 247–253.
- Schafer K. A. (1998) The cell cycle: a review. *Vet. Pathol.* **35**, 461–478.
- Schägger H., Link T. A., Engel W. D., Jagow G. von (1986) Isolation of the eleven protein subunits of the bc₁ complex from beef heart. *Methods Enzymol.* **126**, 224–237.
- Schapansky J., Khasnavis S., DeAndrade M. P., Nardoizzi J. D., Falkson S. R., Boyd J. D., Sanderson J. B., Bartels T., Melrose H. L., LaVoie M. J. (2018) Familial knockin mutation of LRRK2 causes lysosomal dysfunction and accumulation of endogenous insoluble α -synuclein in neurons. *Neurobiol. Dis.* **111**, 26.
- Schapira A. H. V. (2007) *Mitochondrial dysfunction in Parkinson's disease.*
- Schapira A. H. V. (2011) Mitochondrial Pathology in Parkinson's Disease. *Mt. Sinai J. Med. A J. Transl. Pers. Med.* **78**, 872–881.
- Schapira A. H. V., Cooper J. M., Dexter D., Clark J. B., Jenner P., Marsden C. D. (1990) Mitochondrial Complex I Deficiency in Parkinson's Disease. *J. Neurochem.* **54**, 823–827.
- Schneider L., Giordano S., Zelickson B. R., Johnson M., Benavides G., Ouyang X., Fineberg N., Darley-usmar V. M. (2012) Differentiation of SH-SY5Y cells to a neuronal phenotype changes cellular bioenergetics and the response to oxidative stress. **51**, 2007–2017.
- Schneider S. A., Tahirovic S., Hardy J., Strupp M., Bremova-Ertl T. (2021) Do heterozygous mutations of Niemann–Pick type C predispose to late-onset neurodegeneration: a review of the literature. *J. Neurol.* **268**, 2055–2064.
- Schwake M., Schröder B., Saftig P. (2013) Lysosomal Membrane Proteins and Their Central Role in Physiology. *Traffic* **14**, 739–748.
- Schwarz T. L. (2013) Mitochondrial Trafficking in Neurons. *Cold Spring Harb Perspect Biol* **5**.

- Seaman M. N. J. (2004) Cargo-selective endosomal sorting for retrieval to the Golgi requires retromer. *J. Cell Biol.* **165**, 111–122.
- Segawa M. (2011) Hereditary progressive dystonia with marked diurnal fluctuation. *Brain Dev.* **33**, 195–201.
- Seibler P., Graziotto J., Jeong H., Simunovic F., Klein C., Krainc D. (2011) Mitochondrial Parkin recruitment is impaired in neurons derived from mutant PINK1 induced pluripotent stem cells. *Soc Neurosci.*
- Seiden L. S., Carlsson A. (1963) Temporary and partial antagonism by l-DOPA of reserpine-induced suppression of a conditioned avoidance response. *Psychopharmacol.* **1963 46 4**, 418–423.
- Şentürk M., Lin G., Zuo Z., Mao D., Watson E., Mikos A. G., Bellen H. J. (2019) Ubiquilins regulate autophagic flux through mTOR signalling and lysosomal acidification. *Nat. Cell Biol.* **21**, 384–396.
- Serrano-Puebla A., Boya P. (2016) Lysosomal membrane permeabilization in cell death: new evidence and implications for health and disease. *Ann. N. Y. Acad. Sci.* **1371**, 30–44.
- Settembre C., Malta C. Di, Polito V. A., Arencibia M. G., Vetrini F., Erdin S., Erdin S. U., et al. (2011) TFEB links autophagy to lysosomal biogenesis. *Science* **332**, 1429–1433.
- Settembre C., Polito V. A., Garcia M., Vetrini F., Erdin S., Erdin S. U., Huynh T., et al. (2013) Europe PMC Funders Group Europe PMC Funders Author Manuscripts TFEB Links Autophagy to Lysosomal Biogenesis. *Science (80- .)* **332**, 1429–1433.
- Settembre C., Zoncu R., Medina D. L., Vetrini F., Erdin S., Erdin S., Huynh T., et al. (2012) A lysosome-to-nucleus signalling mechanism senses and regulates the lysosome via mTOR and TFEB. *EMBO J.* **31**, 1095–1108.
- Sevlever D., Jiang P., Yen S. H. C. (2008) Cathepsin D is the main lysosomal enzyme involved in the degradation of α -synuclein and generation of its carboxy-terminally truncated species. *Biochemistry* **47**, 9678–9687.
- Shen S.-L., Chen X.-P., Zhang X.-F., Miao J.-Y., Zhao B.-X. (2015) A

- rhodamine B-based lysosomal pH probe. *J. Mater. Chem. B* **3**, 919–925.
- Shepherd D., Garland P. B. (1969) The kinetic properties of citrate synthase from rat liver mitochondria. *Biochem. J.* **114**, 597–610.
- Shiple M. M., Mangold C. A., Szpara M. L. (2016) Differentiation of the SH-SY5Y human neuroblastoma cell line. *J. Vis. Exp.* **2016**, 53193.
- Sian J., Dexter D. T., Lees A. J., Daniel S., Agid Y., Javoy-Agid F., Jenner P., Marsden C. D. (1994) Alterations in glutathione levels in Parkinson's disease and other neurodegenerative disorders affecting basal ganglia. *Ann. Neurol.* **36**, 348–355.
- Sidranskyl E. (2009) International Multi-Center Analysis of Glucocerebrosidase Mutations in Parkinson Disease. *Mol. Genet. ...* **361**, 1651–1661.
- Siebert M., Sidransky E., Westbroek W. (2014) Glucocerebrosidase is shaking up the synucleinopathies. *Brain* **137**, 1304–1322.
- Simões R. F., Ferrão R., Silva M. R., Pinho S. L. C., Ferreira L., Oliveira P. J., Cunha-Oliveira T. (2021) Refinement of a differentiation protocol using neuroblastoma SH-SY5Y cells for use in neurotoxicology research. *Food Chem. Toxicol.* **149**, 111967.
- Sivanandy P., Leey T. C., Xiang T. C., Ling T. C., Ang S., Han W., Lia S., Semilan A., Hong P. K. (2022) Systematic Review on Parkinson's Disease Medications, Emphasizing on Three Recently Approved Drugs to Control Parkinson's Symptoms.
- Smeyne M., Smeyne R. J. (2013) Glutathione metabolism and Parkinson's disease. *Free Radic Biol Med* **62**, 13–25.
- Smith A. N., Jouret F., Bord S., Borthwick K. J., Al-Lamki R. S., Wagner C. A., Ireland D. C., et al. (2005) Vacuolar H⁺-ATPase d2 subunit: molecular characterization, developmental regulation, and localization to specialized proton pumps in kidney and bone. *J. Am. Soc. Nephrol.* **16**, 1245–1256.
- Sofic E., Lange K. W., Jellinger K., Riederer P. (1992) Reduced and oxidized glutathione in the substantia nigra of patients with Parkinson's disease. *Neurosci. Lett.* **142**, 128–130.

- Soubannier V., McLelland G. L., Zunino R., Braschi E., Rippstein P., Fon E. A., McBride H. M. (2012) A vesicular transport pathway shuttles cargo from mitochondria to lysosomes. *Curr. Biol.* **22**, 135–141.
- Spina M. B., Cohen G. (1989) Dopamine turnover and glutathione oxidation: Implications for Parkinson disease (hydrogen peroxide/monoamine oxidase/nigrostriatal tract). *Neurobiology* **86**, 1398–1400.
- Stansley B. J., Yamamoto B. K. (2013) L-dopa-induced dopamine synthesis and oxidative stress in serotonergic cells. *Neuropharmacology* **67**, 243–251.
- Stefanis L. (2012) α -Synuclein in Parkinson's disease. *Cold Spring Harb. Perspect. Med.* **2**.
- Stoka V., Turk V., Turk B. (2016) Lysosomal cathepsins and their regulation in aging and neurodegeneration. *Ageing Res Rev* **32**, 22–37.
- Straus W. (1954) Isolation and biochemical properties of droplets from the cells of rat kidney. *J. Biol. Chem.* **207**, 745–55.
- Südhof T. C. (2012) Calcium Control of Neurotransmitter Release. *Cold Spring Harb. Perspect. Biol.* **4**.
- Sugiura A., McLelland G.-L., Fon E. A., McBride H. M. (2014) A new pathway for mitochondrial quality control: mitochondrial-derived vesicles. *EMBO J.* **33**, 2142–2156.
- Sulzer D., Bogulavsky J., Larsen K. E., Behr G., Karatekin E., Kleinman M. H., Turro N., et al. (2000) Neuromelanin biosynthesis is driven by excess cytosolic catecholamines not accumulated by synaptic vesicles. *Proc. Natl. Acad. Sci. U. S. A.* **97**, 11869–11874.
- Sun J., Trumpower B. L. (2003) Superoxide anion generation by the cytochrome bc1 complex. *Arch. Biochem. Biophys.* **419**, 198–206.
- Surmeier D. J., Obeso J. A., Halliday G. M. (2017) *Selective neuronal vulnerability in Parkinson disease*. *Nat Rev Neurosci.*
- Swerdlow R. H., Kish S. J. (2002) Mitochondria in Alzheimer's disease. *Int. Rev. Neurobiol.* **53**, 341–385.

- Swerdlow R. H., Parks J. K., Pattee G., Parker W. D. (2000) Role of mitochondria in amyotrophic lateral sclerosis. *Amyotroph. Lateral Scler. Other Motor Neuron Disord.* **1**, 185–190.
- Swoboda K. J., Saul J. P., McKenna C. E., Speller N. B., Hyland K. (2003) Aromatic L-amino acid decarboxylase deficiency: overview of clinical features and outcomes. *Ann. Neurol.* **54 Suppl 6**.
- Szigetvari P. D., Muruganandam G., Kallio J. P., Hallin E. I., Fossbakk A., Loris R., Kursula I., et al. (2019) The quaternary structure of human tyrosine hydroxylase: effects of dystonia-associated missense variants on oligomeric state and enzyme activity. *J. Neurochem.* **148**, 291–306.
- Takahashi K., Yamanaka S. (2006) Induction of pluripotent stem cells from mouse embryonic and adult fibroblast cultures by defined factors. *Cell* **126**, 663–676.
- Tamargo R. J., Velayati A., Goldin E., Sidransky E. (2012) The role of saposin C in Gaucher disease. *Mol. Genet. Metab.* **106**, 257–263.
- Tanner C. M., Kame F., Ross G. W., Hoppin J. A., Goldman S. M., Korell M., Marras C., et al. (2011) Rotenone, paraquat, and Parkinson's disease. *Environ. Health Perspect.* **119**, 866–872.
- Tatsuta T., Scharwey M., Langer T. (2014) Mitochondrial lipid trafficking. *Trends Cell Biol* **24**, 44–52.
- Tayebi N., Callahan M., Madike V., Stubblefield B. K., Orvisky E., Krasnewich D., Fillano J. J., Sidransky E. (2001) Gaucher Disease and Parkinsonism: A Phenotypic and Genotypic Characterization.
- Tayebi N., Walker J., Stubblefield B., Orvisky E., LaMarca M. E., Wong K., Rosenbaum H., Schiffmann R., Bembi B., Sidransky E. (2003) Gaucher disease with parkinsonian manifestations: Does glucocerebrosidase deficiency contribute to a vulnerability to parkinsonism? *Mol. Genet. Metab.* **79**, 104–109.
- Tekin I., Roskoski R., Carkaci-Salli N., Vrana K. E. (2014) *Complex molecular regulation of tyrosine hydroxylase.*

- Tempio A., Niso M., Laera L., Trisolini L., Favia M., Ciranna L., Marzulli D., et al. (2020) Mitochondrial Membranes of Human SH-SY5Y Neuroblastoma Cells Express Serotonin 5-HT₇ Receptor. *Int. J. Mol. Sci.* **21**, 1–10.
- Thomas K. J., McCoy M. K., Blackinton J., Beilina A., Brug M. van der, Sandebring A., Miller D., Maric D., Cedazo-Minguez A., Cookson M. R. (2011) DJ-1 acts in parallel to the PINK1/parkin pathway to control mitochondrial function and autophagy. *Hum. Mol. Genet.* **20**, 40–50.
- Timón-Gómez A., Yvltová E. N. ´, Abriata L. A., Vila A. J., Hosler J., Barrientos A. (2018) Mitochondrial cytochrome c oxidase biogenesis: Recent developments. *Semin. Cell Dev. Biol.* **76**, 163–178.
- Titova N., Chaudhuri K. R. (2017) Personalized medicine in Parkinson's disease: Time to be precise. *Mov. Disord.* **32**, 1147–1154.
- Toei M., Saum R., Forgac M. (2010) Regulation and isoform function of the V-ATPases. *Biochemistry* **49**, 4715–4723.
- Tohgi H., Abe T., Takahashi S., Takahashi J., Hamato H. (1993) Concentrations of serotonin and its related substances in the cerebrospinal fluid of Parkinsonian patients and their relations to the severity of symptoms. *Neurosci. Lett.* **150**, 71–74.
- Torres G. E., Gainetdinov R. R., Caron M. G. (2003) Plasma membrane monoamine transporters: structure, regulation and function. *Nat. Rev. Neurosci.* **4**, 13–25.
- Toyomura T., Murata Y., Yamamoto A., Oka T., Sun-Wada G. H., Wada Y., Futai M. (2003) From lysosomes to the plasma membrane: localization of vacuolar-type H⁺-ATPase with the a3 isoform during osteoclast differentiation. *J. Biol. Chem.* **278**, 22023–22030.
- Turrens J. F., Alexandre A., Lehninger A. L. (1985) Ubisemiquinone is the electron donor for superoxide formation by complex III of heart mitochondria. *Arch. Biochem. Biophys.* **237**, 408–414.
- Turrens J. F., Boveris A. (1980) Generation of superoxide anion by the NADH dehydrogenase of bovine heart mitochondria. *Biochem. J.* **191**, 421–427.

- Tüshaus J., Kataka E. S., Zaucha J., Frishman D., Müller S. A., Lichtenthaler S. F. (2021) Neuronal Differentiation of LUHMES Cells Induces Substantial Changes of the Proteome. *Proteomics* **21**, e2000174.
- Tysnes O.-B., Storstein A. (2017) Epidemiology of Parkinson's disease. *J. Neural Transm.* **124**, 901–905.
- Usenovic M., Tresse E., Mazzulli J. R., Taylor J. P., Krainc D. (2012) Deficiency of ATP13A2 leads to lysosomal dysfunction, α -synuclein accumulation, and neurotoxicity. *J. Neurosci.* **32**, 4240–4246.
- Valente E. M., Abou-Sleiman P. M., Caputo V., Muqit M. M. K., Harvey K., Gispert S., Ali Z., et al. (2004) Hereditary early-onset Parkinson's disease caused by mutations in PINK1. *Science* **304**, 1158–1160.
- Valsecchi F., Koopman W. J. H., Manjeri G. R., Rodenburg R. J., Smeitink J. A. M., Willems P. H. G. M. (2010) Complex I disorders: causes, mechanisms, and development of treatment strategies at the cellular level. *Dev. Disabil. Res. Rev.* **16**, 175–182.
- Vanier M. T. (2013) Niemann-Pick diseases. *Handb. Clin. Neurol.* **113**, 1717–1721.
- Veen S. van, Martin S., Haute C. Van den, Benoy V., Lyons J., Vanhoutte R., Kahler J. P., et al. (2020) ATP13A2 deficiency disrupts lysosomal polyamine export. *Nat.* 2020 5787795 **578**, 419–424.
- Verney C., Berger B., Adrien J., Vigny A., Gay M. (1982) Development of the dopaminergic innervation of the rat cerebral cortex. A light microscopic immunocytochemical study using anti-tyrosine hydroxylase antibodies. *Dev. Brain Res.* **5**, 41–52.
- Vinothkumar K. R., Zhu J., Hirst J. (2014) Architecture of mammalian respiratory complex I. *Nat.* 2014 5157525 **515**, 80–84.
- Vives-Bauza C., Przedborski S. (2011) Mitophagy: the latest problem for Parkinson's disease. *Trends Mol. Med.* **17**, 158–165.
- Wakabayashi K., Takahashi H., Obata K., Ikuta F. (1992) Immunocytochemical localization of synaptic vesicle-specific protein in Lewy body-containing

neurons in Parkinson's disease. *Neurosci. Lett.* **138**, 237–240.

Wakabayashi K., Tanji K., Odagiri S., Miki Y., Mori F., Takahashi H. (2013) The Lewy body in Parkinson's disease and related neurodegenerative disorders. *Mol. Neurobiol.* **47**, 495–508.

Walton J. D., Kattan D. R., Thomas S. K., Spengler B. A., Guo H. F., Biedler J. L., Cheung N. K. V., Ross R. A. (2004) Characteristics of stem cells from human neuroblastoma cell lines and in tumors. *Neoplasia* **6**, 838–845.

Wanet A., Arnould T., Najimi M., Renard P. (2015) Connecting Mitochondria, Metabolism, and Stem Cell Fate. *Stem Cells Dev.* **24**, 1957–1971.

Wang H. Q., Imai Y., Kataoka A., Takahashi R. (2007) Cell Type-Specific Upregulation of Parkin in Response to ER Stress. *Antioxid. Redox Signal.* **9**, 533–542.

Wang K., Zhan Y., Chen B., Lu Y., Yin T., Zhou S., Zhang W., et al. (2020a) Tubeimoside I-induced lung cancer cell death and the underlying crosstalk between lysosomes and mitochondria. *Cell Death Dis.* **11**.

Wang N., Zhu P., Huang R., Wang C., Sun L., Lan B., He Y., Zhao H., Gao Y. (2020b) PINK1: The guard of mitochondria. *Life Sci.* **259**, 118247.

Wang R., Wang J., Hassan A., Lee C.-H., Xie X.-S., Li X. (2021) Molecular basis of V-ATPase inhibition by bafilomycin A1. *Nat. Commun.* **12**.

Wang X., Su B., Liu W., He X., Gao Y., Castellani R. J., Perry G., Smith M. A., Zhu X. (2011) DLP1-dependent mitochondrial fragmentation mediates 1-methyl-4-phenylpyridinium toxicity in neurons: Implications for Parkinson's disease. *Aging Cell* **10**, 807–823.

Wassenberg T., Molero-Luis M., Jeltsch K., Hoffmann G. F., Assmann B., Blau N., Garcia-Cazorla A., et al. (2017) Consensus guideline for the diagnosis and treatment of aromatic L-amino acid decarboxylase (AADC) deficiency. *Orphanet J. Rare Dis.* **12**, 1–21.

Watabe M., Nakaki T. (2008) Mitochondrial complex I inhibitor rotenone inhibits and redistributes vesicular monoamine transporter 2 via nitration in human dopaminergic SH-SY5Y cells. *Mol. Pharmacol.* **74**, 933–940.

- Weiduschat N., Mao X., Hupf J., Armstrong N., Kang G., Lange D. J., Mitsumoto H., Shungu D. C. (2014) Motor cortex glutathione deficit in ALS measured in vivo with the J-editing technique. *Neurosci. Lett.* **570**, 102–107.
- Weil H., Willams T. I. (1950) History of Chromatography. *Nat.* 1950 1664232 **166**, 1000–1001.
- Westbroek W., Gustafson A. M., Sidransky E. (2011) Exploring the link between glucocerebrosidase mutations and parkinsonism. *Trends Mol. Med.* **17**, 485–493.
- Westlund K. N., Denney R. M., Kochersperger L. M., Rose R. M., Abell C. W. (1985) Distinct monoamine oxidase A and B populations in primate brain. *Science (80-)*. **230**, 181–183.
- Wharton D. C., Tzagoloff A. (1967) [45] Cytochrome oxidase from beef heart mitochondria. *Methods Enzymol.* **10**, 245–250.
- Whitaker-Azmitia P. M. (1999) The Discovery of Serotonin and its Role in Neuroscience. *Neuropsychopharmacol.* 1999 211 **21**, 2–8.
- Whitehead R. E., Ferrer J. V., Javitch J. A., Justice J. B. (2001) Reaction of oxidized dopamine with endogenous cysteine residues in the human dopamine transporter. *J. Neurochem.* **76**, 1242–1251.
- Wiegand G., Remington S. J. (1986) Citrate synthase: structure, control, and mechanism. *Annu. Rev. Biophys. Biophys. Chem.* **15**, 97–117.
- Wijemanne S., Jankovic J. (2015) *Dopa-responsive dystonia - Clinical and genetic heterogeneity.*
- Willemsen M. A., Verbeek M. M., Kamsteeg E. J., Rijk-Van Andel J. F. De, Aeby A., Blau N., Burlina A., et al. (2010) Tyrosine hydroxylase deficiency: A treatable disorder of brain catecholamine biosynthesis. *Brain* **133**, 1810–1822.
- Wilson H., Dervenoulas G., Pagano G., Koros C., Yousaf T., Picillo M., Polychronis S., et al. (2019) Serotonergic pathology and disease burden in the premotor and motor phase of A53T α -synuclein parkinsonism: a cross-

sectional study. *Lancet Neurol.* **18**, 748–759.

Wilson M. A. (2011) The Role of Cysteine Oxidation in DJ-1 Function and Dysfunction. *Antioxid. Redox Signal.* **15**, 111–122.

Windahl M. S., Boesen J., Karlsen P. E., Christensen H. E. M. (2009) Expression, purification and enzymatic characterization of the catalytic domains of human tryptophan hydroxylase isoforms. *Protein J.* **28**, 400–406.

Wong Y. C., Ysselstein D., Krainc D. (2018) Mitochondria-lysosome contacts regulate mitochondrial fission via RAB7 GTP hydrolysis. *Nature* **554**, 382–386.

Woodard C. M., Campos B. A., Kuo S. H., Nirenberg M. J., Nestor M. W., Zimmer M., Mosharov E. V., et al. (2014) iPSC-derived dopamine neurons reveal differences between monozygotic twins discordant for Parkinson's disease. *Cell Rep.* **9**, 1173–1182.

Xicoy H., Peñuelas N., Vila M., Laguna A. (2019) *Autophagic- and Lysosomal-Related Biomarkers for Parkinson's Disease: Lights and Shadows.*

Xicoy H., Wieringa B., Martens G. J. M. (2017) The SH-SY5Y cell line in Parkinson's disease research: a systematic review. *Mol. Neurodegener.* **12**, 10.

Xie B., Lin F., Peng L., Ullah K., Wu H., Qing H., Deng Y. (2014) Methylglyoxal increases dopamine level and leads to oxidative stress in SH-SY5Y cells. *Acta Biochim. Biophys. Sin. (Shanghai).* **46**, 950–956.

Xie Y., Zhou B., Lin M. Y., Sheng Z. H. (2015) Progressive endolysosomal deficits impair autophagic clearance beginning at early asymptomatic stages in FALS mice. *Autophagy* **11**, 1934–1936.

Xu J., Kao S. Y., Lee F. J. S., Song W., Jin L. W., Yankner B. A. (2002) Dopamine-dependent neurotoxicity of alpha-synuclein: a mechanism for selective neurodegeneration in Parkinson disease. *Nat. Med.* **8**, 600–606.

Xu Y., Stokes A. H., Roskoski R., Vrana K. E. (1998) Dopamine, in the presence of tyrosinase, covalently modifies and inactivates tyrosine

- hydroxylase. *J. Neurosci. Res.* **54**, 691–697.
- Xue L., Fletcher G. C., Tolkovsky A. M. (2001) Mitochondria are selectively eliminated from eukaryotic cells after blockade of caspases during apoptosis. *Curr. Biol.* **11**, 361–365.
- Yang J. C., Cortopassi G. A. (1998) Induction of the mitochondrial permeability transition causes release of the apoptogenic factor cytochrome c. *Free Radic. Biol. Med.* **24**, 624–631.
- Yang S. yu, Gegg M., Chau D., Schapira A. (2020) Glucocerebrosidase activity, cathepsin D and monomeric α -synuclein interactions in a stem cell derived neuronal model of a PD associated GBA1 mutation. *Neurobiol. Dis.* **134**.
- Yoshimori T., Yamamoto A., Moriyama Y., Futai M., Tashiro Y. (1991) Bafilomycin A1, a specific inhibitor of vacuolar-type H⁺-ATPase, inhibits acidification and protein degradation in lysosomes of cultured cells. *J. Biol. Chem.* **266**, 17707–17712.
- Youdim M. B. H., Finberg J. P. M., Tipton K. F. (1988) Monamine Oxidase. 119–192.
- Yu W., Gong J. S., Ko M., Garver W. S., Yanagisawa K., Michikawa M. (2005) Altered Cholesterol Metabolism in Niemann-Pick Type C1 Mouse Brains Affects Mitochondrial Function. *J. Biol. Chem.* **280**, 11731–11739.
- Zaidi N., Maurer A., Nieke S., Kalbacher H. (2008) Cathepsin D: A cellular roadmap. *Biochem. Biophys. Res. Commun.* **376**, 5–9.
- Zamzami N., Susin S. A., Marchetti P., Hirsch T., Gómez-Monterrey I., Castedo M., Kroemer G. (1996) Mitochondrial control of nuclear apoptosis. *J. Exp. Med.* **183**, 1533–1544.
- Zecca L., Zucca F. A., Wilms H., Sulzer D. (2003) Neuromelanin of the substantia nigra: a neuronal black hole with protective and toxic characteristics. *Trends Neurosci.* **26**, 578–580.
- Zeng X. S., Geng W. S., Jia J. J., Chen L., Zhang P. P. (2018) Cellular and molecular basis of neurodegeneration in Parkinson disease. *Front. Aging Neurosci.* **10**, 109.

- Zhang X., Cheng X., Yu L., Yang J., Calvo R., Patnaik S., Hu X., et al. (2016) MCOLN1 is a ROS sensor in lysosomes that regulates autophagy. *Nat. Commun.* **7**.
- Zhang Z., Yue P., Lu T., Wang Y., Wei Y., Wei X. (2021) Role of lysosomes in physiological activities, diseases, and therapy. **14**.
- Zhao R. Z., Jiang S., Zhang L., Yu Z. Bin (2019) Mitochondrial electron transport chain, ROS generation and uncoupling (Review). *Int. J. Mol. Med.* **44**, 3–15.
- Zhou J., Tan S. H., Nicolas V., Bauvy C., Yang N. Di, Zhang J., Xue Y., Codogno P., Shen H. M. (2013) Activation of lysosomal function in the course of autophagy via mTORC1 suppression and autophagosome-lysosome fusion. *Cell Res.* **23**, 508–523.
- Zhou Q. Y., Quaife C. J., Palmiter R. D. (1995) Targeted disruption of the tyrosine hydroxylase gene reveals that catecholamines are required for mouse fetal development. *Nature* **374**, 640–643.
- Ziemssen T., Reichmann H. (2007) Non-motor dysfunction in Parkinson's disease. *Parkinsonism Relat. Disord.* **13**, 323–332.
- Zimprich A., Benet-Pagès A., Struhal W., Graf E., Eck S. H., Offman M. N., Haubenberger D., et al. (2011) A Mutation in VPS35, Encoding a Subunit of the Retromer Complex, Causes Late-Onset Parkinson Disease. *Am. J. Hum. Genet.* **89**, 168–175.
- Zimprich A., Biskup S., Leitner P., Lichtner P., Farrer M., Lincoln S., Kachergus J., et al. (2004) Mutations in LRRK2 Cause Autosomal-Dominant Parkinsonism with Pleomorphic Pathology. *Neuron* **44**, 601–607.

Publications

- ❖ The findings in chapter 4, 7 and 8 are published in the following publications:
 - **Alrashidi H**, Eaton S, Heales S. **Biochemical characterization of proliferative and differentiated SH-SY5Y cell line as a model for Parkinson's disease.** Neurochem Int. 2021 May;145:105009. doi: 10.1016/j.neuint.2021.105009. Epub 2021 Mar 5. PMID: 33684546.
 - Rossignoli G, Krämer K, Lugarà E, **Alrashidi H**, Pope S, De La Fuente Barrigon C, Barwick K, Bisello G, Ng J, Counsell J, Lignani G, Heales SJR, Bertoldi M, Barral S, Kurian MA. **Aromatic l-amino acid decarboxylase deficiency: a patient-derived neuronal model for precision therapies.** Brain. 2021 Sep 4;144(8):2443-2456. doi: 10.1093/brain/awab123. PMID: 33734312; PMCID: PMC8418346.
 - Sonia Gandhi, Gurvir Virdi, Minee Choi, James Evans, Zhi Yao, Dilan Athauda, Stephanie Strohbuecker, Raja Nirujogi, Anna Wernick, Noelia Pelegrina-Hidalgo, Craig Leighton, Rebecca Saleeb, Olga Kopach, **Haya Alrashidi**, Daniela Melandri, Jimena Perez Lloret, Plamena Angelova, Sergiy Sylantyev, Simon Eaton, Simon Heales, Dmitri Rusakov, Dario Alessi, Tilo Kunath, Mathew Horrocks, Andrey Abramov, Rickie Patani. **Protein aggregation and calcium dysregulation are hallmarks of familial**

Parkinson's disease in midbrain dopaminergic neurons.

Accepted in npr Parkinson's. Pending publication.

❖ Work related to this thesis has been published in:

- Ng J, Barral S, De La Fuente Barrigon C, Lignani G, Erdem FA, Wallings R, Privolizzi R, Rossignoli G, **Alrashidi H**, Heasman S, Meyer E, Ngoh A, Pope S, Karda R, Perocheau D, Baruteau J, Suff N, Antinao Diaz J, Schorge S, Vowles J, Marshall LR, Cowley SA, Sucic S, Freissmuth M, Counsell JR, Wade-Martins R, Heales SJR, Rahim AA, Bencze M, Waddington SN, Kurian MA. **Gene therapy restores dopamine transporter expression and ameliorates pathology in iPSC and mouse models of infantile parkinsonism.** Sci Transl Med. 2021 May 19;13(594):eaaw1564. doi: 10.1126/scitranslmed.aaw1564. PMID: 34011628; PMCID: PMC7612279.

A copy of the publications is attached at the end

Conference abstracts

European Society for Neurochemistry 7th Conference on Molecular Mechanisms of Regulation in the Nervous System - Milan, Italy 2019

Title: Dopamine and Serotonin Metabolism in Parkinsonian Disorders:

SH-SY5Y cell line as a disease model.

Authors: Haya Alrashidi, Simon Eaton and Simon Heales

The major pathological feature of Parkinson's Disease (PD) is dopamine depletion and death of dopaminergic neurons of the substantia nigra. Dysregulations to the serotonin system are also reported. The cause of neuronal death is still unknown. Loss mitochondrial of complex 1 is well documented. Furthermore, compromised lysosomal glucocerebrosidase (GBA) enzyme activity has been described in brain tissue of sporadic PD patients and patients with GBA mutations. Recent work, by our group, suggests the importance of functional mitochondria and lysosomes for optimal dopamine and serotonin metabolism. In addition, decreased levels of glutathione, the cell's major antioxidant, are also reported. However, the pathological mechanism of PD remains unclear. Appropriate models are imperative for any scientific study. Dopaminergic neuronal cell models are necessary for studying PD mechanism and for development of therapeutics. The SH-SY5Y cell line is one of the most widely used cell model for PD research however, reports of its dopaminergic nature are conflicted in literature. A more neuronal like cell model can be generated by differentiation of SH-SY5Y cells using retinoic acid and 12-O-Tetradecanoylphorbol-13-acetate. In this study, we have compared dopamine/serotonin metabolism in these cells and compared this to proliferative

cells. Notable differences were 79% decrease in extracellular dopamine and a 160% increase in its turnover. Serotonin metabolism however was comparable. These data further indicate the importance of utilising an appropriate model system for studying parkinsonian disorders.

Declaration Form: referencing doctoral candidate's own published work(s) in thesis

Please use this form to declare if parts of your thesis are already available in another format, e.g. if data, text, or figures:

- have been uploaded to a preprint server;
- are in submission to a peer-reviewed publication;
- have been published in a peer-reviewed publication, e.g. journal, textbook.

This form should be completed as many times as necessary. For instance, if a student had seven thesis chapters, two of which having material which had been published, they would complete this form twice.

- **For a research manuscript that has already been published** (if not yet published, please skip to section 2):
 - **Where was the work published?** (e.g. journal name)
 - Neurochemistry international
 - **Who published the work?** (e.g. Elsevier/Oxford University Press)
 - Elsevier
 - **When was the work published?**
 - March 2021
 - **Was the work subject to academic peer review?** YES / NO
 - **Have you retained the copyright for the work?** YES / NO [If no, please seek permission from the relevant publisher and check the box next to the below statement:
 - *I acknowledge permission of the publisher named under 1b to include in this thesis portions of the publication named as included in 1a.*
- **For multi-authored work, please give a statement of contribution covering all authors** (if single-author, please skip to section 4):

- **Haya Alrashidi** Methodology, Investigation, Formal analysis, Writing - Original Draft
- **Simon Eaton** Supervision, Writing - Review & Editing
- **Simon Heales** Conceptualization, Supervision, Writing - Review & Editing

- **In which chapter(s) of your thesis can this material be found?**

- Chapter 4

- **Candidate's e-signature:**

- **Date: 30/06/2022**

- **Supervisor/senior author(s) e-signature:**

- **Date: 30/06/2022**

Declaration Form: referencing doctoral candidate's own published work(s) in thesis

Please use this form to declare if parts of your thesis are already available in another format, e.g. if data, text, or figures:

- have been uploaded to a preprint server;
- are in submission to a peer-reviewed publication;
- have been published in a peer-reviewed publication, e.g. journal, textbook.

This form should be completed as many times as necessary. For instance, if a student had seven thesis chapters, two of which having material which had been published, they would complete this form twice.

- **For a research manuscript that has already been published** (if not yet published, please skip to section 2):
 - **Where was the work published?** (e.g. journal name)
 - **Brain**
 - **Who published the work?** (e.g. Elsevier/Oxford University Press)
 - Oxford academic press
 - **When was the work published?**
 - 2021
 - **Was the work subject to academic peer review?** YES / NO
 - **Have you retained the copyright for the work?** YES / NO [If no, please seek permission from the relevant publisher and check the box next to the below statement:
 - *I acknowledge permission of the publisher named under 1b to include in this thesis portions of the publication named as included in 1a.*
- **For multi-authored work, please give a statement of contribution covering all authors** (if single-author, please skip to section 4):
 - **Haya Alrashidi:** HPLC measurement of dopamine metabolites and interpreting the data.
- **In which chapter(s) of your thesis can this material be found?**
 - Chapter 7

- **Candidate's e-signature:**
 - **Date: 30/06/2022**

- **Supervisor/senior author(s) e-signature:**
 - **Date: 30/06/2022**

Declaration Form: referencing doctoral candidate's own published work(s) in thesis

Please use this form to declare if parts of your thesis are already available in another format, e.g. if data, text, or figures:

- have been uploaded to a preprint server;
- are in submission to a peer-reviewed publication;
- have been published in a peer-reviewed publication, e.g. journal, textbook.

This form should be completed as many times as necessary. For instance, if a student had seven thesis chapters, two of which having material which had been published, they would complete this form twice.




- **For a research manuscript that has already been published** (if not yet published, please skip to section 2):
 - **Where was the work published?** (e.g. journal name)
 - **NPJ Parkinson's disease**
 - **Who published the work?** (e.g. Elsevier/Oxford University Press)
 - Springer Nature
 - **When was the work published?**
 - October 2022
 - **Was the work subject to academic peer review?** YES / NO
 - **Have you retained the copyright for the work?** YES / NO [If no, please seek permission from the relevant publisher and check the box next to the below statement:
 - *I acknowledge permission of the publisher named under 1b to include in this thesis portions of the publication named as included in 1a.*
- **For multi-authored work, please give a statement of contribution covering all authors** (if single-author, please skip to section 4):
 - **Haya Alrashidi:** HPLC measurement of dopamine metabolites and interpreting the data.
- **In which chapter(s) of your thesis can this material be found?**
 - Chapter 8

- **Candidate's e-signature:**
 - **Date: 31/10/22**

- **Supervisor/senior author(s) e-signature:**
 - **Date: 31/10/2022**



Aromatic L-amino acid decarboxylase deficiency: a patient-derived neuronal model for precision therapies

Giada Rossignoli,^{1,2} Karolin Krämer,¹ Eleonora Lugarà,³ Haya Alrashidi,⁴ Simon Pope,⁵ Carmen De La Fuente Barrigon,⁴ Katy Barwick,¹  Giovanni Bisello,² Joanne Ng,^{1,6} John Counsell,¹  Gabriele Lignani,³ Simon J. R. Heales,^{5,7}  Mariarita Bertoldi,² Serena Barral¹ and Manju A. Kurian^{1,8}

Aromatic L-amino acid decarboxylase (AADC) deficiency is a complex inherited neurological disorder of monoamine synthesis which results in dopamine and serotonin deficiency. The majority of affected individuals have variable, though often severe cognitive and motor delay, with a complex movement disorder and high risk of premature mortality. For most, standard pharmacological treatment provides only limited clinical benefit. Promising gene therapy approaches are emerging, though may not be either suitable or easily accessible for all patients.

To characterize the underlying disease pathophysiology and guide precision therapies, we generated a patient-derived midbrain dopaminergic neuronal model of AADC deficiency from induced pluripotent stem cells.

The neuronal model recapitulates key disease features, including absent AADC enzyme activity and dysregulated dopamine metabolism. We observed developmental defects affecting synaptic maturation and neuronal electrical properties, which were improved by lentiviral gene therapy. Bioinformatic and biochemical analyses on recombinant AADC predicted that the activity of one variant could be improved by L-3,4-dihydroxyphenylalanine (L-DOPA) administration; this hypothesis was corroborated in the patient-derived neuronal model, where L-DOPA treatment leads to amelioration of dopamine metabolites.

Our study has shown that patient-derived disease modelling provides further insight into the neurodevelopmental sequelae of AADC deficiency, as well as a robust platform to investigate and develop personalized therapeutic approaches.

1 Developmental Neurosciences, GOS Institute of Child Health, University College London, London WC1N 1EH, UK

2 Biological Chemistry, NBM Department, University of Verona, 37134 Verona, Italy

3 Clinical and Experimental Epilepsy, Queen Square Institute of Neurology, University College London, London WC1N 3BG, UK

4 Genetics and Genomic Medicine, GOS Institute of Child Health, University College London, London WC1N 1EH, UK

5 Neurometabolic Unit, National Hospital for Neurology and Neurosurgery, Queen Square, London WC1N 3BG, UK

6 Gene Transfer Technology Group, EGA-Institute for Women's Health, University College London, London WC1E 6HU, UK

7 Centre for Inborn Errors of Metabolism, GOS Institute of Child Health, University College London, London WC1N 1EH, UK

8 Department of Neurology, Great Ormond Street Hospital, London WC1N 3JH, UK

Correspondence to: Prof Manju Kurian
Zayed Centre for Research
UCL Great Ormond Street Institute of Child Health

Received August 27, 2020. Revised January 25, 2021. Accepted February 08, 2021. Advance access publication March 18, 2021

© The Author(s) (2021). Published by Oxford University Press on behalf of the Guarantors of Brain.

This is an Open Access article distributed under the terms of the Creative Commons Attribution License (<http://creativecommons.org/licenses/by/4.0/>), which permits unrestricted reuse, distribution, and reproduction in any medium, provided the original work is properly cited.

20 Guilford St, London WC1N 1DZ, UK
E-mail: manju.kurian@ucl.ac.uk

Correspondence may also be addressed to: Prof Mariarita Bertoldi
Department of Neuroscience, Biomedicine and Movement Sciences
Biological Chemistry Section, Room 1.24
Strada le Grazie 8, 37134 Verona, Italy
E-mail: mita.bertoldi@univr.it

Keywords: induced pluripotent stem cells; dopaminergic neurons; aromatic L-amino acid decarboxylase deficiency; neurodevelopment; personalized medicine

Abbreviations: AADC = aromatic L-amino acid decarboxylase; DEGs = differentially expressed genes; HPLC = high performance liquid chromatography; HVA = homovanillic acid; iPSC = induced pluripotent stem cell; L-DOPA = L-3, 4-dihydroxyphenylalanine; mDA = midbrain dopaminergic; PLP = pyridoxal 5'-phosphate

Introduction

Neurodevelopmental processes are commonly disrupted in the vast majority of inborn errors of metabolism, resulting in a wide repertoire of clinical manifestations from severe cognitive, neuropsychiatric, and motor problems to more subtle learning difficulties.¹ Aromatic L-amino acid decarboxylase (AADC) deficiency is a rare inborn error of neurotransmitter metabolism due to bi-allelic mutations in *DDC*, which encodes the enzyme that catalyses the final step of serotonin and dopamine synthesis.² The resultant enzyme deficiency leads to combined serotonin and catecholamine (dopamine, norepinephrine, epinephrine) deficiency.³ Although there is a wide phenotypic spectrum,^{4,5} the majority of affected patients show many of the typical features seen in recessively inherited, early-onset neurotransmitter disorders,⁶ including severe global neurodevelopmental delay, oculogyric crises, a complex movement disorder (characterized by central and peripheral hypotonia, commonly with features of dystonia/chorea) and symptoms of dysautonomia, as well as secondary gastrointestinal, respiratory and orthopaedic complications.^{7,8} As a result, most patients have significant disability and high risk of premature mortality. AADC deficiency is associated with a characteristic CSF monoamine profile, with reduced 5-hydroxyindoleacetic acid (5-HIAA), homovanillic acid (HVA), and 3,4-dihydroxyphenylacetic acid (DOPAC), and a concomitant increase in 5-hydroxytryptophan (5-HTP), L-3,4-dihydroxyphenylalanine (L-DOPA), and 3-O-methyl-dopa (3-OMD). Definitive diagnosis is ideally achieved by confirming a decrease or absence of plasma AADC enzymatic activity, and *DDC* gene sequencing. To date, there are no clear correlations between patient genotype, CSF monoamine profile, AADC enzyme activity and phenotype.

A recently published consensus guideline outlines recommendations for the diagnosis and management of AADC deficiency.⁸ Pharmacological therapy provides some, though often limited, clinical benefit and patients often show variable drug response. It has been postulated that the variability in disease severity and medication response may be partly attributed to genotype^{9,10} and as a result, a number of studies have focused on characterizing the underlying molecular defects caused by different pathogenic variants.^{11–15} More recently, promising gene therapy approaches are emerging for AADC deficiency, with a number of clinical trials evaluating the safety and efficacy of targeted intraparenchymal delivery of AAV2-based vectors.^{16–18} It is hoped that with time, these studies may clarify the effect of patient genotype, age at surgery, pretreatment motor function and target delivery site on overall therapeutic efficacy. Although early clinical studies on AADC

gene therapy are encouraging, it is likely that this therapeutic strategy may not be either viable, suitable or easily accessible for a proportion of patients. Moreover, with advances in diagnostic testing, the global incidence and prevalence of AADC deficiency continues to increase,¹⁹ and the need for alternative precision therapies is increasingly apparent.

Recently, patient-derived cellular models of neurodevelopmental disorders have proven to be a valuable experimental system to unravel disease mechanisms and test novel therapeutic strategies with translational potential.²⁰ As such, we have developed a humanized neuronal model of AADC deficiency, by reprogramming patient fibroblasts into induced pluripotent stem cells (iPSCs) for differentiation into midbrain dopaminergic (mDA) neurons. This model system has allowed us to gain further insight into the neurodevelopmental consequences of AADC deficiency, with effects on synaptic maturation and neuronal function. Moreover, it has also provided a suitable platform to evaluate the effects of precision medicine approaches at a cellular level, demonstrating the potential for rational development of patient-specific strategies in such rare monogenic disorders.

Materials and methods

Induced pluripotent stem cell generation and maintenance

Generation of iPSCs from patient dermal fibroblasts was approved by the Local Research Ethics Committee (Reference 13/LO/0171). Written informed consent was obtained from all patients. Age-matched healthy control fibroblasts were collected from the MRC Centre for Neuromuscular Disorders Biobank. Patient fibroblasts were isolated from skin biopsies and maintained in DMEM (Gibco), 10% foetal bovine serum (Gibco), 2 mM L-glutamine (Gibco), 1% MEM non-essential amino acids (Gibco), and 1% penicillin/streptomycin (P/S, Gibco), and tested for mycoplasma contamination. Reprogramming was performed using the commercially available CytoTune[®]-iPS 2.0 Sendai Reprogramming kit (Invitrogen), following manufacturer's instructions. Fibroblast were transduced at 80% confluence ($1\text{--}1.5 \times 10^5$ cells/well). After 6 days, infected cells were harvested with TrypLE[™] (Invitrogen) and 8000 cells/well were seeded onto gamma-irradiated mouse embryonic fibroblasts. After 24 h, cells were cultured into KO-DMEM (Gibco), 20% serum replacement (Gibco), 2 mM L-glutamine, 50 μ M 2-mercaptoethanol, 1% MEM non-essential amino acids, 1% P/S, and 10 ng/ml basic fibroblast growth factor (Gibco). 13 days post-transfection, cells

were cultured in gamma-irradiated mouse embryonic fibroblasts-conditioned medium. Around Day 30 post-transduction, 8–10 independent colonies with iPSCs-like morphology were collected and expanded using ReLeSR™ (Stemcell Technologies). Between passage 15 and 20, three colonies were converted to mTeSR1 medium (Stemcell Technologies) on Matrigel® (Corning®) coated plates. Derived iPSC lines were maintained in the mTeSR1/Matrigel system, regularly passaged with EDTA, 0.02% solution (Sigma-Aldrich) and again tested for mycoplasma infection, as previously. Two iPSC lines for each patient (Patients 1-04, 1-10, 2-01 and 2-06) and the age-matched healthy control (Control-05 and Control-03) were characterized at the iPSCs stage and further differentiated into mDA neurons to exclude clonal variability. Given the relative homogeneity reported in clonal lines with respect to transcriptome, growth, and capability of germ layer formation,^{21,22} one clone per patient (Patient 1-04; Patient 2-01) and age-matched healthy control (Control-05) were then used for downstream experiments.

Differentiation of induced pluripotent stem cells into midbrain dopaminergic neurons

iPSCs were differentiated into mDA neurons as previously described.²³ Briefly, iPSCs were harvested using TrypLE™ (Invitrogen), and plated onto non-adherent bacterial dishes at a concentration of 1.5×10^5 cells/cm² in DMEM/F12:Neurobasal™ (1:1), N2 (1:100) and B27 minus vitamin A (1:50) supplements (Invitrogen), 2 mM L-glutamine and ROCK-inhibitor for the first 2 days. Embryoid bodies were plated at Day 4 onto polyornithine (PO; 15 µg/ml; Sigma), fibronectin (FN; 5 µg/ml Gibco) and laminin (LN; 5 µg/ml; Sigma) coated dishes in DMEM/F12:Neurobasal™ (1:1), N2 (1:200), B27 minus vitamin A (1:100), 2 mM L-glutamine. From Day 0 to Day 9, medium was supplemented with: 10 µM SB431542 (Tocris Bioscience), 100 nM LDN193189 (Stemgent Inc), 0.8 µM CHIR99021 (Tocris Bioscience) and 100 ng/ml hSHH-C24-II (R&D Systems). On Day 2, 0.5 µM purmorphamine (Cambridge Bioscience) was added. SB431542 was withdrawn on Day 6. On Day 11, cells were either processed for mDA precursors analysis or harvested with Accumax and replated on PO/FN/LN coated dishes in droplets of $1\text{--}1.5 \times 10^4$ cells/µl in Neurobasal™/B27 minus vitamin A (1:50), 2 mM L-glutamine, 0.2 mM ascorbic acid and 20 ng/ml BDNF (Miltenyi Biotech). On Day 14 of differentiation, 0.5 mM dibutyryl cAMP (Sigma-Aldrich) and 20 ng/ml GDNF (Miltenyi Biotech) were added. On Day 30 of differentiation, cells were replated as describe above onto PO/FN/LN coated dishes or Lab-Tek™ slides (Nunc™), and γ -secretase inhibitor DAPT (10 µM, Tocris) was added until final differentiation at Day 65. Cells were then harvested or processed for further analysis.

AADC activity assay

AADC enzyme assay was performed using the refined method developed in Allen²⁴ from Hyland and Clayton.²⁵ Neuronal cultures at Day 65 in phenol red-free medium were harvested and lysed by snap freezing twice in liquid nitrogen in 100 µl of 10 mM Tris pH 7.4 (Sigma-Aldrich), 1 mM EDTA, 320 mM sucrose (Sigma-Aldrich) and protease inhibitor cocktail (Roche). Cell lysate (50 µl) was incubated with 70 µM pyridoxal 5'-phosphate (PLP, Sigma-Aldrich) in assay buffer composed by 500 mM sodium phosphate pH 7.0, 0.167 mM EDTA, and 39 mM dithiothreitol (Sigma-Aldrich) for 120 min at 37°C, and subsequently 2 mM final concentration of L-DOPA (Sigma-Aldrich) was added and incubated for 20 min at 37°C. The reaction was stopped with 250 µl of 0.8 M perchloric acid (final concentration 0.4 M) for 10 min at room temperature and centrifuged at 12 000g for 5 min at 4°C. A substrate blank with no L-DOPA and a

sample blank without cell lysate were performed for each sample. Dopamine in the supernatant was then quantified by high performance liquid chromatography (HPLC).

High performance liquid chromatography for quantification of activity assay and metabolic profile

Dopamine produced in the activity assay was separated by reverse-phase HPLC using a HiQsil C18 column 250 × 4.6 mm (Kya Technologies) and detected by coulometric electrochemical detection using a Coulochem® III detector (ESA) with 5010 analytical cell (ESA) setting the detector electrode at 350 mV and the screening electrode at 20 mV. The mobile phase consisted of 50 mM sodium phosphate pH 3.6, 5 mM octaensulfonic acid, 67 µM EDTA, 43 mM orthophosphoric acid and 230 ml/l methanol diluted in 18.2 Ω HPLC grade water, at a flow rate of 1.2 ml/min at 25°C. Dopamine was quantified with Azur software package using a 1000 nM external standard and enzymatic activity was expressed as pmol/min/mg protein.

HPLC analysis of metabolic profile in derived mature cultures was performed on the phenol red-free medium incubated for 48 h on Day 65 mDA neurons. 1:1 medium was mixed with perchloric acid to a final concentration of 0.4 M, incubated 10 min at 4°C in the dark, centrifuged at 12 000g for 5 min at 4°C, and supernatant was collected for analysis by HPLC.²⁶ Metabolites were separated by reverse-phase HPLC using a C18HS column 250 mm × 4.5 mm (Kromatek) and detected by coulometric electrochemical detection using a Coulochem® III detector (ESA) with 5010A analytical cell (Thermo Fisher Scientific) setting the detector electrode at 450 mV and the screening electrode at 20 mV. Mobile phase consisted of 20 mM sodium acetate trihydrate pH 3.45, 12.5 mM citric acid monohydrate, 100 µM EDTA, 3.35 mM octaensulfonic acid and 16% methanol diluted in 18.2 Ω HPLC grade water, at a flow rate of 1.5 ml/min at 27°C. Metabolites were quantified with EZChrom Elite™ chromatography software (JASCO) using a 500 nM external standard mixture, and expressed as pmol/mg protein.

Bulk RNA sequencing analysis

Total RNA was isolated using the RNeasy® mini kit (Qiagen) following manufacturer's instructions. RNA libraries were prepared from 100 ng of total RNA using KAPA mRNA HyperPrep kit (Roche) according to the manufacturer's protocol and sequenced with Illumina NextSeq 500 Mid Output 75 bp paired-end (~22 M reads/sample). FASTQ obtained files were uploaded to Galaxy web platform, and the public server at usegalaxy.org was used for downstream analyses.²⁷ FASTQ files were filtered with Trimmomatic (v.0.38), with SLIDINGWINDOW trimming and low quality (phread score <20) reads filter.²⁸ Obtained reads were mapped to human reference genome (GRCh38) with HISAT2 (v.2.1.0).²⁹ Fragments counts for genes were extracted with featureCounts (v.1.6.4) excluding duplicates, multimapping reads and chimeric fragments.³⁰ Differential gene expression was analysed using edgeR (v.3.24.1), filtering low counts at 0.35 minimum counts per million, in at least three samples,³¹ and comparing disease status (patients versus control) and disease-specific genotype (Patient 2 versus Patient 1). Differentially expressed genes (DEGs) with a P-value < 0.05 and absolute fold change >2 were considered as statistically significant. Heat maps were generated from the row-scaled z-score of DEGs normalized counts obtained by EdgeR with complete-linkage Euclidean hierarchical clustering. Gene ontology (GO) enrichment analyses were performed using ShinyGO v0.61³² for biological process, and ClueGO v.2.5.7³³ for cellular component and molecular function enrichments and groupings, with Benjamini-Hochberg P-value correction of false discovery rate

(FDR) < 0.05 for statistical significance. Results from the expression analysis along with the raw sequence data were deposited in GEO (Gene Expression Omnibus), under accession GSE153990.

Electrophysiology

Current-clamp recordings were performed on neurons at Day 65 of differentiation. The internal solution contained 135 mM K-gluconate, 4 mM KCl, 10 mM HEPES, 4 mM Mg-ATP, 0.3 mM Na-GTP, and 10 mM of Na₂-phosphocreatine, at pH 7.3 and mOsm 291–295. The recording extracellular solution contained 125 mM NaCl, 2.5 mM KCl, 2 mM MgCl₂, 1.25 mM KH₂PO₄, 2 mM CaCl₂, 30 mM glucose, and 25 mM of HEPES at pH 7.4. Experiments were performed at room temperature (22–24°C). Neurons with unstable resting potential (or > -50 mV), bridge-balance > 20 MΩ and/or holding current > 200 pA were discarded. Bridge balance compensation was applied in current clamp and the resting membrane potential was held at -70 mV. A current steps protocol was used to evoke action potentials injecting 250 ms long depolarizing current steps of increasing amplitude ($\Delta 10$ pA). Action potentials were triggered holding the neurons around -60 mV/-55 mV. Neurons with repetitive spontaneous action potentials and repetitive evoked action potentials were considered to be functional mature mDA neurons. Recordings were acquired using a Multiclamp 700A amplifier (Axon Instruments, Molecular Devices) at 10 kHz and filtered at 2 kHz (Bessel) using WinEDR (John Dempster, University of Strathclyde). Recordings were not corrected for liquid junction potentials. The approximate cell capacitance was computed as: $capacitance = \tau/R_i$, whereby the time constant τ was found by fitting a single exponential function to the time points where the membrane voltage was between 10% and 95% of the initial charging decay slope of a negative hyperpolarizing current step. Input resistance was calculated fitting $\Delta V/\Delta I$ at two hyperpolarizing steps (-20 and -10 pA) and a positive one (+10 pA). Action potentials were identified when the voltage signal crossed 0 V. Spontaneous excitatory postsynaptic currents were recorded in a voltage clamp and automatically detected with a template-based algorithm using Clampfit (Molecular Devices).

Treatment with L-DOPA and cytotoxicity assay

Neuronal cultures at Day 65 of differentiation were treated with 80 μ M L-DOPA in phenol red-free medium for 24 h. The medium was subsequently removed and analysed by HPLC, as described

above. Dead-cell protease release measurements were performed using CytoTox-Glo™ Cytotoxicity Assay (Promega) according to the manufacturer's instructions.

Statistical analysis

Two-tailed Student's t-test for single comparisons and statistical one-way ANOVA followed by Tukey's multiple comparisons test were performed using GraphPad Prism. Results are reported as mean \pm standard error of the mean (SEM) from at least three independent biological replicates, the exact number of which is stated for each experiment in the figure legend. Significance levels were determined by P-value, and shown on graphs with asterisks. P-values are presented as *P = 0.05–0.01, **P = 0.01–0.001, and ***P < 0.001.

Data availability

Data supporting the findings of this study are available from the corresponding authors, upon reasonable request.

Results

Patient-derived midbrain dopaminergic neurons show loss of AADC activity and dysregulated dopamine synthesis

Dermal fibroblasts were obtained from two patients with AADC deficiency (Table 1). Patient 1 (homozygous missense variant c.1039C>G, p.R347G) presented with classical infantile onset disease, with early hypotonia, oculogyric crises and neurodevelopmental delay.¹⁵ He is currently 6.5 years of age, and although he continues to make neurodevelopmental progress, remains non-ambulant and non-verbal. Patient 2 (compound heterozygous variants c.19C>T, p.Arg7*; c.299G>C, p.C100S) had a classical infantile-onset presentation of disease with severe global developmental delay, oculogyric crises and hypoglycaemia, but over time showed a positive response to therapy and had an overall milder disease course. Once AADC deficiency was diagnosed at 3.5 years of age, the instigation of dopaminergic medication and other specific AADC deficiency treatments were associated with neurodevelopmental progress; independent ambulation was achieved by 4.5 years and spoken language by 5.5 years. From 10 to 18 years, adjunct therapies were needed to combat side effects from long-term use of the original treatments to maintain basic motor and verbal

Table 1 Phenotype and genotype features of AADC deficiency patients

Patient number	Patient line	Clinical phenotype	Zygosity	Location of mutation	Type of mutation	Amino acid change
1	Patient 1-04 Patient 1-10	Oculogyric crises (frequent) Hypotonia Movement disorder Non-ambulant Autonomic features Neurodevelopmental delay Non-verbal	Homozygous	Exon 11	Missense	Arg347Gly
2	Patient 2-01 Patient 2-06	Oculogyric crises (infrequent) Mild motor disorder but achieved independent ambulation Neurodevelopmental delay Behavioural issues Autistic traits Psychiatric symptoms	Heterozygous	Exon 2 Exon 3	Nonsense Missense	Arg7* Cys100Ser

function. Now aged 22 years, he has ongoing learning difficulties, mild motor impairments, behavioural issues, autistic traits and neuropsychiatric symptoms of anxiety and intermittent low mood. iPSC lines were generated from dermal fibroblasts of both patients and from an age-matched healthy individual (control). Sequencing of genomic DNA confirmed that patient iPSC lines retained their specific *DDC* mutation (Supplementary Fig. 1A). All iPSCs lines showed clearance of viral transgenes, genomic integrity (Supplementary Fig. 1B and C), and true pluripotency (Supplementary Fig. 2A–D). iPSCs were then differentiated into mDA neurons, and both patient and control iPSC lines showed similar differentiation efficiency. After 11 days of differentiation, all lines showed high levels of mDA progenitors and typical mid-brain precursor gene expression profiles (Supplementary Fig. 3A–C). By 65 days of differentiation, both control and patient lines comparably matured into neurons, in particular with dopaminergic identity (Supplementary Fig. 4A and B). Both control and patient-derived neuronal cultures showed upregulation of midbrain-related genes (Supplementary Fig. 4C). Whole-cell patch clamp electrophysiology confirmed that iPSC-derived mDA neurons were functional and exhibited continuous and rhythmic pacemaker-like activity (Supplementary Fig. 4D). Derived neuronal cultures were almost devoid of serotonergic neurons, restricting all further analyses specifically to the mDA neuronal subtype (Supplementary Fig. 5A).

We first investigated the effect of patient mutations on AADC enzyme activity and protein expression. Measurement of AADC activity showed significantly lower enzymatic function in patients when compared to control-derived neurons (Fig. 1A). HPLC analysis of extracellular metabolites showed a disease-specific absence of dopamine and HVA with significantly reduced levels of DOPAC. In contrast, 3-OMD, a downstream metabolite of the AADC substrate L-DOPA, was significantly increased in patient-derived neurons (Fig. 1B). Analysis of AADC protein levels showed an increase in Patient 1 neuronal cultures when compared to the control subject; in contrast, a significant reduction of AADC protein

was detected in Patient 2 neuronal cultures (Fig. 1C, D and Supplementary Fig. 5B), in line with the second heterozygous early stop codon variant predicted to result in nonsense-mediated mRNA decay.

We then explored whether the aberrant AADC protein levels in patients could be linked to a difference in intrinsic protein stability. Recombinant AADC proteins were produced for the homozygous R347G variant (Patient 1) and C100S variant (Patient 2). Circular dichroism and dynamic light scattering analyses showed comparable values for both mutant and wild-type AADC protein, inferring similar intrinsic protein stability (Supplementary Table 1).

To investigate whether aberrant AADC protein levels related to *DDC* gene expression, quantitative RT-PCR studies were undertaken. In line with protein expression data, we observed a statistically significant increase in *DDC* expression in Patient 1 when compared to the control (Supplementary Fig. 5C). For Patient 2, we observed comparable levels of *DDC* expression to the control (Supplementary Fig. 5C), despite the predicted nonsense-mediated decay of a proportion of transcripts. We also observed an increase in tyrosine hydroxylase (TH) protein and gene expression in both patient lines when compared to the control (Supplementary Fig. 5D and E).

AADC deficiency has mutation-specific effects on neuronal synaptic maturation and connectivity

We then sought to investigate the neurodevelopmental consequences of AADC deficiency in our *in vitro* model. Immunofluorescence analysis of the mature neuronal marker NeuN showed comparable levels in Patient 1 and control mDA neurons, while Patient 2 cultures showed a significant decrease in NeuN positivity when compared to both control and Patient 1 lines (Fig. 2A and B). Moreover, analysis of the vesicular protein synaptophysin revealed a significant decrease in protein levels for both

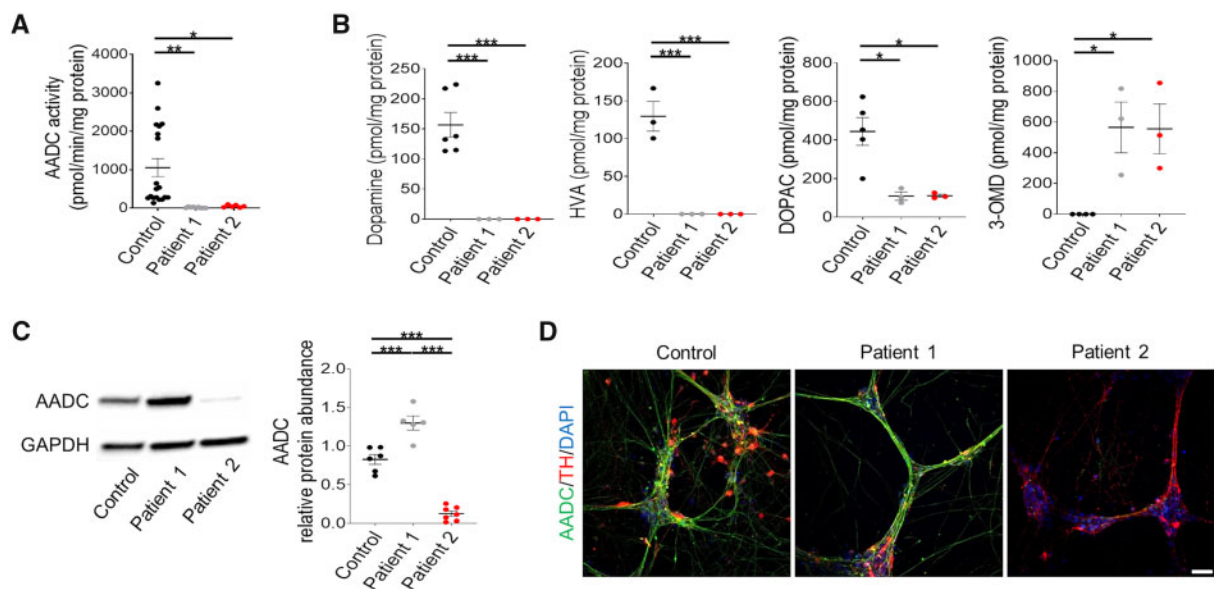


Figure 1 Patient-derived neurons show loss of AADC enzymatic activity and dysregulated dopamine synthesis. (A) AADC activity assay relative to total protein ($n = 19, 9$, and 6 for the control subject, Patient 1 and Patient 2, respectively). (B) HPLC detection of extracellular dopamine, HVA, DOPAC and 3-OMD in control, Patient 1 and Patient 2-derived neuronal cultures. Values are relative to total protein ($n = 6, 3, 3$; $n = 3, 3, 3$; $n = 5, 3, 3$; $n = 4, 3, 3$, respectively). (C) Immunoblot analysis for AADC protein in control, Patient 1 and Patient 2-derived neurons at Day 65 of differentiation. Quantification relative to loading control (GAPDH) ($n = 6, 5, 7$, respectively). (D) Representative images for AADC and TH immunofluorescence in derived neurons. Scale bar = $100 \mu\text{m}$. Data are presented as mean \pm SEM. * $P < 0.05$; ** $P < 0.01$; *** $P < 0.001$, one-way ANOVA followed by Tukey's multiple comparisons test.

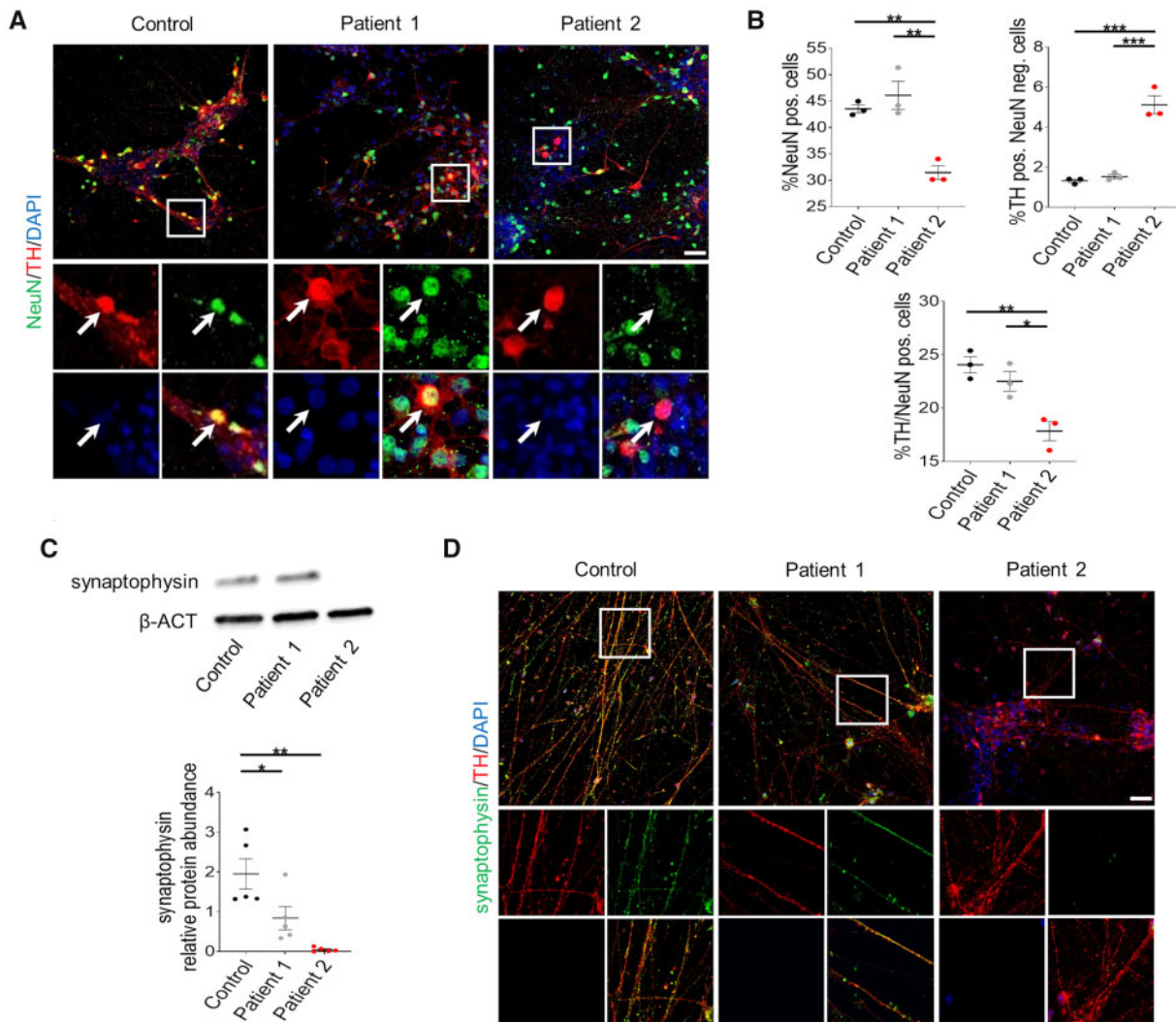


Figure 2 Patient-derived neurons show defects in developmental maturation. (A) Representative immunofluorescence images for NeuN and TH in control and patient-derived neurons. Arrows indicate double positive cells. Scale bar = 100 μ m. *Insets* show higher magnification of NeuN-positive dopaminergic neurons. (B) Quantification of NeuN-positive, TH-positive and NeuN-negative, and TH/NeuN double-positive cells in derived neuronal cultures ($n = 3$ for all). (C) Representative immunoblot for synaptophysin and loading control (β -ACT) and quantification of relative synaptophysin abundance in total neuronal cell lysates ($n = 5$ for all). (D) Representative immunofluorescence for synaptophysin and TH in derived neurons. Scale bar = 100 μ m. *Insets* show higher magnification of synaptophysin-positive dopaminergic neurons. Data are presented as mean \pm SEM. * $P < 0.05$; ** $P < 0.01$; *** $P < 0.001$, one-way ANOVA followed by Tukey's multiple comparisons test.

Patients 1 and 2 when compared to control-derived neuronal cultures (Fig. 2C and D).

To investigate the neurodevelopmental effects of AADC deficiency, we undertook bulk RNA sequencing for analysis of DEGs between patient and control-derived neurons, with a particular focus on protein-coding genes. In a combined analysis of Patient 1 and Patient 2-derived neuronal cultures, we identified 750 DEGs (75% underexpressed and 25% overexpressed) when compared to the control (Fig. 3A). GO analysis of underexpressed DEGs revealed a strong enrichment in synaptic transmission-related biological processes and nervous system development, whilst overexpressed DEGs mainly enriched protein transcription and general organ developmental processes (Fig. 3B). Furthermore, underexpressed DEGs were associated with membranous cellular compartments (in particular, the cell periphery and synaptic region), and enriched in gated channels and regulators of membrane transport (Fig. 3C). In contrast, overexpressed DEGs were associated with non-membrane-bounded cell compartments (nucleus), with enrichment in transcriptional regulator proteins (Fig. 3D).

Considering the previously detected differences between the two patient lines (Fig. 2), single-comparison RNA sequencing analysis was also performed. We identified 842 protein-coding DEGs for Patient 1 compared to the control (Supplementary Fig. 6A) and 871 protein-coding DEGs for Patient 2 compared to the control (Supplementary Fig. 7A). For both analyses, underexpressed genes showed common enrichment for synaptic transmission (Supplementary Figs 6B and 7B)—reflected in the significant P -values observed in the combined analysis (Fig. 3B)—representing genes encoding proteins mainly localized at the cell periphery or synapses, and associated with ion channel function (Patients 1 and 2) and gated channel function (for Patient 2 in particular) (Supplementary Figs 6C and 7C). Differences in separate single Patient 1 and Patient 2 comparisons with the control were mainly detected for upregulated genes with regard to biological processes and significance (Supplementary Figs 6B and 7B): for Patient 1, overexpressed DEGs were enriched for developmental and cell projection assembly genes (Supplementary Fig. 6B and D), whereas for Patient 2 overexpressed DEGs were enriched for genes encoding endoplasmic reticulum and

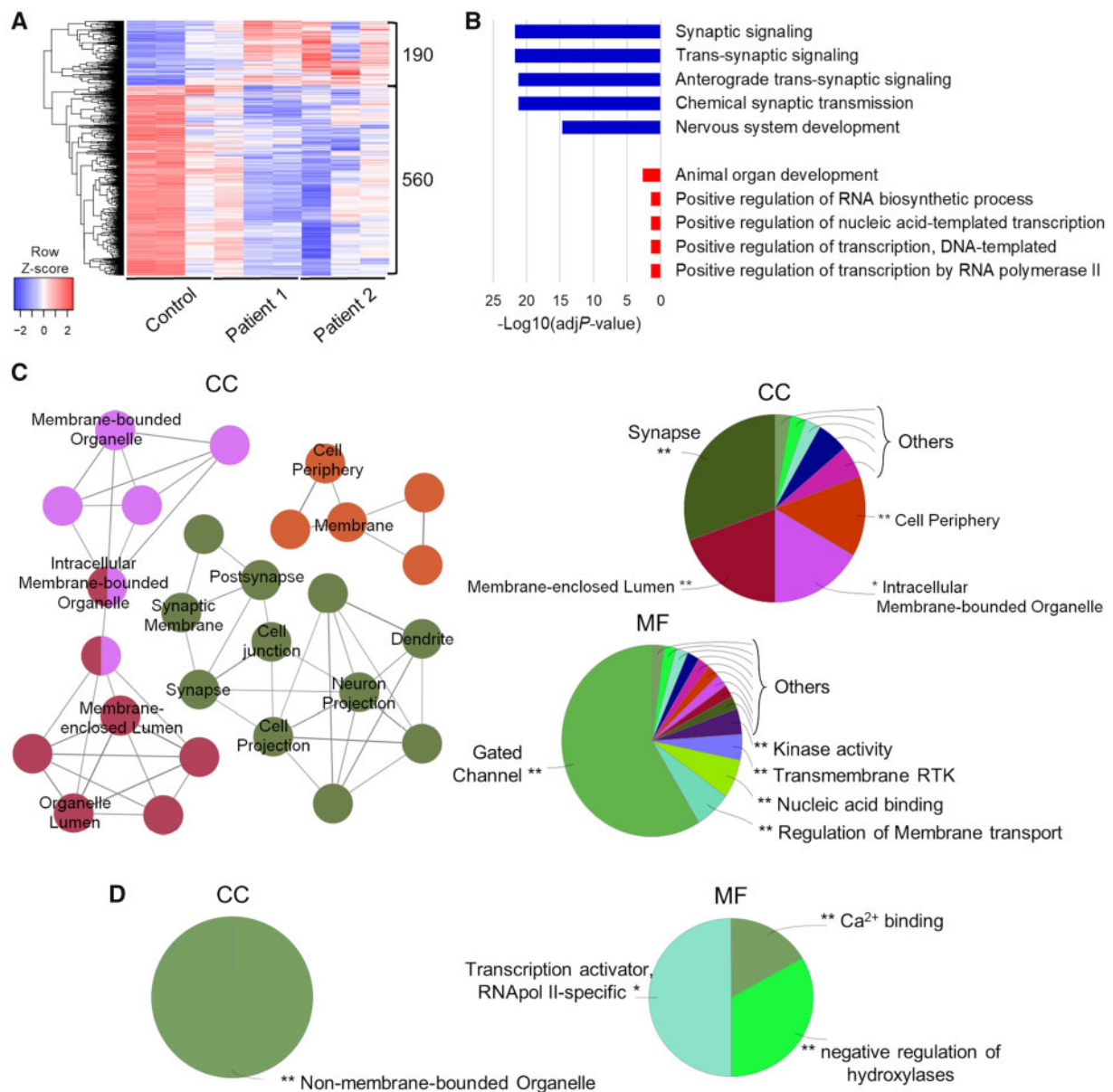


Figure 3 Bulk RNA sequencing analysis shows an abnormal gene expression profile in AADC deficiency patients. (A) Heat map showing hierarchical clustering of protein-coding DEGs in AADC deficiency patients compared to control (n = 3). (B) GO terms enrichment for biological process of under-expressed (blue) protein-coding and over-expressed (red) protein-coding DEGs. The top five categories are shown. (C and D) ClueGO analysis of GO terms enrichment of (C) under- and (D) over-expressed protein-coding DEGs, showing network graph and pie chart for cellular component (CC), and pie chart for molecular function (MF). Network graph nodes represent GO terms (the most significant are named) and edges indicate shared genes between GO terms. Functional groups of GO terms are indicated by the same colour. Pie charts show the percentages of each functional group representation, named with the most significant term. GO functional groups exhibiting higher statistically significant differences using Benjamini-Hochberg P-value correction (FDR < 0.05) are shown.

membrane-targeting processes and function (Supplementary Fig. 7B and D). Despite these inter-patient differences, the combined analysis reflects a common, disease-specific overexpression of developmental and transcriptional/translational processes from both single comparisons (Fig. 3B).

We then explored DEGs between the two different patient-derived neuronal cultures. We identified a total of 763 protein-coding DEGs for Patient 2 when compared to Patient 1 (Fig. 4A). The underexpressed DEGs showed enrichment in cell adhesion and membrane transport-related processes, while overexpressed DEGs enriched endoplasmic reticulum and membrane-targeting processes categories (Fig. 4B). Underexpressed DEGs corresponded to proteins localized both in cell periphery/membrane regions and

nuclear compartment, with enrichment for genes regulating transcription and transmembrane transport (Fig. 4C). Overexpressed DEGs showed enrichment in both cytosolic transcriptional and extracellular compartments, with molecular functions mainly linked to structural/binding molecules, and transcriptional/activity regulators (Fig. 4D), resembling the result from the single comparison between Patient 2 and control (Supplementary Fig. 7B and D).

Whole-cell patch clamp electrophysiology studies were undertaken to determine whether the observed differences in gene expression were associated with functional differences in neuronal activity. The parameters analysed were similar to other studies using iPSC-derived dopaminergic neurons, with comparable findings for firing pattern, pacemaker and synaptic activity in

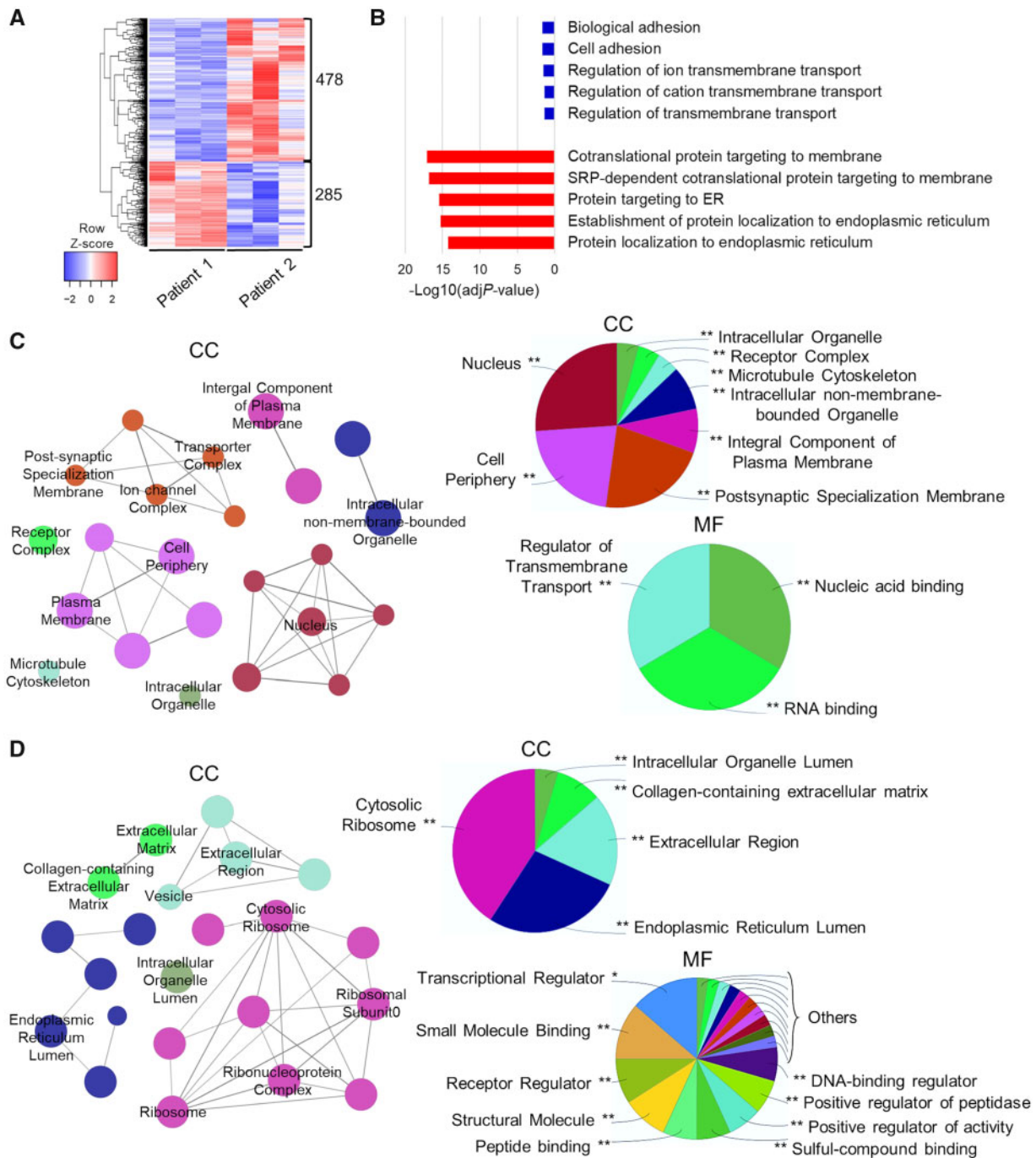


Figure 4 Bulk RNA-Seq analysis reveals differences in gene expression profiles between Patient 1 and 2-derived neurons. (A) Heat map showing hierarchical clustering of protein-coding DEGs in Patient 2, compared to Patient 1 ($n = 3$). (B) GO terms enrichment for biological process of underexpressed (blue) protein-coding and overexpressed (red) protein-coding DEGs. The top five categories are shown. (C and D) ClueGO analysis of GO terms enrichment of (C) under- and (D) over-expressed protein-coding DEGs, showing network graph and pie chart for cellular component (CC), and pie chart for molecular function (MF). Network graph nodes represent GO terms (the most significant are named) and edges indicate shared genes between GO terms. Functional groups of GO terms are indicated by the same colour. Pie charts show the percentages of each functional group representation, named with the most significant term. GO functional groups exhibiting higher statistically significant differences using Benjamini-Hochberg P-value correction ($FDR < 0.05$) are shown.

controls.^{34–37} Recordings with increasing current amplitude (Fig. 5A) showed that the current threshold to elicit an action potential for Patient 2 was significantly lower than for the control (Fig. 5B and C) and failed to follow current injection up to 100 pA (Fig. 5D).

On investigation of passive neuronal properties, both patients displayed lower capacitance compared to control neurons without affecting input resistance (Fig. 5C), in accordance with a decreased average number of primary neurite branches (Fig. 5E). For both

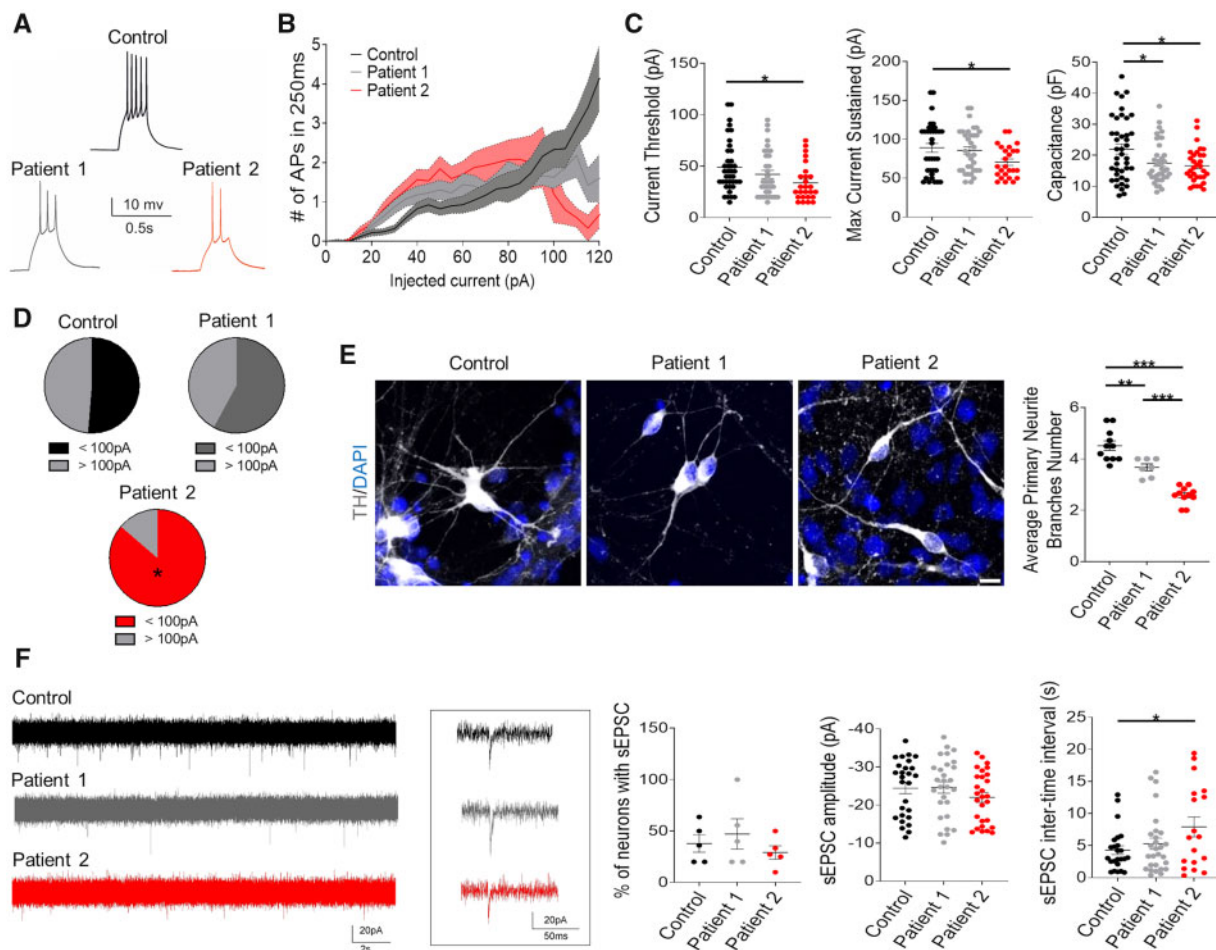


Figure 5 Patient-derived neurons show altered neuronal electrophysiological properties and defects in primary neurite branching. (A) Representative traces of action potentials (APs) elicited by injecting a 40 pA current in patients and control lines. (B) Input/output plot showing number of action potentials triggered by incremental current steps. (C) Active (current threshold and max current sustained) and passive (capacitance) properties of neurons in control, Patient 1 and Patient 2 neurons ($n = 39, 34, 26, n = 35, 34, 25,$ and $n = 41, 38, 32,$ respectively, from four biological replicates). (D) Percentage of neurons that sustain >100 pA current injection. (E) Representative images for dopaminergic neurons branching (scale bar = $10\ \mu\text{m}$) and quantification of average primary neurite branching in control, Patient 1 and Patient 2 mDA neurons ($n = 11, 7, 11,$ respectively). (F) Representative traces showing spontaneous excitatory postsynaptic currents (sEPSCs) at -70 mV and quantification of neurons with sEPSC, sEPSC amplitude and inter-time intervals in control, Patient 1 and Patient 2 neurons ($n = 5$ for all, $n = 27, 28, 28,$ and $n = 24, 28, 18,$ respectively, from four biological replicates). Data are presented as mean \pm SEM. * $P < 0.05$; ** $P < 0.01$; *** $P < 0.001$, one-way ANOVA followed by Tukey's multiple comparisons test and chi-square test in D.

control and patient-derived neurons showing spontaneous excitatory postsynaptic currents, we observed no differences in either the percentage of functionally connected neurons or current amplitude, although the interevent interval was significantly higher in Patient 2-derived neurons (Fig. 5F).

DDC lentiviral gene transfer significantly improves neurodevelopmental defects in patient-derived neurons

Given that gene therapy is an emerging new treatment for AADC deficiency,^{16–18} we sought to investigate the cellular effects of human DDC transgene delivery in our model; in particular we wished to evaluate whether this therapeutic approach could improve the neurodevelopment sequelae of AADC deficiency, independent of genetic background. We generated a lentiviral construct for the delivery of human DDC under the control of the neuronal-specific promoter human synapsin (hSYN1) (Supplementary Fig. 8). Patient-derived mDA precursors were transduced at Day 24 of differentiation and analysed at Day 65. For

both patient lines, lentiviral gene transfer resulted in an increase in AADC protein levels (Supplementary Fig. 9A and B), and rescued enzymatic activity to levels comparable to those observed in control neurons (Supplementary Fig. 9C). Furthermore, Patient 2 transduced neurons showed a significant increase in the NeuN-positive neuronal population, and in particular mDA neurons, to levels comparable to Patient 1 (Fig. 6A, B and Supplementary Fig. 10A). Human DDC lentiviral delivery also resulted in a significant increase in synaptophysin protein levels in both patients-derived neuronal cultures (Fig. 6C) and more specifically in the mDA neuronal subpopulation (Fig. 6D and Supplementary Fig. 10B), with a significant increase in primary branching (Fig. 6E).

In silico and recombinant biochemical analyses predict a mutation-specific L-DOPA response in Patient 2

The different mutations harboured by Patients 1 and 2 were further investigated to determine whether they had differential effects on enzymatic function. For Patient 1, despite

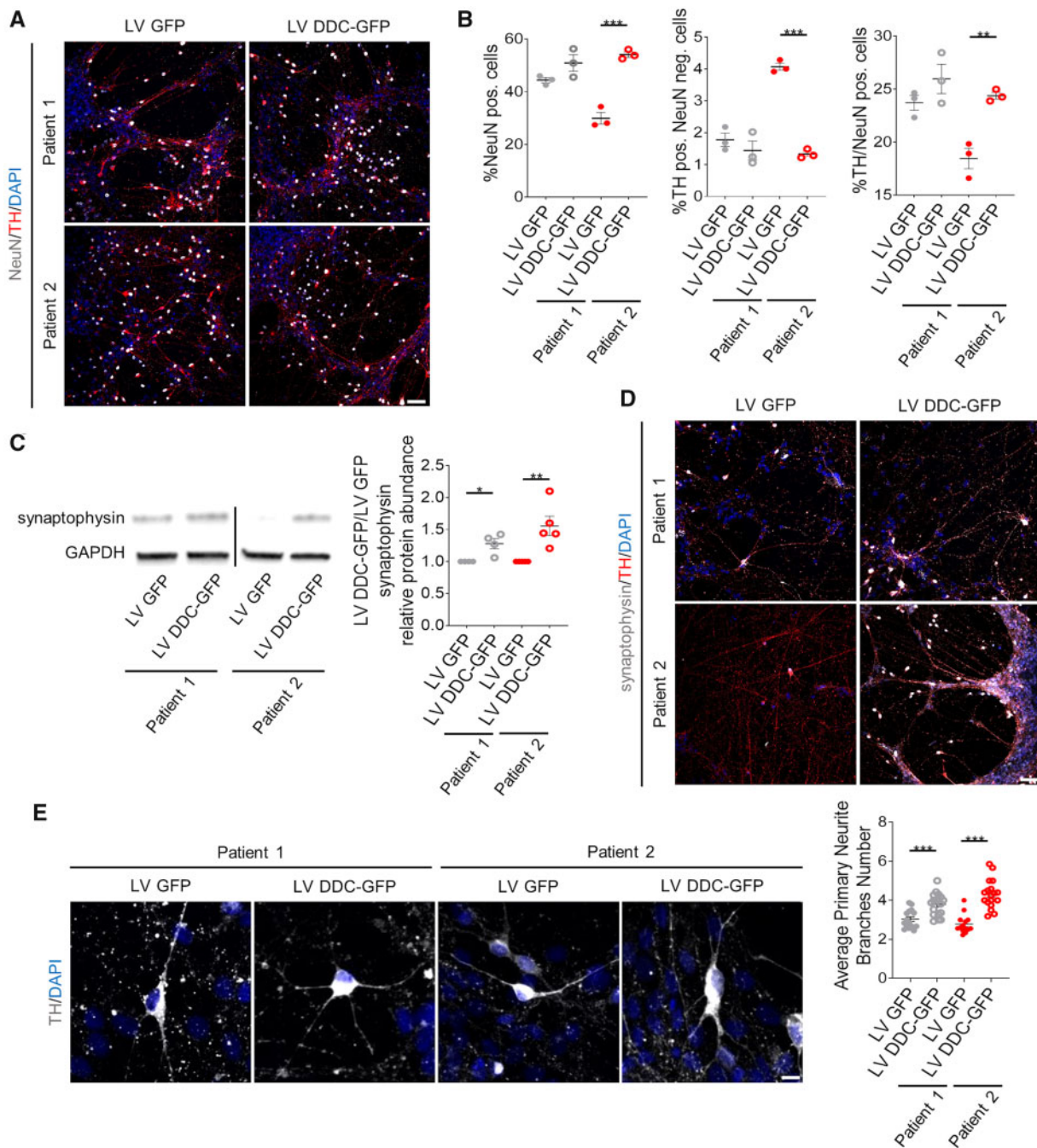


Figure 6 Gene therapy significantly improves maturation defects in patient-derived neurons. (A) Representative immunofluorescence for NeuN and TH of patient-derived neurons transduced with a lentiviral construct expressing only GFP (LV GFP) or human DDC and GFP (LV DDC-GFP). Scale bar = 100 μ m. (B) Quantification of NeuN-positive, TH-positive and NeuN-negative, and TH/NeuN double-positive cells in patient-derived neuronal cultures transduced with LV GFP and LV DDC-GFP ($n = 3$ each). (C) Representative immunoblot for synaptophysin and loading control (GAPDH), and quantification of relative synaptophysin abundance from total cell lysates extracted from LV GFP and LV DDC-GFP transduced neurons. Results are normalized to the corresponding LV GFP for each patient ($n = 4, 4, 5, 5$, respectively). (D) Representative immunofluorescence for synaptophysin and TH in patient-derived neurons transduced with LV GFP or LV DDC-GFP. Scale bar = 100 μ m. (E) Representative images for dopaminergic neurons branching (scale bar = 10 μ m) and quantification of average primary neurite branches in patient-derived neurons transduced with LV GFP or LV DDC-GFP ($n = 15, 18, 13, 18$, respectively). Data are presented as mean \pm SEM. * $P < 0.05$; ** $P < 0.01$; *** $P < 0.001$, two-tailed Student's *t*-test.

supraphysiological levels of protein expression (Fig. 1C), the homozygous missense substitution R347G significantly impairs catalytic function of AADC leading to undetectable enzyme activity (Fig. 1A) without impacting the protein structure by a molecular mechanism extensively investigated in Montioli et al.¹⁵ In contrast, despite significantly low levels of AADC protein in Patient 2-derived

neuronal cultures (Fig. 1C), residual enzymatic activity was still detected, albeit at a fraction of that evident in the control line (Fig. 1A). It is likely that this residual AADC enzyme activity can be attributed to the p.C100S variant, since the second heterozygous mutation leads to an early stop codon at Arg7, predicted to result in nonsense-mediated mRNA decay and absent protein

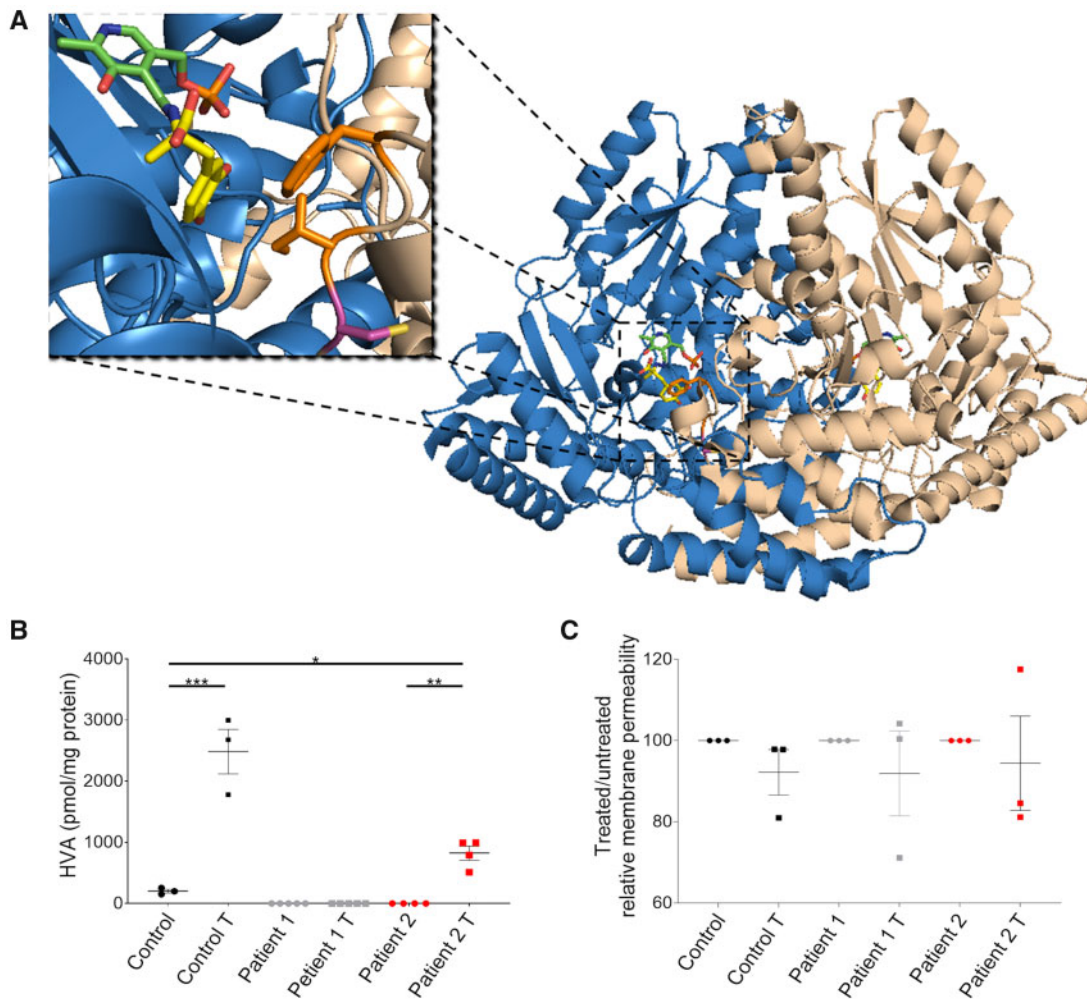


Figure 7 L-DOPA treatment increases dopamine metabolite production in Patient 2-derived neuronal cultures, with no evidence of cellular toxicity. (A) Localization of Cys100 in AADC protein structure. The structure corresponds to *Sus scrofa* holoenzyme (PDB code: 1J53), solved in complex with PLP and carbidopa, and rendered using PyMol™ software. AADC is shown as a schematic, with the two monomers composing the native rearrangement of the enzyme (wheat and marine blue, respectively). PLP and carbidopa are represented as green and yellow sticks, respectively. The side chain of Cys100 is represented as a pink stick. Side chains of Ile101 and Phe103 are represented as orange sticks. (B) HPLC detection of extracellular HVA after 80 μ M L-DOPA treatment of neuronal cultures for 24 h. Values are relative to total protein ($n = 3, 3, 5, 4, 4$, respectively). (C) Dead-cell protease release assay after treatment. Results are normalized to the corresponding non-treated condition ($n = 3$ for all). Data are presented as mean \pm SEM. * $P < 0.05$; ** $P < 0.01$; *** $P < 0.001$, one-way ANOVA followed by Tukey's multiple comparisons test.

production. The missense mutation C100S results in an amino acid substitution at the beginning of an essential loop (loop 2, residues 100–110), which contains key hydrophobic active site residues involved in substrate binding, in particular Ile101 and Phe103.³⁸ The cysteine-to-serine amino acid substitution has the potential to alter the conformation of loop 2 and consequently the substrate-binding cleft, thereby affecting substrate affinity (Fig. 7A). AADCC100S was produced *in vitro* in recombinant form to characterize the effects of this mutation through spectroscopic, circular dichroism and fluorescence analyses, and calculation of kinetic parameters. A minor perturbation of PLP cofactor micro-environment (in particular for the enolimine tautomer) was observed (Supplementary Fig. 11A and B). However, PLP binding affinity (Supplementary Table 1) was not particularly affected, with a $K_{D(PLP)}$ consistently lower than previously reported values for AADC variants with cofactor binding impairment.¹³ Calculation of kinetic parameters (Supplementary Table 1) revealed that AADCC100S retains more residual enzyme activity than that reported for other AADC variants.^{12,13} The catalytic activity (k_{cat}) of

AADCC100S was indeed similar to that observed for wild-type, with the actual decrease in overall AADCC100S catalytic efficiency (k_{cat}/K_M) attributed to a slight decrease in L-DOPA affinity (K_M) (Supplementary Table 1). As such, we postulated that dopamine production by AADCC100S could be enhanced with L-DOPA administration, as demonstrated for other AADC variants.³⁹

Patient 2-derived midbrain dopaminergic neurons specifically respond to L-DOPA administration

To determine whether the C100S mutation resulted in L-DOPA responsivity, we sought to investigate the effect of L-DOPA treatment in Patient 2-derived mDA neurons. After 65 days of differentiation, both patients and control-derived neuronal cultures were incubated with 80 μ M L-DOPA for 24 h, a dose just below that considered to be toxic in neuronal and other cellular systems.^{40,41} Subsequent HPLC analysis of extracellular metabolites was then undertaken. As expected in a system with catalytically competent AADC, HVA levels were significantly higher in treated control

compared to untreated control neurons (Fig. 7B). Furthermore, as predicted, there was no detectable HVA in Patient 1-derived neuronal cultures both pre and post L-DOPA treatment. However, for Patient 2, we observed a significant increase of HVA levels in L-DOPA treated cultures when compared to untreated cultures (Fig. 7B). To evaluate any potential toxicity related to L-DOPA administration⁴⁰ or dopamine production,⁴² we measured dead-cell protease release and found no increase in membrane permeability for both patients and control-derived neuronal cultures treated with 80 µM L-DOPA for 24 h (Fig. 7C). Moreover, analysis of JNK protein phosphorylation, which increases in response to toxic levels of dopamine,⁴³ showed a significant increase in the phosphorylated form of this kinase in treated control neurons only, while no significant increase was detected in both treated Patient 1 and 2 cultures (Supplementary Fig. 11C).

Discussion

AADC deficiency is a complex and often pharmaco-resistant neurological disorder, with a broad phenotypic spectrum, variable drug response, substantial burden of disease and significant risk of premature mortality.⁷ Improved understanding of the underlying pathogenic mechanisms and the development of better targeted treatments, such as gene therapy and other personalized medicine approaches, will be key in modifying disease and long-term outcome. In this study, we have developed a new humanized model of AADC deficiency. Our *in vitro* patient-derived mDA neuronal model of AADC deficiency has provided further insight into mechanisms governing disease, as well as an ideal system to evaluate the impact of approaches such as gene therapy at cellular level and a unique research platform to evaluate mutation-specific precision medicine approaches.

Importantly, our patient-derived mDA model recapitulates key features of the human phenotype with near-absent AADC enzyme activity and impaired dopamine metabolism. In our dopaminergic model, we observed a greater degree of residual AADC enzyme activity in Patient 2, which may relate to the more advanced motor gains observed in this patient. We also observed patient-specific altered levels of AADC protein. The reasons for this are not entirely clear, given that little is known about factors that govern AADC enzyme regulation. Our biochemical investigations did not show a differential intrinsic protein stability between mutant and wild-type protein. We did, however, observe a clear patient-specific increase in DDC gene expression for Patient 1 and higher than expected levels of DDC expression for Patient 2, given the predicted nonsense-mediated decay of a proportion of Patient 2 transcripts. Furthermore for both patients there was an increase in TH gene and protein expression; interestingly, TH gene and protein expression has previously been shown to increase in Parkinson's disease, as a likely compensatory response to a state of dopamine deficiency in the context of striatonigral degeneration.^{44,45} As such, it is plausible that the similar state of dopamine deficiency in AADC-deficient patient lines drives a positive feedback mechanism to modulate neuronal levels of key enzymes driving dopamine synthesis.

Moreover, our study suggests that AADC dysfunction may have widespread effects on gene expression that may impact neuronal development and functional maturation. As well as its pivotal role in monoamine neurotransmission, dopamine is postulated to have important functions in modulating neuronal structure and connectivity.⁴⁶ The early production of dopamine in midbrain development suggests that it may have neurodevelopmental influence,⁴⁷ a notion that is further corroborated by DDC knock-in mice and knockout zebrafish which show abnormal development.^{48,49} Interestingly, our patient-derived cell model also shows that defective AADC enzymatic activity and dysregulated dopamine

metabolism affects neuronal maturity, with altered expression of genes involved in neurodevelopment and synaptic formation, as well as disruption of electrophysiological properties and functional activity. Considering that iPSC-derived neurons resemble foetal neurons,⁵⁰ it is possible that the neuronal maturation defects observed in our *in vitro* model correlate with prenatal disease onset in humans. This is not surprising, given that many affected patients present with their first clinically discernible symptoms in early infancy. Our results are particularly relevant in the current climate of emerging gene therapy approaches,¹⁸ where neuronal plasticity is considered to be an important requisite for clinical benefit.⁵¹ It is likely that gene therapy within this 'therapeutic window' of brain plasticity may predict a more favourable long-term neurodevelopmental outcome.

In our system, we identified around the same number of differentially expressed genes between patients (when combined) and control and between the two patients; the latter observation likely reflects both the biological and clinical differences between patients affected by a disease with a broad phenotypic continuum. Patient 2-derived cultures showed indeed a greater degree of neuronal immaturity. Notably, Patient 2 had a number of behavioural issues, significant autistic traits and prominent neuropsychiatric symptoms, features that were less evident in Patient 1. Our data may indicate that the greater degree of neuronal immaturity evident in Patient 2 lines as seen on maturation marker analysis, transcriptome profiling and electrophysiology may contribute to the aforementioned neurodevelopmental symptoms. Importantly, lentiviral treatment of patient-derived neurons restored AADC protein levels and enzymatic activity with significant improvement in neuronal maturity. Whether AADC protein has additional functions in governing neurodevelopment processes, that are independent of its catalytic activity in dopamine production, remains yet to be determined. Further studies with a greater number of patient lines and age-matched/isogenic controls, or analysis of multiple clones from each line, will help confirm and further delineate the complex neurodevelopmental biological phenotypes identified in this study. Additional genetic, epigenetic and environmental factors may also play a role in such phenotypic variability seen in the cell model and human phenotype; over time, advances in next generation sequencing technologies may also help further elucidate some of the underlying contributory genetic factors.

Our patient-derived model of AADC deficiency has proven to be a useful tool for evaluating therapeutic approaches. We have shown recovery of AADC enzyme activity and specific neuronal maturation defects using a gene therapy approach in patient-derived neurons. In tandem with other models, such therapeutic testing in iPSC-based systems may in the future guide and influence clinical trial design. Our model has also demonstrated the potential utility of L-DOPA treatment for some patients with AADC deficiency. Although L-DOPA is not traditionally used in the majority of patients,⁸ it has been previously empirically used in patients suspected to have L-DOPA responsive AADC deficiency.³⁹ Our study confirms that it may indeed have a role for patients with specific DDC mutations associated with residual enzymatic activity due to altered substrate affinity. A planned therapeutic trial will further inform whether the positive effects of L-DOPA observed *in vitro* are recapitulated *in vivo*. More generally, our study shows that better definition of the physicochemical properties of specific mutations with subsequent validation in patient-relevant models has great potential in guiding personalized pharmacological strategies for rare disorders.

In conclusion, as new therapeutic avenues emerge for patients with AADC deficiency, our study shows the clear utility of an iPSC-based modelling system to elucidate disease mechanisms and evaluate therapeutic strategies.

Acknowledgements

We sincerely thank the AADC Research Trust for inspiring us to undertake this study, and our patients and their families for participating in this study. We also thank the MRC Centre for Neuromuscular Disorders Biobank for providing age-matched control fibroblasts.

Funding

G.R., K.K., M.B. and M.A.K. received funding from the AADC Research Trust. E.L. and G.L. have been supported by European Union's Horizon 2020 research and innovation program under Marie Skłodowska-Curie grant agreement 642881 and an Epilepsy Research UK Fellowship (G.L.: ERUK F1701). H.A. received funding from Kuwait University. J.N. received funding from MRC MR/K02342X/1 and MR/R015325/1. J.C. has been supported by Wellcome Innovator Award (210774/2/18/Z). M.B. was supported by University of Verona Grant FUR2019. S.B. and M.A.K. have received funding support from the Wellcome Trust (M.A.K.: Wellcome Intermediate Clinical Fellowship WT098524MA) and from the Rosetrees Trust (M810). M.A.K. is funded by an NIHR Research Professorship (NIHR-RP-2016-07-019) and the Sir Jules Thorn Award for Biomedical Research (17JTA).

This research was supported by the NIHR Great Ormond Street Hospital Biomedical Research Centre. The views expressed are those of the author(s) and not necessarily those of the NHS, the NIHR or the Department of Health.

Competing interests

The authors report no competing interests.

Supplementary material

[Supplementary material](#) is available at *Brain* online.

References

- Saudubray JM, Garcia-Cazorla A. An overview of inborn errors of metabolism affecting the brain: From neurodevelopment to neurodegenerative disorders. *Dialogues Clin Neurosci*. 2018;20(4):301–325.
- Ng J, Papandreou A, Heales SJ, Kurian MA. Monoamine neurotransmitter disorders—Clinical advances and future perspectives. *Nat Rev Neurol*. 2015;11(10):567–584.
- Hyland K, Clayton PT. Aromatic amino acid decarboxylase deficiency in twins. *J Inherit Metab Dis*. 1990;13(3):301–304.
- Dai W, Lu D, Gu X, Yu Y.; the Mainland Chinese League of AADC Rare Disease. Aromatic L-amino acid decarboxylase deficiency in 17 Mainland China patients: Clinical phenotype, molecular spectrum, and therapy overview. *Mol Genet Genomic Med*. 2020;8(3):e1143.
- Helman G, Pappa MB, Pearl PL. Widening phenotypic spectrum of AADC deficiency, a disorder of dopamine and serotonin synthesis. *JIMD Rep*. 2014;17:23–27.
- Kurian MA, Gissen P, Smith M, Heales SJR, Clayton PT. The monoamine neurotransmitter disorders: An expanding range of neurological syndromes. *Lancet Neurol*. 2011;10(8):721–733.
- Pearson TS, Gilbert L, Opladen T, et al. AADC deficiency from infancy to adulthood: Symptoms and developmental outcome in an international cohort of 63 patients. *J Inherit Metab Dis*. 2020;43(5):1121–1130.
- Wassenberg T, Molero-Luis M, Jeltsch K, et al. Consensus guideline for the diagnosis and treatment of aromatic L-amino acid decarboxylase (AADC) deficiency. *Orphanet J Rare Dis*. 2017;12(1):12.
- Cellini B, Montioli R, Oppici E, Voltattorni CB. Biochemical and computational approaches to improve the clinical treatment of Dopa decarboxylase-related diseases: An overview. *Open Biochem J*. 2012;6(1):131–138.
- Himmelreich N, Montioli R, Bertoldi M, et al. Aromatic amino acid decarboxylase deficiency: Molecular and metabolic basis and therapeutic outlook. *Mol Genet Metab*. 2019;127(1):12–22.
- Montioli R, Battini R, Paiardini A, et al. A novel compound heterozygous genotype associated with aromatic amino acid decarboxylase deficiency: Clinical aspects and biochemical studies. *Mol Genet Metab*. 2019;127(2):132–137.
- Montioli R, Bisello G, Dindo M, Rossignoli G, Voltattorni CB, Bertoldi M. New variants of AADC deficiency expand the knowledge of enzymatic phenotypes. *Arch Biochem Biophys*. 2020;682:108263.
- Montioli R, Dindo M, Giorgetti A, Piccoli S, Cellini B, Voltattorni C. O. A comprehensive picture of the mutations associated with aromatic amino acid decarboxylase deficiency: from molecular mechanisms to therapy implications. *Hum Mol Genet*. 2014;23(20):5429–5440.
- Montioli R, Janson G, Paiardini A, Bertoldi M, Borri Voltattorni C. Heterozygosis in aromatic amino acid decarboxylase deficiency: Evidence for a positive interallelic complementation between R347Q and R358H mutations. *IUBMB Life*. 2018;70(3):215–223.
- Montioli R, Paiardini A, Kurian MA, et al. The novel R347g pathogenic mutation of aromatic amino acid decarboxylase provides additional molecular insights into enzyme catalysis and deficiency. *Biochim Biophys Acta Proteins Proteomics*. 2016;1864(6):676–682.
- Chien YH, Lee NC, Tseng SH, et al. Efficacy and safety of AAV2 gene therapy in children with aromatic L-amino acid decarboxylase deficiency: An open-label, phase 1/2 trial. *Lancet Child Adolesc Heal*. 2017;1(4):265–273.
- Hwu WL, Muramatsu SI, Tseng SH, et al. Gene therapy for aromatic L-amino acid decarboxylase deficiency. *Sci Transl Med*. 2012;4(134):134ra61.
- Kojima K, Nakajima T, Taga N, et al. Gene therapy improves motor and mental function of aromatic L-amino acid decarboxylase deficiency. *Brain*. 2019;142(2):322–333.
- Hyland K, Reott M. Prevalence of aromatic L-amino acid decarboxylase deficiency in at-risk populations. *Pediatr Neurol*. 2020;106:38–42.
- Lee KM, Hawi ZH, Parkington HC, et al. The application of human pluripotent stem cells to model the neuronal and glial components of neurodevelopmental disorders. *Mol Psychiatry*. 2020;25(2):368–378.
- Schuster J, Halvardson J, Pilar Lorenzo L, et al. Transcriptome profiling reveals degree of variability in induced pluripotent stem cell lines: Impact for human disease modeling. *Cell Reprogram*. 2015;17(5):327–337.
- Matsa E, BurrIDGE PW, Yu KH, et al. Transcriptome profiling of patient-specific human iPSC-cardiomyocytes predicts individual drug safety and efficacy responses in vitro. *Cell Stem Cell*. 2016;19(3):311–325.
- Lehnen D, Barral S, Cardoso T, et al. IAP-based cell sorting results in homogeneous transplantable dopaminergic precursor cells derived from human pluripotent stem cells. *Stem Cell Rep*. 2017;9(4):1207–1220.
- Allen GFG. *The neurochemical consequences of aromatic L-amino acid decarboxylase deficiency*. PhD thesis. UCL Institute of Neurology, London, UK; 2011.

25. Hyland K, Clayton PT. Aromatic L-amino acid decarboxylase deficiency: Diagnostic methodology. *Clin Chem.* 1992;38(12):2405–2410.
26. de la Fuente C, Burke DG, Eaton S, Heales SJR. Inhibition of neuronal mitochondrial complex I or lysosomal glucocerebrosidase is associated with increased dopamine and serotonin turnover. *Neurochem Int.* 2017;109:94–100.
27. Afgan E, Baker D, Batut B, et al. The Galaxy platform for accessible, reproducible and collaborative biomedical analyses: 2018 update. *Nucleic Acids Res.* 2018;46(W1):W537–W544.
28. Bolger AM, Lohse M, Usadel B. Trimmomatic: A flexible trimmer for Illumina sequence data. *Bioinformatics.* 2014;30(15):2114–2120.
29. Kim D, Langmead B, Salzberg SL. HISAT: A fast spliced aligner with low memory requirements. *Nat Methods.* 2015;12(4):357–360.
30. Liao Y, Smyth GK, Shi W. FeatureCounts: An efficient general purpose program for assigning sequence reads to genomic features. *Bioinformatics.* 2014;30(7):923–930.
31. Liu R, Holik AZ, Su S, et al. Why weight? Modelling sample and observational level variability improves power in RNA-seq analyses. *Nucleic Acids Res.* 2015;43(15):e97.
32. Ge SX, Jung D, Jung D, Yao R. ShinyGO: A graphical gene-set enrichment tool for animals and plants. *Bioinformatics.* 2020;36(8):2628–2629.
33. Bindea G, Mlecnik B, Hackl H, et al. ClueGO: A Cytoscape plug-in to decipher functionally grouped gene ontology and pathway annotation networks. *Bioinformatics.* 2009;25(8):1091–1093.
34. Hartfield EM, Yamasaki-Mann M, Ribeiro Fernandes HJ, et al. Physiological characterisation of human iPSC-derived dopaminergic neurons. *PLoS One.* 2014;9(2):e87388.
35. Wakeman DR, Hiller BM, Marmion DJ, et al. Cryopreservation maintains functionality of human iPSC dopamine neurons and rescues parkinsonian phenotypes in vivo. *Stem Cell Rep.* 2017;9(1):149–161.
36. Xi J, Liu Y, Liu H, Chen H, Emborg ME, Zhang SC. Specification of midbrain dopamine neurons from primate pluripotent stem cells. *Stem Cells.* 2012;30(8):1655–1663.
37. Doi D, Magotani H, Kikuchi T, et al. Pre-clinical study of induced pluripotent stem cell-derived dopaminergic progenitor cells for Parkinson's disease. *Nat Commun.* 2020;11(1):3369.
38. Burkhard P, Dominici P, Borri-Voltattorni C, Jansonius JN, Malashkevich VN. Structural insight into Parkinson's disease treatment from drug-inhibited DOPA decarboxylase. *Nat Struct Biol.* 2001;8(11):963–967.
39. Chang YT, Sharma R, Marsh JL, et al. Levodopa-responsive aromatic L-amino acid decarboxylase deficiency. *Ann Neurol.* 2004;55(3):435–438.
40. Sabens Liedhegner EA, Steller KM, Mיעאל JJ. Levodopa activates apoptosis signaling kinase 1 (ASK1) and promotes apoptosis in a neuronal model: Implications for the treatment of Parkinson's disease. *Chem Res Toxicol.* 2011;24(10):1644–1652.
41. Park KH, Shin KS, Zhao TT, Park HJ, Lee KE, Lee MK. L-DOPA modulates cell viability through the ERK-c-Jun system in PC12 and dopaminergic neuronal cells. *Neuropharmacology.* 2016;101:87–97.
42. Blum D, Torch S, Lambeng N, et al. Molecular pathways involved in the neurotoxicity of 6-OHDA, dopamine and MPTP: Contribution to the apoptotic theory in Parkinson's disease. *Prog Neurobiol.* 2001;65(2):135–172.
43. Jiang H, Ren Y, Zhao J, Feng J. Parkin protects human dopaminergic neuroblastoma cells against dopamine-induced apoptosis. *Hum Mol Genet.* 2004;13(16):1745–1754.
44. Zigmond MJ. Do compensatory processes underlie the preclinical phase of neurodegenerative disease? Insights from an animal model of Parkinsonism. *Neurobiol Dis.* 1997;4(3-4):247–253.
45. Tong ZY, Kingsbury AE, Foster OJF. Up-regulation of tyrosine hydroxylase mRNA in a sub-population of A10 dopamine neurons in Parkinson's disease. *Mol Brain Res.* 2000;79(1-2):45–54.
46. Money KM, Stanwood GD. Developmental origins of brain disorders: Roles for dopamine. *Front Cell Neurosci.* 2013;7: 260.
47. Arenas E, Denham M, Villaescusa JC. How to make a midbrain dopaminergic neuron. *Dev.* 2015;142(11):1918–1936.
48. Lee NC, Shieh YD, Chien YH, et al. Regulation of the dopaminergic system in a murine model of aromatic l-amino acid decarboxylase deficiency. *Neurobiol Dis.* 2013;52:177–190.
49. Shih DF, Hsiao C, Der Min MY, et al. Aromatic L-amino acid decarboxylase (AADC) is crucial for brain development and motor functions. *PLoS One.* 2013;8(8):e71741.
50. La Manno G, Gyllborg D, Codeluppi S, et al. Molecular diversity of midbrain development in mouse, human, and stem cells. *Cell.* 2016;167(2):566–580.e19.
51. Tseng CH, Chien YH, Lee NC, et al. Gene therapy improves brain white matter in aromatic l-amino acid decarboxylase deficiency. *Ann Neurol.* 2019;85(5):644–652.

Gene therapy restores dopamine transporter expression and ameliorates pathology in iPSC and mouse models of infantile parkinsonism

Joanne NgSerena BarralCarmen De La Fuente BarrigonGabriele LignaniFatma A. ErdemRebecca WallingsRiccardo PrivolizziGiada RossignoliHaya AlrashidiSonja HeasmanEsther MeyerAdeline NgohSimon PopeRajvinder KardaDany PerocheauJulien BaruteauNatalie SuffJuan Antinao DiazStephanie SchorgeJane VowlesLucy R. MarshallSally A. CowleySonja SucicMichael FreissmuthJohn R. CounsellRichard Wade-MartinsSimon J. R. HealesAhad A. RahimMaximilien BenczeSimon N. WaddingtonManju A. Kurian

Sci. Transl. Med., 13 (594), eaaw1564. • DOI: 10.1126/scitranslmed.aaw1564

Delivering a transporter

Dopamine transporter deficiency syndrome (DTDS) is a rare neurodegenerative disease caused by biallelic loss-of-function mutations in SLC6A3, the gene encoding the dopamine transporter (DAT). There is no effective treatment for this disease and the pathophysiology is still unclear; patients develop infantile parkinsonism that often leads to premature death. Here, Ng *et al.* developed a gene therapy for DTDS using patient-derived induced pluripotent stem cell (iPSC) and a mouse model. Delivery of human SLC6A3 improved DAT activity and reduced neurodegeneration in vitro in iPSC-derived neurons. In vivo, injection of SLC6A3 in the midbrain of adult DTDS mice using an adeno-associated virus vector had therapeutic effects, suggesting that the approach might be effective in patients.

View the article online

<https://www.science.org/doi/10.1126/scitranslmed.aaw1564>

Permissions

<https://www.science.org/help/reprints-and-permissions>

Use of this article is subject to the [Terms of service](#)

ARTICLE OPEN



Protein aggregation and calcium dysregulation are hallmarks of familial Parkinson's disease in midbrain dopaminergic neurons

Gurvir S. Virdi^{1,2,3}, Minee L. Choi^{1,2,3}, James R. Evans^{1,2,3}, Zhi Yao^{1,2}, Dilan Athauda^{1,2}, Stephanie Strohbuecker¹, Raja S. Nirujogi^{3,4}, Anna I. Wernick^{1,2,3}, Noelia Pelegrina-Hidalgo^{5,6}, Craig Leighton^{5,6}, Rebecca S. Saleeb⁵, Olga Kopach⁷, Haya Alrashidi⁸, Daniela Melandri⁹, Jimena Perez-Lloret¹, Plamena R. Angelova², Sergiy Sylantsev¹⁰, Simon Eaton¹¹, Simon Heales⁸, Dmitri A. Rusakov⁷, Dario R. Alessi^{3,4}, Tilo Kunath⁶, Mathew H. Horrocks⁵, Andrey Y. Abramov², Rickie Patani^{1,11} and Sonia Gandhi^{1,2,3}

Mutations in the *SNCA* gene cause autosomal dominant Parkinson's disease (PD), with loss of dopaminergic neurons in the substantia nigra, and aggregation of α -synuclein. The sequence of molecular events that proceed from an *SNCA* mutation during development, to end-stage pathology is unknown. Utilising human-induced pluripotent stem cells (hiPSCs), we resolved the temporal sequence of *SNCA*-induced pathophysiological events in order to discover early, and likely causative, events. Our small molecule-based protocol generates highly enriched midbrain dopaminergic (mDA) neurons: molecular identity was confirmed using single-cell RNA sequencing and proteomics, and functional identity was established through dopamine synthesis, and measures of electrophysiological activity. At the earliest stage of differentiation, prior to maturation to mDA neurons, we demonstrate the formation of small β -sheet-rich oligomeric aggregates, in *SNCA*-mutant cultures. Aggregation persists and progresses, ultimately resulting in the accumulation of phosphorylated α -synuclein aggregates. Impaired intracellular calcium signalling, increased basal calcium, and impairments in mitochondrial calcium handling occurred early at day 34–41 post differentiation. Once midbrain identity fully developed, at day 48–62 post differentiation, *SNCA*-mutant neurons exhibited mitochondrial dysfunction, oxidative stress, lysosomal swelling and increased autophagy. Ultimately these multiple cellular stresses lead to abnormal excitability, altered neuronal activity, and cell death. Our differentiation paradigm generates an efficient model for studying disease mechanisms in PD and highlights that protein misfolding to generate intraneuronal oligomers is one of the earliest critical events driving disease in human neurons, rather than a late-stage hallmark of the disease.

npj Parkinson's Disease (2022)8:162; <https://doi.org/10.1038/s41531-022-00423-7>

INTRODUCTION

Parkinson's disease (PD) is a progressive neurodegenerative disease primarily characterised by the loss of dopaminergic neurons in the substantia nigra of the midbrain¹. Studying the mechanisms that contribute to disease is of immense importance, but has been somewhat limited by a paucity of relevant human models. The development of human-induced pluripotent stem cells (hiPSCs) from patients with familial forms of PD has vastly improved our capability to model and study PD. Taking this advance further, directed differentiation strategies to generate the relevant cell type from the relevant brain region, should allow us to discover mechanisms of disease and define the basis for selective cellular vulnerability. For PD, amongst the earliest and most vulnerable cell populations is the midbrain dopaminergic neuron, and therefore modelling disease with precision requires the ability to robustly generate this neuronal type.

Several protocols have transformed our ability to generate midbrain dopaminergic (mDA) neurons^{2–5}: these mimic *in vivo* developmental programmes, directing neural induction via dual-SMAD inhibition⁶, and subsequent patterning via activation of sonic hedgehog (Shh), Wnt, and fibroblast growth factor 8 (FGF8) signalling through the use of small-molecules and/or recombinant morphogens. The resulting cells acquire midbrain-specific molecular attributes, based on the expression of key genes and proteins, as well as functional and physiological characteristics resembling *in vivo* mDA neurons⁷. The efficiency of mDA neuron production varies between current differentiation protocols⁸, and cellular heterogeneity can be challenging when modelling disease. Against this background, we adapted well-established protocols to obtain highly enriched mDA neurons, and we tested their capacity to reliably model key aspects of PD pathogenesis and specifically to identify early phenotypes.

The pathological hallmark of PD is the presence of insoluble aggregated forms of the protein α -synuclein, encoded by the

¹The Francis Crick Institute, 1 Midland Road, London NW1 1AT, UK. ²Department of Clinical and Movement Neurosciences, UCL Queen Square Institute of Neurology, Queen Square, London WC1N 3BG, UK. ³Aligning Science Across Parkinson's (ASAP) Collaborative Research Network, Chevy Chase, MD 20815, USA. ⁴Medical Research Council (MRC) Protein Phosphorylation and Ubiquitylation Unit, School of Life Sciences, University of Dundee, Dow Street, Dundee DD1 5EH, UK. ⁵EaStCHEM School of Chemistry, University of Edinburgh, Edinburgh EH9 3FJ, UK. ⁶Center for Regenerative Medicine, University of Edinburgh, Edinburgh EH16 4UU, UK. ⁷Department of Clinical and Experimental Epilepsy, UCL Queen Square Institute of Neurology, London WC1N 3BG, UK. ⁸UCL Great Ormond Street Institute of Child Health, London WC1N 1EH, UK. ⁹Department of Neurodegenerative Diseases, UCL Queen Square Institute of Neurology, Queen Square, London WC1N 3BG, UK. ¹⁰Rowett Institute, University of Aberdeen, Ashgrove Rd West, Aberdeen AB25 2ZD, UK. ¹¹Department of Neuromuscular Disease, UCL Queen Square Institute of Neurology, Queen Square, London WC1N 3BG, UK. ✉email: rickie.patani@crick.ac.uk; sonia.gandhi@crick.ac.uk

SNCA gene⁹. Modelling synucleinopathy in vitro may therefore be achieved by utilising hiPSC lines with *SNCA* mutations. A range of mutations and multiplications have been discovered in *SNCA*, including the p.A53T point mutation and the triplication of the *SNCA* locus. Both of these genetic changes cause the early onset and rapidly progressive form of PD^{10–12}. HiPSC-derived models harbouring *SNCA* mutations have highlighted a range of cellular phenotypes that may lead to cell vulnerability, including mitochondrial dysfunction^{13–15}, ER stress¹⁶, lysosomal dysfunction¹⁷, oxidative stress, and calcium dysregulation^{18,19}. Nonetheless, disease models are dominated by multiple forms of cellular stress, and it has not been possible to determine the emergence of cellular dysfunction, and resolve the events spatially and temporally.

In this study, we established a modified approach to obtain highly enriched mDA neurons and we demonstrate their capacity to faithfully model key aspects of PD pathogenesis with temporal resolution. Our study reveals that protein misfolding to generate intraneuronal oligomers, and impaired calcium signalling, are early events in patient-derived PD neurons, and precede the appearance of mitochondrial, oxidative and lysosomal pathology.

RESULTS

Highly enriched midbrain dopaminergic neurogenesis from hiPSCs

To generate mDA neurons from hiPSCs, neural conversion was achieved using dual-SMAD inhibition⁶ followed by midbrain patterning using small molecule agonists of Shh and Wnt, purmorphamine and CHIR99021, respectively (Fig. 1a). After 14–20 days, we confirmed mDA neural precursor cell (NPC) identity using RT-PCR for *LMX1A*, *FOXA2*, and *EN1* ($P < 0.005$) (Fig. 1b) and immunocytochemistry (ICC) for *LMX1A*, *FOXA2* and *OTX2* (Fig. 1c). Crucially, high co-expression of all three markers, *LMX1A*, *FOXA2* and *OTX2*, confirmed an enriched culture of mDA NPCs (Ctrl 1: 83% ± 3.5, Ctrl 2: 81.4% ± 2.4, Ctrl 3: 88.7% ± 3.1, Ctrl 4: 88.4% ± 2.2) (Fig. 1d). After midbrain patterning, NPCs were maintained in culture for 4 days before terminal differentiation. Neuronal differentiation was induced using a Notch pathway inhibitor and a Rho-associated protein kinase (ROCK) inhibitor, encouraging cell cycle exit and cell survival, respectively. Maturation of terminally differentiated mDA neurons was confirmed by an increase of TH-positive cells (Fig. 1e and Supplementary Fig. 1a). Over 75% of TH-positive cells were obtained after 41 days of differentiation using ICC (Ctrl 1: 84.1% ± 2.8, Ctrl 2: 73.1% ± 4.5, Ctrl 3: 75.8% ± 5.8) (Fig. 1f, g), across three different hiPSC lines and four neuronal inductions (Supplementary Fig. 1b). Flow cytometry confirmed ~88% expression of both TH and β -III Tubulin (88.8% ± 1.9) (Fig. 1h, i and Supplementary Fig. 1c, d). Overall, the data confirm the high efficiency of neuronal differentiation, specifically into TH-positive neurons in 80–90% of the whole culture, with comparable efficiencies across three control hiPSC lines. qPCR for specific genes, including *NR4A2* (Nurr1), *KCNJ6* (GIRK2), and *SLC6A3* (DAT) at day 41–48-old mDA neurons showed an increase in the expression of these transcriptional markers of terminally differentiated mDA neurons relative to midbrain NPCs (Supplementary Fig. 1e). ICC quantification using a knockout validated GIRK2 antibody confirmed the expression of GIRK2 in mDA neurons which further supports the midbrain identity (Supplementary Fig. 1f, g), given that GIRK2 is highly expressed in dopaminergic neurons in the A9 region of the midbrain.

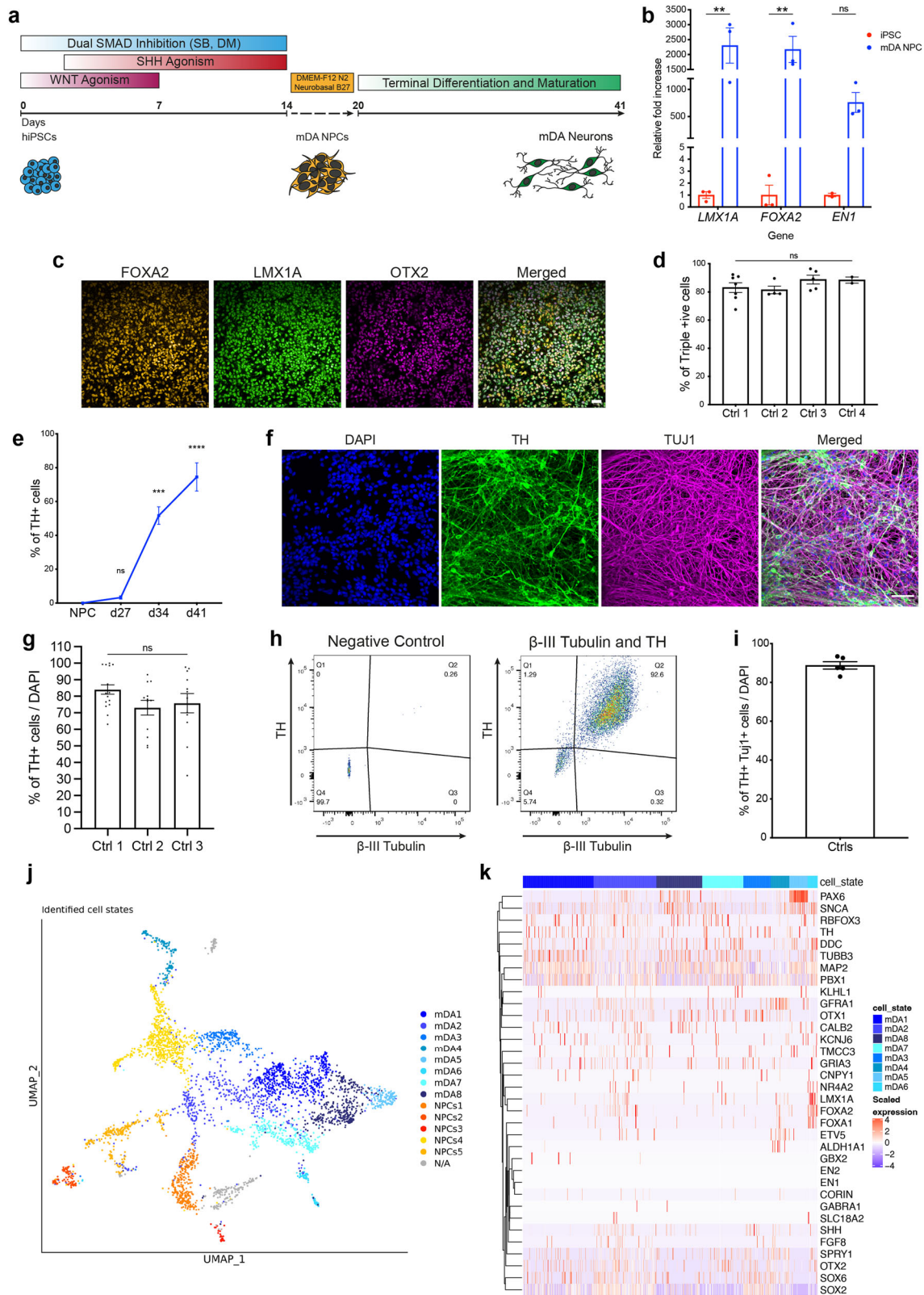
Single-cell RNA-seq was performed on day 48 mDA neurons. Cells were clustered into identities based on their transcriptional profiles, revealing 14 clusters, of which 8 expressed key mDA neuron genes, confirming their identity as mDA neurons (Fig. 1j). Key mDA genes expressed include GDNF receptor (*GFRA1*), *SOX6*,

PBX1, *TH*, *KCNJ6*, *NR4A2*, and *DDC*, suggesting that the majority of captured cells were of mDA identity, and were abundant within the culture (Fig. 1k) (Supplementary Fig. 2a). Several clusters were similar to mDA NPCs, or early neurons (5 clusters) (Fig. 1j). These clusters expressed key NPC genes e.g. *FOXA2*, *LMX1A*, *OTX2*, *FGF8*, and *SHH*, as well as mDA neuronal markers including *GFRA1*, *DDC*, *NR4A2*, *TH*, and *KCNJ6* (Supplementary Fig. 2b–d). In addition, most clusters expressed *SNCA*, highlighting the potential to use the protocol to model synucleinopathy (Supplementary Fig. 1h). Bulk proteomics was performed on terminally differentiated mDA neurons from three control lines across multiple inductions. Copy number analysis confirms the expression of key markers, including TH, DDC, FOXA2, and SHH (Fig. 2a), which varies across inductions and lines, but with no significant differences (Supplementary Fig. 2e). Copy number proteomics further confirmed the expression of several key proteins involved in PD in terminally differentiated mDA neurons (Fig. 2a).

We performed RNA velocity analysis, scVelo²⁰ in single-cell RNA-seq data on day 48-old mDA neuronal cultures²¹. RNA velocity, i.e., the change in RNA abundance for each gene in a single cell, can be used to predict the future transcriptomic state of a cell, and thus infer developmental trajectories. The expected neuronal differentiation trajectory from the NPC clusters towards mature mDA neurons was confirmed (Fig. 2b, c), and additional differentiation trajectories from several mDA neuron clusters to other mDA neuron clusters were identified (Fig. 2d). The dynamical model used by scVelo allowed us to recover latent time, and reconstruct the temporal sequence of cellular fates: NPC cell clusters were earlier than mDA neurons in latent time, and were spread across latent time, suggesting different clusters were at different points on the path to form mature mDA neurons (Fig. 2e). The dynamic behaviour of the top genes for each cluster systematically detected by likelihoods (where the genes associated with mDA differentiation include *STMN2*, *DCX*, and *SYT1*, and the genes for NPC clusters include *OTX2*, *LMX1A* and *QKI*) can be seen across latent time (Fig. 2f) and across clusters (Supplementary Fig. 3b), as well as the different confidence probability of the predicted mDA neuronal cluster trajectory path (Supplementary Fig. 3c). We performed gene ontology (GO) enrichment²² for the top 100 identified genes for each cluster. NPC clusters were associated with GO terms related to proliferation, as well as neuronal differentiation (Fig. 2g). mDA neuron clusters showed enrichment in GO terms associated with complex synapse formation, as well as ion transport development (Fig. 2h) (Supplementary Table 4). Our analysis demonstrates that, at 48 days of differentiation, our method predominantly generates cells of mDA neuronal identity, with a clear developmental trajectory defined for the remaining NPCs to differentiate into mDA neurons.

hiPSC-derived mDA neurons exhibit functional neuronal and dopaminergic identity

To test the functional properties of the neurons, we first determined whether they expressed voltage-dependent calcium channels (VDCCs). Opening of calcium channels was induced using a high concentration of KCl (50 mM), which depolarises the plasma membrane, opening VDCCs, resulting in a large influx of Ca^{2+} into the neurons. Bath application of KCl induced a cytosolic Ca^{2+} rise in all cultures with ~65% of cells responding after day 34, increasing to over 85% after day 55 of differentiation (day 34 = 65.5% ± 5.7, day 41 = 73.1% ± 2.3, day 48 = 73.2 ± 1.7, day 55 = 88.6% ± 1.8, $P = 0.0075$) (Fig. 3a, b and Supplementary Fig. 4a). After day 41 of differentiation, we observed spontaneous calcium fluctuations in neurons (Fig. 3c), which are a key hallmark of mDA dopaminergic neurons in the substantia nigra and contribute to the cell pace-making activity²³.



We investigated the electrophysiological characteristics of the mDA neurons. We confirmed the generation of action potentials (AP) activated by a depolarising voltage step, involving the classical tetrodotoxin (TTX)-sensitive voltage-gated sodium channels (Fig. 3d). We next confirmed the presence of excitatory NMDA

receptors, shown by the triggered single-channel openings in outside-patches pulled from cell soma upon application of 10 mM glutamate + 10 mM glycine, and fully inhibited by further application of 50 mM APV, a selective antagonist of NMDA receptors (Fig. 3e). Whole-cell voltage-clamp recording of

Fig. 1 Characterisation of an enriched population of mDA NPCs and neurons. **a** Differentiation protocol to generate mDA neurons. **b** Quantitative PCR at day 14–20 of differentiation showing mRNA for *LMX1A*, *FOXA2*, and *EN1* relative to hiPSCs (ns $P > 0.05$, $***P < 0.005$). **c** Representative ICC images showing expression of *FOXA2*, *LMX1A*, and *OTX2* (scale bar = 50 μm). **d** Quantification showing >80% of cells co-express *FOXA2*, *LMX1A* and *OTX2* (ns $P > 0.05$, ordinary one-way ANOVA). **e** Quantification of ICC images showing the increase in expression of the mDA marker, TH over differentiation (weeks) (ns $P > 0.05$, $***P < 0.0005$, $****P < 0.0001$, ordinary one-way ANOVA). **f** Representative ICC images showing TH and TUJ1 expression after 41 days of differentiation (scale bar = 50 μm). **g** ICC Quantification showing approximately 80% cells express TH (ns $P > 0.05$, ordinary one-way ANOVA). **h** Representative dot plots of single-cell suspensions showing % TH and β -III Tubulin +ve cells (day 41). A negative control (DAPI only) was used to determine quantification thresholds ($n = 10,000$ events recorded per measurement). **i** Quantification of flow cytometry showing >80% of DAPI-positive cells co-express TH and β -III Tubulin. **j** A UMAP plot showing the 14 clusters identified from single-cell RNA-seq after day 48 of differentiation. Neuronal mDA (mDA1–8) clusters are in blue, and NPC clusters (NPCs1–5) are in red, orange and yellow. An unidentified cluster (N/A) is coloured in grey. **k** Heatmap showing expression of genes in clusters identified as mDA neurons (mDA1–8). Each line represents a cell from that cluster. All data plotted as \pm s.e.m. All N numbers for each experiment can be found in Supplementary Table 5.

spontaneous postsynaptic activity revealed postsynaptic currents, which were suppressed by 50 mM of the selective antagonist of GABA_A receptor, picrotoxin (Supplementary Fig. 4c). This confirms functional synapses, with synaptic transmission mediated by the main type of inhibitory receptors, GABA_A receptors and spontaneously released GABA. Lastly, we tested whether the functional network made by mDA neurons could trigger evoked responses via extracellular electrical stimulation. We recorded the stimulus-evoked APs of a classical shape (Fig. 3g). We observed a clear increase between membrane capacitance (C_m) value under normal Ca^{2+} concentration and after an elevated Ca^{2+} concentration (Fig. 3f), confirming Ca^{2+} -dependent presynaptic vesicle release. Thus, the mDA neurons display complex electrophysiological characteristics of neurons, and are able to form functional networks.

Active dopamine transport can be assessed by measuring the uptake of the fluorogenic dopamine transporter (DAT) substrate FFN102 (FFN)²⁴. When incubated with FFN, followed by a wash, the dye can be seen inside mDA neurons (Supplementary Fig. 4b). The uptake of FFN in neurons is further activated upon KCl-induced Ca^{2+} influx in the majority of neurons (Fig. 3h, k) (cells activated by KCl = 79.5% \pm 2.5). Inhibition of the DAT using the compound nomifensine resulted in a significantly reduced uptake rate of FFN into neurons (No treatment = 1.00 \pm 0.00, nomifensine = 0.53 \pm 0.05, $P = 0.0024$) (Fig. 3j) (Supplementary Fig. 4d), as well as a reduced KCl stimulated uptake (Fig. 3i). These data suggest that the mDA neurons exhibit dopamine transport.

HPLC with electrochemical detection was used to investigate dopamine metabolism in the mDA neurons. Under basal conditions, mDA neurons released dopamine metabolite 3,4-Dihydroxyphenylacetic acid (DOPAC), which increased with time in vitro (Fig. 3l) (lysate: d41 = 86.5 nmol/L \pm 9, d48 = 212.6 nmol/L \pm 13, $P > 0.05$; media: d41 = 1072 nmol/L \pm 24, d48 = 2212 nmol/L \pm 56, $P = 0.0041$). Therefore, the cells were able to synthesise and metabolise dopamine under basal conditions. Following pre-treatment of the mDA neurons with the dopamine precursor, L-3,4-dihydroxyphenylalanine (L-Dopa), we detected the presence of dopamine, and its metabolites (DOPAC, homovanillic acid [HVA]) in day 41 and 48 terminally differentiated neurons (Fig. 3n). The lack of detection of the main serotonin metabolite 5-hydroxyindoleacetic acid (5-HIAA), usually present in neuronal cells that show mixed dopaminergic/serotonergic characteristics²⁵, suggests the mDA neurons are specifically dopaminergic in nature (Fig. 3m). In addition, we found no difference in cell death between treatments, ruling out non-specific release of dopamine from cytotoxicity caused by L-Dopa (Supplementary Fig. 4e). Quantification showed that all metabolites were higher in the media compared to the cell lysate (Fig. 3n), with the metabolites DOPAC and HVA being present in the highest amounts in the media of day 48 mDA neurons (DOPAC = 3493 nmol/L \pm 401, HVA = 6494 nmol/L \pm 898), and the levels of dopamine being consistent between day 41 and 48 neurons (lysate: day 41 = 312 nmol/L \pm 80, day 48 = 274 nmol/L \pm 12.8; media: day

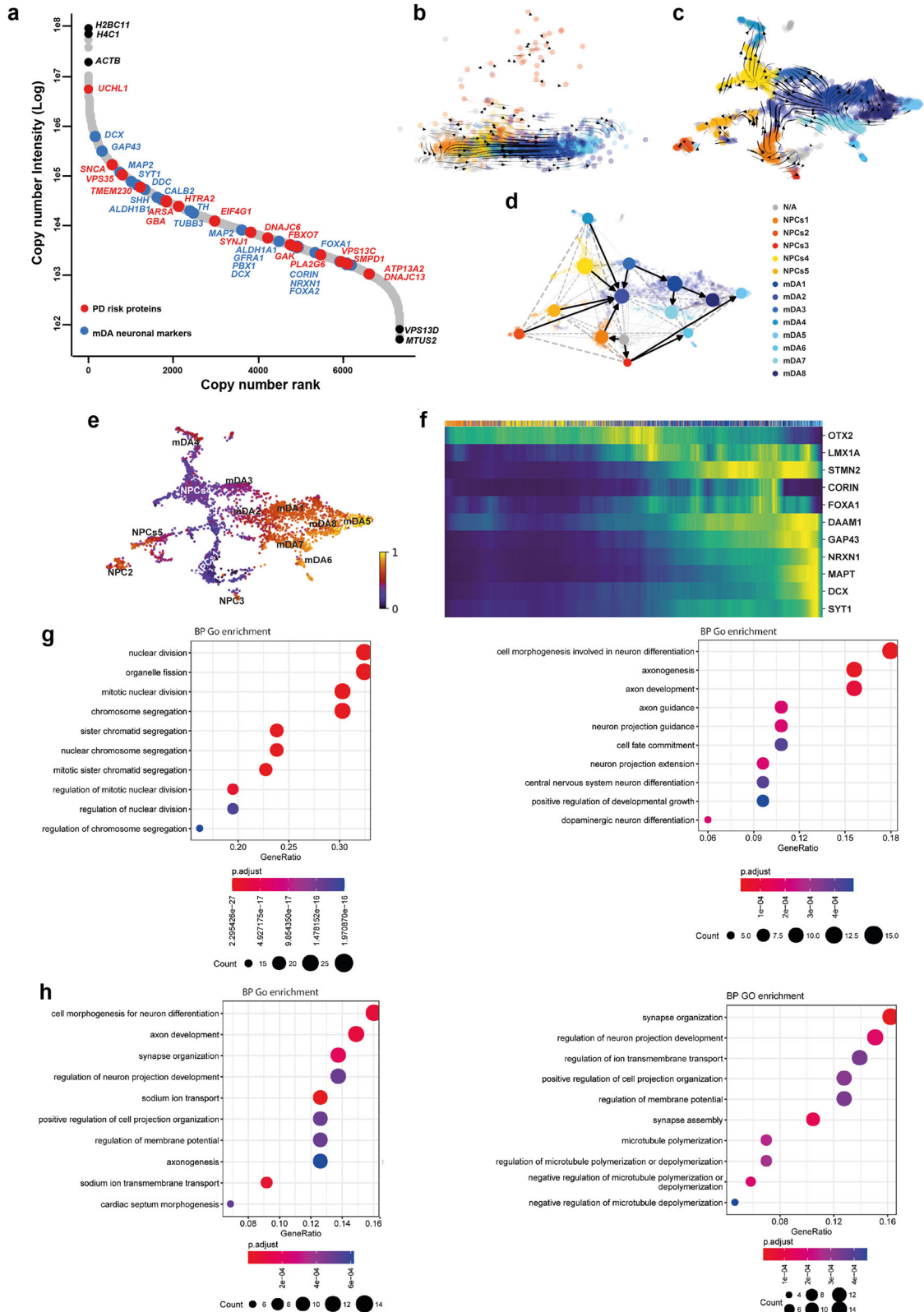
41 = 6029 nmol/L \pm 1153, day 48 = 6277 nmol/L \pm 1387, $P > 0.05$). Together, we show that mDA neurons exhibit dopamine metabolism and secretion by day 41 of differentiation.

Establishing a synucleinopathy PD model from patient-derived hiPSCs with *SNCA* mutations

Mutations in *SNCA* cause an autosomal dominant form of PD (*SNCA*-PD). hiPSCs from patients with a p.A53T mutation, triplication of the *SNCA* locus (*SNCA* x3), their isogenic pairs and healthy donors were differentiated into mDA neurons using the protocol described above. All three mutant lines (two hiPSC lines with the p.A53T mutation, and 1 hiPSC with the *SNCA* x3 mutation) were successfully differentiated into mDA neurons, highlighted by the high enrichment of TH and MAP2 or β III-Tubulin protein after 41 days of differentiation (Ctrl = 82.6% \pm 3.2 TH-positive, 91.3% \pm 1.9 MAP2/ β III-positive, A53T = 78.2% \pm 4.6 TH-positive, 84.5% \pm 2.2 MAP2/ β III-positive, *SNCA* x3 = 80.2% \pm 3.0 TH-positive, 86.6% \pm 2.9 MAP2/ β III-positive, $P > 0.05$) (Fig. 4a, b). Using RT-qPCR, we first found a 3–4-fold increase in *SNCA* mRNA in the *SNCA* x3 line compared to the control lines at 41 days of differentiation (Supplementary Fig. 5a). The A53T lines exhibited a similar amount of *SNCA* mRNA compared to the control lines (Ctrl = 1.0 \pm 0.13, A53T = 1.4 \pm 0.04, *SNCA* x3 = 3.6 \pm 0.5, $P < 0.0001$). Using an antibody that recognises total α -synuclein, we detected α -synuclein protein expression across all lines at day 48 of differentiation, with a significant increase in the expression of α -synuclein in the *SNCA* x3 line, in fluorescence intensity and area (Supplementary Fig. 5b–e).

α -synuclein aggregation and abnormal calcium signalling are early and persistent phenotypes in *SNCA* PD mDA neurons

During disease, monomeric α -synuclein aggregates to form small soluble oligomers, with the accumulation of β -sheet structure, and later fibrils^{26,27}. We investigated whether *SNCA*-PD mDA neurons exhibited early aggregate formation using a single-stranded oligonucleotide aptamer, which binds to β -sheet-rich protein structures containing α -synuclein²⁸. Due to the small size of oligomers (often below the diffraction limit of light \approx 250 nm), we employed a previously described super-resolution technique, aptamer-based DNA-PAINT (point accumulation in nanoscale topography) (AD-PAINT) to visualise and quantify α -synuclein oligomers. This consists of an aptamer probe that is conjugated to an oligonucleotide sequence which is recognised by the fluorophore-conjugated DNA imaging strand²⁸. To demonstrate the specificity of the aptamer for α -synuclein aggregates, we performed aptamer-based DNA-PAINT on neuroblastoma cells pre-treated with α -synuclein preformed fibrils (PFFs). Seeding in the neuroblastoma cells results in aptamer detection of increased numbers of clusters, which are larger (in length and area) compared to unseeded cells. (Supplementary Fig. 6a, b). After day 27 of differentiation, mDA neurons were incubated with the aptamer, as well as the actin probe, Phalloidin-647. Using a combination of dSTORM (direct stochastic optical reconstruction



microscopy) and AD-PAINT, we visualised aggregates at single-cell resolution (Fig. 4c and Supplementary Fig. 6c). Performance of a clustering algorithm analysis, DBSCAN, quantified the clusters based on localisations that were within 60 nm of each other and contained at least 15 localisations (to remove non-specific localisations) (last

panel, Fig. 4c). As early as day 27 of differentiation, prior to functional neuronal identity, both A53T and SNCA x3 cells displayed a significantly higher number of aggregates per cell (Fig. 4d and Supplementary Fig. 6d) (Ctrl = 22 ± 3.1, A53T = 127 ± 18.2, SNCA x3 = 71 ± 16.7, $P < 0.005$). In addition, the average length of the

Fig. 2 RNA velocity demonstrates developmental streams from NPCs into mDA neurons reminiscent of a developing midbrain. **a** Rank abundance plot showing copy number of proteins from proteomic analysis with expression of mDA proteins in blue and PD-linked proteins in red. **b** PCA visualises the progression from precursor cells (NPCs) (yellow-red colours) towards mDA neuronal cells (blue colours). RNA velocity trajectories are indicated by arrows. **c** Velocity stream visualised in UMAP reveals a more detailed progression of the direction of differentiation. **d** PAGA graph showing the NPC cluster transition into mDA neuron clusters. **e** Velocity inferred latent time analysis visualised in UMAP, showing mDA clusters are later (brighter colour) in time than NPC clusters (darker colours). **f** A heatmap listing a selection of cluster driver genes sorted according to their inferred latent time. **g, h** GO enrichment analysis to clarify gene categories per cell cluster based on the functional characteristics of the driver genes. **g** Example of GO enrichment of two NPC clusters showing that some clusters are more proliferative (left graph), and some are more differentiated and on the neuronal pathway (right graph). **h** Example of two mDA neuron clusters showing complex neuronal pathways which are highly activated.

aggregates was higher in A53T, and *SNCA* x3 cells (Fig. 4e and Supplementary Fig. 6e) (Ctrl = $80.0 \text{ nm} \pm 0.99$, A53T = $94.9 \text{ nm} \pm 0.83$, *SNCA* x3 = $105.2 \text{ nm} \pm 1.32$, $P < 0.0001$). In order to rule out non-specific binding of oligonucleotides, cells were incubated with only the imaging strand. The number of single-molecule localisations was low when incubated with only the imaging strand and was significantly increased upon the addition of the aptamer (Supplementary Fig. 6f–h), confirming that the majority of localisations detected are due to the aptamer binding to its target.

Calcium dysregulation is one of the key phenotypes related to α -synuclein aggregation^{19,30}. We investigated whether physiological calcium responses were altered by the presence of *SNCA* mutations. We stimulated hiPSC-derived *SNCA* PD mDA neurons with KCl (50 mM) to induce the VDCC-mediated cytosolic calcium signal of neurons at various stages of mDA differentiation. By day 34 differentiation, a similar proportion of control and *SNCA*-PD neurons (60–70%) showed a cytosolic Ca^{2+} increase in response to KCl using the Fluo-4 probe (Ctrl = $63.1\% \pm 3.5$, A53T = $68.4\% \pm 3.6$, *SNCA* x3 = $63.0\% \pm 3.0$, $P > 0.05$) (Fig. 4f–h). Neurons harbouring *SNCA* mutations displayed a significantly impaired recovery of cytosolic Ca^{2+} in response to KCl from day 34 of differentiation (Ctrl = 1.00 ± 0.08 , A53T = 0.50 ± 0.10 , *SNCA* x3 = 0.43 ± 0.10 , $P < 0.0005$) (Fig. 4i, j). At day 41 of differentiation, using the ratiometric calcium indicator, Fura-2, both A53T and *SNCA* x3 mDA neurons displayed higher basal $[\text{Ca}^{2+}]_c$ levels (Ctrl = 1.00 ± 0.01 , A53T = 1.13 ± 0.03 , *SNCA* x3 = 1.23 ± 0.03 , $P < 0.0005$) (Fig. 4k, l). In addition, there was a delayed calcium recovery rate of KCl-induced $[\text{Ca}^{2+}]_c$ in both A53T and *SNCA* x3 mDA neurons (Ctrl = 0.96 ± 0.07 , A53T = 0.45 ± 0.05 , *SNCA* x3 = 0.31 ± 0.05 , $P < 0.0001$) (Fig. 4m), as well as a significantly reduced KCl-induced $[\text{Ca}^{2+}]_c$ amplitude (Supplementary Fig. 6i).

To determine if these phenotypes persist in older mDA neurons (>48 days of differentiation), $[\text{Ca}^{2+}]_c$ was investigated in >day 48 mDA neurons. Both A53T and *SNCA* x3 mDA neurons displayed a higher basal $[\text{Ca}^{2+}]_c$ (Ctrl = 1.01 ± 0.02 , A53T = 1.74 ± 0.09 , *SNCA* x3 = 1.32 ± 0.03 , $P < 0.0001$) (Fig. 5a, b), as well as a delayed recovery following KCl stimulation (Ctrl = 1.02 ± 0.07 , A53T = 0.51 ± 0.11 , *SNCA* x3 = 0.36 ± 0.04 , $P < 0.0001$) compared to control neurons (Fig. 5c). In addition, A53T and *SNCA* x3 neurons had a lower amplitude of KCl-induced $[\text{Ca}^{2+}]_c$ rise compared to control neurons (Supplementary Fig. 7c). During cytosolic calcium influx, mitochondria act as the major buffer for calcium, shaping the cytosolic calcium signal and maintaining calcium homeostasis²⁹. Upon KCl-induced calcium influx, we observed a concomitant increase in mitochondrial calcium, measured by the fluorescent dye X-Rhod-1 (Fig. 5d). However, the recovery of the mitochondrial calcium signal was significantly delayed in the *SNCA*-mutant neurons compared to controls, suggesting a potential impairment of mitochondrial calcium efflux (Fig. 5e–h) (Fluo-4: Ctrl = 1.00 ± 0.08 , A53T = 0.42 ± 0.06 , *SNCA* x3 = 0.62 ± 0.10 , $P < 0.005$) (X-Rhod-1: Ctrl = 0.99 ± 0.11 , A53T = 0.67 ± 0.07 , *SNCA* x3 = 0.54 ± 0.07 , $P < 0.05$). Taken together, these results suggest intracellular calcium dysregulation persists as a late phenotype in older mDA neurons and also affects organellar calcium homeostasis.

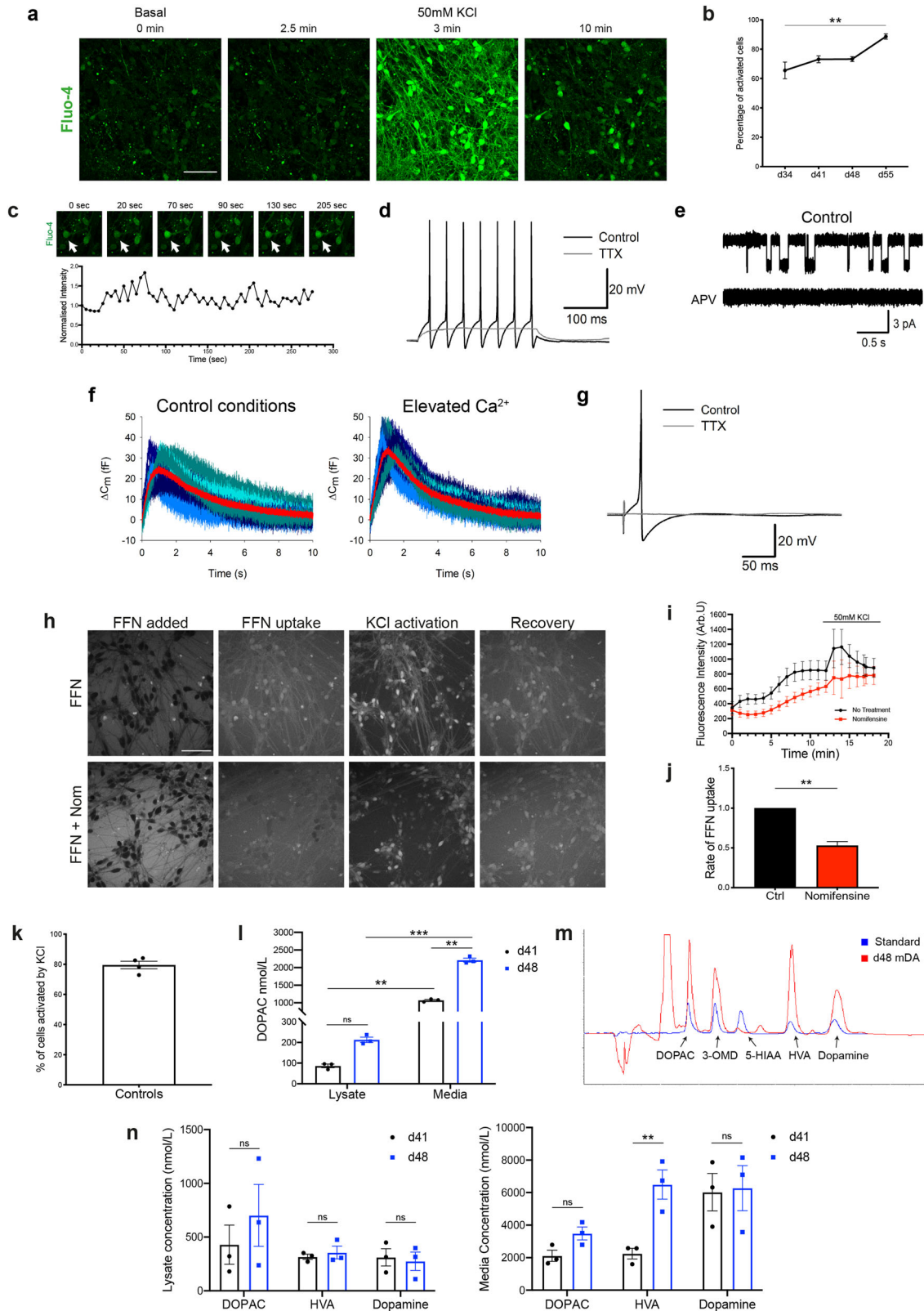
As we showed that α -synuclein aggregation is an early pathological event along with calcium dysregulation, we investigated if it also persisted as a late phenotype in older mDA neurons, using a range of approaches. Using a conformation-specific antibody that recognises all types of aggregated forms of α -synuclein³⁰ at day 62 of differentiation, we observed the presence of aggregated filamentous α -synuclein in both the A53T and the *SNCA* x3 lines which were significantly increased compared to control neurons (Fig. 5i), confirmed by quantification of fluorescence intensity (Fig. 5j) (Ctrl = 100 ± 2.4 , A53T = 121 ± 3.2 , *SNCA* x3 = 118 ± 1.9 , $P < 0.0001$) and the average size of the aggregate puncta (Fig. 5k) (Ctrl = $0.57 \mu\text{m}^2 \pm 0.05$, A53T = $1.47 \mu\text{m}^2 \pm 0.24$, *SNCA* x3 = $1.26 \mu\text{m}^2 \pm 0.15$, $P = 0.0082$; $P = 0.0007$). In addition, serine-129 phosphorylated α -synuclein species, a hallmark of Lewy bodies³¹ was detected in neuronal processes of mDA neurons after day 48 (Supplementary Figs. 6j and 7a, b). We also used the aptamer to detect α -synuclein aggregates from day 62 neuronal lysate and confirm a significantly higher aggregate load in *SNCA* x3 neurons (Fig. 5l) (Ctrl = 42.7 ± 2.7 , *SNCA* x3 = 137.8 ± 15.3 , $P = 0.0073$). Finally, we used an α -synuclein aggregate sensitive ELISA and similarly found higher levels of aggregates in A53T and *SNCA* x3 neurons in old mDA neurons relative to their respective isogenic control (Supplementary Fig. 7k).

Collectively, our data demonstrate that, using highly sensitive methods, we were able to detect and measure the formation of β -sheet-rich, toxic, oligomeric species. Along with aberrant calcium signalling, they both present as the earliest pathological hallmark in *SNCA* neurons. Temporally, aggregation progresses to form phosphorylated and filamentous aggregates that become detectable by traditional immunocytochemical methods.

Mitochondrial, lysosomal dysfunction and oxidative stress are late *SNCA*-induced phenotypes

We assessed the mitochondrial function of *SNCA*-mutant PD neurons using the lipophilic cationic dye TMRM, which accumulates less in depolarised mitochondria upon the loss of mitochondrial membrane potential. Depolarisation of the mitochondria emerges after day 48 of differentiation in *SNCA*-mutant mDA neurons shown by a reduction in mitochondrial membrane potential (Fig. 6a, b) (Ctrl = $100\% \pm 4.7$, A53T = $78.1\% \pm 3.7$, *SNCA* x3 = $77.5\% \pm 5.5$, $P < 0.005$) (Supplementary Fig. 8a). Mitochondrial depolarisation was not evident in early mDA neurons (between days 27 and 48) (Supplementary Fig. 7d, j).

Mitochondrial dysfunction can result in the overproduction of mitochondrial and extra-mitochondrial reactive oxygen species (ROS). We measured the generation of cytosolic ROS using the fluorescent reporter dihydroethidium (HEt), which changes fluorescence emission upon oxidation. After day 48 of differentiation, the rate of superoxide production was significantly higher in the A53T neurons, and approximately 20% higher in the *SNCA* x3 line compared to controls (Ctrl = $100\% \pm 6.3$, A53T = $194.0\% \pm 23.7$, *SNCA* x3 = $123.6\% \pm 7.5$, $P < 0.0005$) (Fig. 6c, d and Supplementary Fig. 8b). At the same neuronal age, we also measured the levels of the endogenous antioxidant glutathione using the Monochlorobimane (MCB) fluorescence indicator, which showed



a significant reduction of glutathione in both, A53T and SNCA x3 lines compared to the controls (Ctrl = $100\% \pm 3.7$, A53T = $77.2\% \pm 1.8$, SNCA x3 = $86.5\% \pm 2.6$, $P < 0.05$; $P = 0.0009$) (Fig. 6e, f and Supplementary Fig. 8c). Oxidative stress was absent in early neurons (Supplementary Fig. 7e–g, j). The combination of

increased ROS production together with depleted antioxidant levels suggests that both A53T and SNCA x3 mDA neurons exhibit oxidative stress as a late phenotype.

We measured the lysosomal compartment in SNCA-PD neurons using LysoTracker Deep red; a cationic fluorescent dye that only

Fig. 3 Functional characterisation of mDA neurons. **a** Representative time series images of mDA neurons at day 55 of differentiation, in response to KCl (scale bar = 50 μ m). **b** Quantification of the number of cells with calcium response (ns $P > 0.05$, $**P = 0.0075$, two-way ANOVA). **c** Representative time series images of spontaneous calcium activity at day 41 of differentiation, with the Fluo-4 intensity trace of the highlighted cell (arrow) plotted below. **d** APs triggered by current injection in mDA neurons at day 30 of differentiation. 1 mM tetrodotoxin (TTX) suppresses APs. **e** Single-channel openings of NMDA receptors in an outside-out patch excised from mDA neurons at day 30 of differentiation. Top trace: application of 10 mM glutamate + 10 mM glycine triggers single-channel openings. Bottom trace: 50 mM APV suppresses single-channel opening. **f** Changes in whole-cell membrane capacitance confirm elevated intensity of vesicle release in mDA neurons at day 70 of differentiation. Shadows of blue, high noise. Red trace with low noise: averaged trace. Left: control. Right: elevated Ca^{2+} magnifies the effect on membrane capacitance. **g** AP generation in response to field stimulation in mDA neurons at day 105 of differentiation. **h** Representative images showing sequential uptake and stimulation with 50 mM KCl of the DAT fluorescent substrate FFN102 (FFN) in day 41–48 mDA neurons. Lower panels show FFN uptake in the presence of the DAT inhibitor, nomifensine (scale bar = 50 μ m). **i** Representative trace showing increase in intracellular FFN with time, as well as response to KCl stimulation. Nomifensine reduces the rate of FFN uptake. Values plotted as \pm s.d. **j** Quantification of the normalised rate of FFN uptake (Welch's t test, $**P = 0.0024$). **k** Quantification of the number of FFN-positive cells once stimulated by KCl. **l** Quantification of the amount of the metabolite DOPAC in basal day 41 (3w) or day (48) old mDA neurons (ns $P > 0.05$, $**P < 0.008$, $***P = 0.0002$, ordinary two-way ANOVA). **m** Example chromatogram from day 48 mDA neuron culture treated with L-Dopa (red trace) against a standard (blue trace) showing the presence or absence (peaks) of the metabolites DOPAC, 3-O-methyl-dopa (3-OMD), 5-HIAA, HVA, Dopamine. **n** Quantification of the metabolites DOPAC, HVA, and Dopamine in lysate, or media of L-Dopa treated day 41 and day 48 mDA neurons (ns $P > 0.05$, $**P < 0.005$, ordinary two-way ANOVA). All values are plotted as \pm s.e.m unless stated otherwise. All N numbers for each experiment can be found in Supplementary Table 5.

accumulates in acidic cellular compartments (lysosomes). We found that both, A53T and *SNCA* x3 neurons after day 48 of differentiation exhibited significantly larger lysosomes compared to the healthy control neurons (Ctrl = 100 ± 2.4 , A53T = 125 ± 3.9 , *SNCA* x3 = 121 ± 3.9 , $P = 0.0002$; $P < 0.0001$) (Fig. 6g, h), which was not detectable in day 27–48 neurons (Supplementary Fig. 7h, j). Control neurons had a higher proportion of smaller lysosomes (mainly between 0–2 μm^2) compared to the A53T and *SNCA* x3 neurons, which had a higher proportion of larger lysosomes (mostly 2–10 μm^2) (Fig. 6i and Supplementary Fig. 8e), suggesting that the lysosomes are swollen, implying lysosomal pathology.

Mitochondrial PTP opening, fragmentation, autophagy and cell death are late phenotypes

To test the consequence of aberrant calcium flux and mitochondrial dysfunction, we loaded *SNCA* and control neurons with cytosolic calcium and membrane potential indicators and tested their response to KCl. In control mDA neurons, KCl induced the opening of the VDCCs, and a cytosolic calcium signal which was associated with the mitochondrial influx of calcium, during which the mitochondria retained their mitochondrial membrane potential (Fig. 6j, k). However, *SNCA* mutant mDA neuronal mitochondria exhibited depolarisation upon calcium influx into the mitochondria, which was induced by the cytosolic calcium signal (Fig. 6k, l) (Ctrl = 97.8 ± 3.7 , A53T = 81.0 ± 4.0 , *SNCA* x3 = 72.4 ± 3.9 , $P < 0.05$), concurrently showing impaired recovery of cytoplasmic calcium (Supplementary Fig. 8f). Rapid depolarisation events in the mitochondria may reflect transient permeability transition pore (PTP) opening, an event triggered by mitochondrial calcium overload that can boost mitochondrial Ca^{2+} efflux. To test the mitochondrial PTP opening threshold in *SNCA* PD, we sequentially applied ferutinin which results in stepwise increases in mitochondrial calcium. PTP opening is measured by a rapid decrease in mitochondrial membrane potential, visualised with TMRM (Supplementary Fig. 8g). In >day 55 *SNCA* x3 neurons, the threshold of mitochondrial PTP opening was significantly reduced compared to control neurons, thereby highlighting mitochondrial damage as a late phenotype (Supplementary Fig. 8h).

Damaged organelles, including mitochondria, as well as protein aggregates, are cleared through the autophagy-lysosomal pathway. Autophagy results in the formation of autophagosomes, which engulf the target, and process them to lysosomes for destruction. We investigated the expression of the autophagosome marker LC3B together with the mitochondrial marker Tomm20 at day 55 of differentiation using a super-resolution approach, structured illumination microscopy (SIM) and iSIM to resolve the contacts between the mitochondria and the

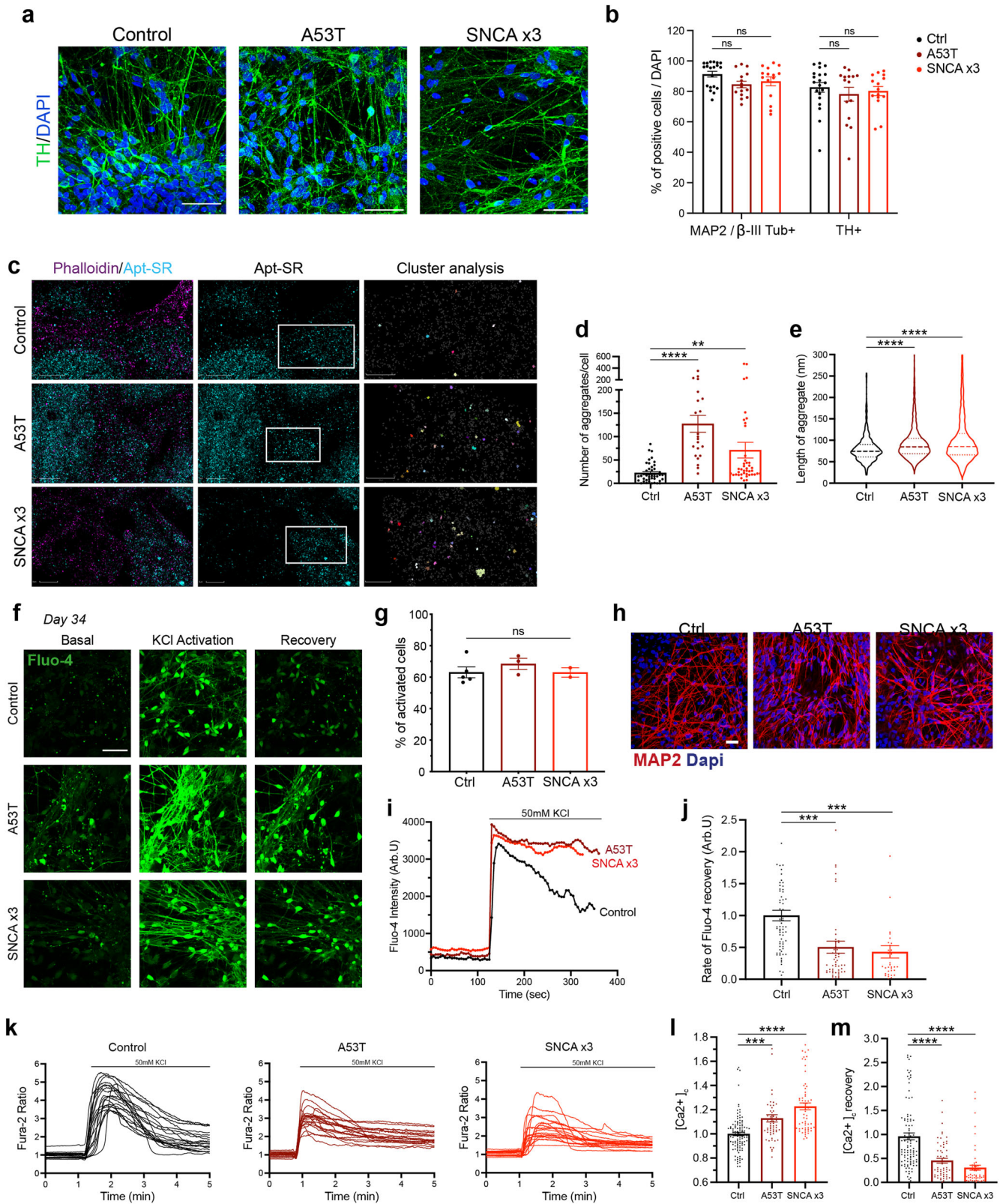
autophagosomes. Mitochondria based on Tomm20 immunolabelling in control day 55 neurons maintain an intact network, in contrast to A53T and *SNCA* x3 neurons which exhibit a fragmented mitochondrial network (Fig. 6m and Supplementary Fig. 8i). We also observed a significant increase in the number of colocalisation between Tomm20 and LC3B in all *SNCA*-PD lines compared to control lines (Fig. 6n) (Ctrl = 176 ± 26 , *SNCA* PD = 292 ± 45 , $P < 0.05$), as well as more LC3B puncta per cell (Fig. 6o and Supplementary Fig. 8j, k) (Ctrl = 385 ± 62 , *SNCA* PD = 679 ± 98 , $P < 0.05$), suggesting close contact between autophagosomes and the mitochondria and an autophagosome response.

Finally, we examined the viability of the *SNCA* mutant neurons using the fluorescent dye SYTOXTM Green to identify dead cells. We observed a significant increase in cell death in both the A53T and *SNCA* x3 lines compared to the healthy control lines from day 48 onwards (Ctrl = $7.6\% \pm 0.6$, A53T = $12.2\% \pm 1.4$, *SNCA* x3 = $12.1\% \pm 1.4$, $P = 0.006$; $P = 0.003$) (Fig. 6p, q and Supplementary Fig. 8d). In contrast, at early time points (day 21–41) there was no difference in cell death (Supplementary Fig. 7i, j).

Late functional consequences of *SNCA* mutations in human mDA neurons

To confirm that *SNCA* is the cause of early and late cellular pathology, we generated isogenic controls from A53T and *SNCA* x3 patient lines, and validated our previous findings. After day 55 of differentiation, using TMRM we observed changes in the mitochondrial network in *SNCA*-mutant neurons, with a reduced area/volume occupied by mitochondria (iso-Ctrl of A53T = $100\% \pm 6.5$, A53T = $78.9\% \pm 4.6$, $P < 0.05$; iso-Ctrl of *SNCA* x3 = $100\% \pm 5.9$, *SNCA* x3 = $74.4\% \pm 5.8$, $P < 0.005$) (Fig. 7a), which was reversed in matching isogenic controls. There was also an increase in the number of lysosomes in both A53T and *SNCA* x3 mDA neurons, which was also reversed in isogenic controls (iso-Ctrl of A53T = $100\% \pm 7.2$, A53T = $74.4\% \pm 4.7$, $P < 0.05$; iso-Ctrl of *SNCA* x3 = $100\% \pm 6.0$, *SNCA* x3 = $67.1\% \pm 7.5$, $P < 0.005$) (Fig. 7b). Similarly, after day 62 of differentiation, there was a significant increase in basal cell death in both *SNCA* PD lines compared to their matching isogenic line (iso-Ctrl of A53T = $100\% \pm 10.7$, A53T = $264.4\% \pm 31.3$, $P < 0.0001$; iso-Ctrl of *SNCA* x3 = $100\% \pm 18.8$, *SNCA* x3 = $222.9\% \pm 27.6$, $P < 0.005$) (Fig. 7c).

We performed patch-clamp recordings in *SNCA*-mutant mDA neurons after day 70 of differentiation (Fig. 7d). In whole-cell configuration, *SNCA* PD mDA neurons displayed a prominently depolarised resting membrane potential (V_{rest}) compared with their age-matched isogenic controls (A53T = -39.55 ± 2.84 mV, A53T isogenic = -53.02 ± 1.94 mV, $P = 0.0004$, *SNCA* x3 = -43.92 ± 1.62 mV, *SNCA* x3 isogenic = -50.80 ± 1.69 mV, $P = 0.0072$) (Fig. 7e).



However, there was no significant difference in other passive membrane properties of hiPSCs between the mutant and isogenic mDA neurons, such as capacitance (A53T isogenic = C_m ; 39.91 pF, A53T = 33.12 pF, $P = 0.19$) and the time constant (A53T isogenic = τ_m ; 99.52 ms, A53T = 100.32 ms, $P = 0.957$) (Supplementary Fig.

9a–c). The similarity of these parameters indicates a similar maturation of biophysical properties between the neuronal groups, with or without *SNCA* mutations. However, the *SNCA*-mutant mDA neurons displayed a significantly increased input resistance, a parameter indicating membrane conductance (A53T R_{in} ;

Fig. 4 Generation of mDA neurons from hiPSC lines from patients with SNCA mutations display early α -synuclein aggregation and calcium dysregulation. **a** Representative ICC images of control, A53T, and SNCA x3 mDA neurons showing high TH expression. Scale bar = 50 μ m. **b** Quantification of % MAP2 and TH-positive cells after day 41 of differentiation (ns $P > 0.05$, two-way ANOVA). **c** Super-resolved images from control, A53T, SNCA x3 day 27 mDA neurons. Left panel shows phalloidin and aptamer. Middle panel shows only super-resolved aptamer binding events. Last panel shows a magnified version of aggregates detected by DBSCAN. Left panel scale bar = 2 μ m. Middle panel scale bar = 2 μ m. Right panel = 1 μ m. **d** Quantification showing the number of aggregates per cell in control, A53T and SNCA x3 mDA neurons (ns $P > 0.05$, * $P < 0.05$, ** $P < 0.005$, one-way ANOVA). **e** Quantification showing the length of all aggregates in control, A53T and SNCA x3 mDA neurons represented in a violin plot (**** $P < 0.0001$, one-way ANOVA). **f** Representative time series Ca^{2+} images in response to KCl (scale bar = 50 μ m). **g** Quantification of the number of cells with KCl-induced calcium signal at day 34 of differentiation (ns $P > 0.05$, one-way ANOVA). **h** Representative images of neuronal marker expression. **i** Representative single-cell trace in patient mDA neurons. **j** Quantification of the normalised rate of recovery of Fluo-4 after stimulation with KCl (*** $P = 0.0002$, one-way ANOVA). **k** Representative traces showing the Fura-2 ratio in response to 50 mM KCl in day 41 control neurons, A53T neurons, and SNCA x3 neurons. **l** Quantification of the basal calcium Fura-2 ratio ($[\text{Ca}^{2+}]_i$) before KCl stimulation (*** $P < 0.0005$, **** $P < 0.0001$, one-way ANOVA). **m** Quantification of the rate of calcium ($[\text{Ca}^{2+}]_i$) recovery in response to KCl (**** $P < 0.0001$, one-way ANOVA). All values are plotted as \pm s.e.m. All N numbers for each experiment can be found in Supplementary Table 5.

2.616 ± 0.592 G Ω , A53T isogenic = 1.209 ± 0.158 G Ω , $P = 0.0415$, SNCA x3 = 3.758 ± 0.418 G Ω , SNCA x3 isogenic = 2.443 ± 0.277 G Ω , $P = 0.017$) (Fig. 7f).

To address how SNCA mutations affect neuronal firing capacity, we next carried out recordings from mDA neurons in the current mode. Electrophysiology revealed an impaired firing in both SNCA PD neurons. All tested AP parameters were severely distorted in mutant neurons compared with their isogenic control. Firstly, the threshold for an AP spike was depolarised compared with that in an isogenic control (a depolarising shift in A53T = ~ 3.3 mV, $P = 0.0108$, SNCA x3 = ~ 4.5 mV, $P < 0.0001$) (Fig. 7g), and the AP was significantly reduced in both SNCA PD lines (a drop in the amplitude by $\sim 90\%$, $P < 0.0001$ in A53T neurons and $\sim 37.6\%$, $P = 0.0011$ in SNCA x3 neurons) (Fig. 7h), as well as a decreased AP overshoot (Supplementary Fig. 9g, h). In addition, the spike kinetics were substantially slower (i.e., a drop in the repolarisation rate by 120.5%, $P = 0.020$ in the A53T neurons and 88.1%, $P = 0.0024$ in SNCA x3 neurons) (Fig. 7i). Finally, there was also an increased rheobase in SNCA mutants – the magnitude of depolarising current required to induce firing. In particular, a two-fold stronger current was needed to bring SNCA x3 neurons to firing compared with control ($P = 0.0026$) (Supplementary Fig. 9f). Together, this demonstrates the pathophysiological excitability of PD SNCA mDA neurons, with a dramatically changed AP waveform – a profile of changes similar to that observed in other neurodegenerative diseases^{32,33}.

In summary, we show that aggregate formation, impaired calcium signalling, mitochondrial and lysosomal homeostasis, and oxidative stress, arise sequentially, alter neuronal excitability and function, and ultimately lead to toxicity to mDA SNCA-PD neurons (Fig. 8).

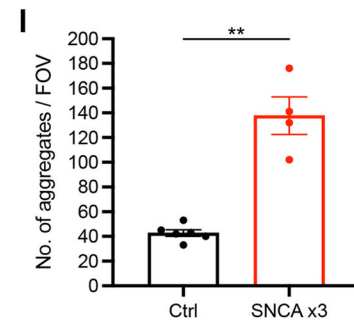
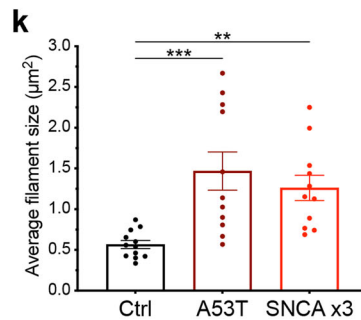
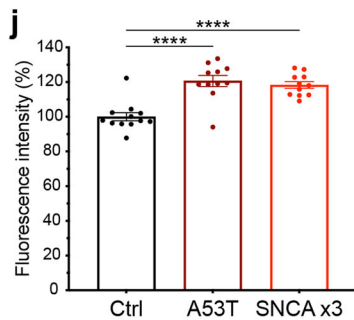
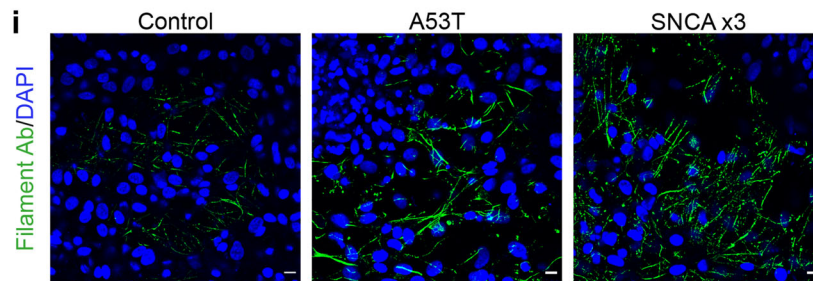
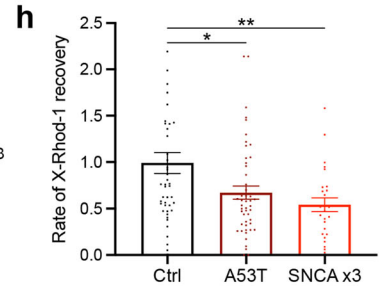
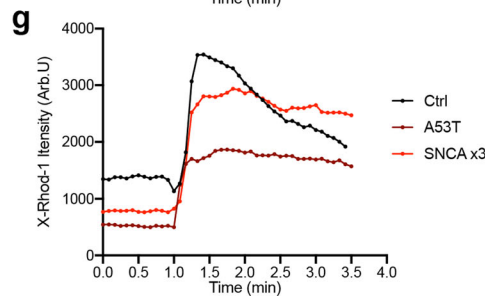
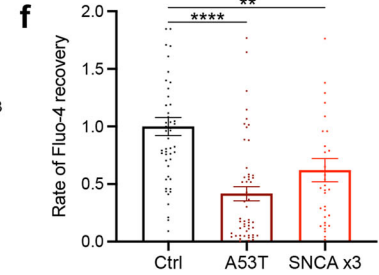
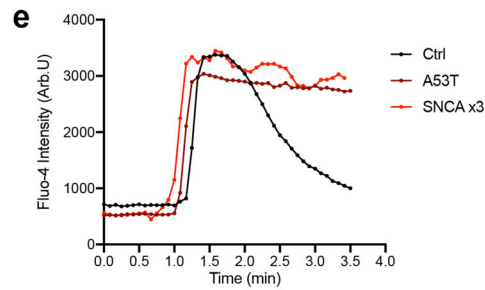
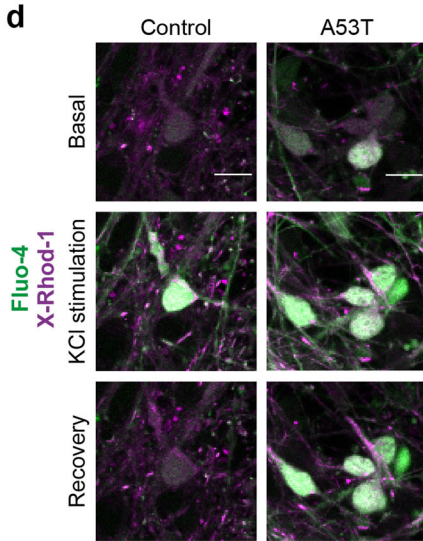
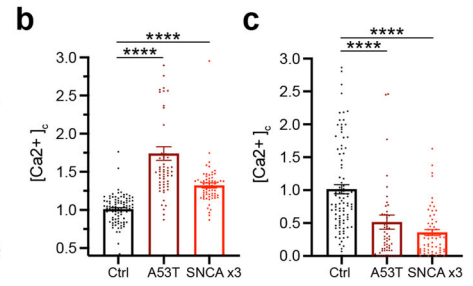
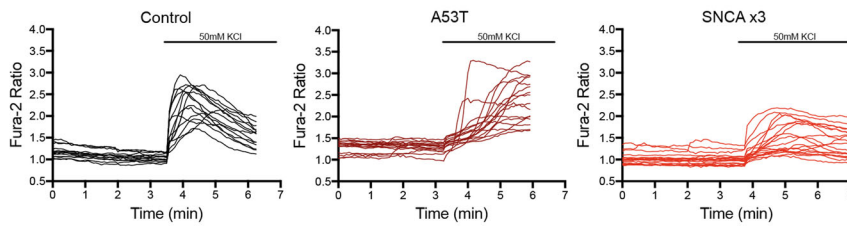
DISCUSSION

Lineage restriction to diverse cellular fates in the neuraxis is the consequence of interplay of multiple developmental signals, which are regulated in a spatio-temporal manner. In vitro, such lineage restriction can be achieved using a small molecule-based approach to recapitulate ontogeny, drawing insights from mouse developmental biology. In keeping with previous protocols, we initiated neuronal induction via small molecule dual-SMAD inhibition⁶, caudalisation to the midbrain via timed activation of Wnt signalling through a GSK-3 β inhibitor, and floor-plate ventralization through Shh signalling activated by small molecule agonism. This yielded a population of enriched mDA progenitors, which has been shown to be vitally important in mouse graft outcome^{34,35}.

Enriched mDA progenitors were subsequently differentiated into enriched mDA TH-positive neurons (>80%) after day 41, using a combination of two molecules (a ROCK inhibitor and a Notch

inhibitor) to allow the mDA NPCs to survive and exit the cell cycle, promoting differentiation into post-mitotic mDA neurons. Diverging from established methods, the mDA NPCs successfully differentiated into enriched mDA neurons without the use of any neurotrophic growth factors³⁴, improving the cost-effectiveness of this approach. Single-cell sequencing identified seven neuronal clusters, which expressed key markers of mDA neurons, and a further five clusters with key markers of midbrain NPCs. RNA velocity and latent time analyses^{20,36} revealed the developmental trajectories within the culture, with NPC clusters representing early cell types that were predicted to generate mDA clusters, of varying identities. Furthermore, we identified lists of genes that were associated with these trajectories, which can be further used to study in vitro midbrain neuronal development^{37,38}. Our mDA neurons displayed functional properties including calcium channel activity, functional DAT activity, and the synthesis, metabolism and secretion of dopamine. The mDA neurons also display typical neuronal electrophysiological behaviour, pre- and postsynaptic currents, and mature into functional neuronal networks. Differentiating hiPSCs from patients with PD yielded highly enriched mDA neurons of similar molecular and functional identity as control hiPSC-derived mDA neurons, confirming that this differentiation approach may be used to generate models of disease.

In vivo and in vitro models of PD have revealed several putative mechanisms that may cause neuronal toxicity in disease, but virtually all models exhibit several forms of cellular stress occurring simultaneously. We harnessed the developmental nature of the hiPSC system to assess the temporal sequence of events that unfold in the context of SNCA mutations, in order to distinguish early, and likely causative events in the cell, from late bystander events. The critical hallmark of synucleinopathy, which is found in the majority of sporadic cases, and therefore the key phenotype for a model to recapitulate, is the detection of aggregated forms of α -synuclein in neurons. Aggregate load in A53T patient lines are reported to be increased due to the mutation³⁹, and in SNCA x3 patient lines, are higher due to an increase in cellular α -synuclein³⁹. Aggregates have been reported at day 35 in mDA cultures⁴⁰. We have previously used single-molecule and super-resolution approaches¹³, to detect the formation of the earliest small soluble oligomers outside cells and within cells, and we defined the most toxic aggregate species as a small soluble oligomer with cross β -sheet structure^{26,30,41}. Here, we applied highly sensitive approaches (super-resolution microscopy) to the SNCA mDA neurons to define when aggregation starts. Small oligomeric species of α -synuclein were detected early into differentiation (day 27), prior to the molecular and functional specification of midbrain dopaminergic neurons, but after the expression of SNCA increased from NPC stage. Both the number and size of these small oligomeric aggregates are higher in SNCA A53T and SNCA x3 PD lines, and, furthermore, a specific conformation of α -synuclein, that is, the β -sheet-rich α -synuclein

a > Day 48: Late phenotypes


oligomers, occurs at early stages. These small oligomers are highly hydrophobic and their accumulation is likely to be responsible for the toxicity to cells^{27,42,43}. Abnormal aggregation of α -synuclein was a persistent phenomenon, and phosphorylated α -synuclein puncta were apparent using diffraction-limited microscopy from day 41 of differentiation, and the accumulation of phosphorylated forms progressed over time in culture. Finally, conformation-

specific antibodies detected fibrillar forms of α -synuclein at later time points, to day 62 of differentiation.

The hydrophobic nature of the oligomer is known to induce a range of cellular stresses, due to its ability to insert and disrupt membranes^{44,45}. Notably, the earliest functional phenotype observed in this model is calcium dysregulation at day 34–41 of differentiation. We noted higher basal levels of cytosolic calcium, an increased calcium influx on stimulation, and a delayed calcium

Fig. 5 α -synuclein aggregation and calcium dysregulation persist in older mDA neurons. **a** Representative traces showing the Fura-2 ratio in response to 50 mM KCl at day 48 of differentiation in control neurons, A53T neurons, and *SNCA* x3 neurons. **b** Quantification of the basal calcium ratio ($[Ca^{2+}]_i$) before KCl stimulation (**** $P < 0.0001$, one-way ANOVA). **c** Quantification of the rate of calcium ($[Ca^{2+}]_i$) recovery in response to KCl (**** $P < 0.0001$, one-way ANOVA). **d** Representative time series snapshots of >day 48 control and A53T neurons loaded with Fluo-4 (green) and X-Rhod-1 (magenta) (scale bar = 10 μ m). **e** Representative single-cell trace showing delayed recovery of Fluo-4 after KCl stimulation in patient mDA neurons. **f** Quantification of the normalised rate of recovery of Fluo-4 after stimulation with KCl in >day 48-old neurons (** $P = 0.003$, **** $P < 0.0001$, one-way ANOVA). **g** Representative single-cell trace showing delayed recovery of X-Rhod-1 after KCl stimulation in patient mDA neurons. **h** Quantification of the normalised rate of recovery of X-Rhod-1 after stimulation with KCl (* $P < 0.05$, ** $P < 0.005$, one-way ANOVA). **i** Representative ICC images showing the expression of aggregated forms of α -synuclein recognised by a conformation-specific antibody, at day 62 of differentiation. Scale bar = 10 μ m. **j** Quantification of the normalised fluorescence intensity of aggregated forms of alpha-synuclein (**** $P < 0.0001$, one-way ANOVA). **k** Quantification of the average puncta size of the aggregated alpha-synuclein (** $P = 0.0082$, **** $P = 0.0007$, one-way ANOVA). **l** Quantification showing the number of aggregates per field of view (FOV) from mDA neuronal lysate at day 62 (** $P < 0.005$, Welch's *t* test). All values plotted as \pm s.e.m. All *N* numbers for each experiment can be found in Supplementary Table 5.

recovery in *SNCA*-PD mDA neurons. We have previously shown that the β -sheet-rich oligomers and not monomers are able to permeabilise cell membranes due to their lipophilic properties, and induce calcium fluxes, leading to increased cytosolic calcium in response to glutamate and KCl^{19,30}. Calcium dysregulation has also been reported in other synucleinopathy models, where it is reported that oligomers interact with receptors and calcium channels^{46,47}. Therefore, we suggest that toxic oligomeric species once formed at low concentrations inside the cell due to either an increase in the concentration of α -synuclein (*SNCA* x3) or a structural change encouraging aggregation (p.A53T) are responsible for early cellular dysfunction.

Mitochondria are fundamental for cellular function and homeostasis, in particular for buffering cytosolic calcium, and ATP generation, and are a large source of ROS generation²⁹. Impairment in calcium fluxes plays an important role in mitochondrial oxidant stress⁴⁸, highlighting the delicate balance between mitochondrial and cellular calcium homeostasis. We previously showed that oligomeric structures of α -synuclein interact with ATP synthase, causing mitochondrial dysfunction and early opening of the mitochondrial PTP, which causes neuronal death in *SNCA* x3 neurons¹³. Recent studies using seeding-based models have shown that aggregates interact with and disrupt organelles including mitochondria, autophagosomes and lysosomes, and that the process of aggregate formation drives cellular pathogenesis⁴⁹. Our work complements these findings, and suggests that endogenous unseeded aggregate formation also drives cellular pathogenesis.

Similarly, oligomers have been shown to induce complex I-dependent mitochondrial dysfunction through mitochondrial calcium, which induced swelling and cytochrome C release⁵⁰. A53T hiPSC-derived neurons exhibit an increase in nitrosative, and ER stress¹⁶, as well as mitochondrial dysfunction⁴⁰. Oligomers further induce the generation of aberrant ROS in both the cytosol and mitochondria^{13,18,30}. In this study, we observed abnormalities in mitochondrial function including a reduced membrane potential, abnormal mitochondrial calcium efflux, and fragmentation of the mitochondrial network. Cytosolic calcium fluxes induced rapid mitochondrial membrane depolarisation, reflecting early PTP opening induced by mitochondrial calcium overload. Oxidative stress was evident, based on aberrant generation of superoxide, with a concomitant reduction in glutathione, by day 48 of differentiation.

Autophagy maintains cellular function through lysosome-dependent degradation of damaged organelles or aggregates⁵¹. In addition to mitochondrial and oxidative stress at a similar time point, we detected a swelling of the lysosomes in the *SNCA* A53T lines. α -synuclein-dependent impairment of lysosomal capacity has been previously reported¹⁷. In addition to lysosomal alterations, high-resolution microscopy revealed *SNCA*-PD mDA neurons exhibit an increase in autophagosomes that are in close physical contact with fragmented mitochondria, similar to previous

studies⁵². Correct electrophysiological properties are vital for neuronal health and function. We found that both *SNCA* mutant lines displayed abnormal AP characteristics, highlighting hypoexcitability as a functional consequence of *SNCA* mutations, similar to other neurodegenerative diseases^{32,33}.

Our results support a mechanistic hypothesis that in the disease process, abnormal α -synuclein leads to three major effects in the cell: (i) β -sheet-rich oligomeric species disrupt cellular membranes resulting in early cytosolic calcium phenotypes, (ii) oligomers induce disruption of mitochondrial function, oxidative stress and fragmentation of the mitochondrial network, and (iii) a lysosomal response to potentially clear the misfolded α -synuclein. Later, the accumulation of both damaged mitochondria and misfolded protein stimulates an autophagic response in the *SNCA* models, which leads to functional excitability abnormalities.

In summary, we successfully generated highly enriched populations of mDA neurons from hiPSCs, that express mDA markers, functional dopamine transport and form neuronal networks. By enriching the cell of interest in patient-derived lines with *SNCA* mutations, we were able to delineate that the earliest abnormality. Our work leads us to understand more generally how small hydrophobic aggregates with a specific β -sheet conformation form early in the neuronal life cycle and can be associated with dysregulation of calcium fluxes and therefore physiological signalling. This is then later associated with cellular stress pathways involving mitochondria and oxidative stress, and affecting protein clearance. Such processes may thus be relevant in all synucleinopathy rather than only the subset of familial PD. Dissecting the temporal sequence of pathological events revealed the first and critical driver of pathogenesis, and subsequent organellar impairment, is the development of toxic protein aggregates.

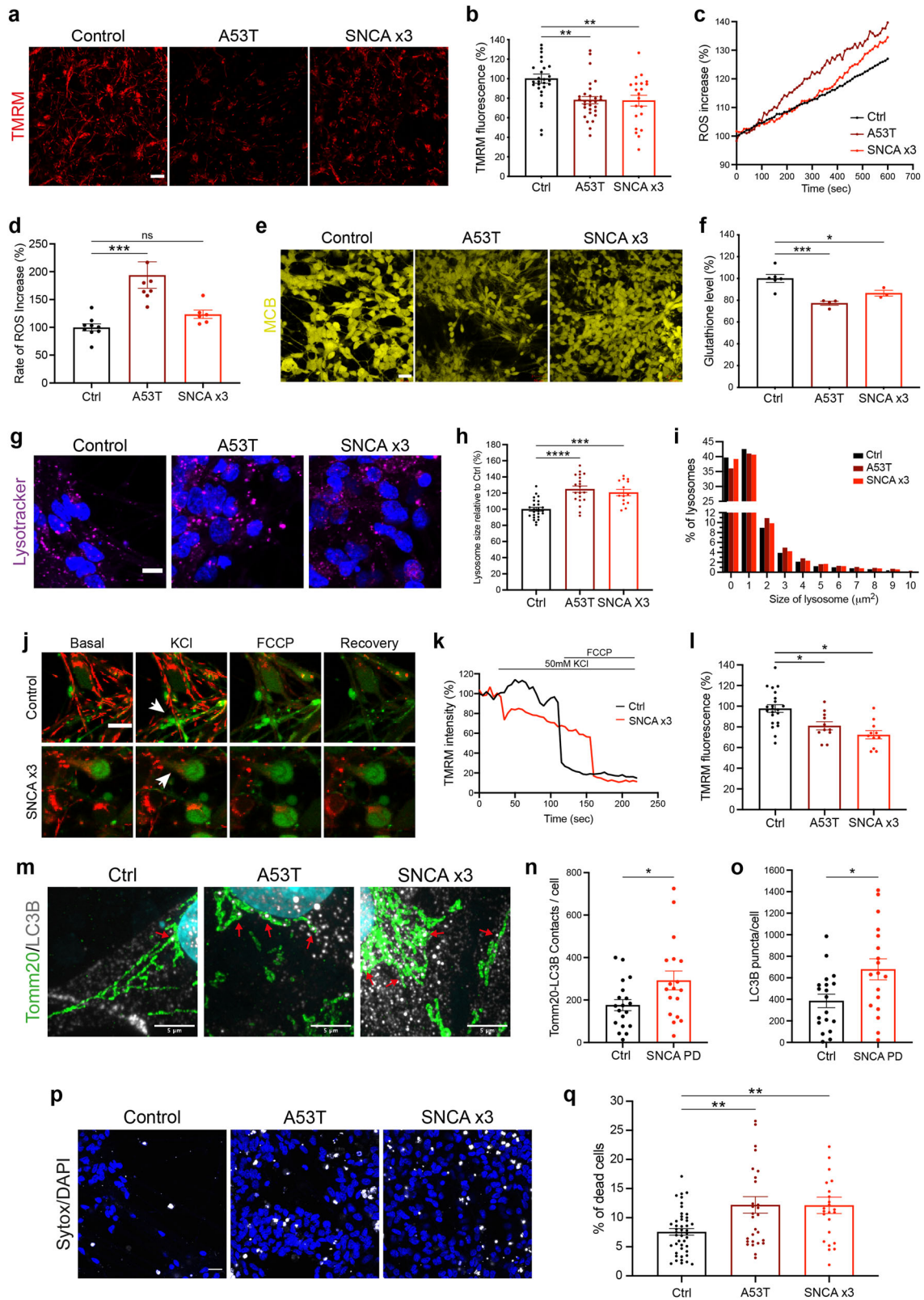
METHODS

Human-induced pluripotent stem cell culture

Human-induced pluripotent stem cells (hiPSCs) were maintained in feeder-free monolayers on Geltrex (ThermoFisherScientific) and fed daily with Essential 8 medium (Life Technologies) or mTeSR 1 (StemCell Technologies). When confluent, hiPSCs were passaged using 0.5 mM EDTA (Life Technologies). All cells were maintained at 37 °C and 5% carbon dioxide. The isogenic control line of *SNCA* A53T was generated using CRISPR/Cas9 editing by Applied StemCell Inc. (USA, project ID: C1729). The isogenic control line of *SNCA* x3 was kindly provided from the Kunath lab and generated using CRISPR/Cas9 editing as published⁵³. All hiPSC lines used in this study are described in Supplementary Table 1.

Midbrain dopaminergic neuron (mDA) differentiation

For all mDA differentiation, hiPSCs were grown to 100% confluency. Media for differentiation was prepared in two separate bottles as:



DMEM/F12 + N2 supplement (17502048), MEM non-essential amino acids (5 ml per 1000 ml), β -mercaptoethanol, 5 μ g/ml insulin (Sigma) and Neurobasal (phenol red free) + B27 supplement (17504044), L-glutamine (5 ml per 1000 ml), 50 U/ml penicillin–streptomycin, (all from ThermoFisherScientific). Differentiation was triggered by

removing old media and replacing it with a 1:1 mix of the DMEM/F12 + N2 and Neurobasal + B27 medias termed “N2B27”. Cells were patterned for 14 days with daily media changes. For the first 2 days, the media was supplemented with the small molecules 5 μ M SB431542 (Tocris Bioscience), 2 μ M Dorsomorphin (Tocris

Fig. 6 Cellular dysfunction and cell death arise later in SNCA PD mDA neurons. **a** Representative live-cell imaging of mitochondrial fluorescence using the lipophilic cationic dye TMRM at day 48 of differentiation. Scale bar = 10 μm . **b** Quantification of the normalised fluorescence intensity of TMRM (** $P < 0.005$, one-way ANOVA). **c** Trace showing the ratiometric measurement of superoxide generation using dihydroethidium (HET) at day 48 of differentiation. **d** Quantification of the rate of superoxide generation based on HET ratiometric fluorescence (ns $P > 0.05$, *** $P < 0.0005$, one-way ANOVA). **e** Representative live-cell imaging of endogenous glutathione using the fluorescent reporter MCB at day 48 of differentiation. Scale bar = 20 μm . **f** Quantification of the endogenous level of glutathione based on MCB fluorescence (* $P < 0.05$, *** $P = 0.0009$, one-way ANOVA). **g** Representative live-cell imaging of lysosomes and nuclear marker Hoechst 33342 at day 48 of differentiation (scale bar = 5 μm). **h** Quantification of the normalised average lysosomal area/size (*** $P = 0.0002$, **** $P < 0.0001$, one-way ANOVA). **i** Histogram plot showing the percentage of total lysosomes in each set area bin (0–10 μm^2). **j** Representative time series snapshots of TMRM (red) and Fluo-4 (green) in day 62 old neurons showing the response to KCl and FCCP. The arrow in the control cell highlights polarised mitochondria and calcium response to KCl and FCCP. Arrowhead in the SNCA x3 cell highlights KCl-induced TMRM intensity decrease. Scale bar = 10 μm . **k** Representative single-cell trace showing TMRM intensity in response to KCl and FCCP in control and SNCA x3 day 62 old neurons. **l** Quantification showing the decrease in TMRM intensity after KCl stimulation in control, A53T and SNCA x3 neurons (* $P < 0.05$, one-way ANOVA). **m** Instant Structured illumination microscopy (iSIM) images of control, A53T, and SNCA x3 day 55 neurons probed for mitochondrial marker Tomm20, and the autophagosome marker LC3B. Scale bar = 5 μm . **n** Quantification of the number of Tomm20-LC3B colocalizations per cell (* $P < 0.05$, Welch's t test). **o** Quantification of the number of LC3B puncta per cell (* $P < 0.05$, Welch's t test). **p** Live-cell images depicting dead cells in mDA neurons at >day 48 of differentiation using the fluorescent dye SYTOX green (scale bar = 20 μm). **q** Quantification of the percentage of dead cells (** $P < 0.005$, one-way ANOVA). All values are plotted as \pm s.e.m. All N numbers for each experiment can be found in Supplementary Table 5.

Bioscience), 1 μM CHIR99021 (Miltenyi Biotec). On day 2, 1 μM Purmorphamine (Merck Millipore) was added. On day 8, CHIR99021, and SB431542 were removed leaving only Dorsomorphin and Purmorphamine in the medium until day 14. Cells were enzymatically dissociated and split on days 4, 10 and 14 using 1 mg/ml of Dispase (ThermoFisherScientific). After patterning, mDA neuronal precursor cells (NPCs) were maintained in N2B27 for 4 days. On day 19, cells were plated onto Geltrex pre-coated Ibidi 8-well chambers (100k/well), clear bottom 96-well plates (50k/well), or 12-well plates (500k/well), and terminally differentiated using N2B27 supplemented with 0.1 μM Compound E (Enzo Life Sciences) and 10 μM Y-27632 dihydrochloride (Rho kinase ROCK inhibitor) (Tocris) from day 20 for the whole duration of terminal differentiation, with two weekly media changes. For super-resolution microscopy, cells were plated on glass-bottom Ibidi eight-well chambers which were pre-coated with poly-D-lysine (PDL) overnight, followed by laminin (Sigma, L2020) in PBS for 1 h. Protocol DOI can be found in Supplementary Table 7.

Immunocytochemistry (ICC)

For ICC, cells at the desired time point of differentiation had the media removed, followed by one wash in PBS, and fixed with 4% paraformaldehyde for 15 min at room temperature (RT). The paraformaldehyde was then removed, and cells were washed once in PBS. For the LC3B antibodies, samples were incubated in -20°C methanol after paraformaldehyde fixation. All samples were then blocked for non-specific binding and permeabilized in 5% bovine serum albumin (BSA) (Sigma) + 0.2% Triton X-100 (Sigma) in PBS for 60 min. The primary antibodies were then made up to the desired dilution (Supplementary Table 2) in 5% BSA and applied to the cells overnight at 4°C . The cells were then washed twice in PBS followed by the application of species-specific, secondary antibodies conjugated to relative AlexaFluor dyes (Supplementary Table 2), at a 1:500 dilution made up in 5% BSA to cells for 60 min at RT in the dark. After secondary antibody incubation, cells were washed once in PBS before being stained with 4',6-diamidino-2-phenylindole nuclear stain (DAPI) in PBS for 5 min at a 1:1000 dilution. After DAPI incubation, cells were washed once with PBS before being submerged in a fluorescence mounting medium (Dako), and stored at 4°C until imaging.

The samples were imaged using Zeiss 880 confocal system with a 40 \times , 1.4 N.A. oil objective, and a pinhole of one airy units (AU). Between 3 and 5 images were collected per sample, all with a Z projection consisting of five slices, and displayed as a maximum projection. Samples were also imaged using the PerkinElmer Opera PhenixTM High Content Screening System with $\times 20$ and $\times 40$ water objective lenses. A minimum of five

fields of view and a Z projection of 3 slices was acquired per well, with the images displayed as a maximum projection. The accompanying software, ColumbusTM was used to store and analyse acquired images (<https://biii.eu/columbus-image-data-storage-and-analysis-system>). The settings for the acquisition of images were kept the same for all samples in the experiment set.

ELISA assay

To determine the concentration of alpha-synuclein oligomer, cell lysates were mechanically collected at various timepoints and stored at -80°C . Oligomeric alpha-synuclein was analysed using the Human α -synuclein oligomer (non-A4 component of amyloid precursor) ELISA kit (CSB-E18033h, CUSABIO) according to the manufacturer's instructions. The levels of oligomeric alpha-synuclein were normalised to the total protein concentration, as determined by the DC Protein Assay (Bio-Rad).

RNA extraction and quantitative polymerase chain reaction (qPCR)

RNA was harvested from snap-frozen cell pellets using the Maxwell[®] RSC simply RNA Cells kit (Promega), and the accompanying Maxwell[®] RSC 48 instrument. After RNA extraction, the RNA concentration and quality using the 260/280 ratio were assessed using the nanodrop. Up to 1 μg of RNA was retro-transcribed into cDNA using the High-Capacity cDNA Reverse Transcription kit (ThermoFisherScientific). The qPCR was performed using TaqManTM Gene Expression Assay (ThermoFisherScientific). For each gene, TaqManTM probes were used (Supplementary Table 3) along with the TaqManTM master mix, and sample cDNA following the manufacturer's protocol. Samples, along with a minus reverse transcriptase control (-RT) were ran for each gene on the QuantStudio 6 Flex Real-Time PCR System (Applied Biosystems). The -RT served as a negative control, and the gene expression levels were normalised to the housekeeping gene GAPDH following the delta-delta Ct method. Gene expression values were expressed as the normalisation to either hiPSCs or mDA NPCs.

Single-cell RNA-seq

Single-cell generation, cDNA synthesis, library construction and sequencing protocol. After 48 days of differentiation, mDA neurons from 3 control hiPSC lines were washed with PBS once, and then incubated with Accutase (GibcoTM) for 5 min to obtain a single-cell suspension. The samples were then diluted 1/3 before usage. The quality and concentration of each single-cell

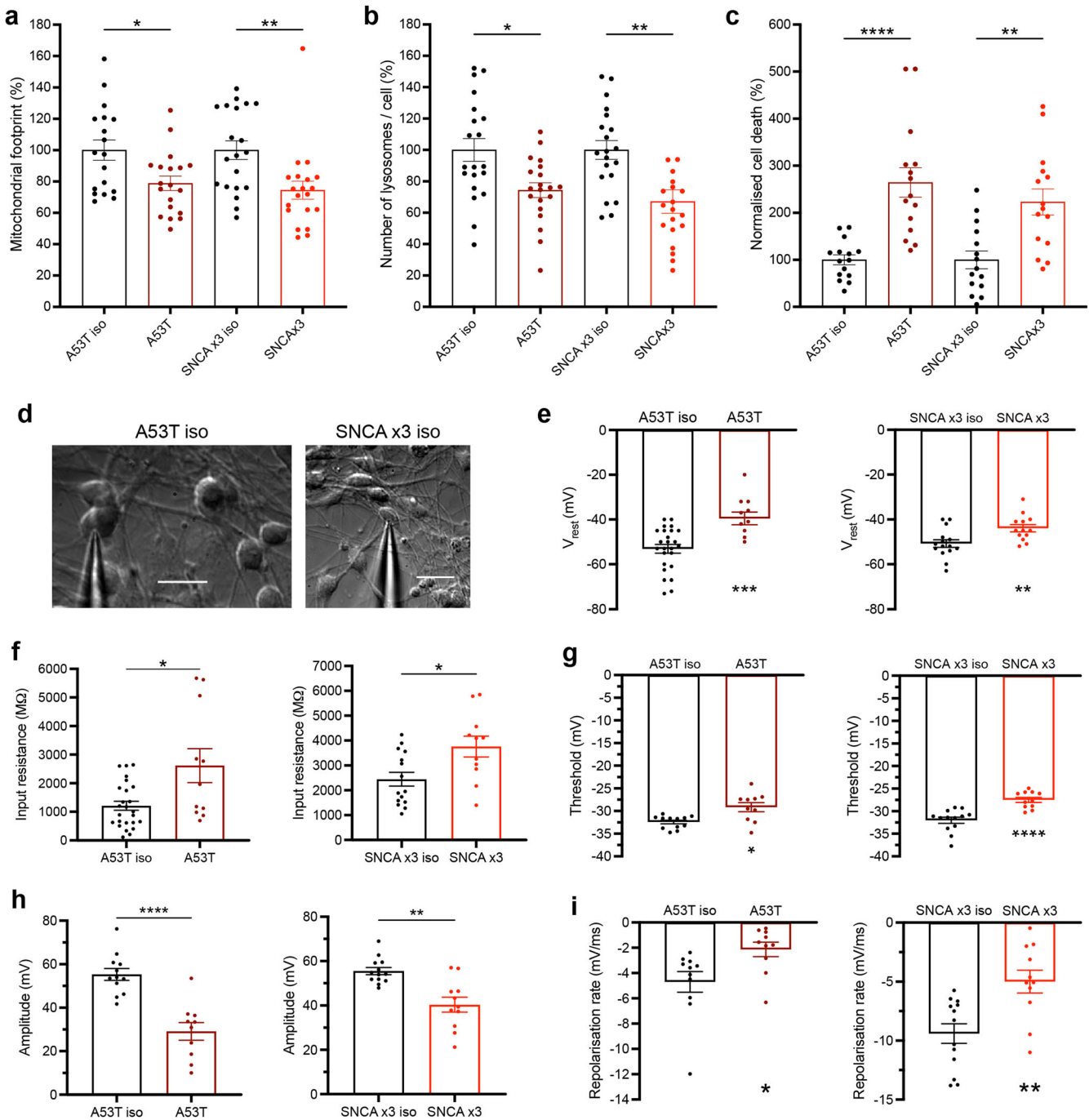


Fig. 7 Functional consequences of SNCA mutations in human mDA neurons. **a** The normalised basal mitochondrial footprint measurement plotted out in control, A53T, and SNCA x3 >day 62 old neurons ($*P < 0.05$, $**P < 0.005$, one-way ANOVA). **b** The normalised basal number of lysosomes per cell in controls, A53T and SNCA x3 >day 62 old neurons ($*P < 0.05$, $**P < 0.005$, one-way ANOVA). **c** The normalised percentage of cell death in control, A53T, and SNCA x3 >day 62 old neurons ($**P < 0.005$, $****P < 0.0001$ one-way ANOVA). **d** Representative bright-field images showing >day 70 neurons patched for electrophysiological recordings. Scale bar = 20 μm . **e** Quantification of electrophysiological recordings showing the resting membrane potential in control and A53T neurons, and control and SNCA x3 neurons ($**P = 0.0068$, $***P = 0.0008$, Welch's t test). **f** Quantification of electrophysiological recordings showing the input resistance in control and A53T neurons, and control and SNCA x3 neurons ($*P < 0.05$, Welch's t test). **g** Quantification of the threshold for AP generation in control and A53T neurons, and control and SNCA x3 neurons ($*P < 0.05$, $****P < 0.0001$, Welch's t test). **h** Quantification of the AP amplitude in control and A53T neurons, and control and SNCA x3 neurons ($**P < 0.005$, $****P < 0.0001$, Welch's t test). **i** Quantification of the AP repolarisation rate in control and A53T neurons, and control and SNCA x3 neurons ($*P < 0.05$, $**P < 0.005$, Welch's t test). All values are plotted as \pm s.e.m. All N numbers for each experiment can be found in Supplementary Table 5.

suspension was measured using Trypan blue and the Eve automatic cell counter. Each sample presented a concentration between a 1200–1700 cell/ μl and viability ranged between 55 and 68%, samples with a viability above 57% were used for

sequencing. Approximately 10,000 cells were loaded for each sample into a separate channel of a Chromium Chip G for use in the 10X Chromium Controller (cat: PN-1000120). The cells were partitioned into nanoliter scale Gel Beads in emulsions (GEMs) and

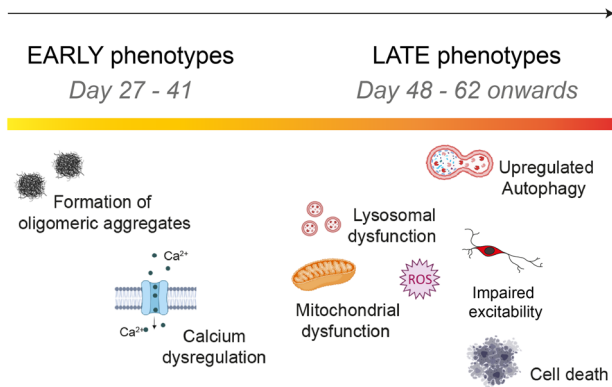


Fig. 8 Cellular phenotypes sequentially appear in mDA neurons.

A schematic illustration showing temporal sequence of cellular phenotypes in the human PD model. The earliest abnormality is the accumulation of small aggregates with a specific beta-sheet conformation (at day 27 of differentiation). This is followed by another early phenotype which is impaired calcium signalling by day 34 of differentiation. When mDA neurons spend longer in culture, only after day 48, mitochondrial dysfunction, oxidative stress, and lysosomal dysfunction appear as late phenotypes, as well as, upregulated autophagy, impaired excitability and cell death.

lysed using the 10x Genomics Single Cell 3' Chip V3.1 GEM, Library and Gel Bead Kit (cat: PN-1000121). cDNA synthesis and library construction were performed as per the manufacturer's instructions. The RNA was reversed transcribed and amplified using 12 cycles of PCR. Libraries were prepared from 10 μ l of the cDNA and 13 cycles of amplification. Each library was prepared using Single Index Kit T Set A (cat: PN-1000213) and sequenced on the HiSeq4000 system (Illumina) using 100 bp paired-end run at a depth of 65–100 million reads. Libraries were generated in independent runs for the different samples.

Pre-processing single-cell RNA-seq (scRNA-seq) data. Using the Cell Ranger (RRID:SCR_017344, <https://support.10xgenomics.com/single-cell-gene-expression/software/pipelines/latest/what-is-cell-ranger>) v3.0.2 Single-Cell Software Suite from 10X Genomics reads were aligned to the human reference genome (Ensembl release 93, GRCh38) (<https://support.10xgenomics.com/single-cell-gene-expression/software/pipelines/latest/what-is-cell-ranger>). The analysis was carried out using Seurat (RRID:SCR_016341) v3.1.0^{54,55} (https://satijalab.org/seurat/get_started.html) in R-3.6.1 (R Core Team, 2019 (RRID:SCR_001905, <http://www.r-project.org/>)). The code used for analysis has been deposited online: (<https://doi.org/10.5281/zenodo.7260558>), (https://github.com/strohstern/Transcriptomic_signatures_iPSC_derived_dopamine_neurons). Cells expressing fewer than 200 genes were excluded from the subsequent analysis. Using default parameter within Seurat v3.1.0^{54,55} data for each sample were normalised across cells using the 'LogNormalize' function with a scale factor of 10,000. A set of highly variable genes was identified using the 'FindVariableFeatures()' function (selection.method = "vst", nfeatures = 2000). Data were centred and scaled using the 'ScaleData()' function with default parameters. Using the highly variable genes, PCA was performed on the scaled data and the first 30 principal components were used to create a Shared Nearest Neighbour (SNN) graph using the 'FindNeighbors()' function (k.param = 20). This was used to find clusters of cells showing similar expression using the 'FindClusters()' function across a range of clustering resolutions (0.2–1.4 in 0.2 increments). Based on the visualisation of average mitochondrial gene expression across different cluster resolutions using the R package Clustree v0.4.1 (RRID:SCR_016293, <https://CRAN.R-project.org/package=clustree>)⁵⁶ we selected a

clustering resolution of 1.0 to exclude cluster with an average mitochondrial gene expression above 7.5% and, concomitantly, an average number of detected features below 1300.

Integration across samples. After filtering of cells/clusters based on mitochondrial gene expression and the number of detected features, we integrated the three samples using the standard workflow from the Seurat v3.1.0 package⁵⁵. After data normalisation and variable feature detection in the individual samples (see above), anchors were identified using the 'FindIntegrationAnchors()' function and datasets were integrated with the 'IntegrateData()' across 50 dimensions for all detected features in the datasets. We then performed dimension reduction (PC1–45) and cluster identification at resolutions 1.4. After removal of a cluster consisting mostly of suspected doublet cells identified using DoubletFinder⁵⁷, we performed data scaling including cell cycle score regression, dimension reduction (PC1–50) and cluster identification (resolutions 0.4–1.8).

Biomarker of each cluster were identified using Seurat's 'FindAllMarkers()' function using the Wilcoxon rank sum test. We limited the test to positive markers for each cluster in comparison to all remaining cells. The positive marker genes had to be detected in 25% of cells in either of the two groups, with limiting testing further to genes which show, on average, at least 0.25-fold difference (log-scale) between the two groups of cells. Cluster identity was determined using visual inspection focusing on the expression of known marker genes.

RNA velocity estimation. For RNA velocity analysis, the spliced and unspliced reads were counted with alevin⁵⁸ as recommended⁵⁹. The count matrices were added to the pre-existing Seurat object which was subsequently used as input into scVelo (v0.2.2, RRID:SCR_018168, <https://github.com/theislab/scvelo>) to calculate RNA velocity values for each gene of each cell. scVelo was used in the "dynamical" mode with default settings. The resulting RNA velocity vector was embedded into the PCA and UMAP space by translating the RNA velocities into likely cell transitions using cosine correlation to compute the probabilities of one cell transitioning into another cell. We identified driver genes, i.e., those genes that show dynamic behaviour, as those genes with a fit likelihood in the dynamical model >0.3. We also used PAGA³⁶ to perform trajectory inference for which directionality was inferred from the RNA velocities.

Flow cytometry

The protocol for immunolabelling cells for flow cytometry analysis was adapted from a previous study⁶⁰. Cells were washed once with PBS, before being detached into a single-cell suspension using Accutase (GibcoTM). A cell suspension of 500 k/ml was prepared in media. Cells were then centrifuged at 200 \times g for 5 min, and the supernatant was removed. Cell pellet was resuspended gently in 4 ml of 4% paraformaldehyde and briefly vortexed at a low speed before being rotated on a rotation spinner for 10 min at RT. After fixation, samples were centrifuged (200 \times g for 5 min) and supernatant removed. Cells were resuspended in 2 ml of 0.1% BSA in PBS. After resuspension, cells were filtered through a 70 μ m strainer (Miltenyi Biotec) to filter out any cell clumps. Cells were then centrifuged (200 \times g for 5 min), and the supernatant was removed. Cell pellets were then resuspended in 1 ml of permeabilization/blocking buffer (0.1% Triton X-100, 1% BSA, 10% normal goat serum (Sigma) in PBS), and incubated on a rotation spinner for 30 min at RT. After permeabilization/blocking, cells were centrifuged (200 \times g for 5 min) and the supernatant was removed. Cells were then resuspended in the primary antibodies (1:200) made up in 0.1% BSA in PBS, and incubated on the rotation spinner for 1 h at RT. After primary antibody incubation, cells were centrifuged (200 \times g

for 5 min), the supernatant removed and washed once in 0.1% BSA in PBS. They were then resuspended in the species-specific secondary antibodies (AlexaFluor 488, 647) at a dilution of 1:500 made up in 0.1% BSA in PBS and incubated in the dark on a rotation spinner for 30 min. After incubation, cells were centrifuged ($200 \times g$ for 5 min), the supernatant removed and washed once in PBS, followed by incubation with DAPI made up in PBS for 5 min. The DAPI + PBS was then removed, followed by one wash in PBS, before being analysed on the flow cytometer.

The samples were run on the LSRII (BD) cell sorter. Scattering was initially used to discard debris as well as cell doublets and larger clumps. The single-cell population was then gated to include DAPI-positive only cells (negative control). The gating threshold for measured channels was determined using the control lacking the antibody of interest (Fluorescence minus one (FMO) control), for both channels being recorded. Once the parameters had been set, 10,000 cell events were recorded, and data were processed and analysed on FlowJo (RRID:SCR_008520, <https://www.flowjo.com/solutions/flowjo>).

Proteomic sample preparation and analysis

In total, 50 μg of lysate from day 55 mDA neurons was taken for proteomic analysis and processed using S-Trap assisted digestion as explained⁶¹ (protocols.io DOI can be found in Supplementary Table 7). Briefly, proteins were reduced by adding final 10 mM TCEP and incubated the samples on a Thermomixer at 60 °C for 30 min at an agitation of 1200 rpm. Samples were brought to room temperature and alkylated by adding 40 mM Iodoacetamide and incubated on a Thermomixer in dark at room temperature for 30 min at an agitation of 1200 rpm. Further, the SDS concentration was adjusted to 5% vol/vol (final) followed by final 1.2% Vol/vol phosphoric acid was added and processed for the sample clean-up using S-Trap micro columns. Six times the volume of samples, the S-Trap buffer (90% methanol in 100 mM TEABC) was added and loaded on to the S-Trap column for removal of SDS or traces of any reagents by centrifugation at $1000 \times g$ at room temperature for a minute. 160 μl of S-Trap wash buffer was added for further clean-up and a total of four washes were given. S-Trap columns were transferred to a new 1.5 ml protein lo-binding Eppendorf tubes for an on-column tryptic digestion, 3.3 μg of Trypsin + Lys-C in 50 μl of 50 mM TEABC buffer was added to the column and subjected to a brief centrifugation ($100 \times g$ for 30 s) the flow through was transferred back to the column and incubated on a Thermomixer at 47 °C for 1.5 h, followed by an overnight incubation at room temperature. Peptides sequentially were eluted by adding 80 μl of 50 mM TEABC buffer, 0.15% (vol/vol) formic acid and 80% (vol/vol) Acetonitrile in 0.15% formic acid respectively by centrifuging at $1000 \times g$ for a minute at each elution step. The eluate was snap-frozen on dry ice and subjected to Speedvac to dryness. Peptides were further stored in -20 freezer until LC-MS/MS analysis. A 2 μg of peptide digest from each sample ($n = 22$) was pooled and subjected High-pH RPLC fractionation as described⁶¹. To generate a spectral library for Data-Independent Acquisition (DIA) analysis. A total of 46 fractions were prepared for LC-MS/MS analysis.

LC-MS/MS analysis: Peptides were dissolved in LC buffer (3% ACN (vol/vol) in 0.1% formic acid (vol/vol)). In total, 2 μg of a peptide from each sample was transferred to LC vial for mass spectrometry analysis on Orbitrap Exploris 480 mass spectrometer in line with Dionex 3000 RSLC nanoliquid chromatography system. Peptides were loaded on to a pre-column (C18, 5 μm , 100 Å , 100 μm , 2-cm nano-viper column # 164564, Thermo Scientific) at 5 $\mu\text{l}/\text{min}$ flow rate and separated on a 50 cm analytical column (C18, 5 μm , 50 cm, 100 Å Easy nano spray column # ES903, Thermo Scientific) at 250 nl/min flow rate by applying non-linear gradient of solvent-B (80% ACN (v/v) in 0.1% formic acid (v/v) for about 125 with a total gradient time and run time of 145 min. The

data were acquired in data-independent acquisition (DIA) mode. Full MS is acquired at 120,000 resolution m/z 200 and measured using Orbitrap mass analyser. The MS2 precursor ions were fragmented using stepped higher energy collisional dissociation (HCD) energies, 25, 28 and 32 and were acquired at 30,000 resolution at m/z 200 and measured using Orbitrap mass analyser. We employed a variable isolation window for MS2-DIA data, a total of 45 vDIA windows were enabled covering the mass range of 350 to 1500 m/z , the details of variable DIA isolation window values are provided in Supplementary table 6. The AGC target for MS1 and MS2 were set at 3000% and ion-injection times were set at 30 ms and 70 ms, respectively.

The spectral library was generated by pooling all samples and generated 46 High-pH RPLC fractions and these were acquired in a Data-dependent Acquisition (DDA) mode on Orbitrap Exploris 240 mass spectrometer. The peptides were separated on a 50 cm analytical column by applying a non-linear gradient for 85 min with a total run time of 100 min. Full MS is acquired at 60,000 resolution at m/z 200 and measured using Orbitrap analyzer in the mass range of 375–1500 m/z . M/MS data were acquired by employing top speed for 2 s in a data-dependent mode at 15,000 resolution at m/z 200 and measured using Orbitrap mass analyser. The quadrupole mass filter isolation window was set to 1.2 m/z and precursor ions were fragmented using normalised HCD of 30%. The AGC target for MS was set at 300% and MS/MS was set as standard and maximum ion injection was set in auto mode. The dynamic exclusion duration was set for 45 s.

Mass spectrometry data analysis: The DDA spectral library data was searched with Biognosys Spectronaut pulsar (version: 14.0)⁶² (<https://biognosys.com/software/spectronaut/>). In total, 46 bRPLC fractions were searched against the Human Uniprot database (Downloaded: 2021/03/16) (Proteome ID: UP000005640). Default search parameters for spectral library generation was used including the data filtered for 1% FDR. The DIA data was searched using Biognosys Spectronaut pulsar software suite (version: 16.0.220606.5300)⁶² (<https://biognosys.com/software/spectronaut/>) against a spectral library generated from the DDA data and Human Uniprot database (proteome ID: UP000005640). Trypsin as a protease with a maximum of two missed cleavages were allowed and Carbamidomethylation of Cys as a fixed modification and Protein N-ter Acetylation and Oxidation of Met were set as variable modifications. The data was filtered for 1% FDR and the protein group Output files were further processed using Perseus software suite⁶³ (RRID:SCR_015753, <http://www.perseus-framework.org>), and protein copy numbers were estimated using Proteomic ruler plugin within Perseus as described⁶⁴.

High-performance liquid chromatography (HPLC) and sample preparation

The mDA neurons from three independent hiPSC lines were at day 41 and day 48 of differentiation were incubated in phenol-free “N2B27” medium for 24 h with and without the presence of 80 μM L-Dopa (Sigma D9628). For extracellular metabolites, media after 24 h was mixed 1:1 in 0.8 M ice-cold perchloric acid. Samples were incubated on ice for 10 min, followed by centrifugation at $12,000 \times g$ for 5 min at 4 °C. The supernatant was removed and frozen in dry ice for HPLC analysis. For intracellular metabolites, after 24 h, the cells were removed and pelleted by centrifugation at $1200 \times g$ for 5 min. The cells were washed once in PBS and lysed on ice using lysis buffer (10 mM Tris (pH 7.4), 1 mM EDTA, 320 mM sucrose in HPLC grade water). The lysate was mixed with 1:1 in 0.8 M ice-cold perchloric acid and incubated on ice for 10 min. The samples were centrifuged at $12,000 \times g$ for 10 min and the supernatant was harvested and frozen for HPLC analysis.

Quantification of neurometabolites (DOPAC, 3-OMD, 5-HIAA, HVA and dopamine) was carried out using reverse phase HPLC and an electrochemical detector following a method by⁶⁵. The mobile phase (flow rate 1.5 ml/min) contained 16% methanol,

20 mM sodium acetate trihydrate, 12.5 mM citric acid monohydrate, 3.35 mM 1-octanesulfonic acid, 0.1 mM EDTA disodium and adjusted to pH 3.45 with 12 M hydrochloric acid (HCl). The stationary phase was maintained at 27 °C. The detector electrode was set at 450 mV and screening electrode at 50 mV. 50 µl of the sample was injected and calculated against a 500 nM external standard solution of the 5 compounds of interest made in HPLC grade water acidified with 12 M HCl. Peak areas were quantified with EZChrom Elite™ chromatography data system software, version 3.1.7 (<https://www.agilent.com/en-us/support/software-informatics/openlab-software-suite/openlab-cds/ezchromelite320>) (JASCO UK Ltd., Great Dunmow, UK).

Electrophysiology

Visualised patch-clamp recordings from cell cultures were performed using an infrared differential interference contrast imaging system and a Multipatch 700B amplifier controlled by pClamp 10.2 software package (Molecular Devices, USA) (RRID:SCR_011323). For the recordings, a neuronal culture on a glass coverslip was placed in a recording chamber mounted on the stage of an Olympus BX51WI upright microscope (Olympus, Japan). The perfusion solution contained the following (in mM): 119 NaCl, 2.5 KCl, 1.3 Na₂SO₄, 2.5 CaCl₂, 26.2 NaHCO₃, 1 NaH₂PO₄, 2 CaCl₂, 2 MgCl₂, 10 glucose (or 22 in some recordings) and was continuously bubbled with 95% O₂ and 5% CO₂, pH 7.4. Whole-cell recordings were performed at 32–34 °C; the patch-clamp pipette resistance was 3–7 MΩ depending on particular experimental conditions. Series resistance was monitored throughout experiments using a +5 mV step command, cells with very high series resistance (above 25 MΩ) or unstable holding current were rejected. The intracellular pipette solution for voltage-clamp experiments contained (in mM): 120.5 CsCl, 10 KOH-HEPES, 2 EGTA, 8 NaCl, 5 QX-314 Br⁻ salt, 2 Na-ATP, 0.3 Na-GTP. For current-clamp experiments, the intracellular solution contained (in mM): 126 K-gluconate, 4 NaCl, 5 HEPES, 15 glucose, 1 K₂SO₄ × 7 H₂O, 2 BAPTA, 3 Na-ATP. pH was adjusted to 7.2 and osmolarity adjusted to 295 mOsm. To isolate response of NMDA receptors we added to a perfusion solution: 50 mM picrotoxin, 20 mM NBQX, 1 mM strychnine, 1 mM CGP-55845, 100 mM MCPG, with zero Mg²⁺. To isolate response of GABA_A receptors, we added 50 mM APV, 20 mM NBQX, 1 mM strychnine, 1 mM CGP-55845, 100 mM MCPG. All chemicals were purchased from Tocris Bioscience. mDA neurons were tested as a subgroup of the set of generated cultures.

In the whole-cell (immediately after membrane breakthrough), iPSC-derived mDA neurons were recorded for the resting membrane potential (V_{rest}), membrane capacitance (C_m), the membrane time constant (τ_m), and input resistance (R_{in}), measured from the hyperpolarizing square current pulse steps in current mode, as described earlier^{32,33}. To assess the firing capability of the cells, a series of sub- and supra-threshold rectangular current pulses were applied to elicit neuronal firing, with a stepwise-increased stimulus intensity (an increment of 5–10 pA). The V_{rest} was set at -60 mV to -70 mV, by injecting a hyperpolarizing bias current where required. The analysis of the AP waveform was performed for the first AP only. The parameters of individual APs were: the spike amplitude (measured from the threshold to the peak), the threshold value, overshoot and the spike width (duration at half-maximal amplitude), the rates of depolarisation and repolarisation phases.

Live-cell imaging

To measure $[Ca^{2+}]_i$, cells were loaded with 5 µM of Fura-2 AM in HBSS for 30 min at room temperature, followed by 2x HBSS washes (Invitrogen). Cells were imaged using epifluorescence on an inverted microscope equipped with a 20x fluorite objective. The cells were excited sequentially at 340 and 380 nm using light

from a Xenon arc lamp. A time series with 1 or 5 s intervals was performed, establishing basal fluorescence before 50 mM KCl was added to depolarise the membrane. The emitted fluorescence was measured at 515 nm on a cooled camera device (CCD). The fluorescence intensity of the bound and unbound Ca²⁺ was then quantified using ratiometric analysis on Fiji ImageJ (RRID:SCR_002285, <http://fiji.sc>). $[Ca^{2+}]_i$ using Fura-2 AM was also imaged on a Nikon Ti2 inverted microscope with Perfect Focus System, an ASI motorised XY stage with piezo Z and an Okolab environmental chamber with a CO₂ mixer. Images were acquired using an Andor iXon Ultra897 EMCCD camera. Cells were excited with a Cairn FuraLED light engine optimised for 340 and 380 nm with a dichroic mirror T400lp (Chroma) and an emission filter ET510/80 m (Chroma), using a 40 × 1.3 NA S Fluor objective. The microscope was controlled with Micro-Manager v2.0⁶⁶ (RRID:SCR_000415, <http://micro-manager.org>).

To measure the level of antioxidant, reactive oxygen species (ROS), mitochondrial membrane potential, lysosomal dynamics, calcium uptake, mitochondrial calcium, and cell death, a confocal microscope (ZEISS LSM 710/880 with an integrated META detection system) which has illumination intensity limited to 0.1–0.2% of laser output to prevent phototoxicity was used.

The antioxidant level was measured using a glutathione indicator, 50 µM Monochlorobimane (mBCL, ThermoFisherScientific) which was incubated for 30 min and measured at 420–550 nm excited by a 405 nm laser. To measure mitochondrial membrane potential, cells were incubated with 25 nM tetramethylrhodamine methyl ester (TMRM, ThermoFisherScientific) in HBSS for 40 min and then imaging was acquired using Zeiss LSM 880 confocal microscope. The 560 nm laser line was used to excite and emission was measured above 560 nm. Approximately 3–5 fields of view with Z projections were taken per sample. To measure lysosomal dynamics, cells were incubated with 50 nM LysoTracker™ Deep Red (ThermoFisherScientific), and Hoechst 33342 in HBSS for 40 min and then imaged using Zeiss LSM 880 confocal microscope where the 405 nm, and 647 nm laser line were used to excite Hoechst 33342 and LysoTracker™ Deep Red, respectively. Approximately 4–5 fields of view with Z projections were taken per sample.

Calcium uptake and dynamics were assessed using the dye Fluo-4 AM (ThermoFisherScientific). Cells were incubated with 5 µM Fluo-4 AM in HBSS for 40 min, followed by two HBSS washes. For measuring mitochondrial calcium, cells were incubated with 2 µM X-Rhod-1 AM and Fluo-4 AM in HBSS for 40 min, followed by two HBSS washes. For measuring calcium and mitochondrial membrane potential, cells were loaded with Fluo-4 AM and 25 nM TMRM for 40 min, followed by two HBSS washes. 25 nM of TMRM was then re-added to cells prior to imaging. Live-cell imaging was performed excited by a 488 nm laser and measured at 520 nm. A time series with 5 s intervals was performed to establish basal fluorescence before 50 mM KCl was added to depolarise the membrane and measure fluorescence intensity increase, and recovery.

To measure cell death, live cells were incubated with 500 nM SYTOX™ Green Nucleic Acid Stain (ThermoFisherScientific), and the nuclear marker Hoechst 33342 for 40 min in HBSS. As SYTOX™ Green is impermeable to live cells, only dead cells were stained, whereas Hoechst 33342 labelled all cells. Cells were imaged using the Zeiss LSM 880 confocal microscope where the 405 nm, and the 488 nm laser line were used to excite Hoechst 33342 and SYTOX Green, respectively. Approximately 4–5 fields of view with Z projections were taken per sample.

To measure ROS, (mainly superoxide) a cooled camera device (CCD) was used, and data were obtained on an epifluorescence inverted microscope equipped with a 20x fluorite objective. Cells were loaded with 2 µM dihydroethidium (HEt, Molecular Probe) in HBSS. A time series with 5–10 s intervals was performed. We generated ratios of the oxidised form (ethidium) excited at 530 nm

and measured using a 560-nm longpass filter versus the reduced form with excitation at 380 nm measured at 415–470 nm.

To investigate mPTP opening, we used a previously described assay⁶⁷. Briefly, cells were washed 2× with HBSS, and then incubated with 5 μM Fluo-4 AM and 25 nM TMRM in HBSS for 40 min at RT. Cells were then washed 2× in HBSS and 25 nM TMRM in HBSS was to cells again. They were then imaged using the 488 nm laser and 561 nm laser to excite Fluo-4 and TMRM, respectively. A time series was started with 10–20 s intervals over a course of 20 min. To overload cells with calcium to induce mPTP opening, ferutinin was added stepwise after every 2 min, building up the concentration of calcium in the neurons till mPTP opening. The mPTP opening threshold was measured at the point at which rapid loss of TMRM signal occurred, accompanied by a rapid increase in Fluo-4 signal after ferutinin application.

Fluorescent false neurotransmitter (FFN) live-cell DAT imaging

To measure the presence and activity of the DAT, we utilised the commercially available fluorescent DAT and VMAT2 substrate FFN102 (Abcam, ab120866). To measure the uptake of the FFN102 dye, a field of view was first found using the bright-field settings on a Zeiss LSM 880 confocal microscope. The cells then had 10 μM of the dye in HBSS added and a time series with an exposure every 5 s using the 405 nm laser was started, to measure uptake of the dye into the cells. As a control to confirm specificity, samples in a different well were pre-treated with 5 μM of the DAT inhibitor nomifensine (Sigma) for 10 min in HBSS. Nomifensine was kept in cell solution also after FFN102 was added. Once the dye had entered cells, the cells were depolarised by the addition of 50 mM KCl to observe FFN102 dynamics. Approximately 20 cells were measured per condition/sample and their rate of fluorescence intensity increase was plotted.

Sample preparation for single-molecule localisation microscopy

For single-molecule localisation microscopy (SMLM), neurons were grown on glass-coated ibidi chambers. Once neurons reached the desired age, they were washed once in PBS, followed by a 15 min fixation in 4% paraformaldehyde + 0.1% glutaraldehyde (both from Electron Microscopy Services) in PBS at RT. The neurons were then reduced in 0.1% sodium borohydride (Sigma) in PBS for 7 min at RT. Cells were then washed 2× in PBS.

To label cells with aptamer and phalloidin, after fixation and PBS washes, cells were permeabilised with 0.25% Triton X-100 in PBS for 10 min at RT. The cells were then blocked in blocking solution (0.1% Triton X-100, 10% normal goat serum (Abcam), 10% salmon sperm DNA (Thermo Fisher Scientific)) in PBS for 2 h at RT. The samples were then incubated with 100 nM of the aptamer (sequence: GCCTGTGGTGTGGGGCGGGTGCCTTATACATCTA) made up in the blocking solution at 4 °C overnight. After incubation, cells were washed 1× in PBS and incubated with phalloidin-647 (1:400) (Thermo Fisher Scientific) made up in the blocking solution for 1 h at RT. Cells were then washed 1× in PBS and either imaged or incubated with DAPI (1:10000) in PBS for 10 min at RT followed by 2× PBS washes before imaging.

To label aggregates in cell lysate, cells were lysed mechanically in PBS before being centrifuged at 3600×g for 5 min. The supernatant was collected and the protein concentration was quantified using the BCA Protein Assay Kit (Thermo Fisher Scientific). 22 × 40 mm, 1 mm thick glass slides, were cleaned with an argon plasma for 1 h, before 22 × 22 gaskets were affixed to the surface to create a well. The cell lysate was diluted 1 in 10 with filtered PBS (0.02 μm) and 100 nM aptamer (sequence: GCCTGTGGTGTGGGGCGGGTGCCTTACCACCACCACCACCA) and incubated on the surface for 10 min. The sample was then washed off with filtered PBS three times before imaging.

Single-molecule localisation microscopy

SMLM was performed on a Nanoimager super-resolution microscope (Oxford Nanoimaging Ltd) equipped with an Olympus 1.4 NA 100× oil immersion super apochromatic objective. To ensure efficient blinking for STORM (AF647-tagged phalloidin), the samples were incubated with a blinking induction buffer (B cubed, ONI). Separately to this, AD-PAINT was also employed which relies on the addition of an imaging strand (sequence: CCAGATGTAT-CY3B) to the buffer. 1 nM of the imaging strand was added to the B cubed buffer before imaging. The laser illumination angle was set to 51° for all imaging leading to total internal reflection fluorescence (TIRF). AF647-tagged phalloidin was first imaged for 4000–8000 frames using the 640 nm laser (80% power). After this, 4000–5000 frames at 30% power for the 561 nm laser was used to image and super-resolve the aptamer. Both were recorded at a frame rate of 50 ms. This was done for 2–3 fields of view per line and condition.

For imaging aggregates in neuronal lysate using AD-PAINT, 2 nM of the imaging strand (sequence: GGTTGGT-ATTO 655) was added. Images were acquired on Oxford Nanoimager at 20 frames s⁻¹, for 8000 frames (20% 635 nm laser power, TIRF).

Structured illumination microscopy (SIM) and instant SIM (iSIM)

Samples for SIM were cultured on glass-bottom ibidi 8-well chambers coated with laminin. They were fixed and immunolabelled for intracellular markers as described in the ICC section. SIM was performed on an Elyra PS.1 microscope (Zeiss), using a 40× oil objective (EC Plan-Neofluar 40×/1.30 Oil DIC M27). Images were acquired as 15 × 0.1 μm Z-planes on a pco.edge sCMOS camera, using 5 grid rotations with the 405 nm (23 μm grating period), the 488 nm (28 μm grating period) and the 561 nm (34 μm grating period) lasers. Images were processed and channels aligned using the automatic settings on the ZEN-Black software (Zeiss) (RRID:SCR_018163, <http://stmichaelshospitalresearch.ca/wp-content/uploads/2015/09/ZEN-Black-Quick-Guide.pdf>).

To perform iSIM, we used an array-scanning confocal super-resolution imaging system (VisiTech International). This consisted of an Olympus IX83 inverted microscope with an ASI motorised XY stage with piezo Z, and images were acquired with a Teledyne-Photometrics BSI Express scientific CMOS camera. All images were acquired using the 150×/1.45NA Apo TIRF objective (Olympus, UAPON150XOTIRF). We used solid-state laser lines: 405, 488, 561, 642 nm with a quad 405/488/561/640 Dichroic mirror (all from Chroma). Images were acquired using the Micro-Manager software and, on-the-fly deconvolution was done using the Mircovolution plugin for Micro-Manager v2.0 (RRID:SCR_000415, <http://micro-manager.org>).

Image analysis

ICC images, lysosomal dynamics, cell death and dynamic live-cell imaging were analysed using Fiji ImageJ. For fluorescent intensity readouts, including ICC images, a threshold value was set using control images. This was then used to measure fluorescent intensity, area, and integrated density readouts for all images in the dataset. For each experiment, values were normalised to the average of all the controls in the dataset. To measure puncta including lysosome size, a threshold value was determined using control lines and a mask was generated in order to generate readouts for intensity and area for each puncta in the field of view. These values were then normalised to the average of all control values.

To determine the positive number of TH and/or MAP2/B-III tubulin-positive cells, a nuclear mask was generated using DAPI/Hoechst 33342. This was then overlaid onto the image of interest and the fluorescent intensity readouts for each cell were recorded.

A positive cell was defined as being over the fluorescent intensity threshold based on negative cells for each marker.

Ratiometric images were generated using the image calculator. For all dynamic calcium experiments, including Fluo-4, Fura-2, ROS (Het), mPTP, FFN and dynamic TMRM experiments, the Fiji ImageJ plugin “Time Series Analyzer V3” was used. Here, ROIs were randomly selected for each field of view and the plugin was used to generate intensity readouts for each step of the time series. These values for the whole time series were then used to generate traces, and were normalised to the average of control values.

To calculate the mitochondrial footprint as a readout of the mitochondrial network, mDA neurons imaged with TMRM were used and put through the imageJ plugin “Mitochondrial Network Analysis—MiNA” as described⁶⁸, to generate mitochondrial footprint values which were normalised to control neurons.

All graphs and traces were plotted on Prism 8 (GraphPad) (RRID:SCR_002798, <http://www.graphpad.com/>).

SMLM analysis was performed using the Oxford Nanoimaging Ltd developed online software, CODI (<https://pages.oni.bio/codi-advanced-ev-characterisation-made-simple>). The super-resolved images are displayed as the output of all super-resolved single-molecule localisations from the entire frame acquisition. Once super-resolution images were uploaded to the software, initially an inbuilt drift correction was performed in order to correct single-molecule localisations in case the sample drifted in the x or y direction during acquisition. After the drift correction, the number of frames was changed to only include the frames where the relevant fluorophore was imaged. Each localisation was fitted to a 2D Gaussian distribution, and any of those with a standard deviation larger than 250 nm were removed. Finally, any localisations with a precision lower than 20 nm were discarded. Once the filtered super-resolved image was generated, density-based spatial clustering of applications with noise (DBSCAN) was performed on the resulting images. Each cluster in DBSCAN needed to have at least 15 localisations, and each localisation had to be within 60 nm of the other. This was to remove any non-specific aptamer binding, and to only detect aggregates that were quite spatially confined.

AD-PAINT images of cell lysate were analysed using the PeakFit plugin (an imageJ/Fiji plugin of the GDSC Single Molecule Light Microscopy package (http://www.sussex.ac.uk/gdsc/intranet/microscopy/imagej/gdsc_plugins) for imageJ using a ‘signal strength’ threshold of 30 and a precision threshold of 20 nm. The localisations were grouped into clusters using the DBSCAN algorithm in Python 3.8 (RRID:SCR_008394, <http://www.python.org/>) (sklearn v0.24.2 (RRID:SCR_019053, <https://scikit-learn.org/stable/modules/generated/sklearn.decomposition.NMF.html>)) using $\epsilon = 1$ pixels and a minimum points threshold of 60 to remove random localisations, which were counted to quantify the number of aggregates per area of coverslip imaged. The code has been deposited on the open-access repository Zenodo <https://doi.org/10.5281/zenodo.7123756>.

Statistical analysis

Statistical analysis was performed on Prism 8. To compare two individual groups, a unpaired, two-tailed *t* test was used to generate a *P* value. When comparing more than two individual groups, an ordinary one-way ANOVA was used with a post hoc Tukey test for multiple comparisons between groups. When comparing two individual variables, an ordinary two-way ANOVA was performed, with a correction of the False Discovery Rate or the Tukey’s range test for multiple comparisons between groups. A *P* value below 0.05 was considered to be statistically significant. Results are represented as means \pm standard error of the mean (SEM), or standard deviation (SD) where stated in the figure legends. The number of hiPSC lines, number of cells, and the number of neuronal inductions used for each experiment is stated in Supplementary Tables 5 and 6. A ‘*n*’ refers to either: the number of cells for single-cell analysis, or number of fields of view (FOV) for

field imaging analyses. A ‘*N*’ refers to either: the number of independent inductions (neuronal induction), or the number of independent hiPSC line (biological repeats). The sizes of the sample for each experiment was selected to ensure that the technical (number of cells, numbers of fields of view, and number of coverslips), and biological (number of hiPSC lines, and number of neuronal inductions) variation was adequately captured, and is listed in Supplementary Table 5.

Reporting summary

Further information on research design is available in the Nature Research Reporting Summary linked to this article.

DATA AVAILABILITY

The data that support the findings of this study are available on the open-access repository Zenodo <https://doi.org/10.5281/zenodo.7138359>. Single-cell RNA-seq raw data were deposited to NCBI Gene Expression Omnibus. The accession code for the data is: GSE213569 (<https://www.ncbi.nlm.nih.gov/geo/>). Mass spectrometry proteomic raw data and search engine output files were deposited to PRIDE ProteomeExchange⁶⁹ repository, and the data can be accessed using the identifier: PXD035500. The login details are, username: reviewer_pxd035500@ebi.ac.uk. Password: 6YwJLSE7. Protocols used in this study can be found on the repository Protocols.io, and the DOIs can be found in Supplementary Table 7.

CODE AVAILABILITY

The code used for all scRNA-seq and RNA velocity analysis has been deposited online: (<https://doi.org/10.5281/zenodo.7260558>), (https://github.com/strohstem/Transcriptomic_signatures_iPSC_derived_dopamine_neurons). The code used for AD-PAINT lysate cluster analysis has been deposited online: (<https://doi.org/10.5281/zenodo.7123756>).

Received: 16 March 2022; Accepted: 27 October 2022;

Published online: 24 November 2022

REFERENCES

- Poewe, W. et al. Parkinson disease. *Nat. Rev. Dis. Prim.* **3**, 17013 (2017).
- Kriks, S. et al. Dopamine neurons derived from human ES cells efficiently engraft in animal models of Parkinson’s disease. *Nature* **480**, 547–551 (2011).
- Kirkeby, A. et al. Generation of regionally specified neural progenitors and functional neurons from human embryonic stem cells under defined conditions. *Cell Rep.* **1**, 703–714 (2012).
- Nolbrant, S., Heuer, A., Parmar, M. & Kirkeby, A. Generation of high-purity human ventral midbrain dopaminergic progenitors for in vitro maturation and intracerebral transplantation. *Nat. Protoc.* **12**, 1962–1979 (2017).
- Doi, D. et al. Isolation of human induced pluripotent stem cell-derived dopaminergic progenitors by cell sorting for successful transplantation. *Stem Cell Rep.* **2**, 337–350 (2014).
- Chambers, S. M. et al. Highly efficient neural conversion of human ES and iPSC cells by dual inhibition of SMAD signaling. *Nat. Biotechnol.* **27**, 275–280 (2009).
- Hartfield, E. M. et al. Physiological characterisation of human iPSC-derived dopaminergic neurons. *PLoS One* **9**, e87388 (2014).
- Marton, R. M. & Ioannidis, J. P. A. A comprehensive analysis of protocols for deriving dopaminergic neurons from human pluripotent stem cells. *Stem Cells Transl. Med.* **8**, 366–374 (2019).
- Spillantini, M. G. et al. Alpha-synuclein in Lewy bodies. *Nature* **388**, 839–840 (1997).
- Farrer, M. et al. Comparison of kindreds with parkinsonism and alpha-synuclein genomic multiplications. *Ann. Neurol.* **55**, 174–179 (2004).
- Spira, P. J., Sharpe, D. M., Halliday, G., Cavanagh, J. & Nicholson, G. A. Clinical and pathological features of a Parkinsonian syndrome in a family with an Ala53Thr alpha-synuclein mutation. *Ann. Neurol.* **49**, 313–319 (2001).
- Singleton, A. B. et al. Alpha-synuclein locus triplication causes Parkinson’s disease. *Science* **302**, 841 (2003).
- Ludtmann, M. H. R. et al. α -synuclein oligomers interact with ATP synthase and open the permeability transition pore in Parkinson’s disease. *Nat. Commun.* **9**, 2293 (2018).
- Ryan, S. D. et al. Isogenic human iPSC Parkinson’s model shows nitrosative stress-induced dysfunction in MEF2-PGC1 α transcription. *Cell* **155**, 1351–1364 (2013).

15. Little, D. et al. A single cell high content assay detects mitochondrial dysfunction in iPSC-derived neurons with mutations in SNCA. *Sci. Rep.* **8**, 9033 (2018).
16. Chung, C. Y. et al. Identification and rescue of α -synuclein toxicity in Parkinson patient-derived neurons. *Science* **342**, 983–987 (2013).
17. Mazzulli, J. R., Zunke, F., Isacson, O., Studer, L. & Krainc, D. α -Synuclein-induced lysosomal dysfunction occurs through disruptions in protein trafficking in human midbrain synucleinopathy models. *Proc. Natl Acad. Sci. USA* **113**, 1931–1936 (2016).
18. Deas, E. et al. Alpha-synuclein oligomers interact with metal ions to induce oxidative stress and neuronal death in Parkinson's Disease. *Antioxid. Redox Signal.* **24**, 376–391 (2016).
19. Angelova, P. R. et al. Ca²⁺ is a key factor in α -synuclein-induced neurotoxicity. *J. Cell Sci.* **129**, 1792–1801 (2016).
20. Bergen, V., Lange, M., Peidli, S., Wolf, F. A. & Theis, F. J. Generalizing RNA velocity to transient cell states through dynamical modeling. *Nat. Biotechnol.* **38**, 1408–1414 (2020).
21. La Manno, G. et al. RNA velocity of single cells. *Nature* **560**, 494–498 (2018).
22. Anney, R. J. L. et al. Gene-ontology enrichment analysis in two independent family-based samples highlights biologically plausible processes for autism spectrum disorders. *Eur. J. Hum. Genet.* **19**, 1082–1089 (2011).
23. Guzman, J. N., Sánchez-Padilla, J., Chan, C. S. & Surmeier, D. J. Robust pacemaking in substantia nigra dopaminergic neurons. *J. Neurosci.* **29**, 11011–11019 (2009).
24. Rodriguez, P. C. et al. Fluorescent dopamine tracer resolves individual dopaminergic synapses and their activity in the brain. *Proc. Natl Acad. Sci. USA* **110**, 870–875 (2013).
25. Arenas, E., Denham, M. & Villaescusa, J. C. How to make a midbrain dopaminergic neuron. *Development* **142**, 1918–1936 (2015).
26. Choi, M. L. & Gandhi, S. Crucial role of protein oligomerization in the pathogenesis of Alzheimer's and Parkinson's diseases. *FEBS J.* **285**, 3631–3644 (2018).
27. Cremades, N. et al. Direct observation of the interconversion of normal and toxic forms of α -synuclein. *Cell* **149**, 1048–1059 (2012).
28. Whiten, D. R. et al. Nanoscopic characterisation of individual endogenous protein aggregates in human neuronal cells. *ChemBiochem* **19**, 2033–2038 (2018).
29. Esteras, N. & Abramov, A. Y. Mitochondrial calcium deregulation in the mechanism of beta-amyloid and tau pathology. *Cells* **9**, 2135 (2020).
30. Angelova, P. R. et al. Alpha synuclein aggregation drives ferroptosis: an interplay of iron, calcium and lipid peroxidation. *Cell Death Differ.* **27**, 2781–2796 (2020).
31. Fujiwara, H. et al. alpha-Synuclein is phosphorylated in synucleinopathy lesions. *Nat. Cell Biol.* **4**, 160–164 (2002).
32. Kopach, O., Esteras, N., Wray, S., Rusakov, D. A. & Abramov, A. Y. Maturation and phenotype of pathophysiological neuronal excitability of human cells in tau-related dementia. *J. Cell Sci.* **133**, jcs241687 (2020).
33. Kopach, O., Esteras, N., Wray, S., Abramov, A. Y. & Rusakov, D. A. Genetically engineered MAPT 10+16 mutation causes pathophysiological excitability of human iPSC-derived neurons related to 4R tau-induced dementia. *Cell Death Dis.* **12**, 716 (2021).
34. Kirkeby, A. et al. Predictive markers guide differentiation to improve graft outcome in clinical translation of hESC-based therapy for Parkinson's disease. *Cell Stem Cell* **20**, 135–148 (2017).
35. Kee, N. et al. Single-cell analysis reveals a close relationship between differentiating dopamine and subthalamic nucleus neuronal lineages. *Cell Stem Cell* **20**, 29–40 (2017).
36. Wolf, F. A. et al. PAGA: graph abstraction reconciles clustering with trajectory inference through a topology preserving map of single cells. *Genome Biol.* **20**, 59 (2019).
37. Ásgrímsdóttir, E. S. & Arenas, E. Midbrain dopaminergic neuron development at the single cell level: in vivo and in stem cells. *Front. Cell Dev. Biol.* **8**, 463 (2020).
38. Wang, Q. et al. The landscape of multiscale transcriptomic networks and key regulators in Parkinson's disease. *Nat. Commun.* **10**, 5234 (2019).
39. Conway, K. A., Harper, J. D. & Lansbury, P. T. Accelerated in vitro fibril formation by a mutant alpha-synuclein linked to early-onset Parkinson disease. *Nat. Med.* **4**, 1318–1320 (1998).
40. Zambon, F. et al. Cellular α -synuclein pathology is associated with bioenergetic dysfunction in Parkinson's iPSC-derived dopamine neurons. *Hum. Mol. Genet.* **28**, 2001–2013 (2019).
41. Hughes, C. D. et al. Picomolar concentrations of oligomeric alpha-synuclein sensitizes TLR4 to play an initiating role in Parkinson's disease pathogenesis. *Acta Neuropathol.* **137**, 103–120 (2019).
42. Iljina, M. et al. Kinetic model of the aggregation of alpha-synuclein provides insights into prion-like spreading. *Proc. Natl Acad. Sci. USA* **113**, E1206–E1215 (2016).
43. Iljina, M. et al. Arachidonic acid mediates the formation of abundant alpha-helical multimers of alpha-synuclein. *Sci. Rep.* **6**, 33928 (2016).
44. Fusco, G. et al. Structural basis of membrane disruption and cellular toxicity by α -synuclein oligomers. *Science* **358**, 1440–1443 (2017).
45. Högen, T. et al. Two different binding modes of α -synuclein to lipid vesicles depending on its aggregation state. *Biophys. J.* **102**, 1646–1655 (2012).
46. Ferreira, D. G. et al. α -Synuclein interacts with PrPC to induce cognitive impairment through mGluR5 and NMDAR2B. *Nat. Neurosci.* **20**, 1569–1579 (2017).
47. Betzer, C. et al. Alpha-synuclein aggregates activate calcium pump SERCA leading to calcium dysregulation. *EMBO Rep.* **19**, e44617 (2018).
48. Guzman, J. N. et al. Oxidant stress evoked by pacemaking in dopaminergic neurons is attenuated by DJ-1. *Nature* **468**, 696–700 (2010).
49. Mahul-Mellier, A.-L. et al. The process of Lewy body formation, rather than simply α -synuclein fibrillization, is one of the major drivers of neurodegeneration. *Proc. Natl Acad. Sci. USA* **117**, 4971–4982 (2020).
50. Luth, E. S., Stavrovskaya, I. G., Bartels, T., Kristal, B. S. & Selkoe, D. J. Soluble, prefibrillar α -synuclein oligomers promote complex I-dependent, Ca²⁺-induced mitochondrial dysfunction. *J. Biol. Chem.* **289**, 21490–21507 (2014).
51. Bonam, S. R., Wang, F. & Muller, S. Lysosomes as a therapeutic target. *Nat. Rev. Drug Discov.* **18**, 923–948 (2019).
52. Ryan, T. et al. Cardiolipin exposure on the outer mitochondrial membrane modulates α -synuclein. *Nat. Commun.* **9**, 817 (2018).
53. Chen, Y. et al. Engineering synucleinopathy-resistant human dopaminergic neurons by CRISPR-mediated deletion of the SNCA gene. *Eur. J. Neurosci.* **49**, 510–524 (2019).
54. Butler, A., Hoffman, P., Smibert, P., Papalexis, E. & Satija, R. Integrating single-cell transcriptomic data across different conditions, technologies, and species. *Nat. Biotechnol.* **36**, 411–420 (2018).
55. Stuart, T. et al. Comprehensive integration of single-cell data. *Cell* **177**, 1888–1902.e21 (2019).
56. Zappia, L. & Oshlack, A. Clustering trees: a visualization for evaluating clusterings at multiple resolutions. *Gigascience* **7**, gjy083 (2018).
57. McGinnis, C. S., Murrow, L. M. & Gartner, Z. J. DoubletFinder: doublet detection in single-cell RNA sequencing data using artificial nearest neighbors. *Cell Syst.* **8**, 329–337.e4 (2019).
58. Srivastava, A., Malik, L., Smith, T., Sudbery, I. & Patro, R. Alevin efficiently estimates accurate gene abundances from dscRNA-seq data. *Genome Biol.* **20**, 65 (2019).
59. Soneson, C., Srivastava, A., Patro, R. & Stadler, M. B. Preprocessing choices affect RNA velocity results for droplet scRNA-seq data. *PLoS Comput. Biol.* **17**, e1008585 (2021).
60. Turaç, G. et al. Combined flow cytometric analysis of surface and intracellular antigens reveals surface molecule markers of human neurogenesis. *PLoS ONE* **8**, e68519 (2013).
61. Nirujogi, R. S. et al. Development of a multiplexed targeted mass spectrometry assay for LRRK2-phosphorylated Rabs and Ser910/Ser935 biomarker sites. *Biochem. J.* **478**, 299–326 (2021).
62. Bruderer, R. et al. Extending the limits of quantitative proteome profiling with data-independent acquisition and application to acetaminophen-treated three-dimensional liver microtissues. *Mol. Cell Proteom.* **14**, 1400–1410 (2015).
63. Tyanova, S. et al. The Perseus computational platform for comprehensive analysis of (pro)teomics data. *Nat. Methods* **13**, 731–740 (2016).
64. Wiśniewski, J. R., Hein, M. Y., Cox, J. & Mann, M. A “proteomic ruler” for protein copy number and concentration estimation without spike-in standards. *Mol. Cell Proteom.* **13**, 3497–3506 (2014).
65. de la Fuente, C., Burke, D. G., Eaton, S. & Heales, S. J. R. Inhibition of neuronal mitochondrial complex I or lysosomal glucocerebrosidase is associated with increased dopamine and serotonin turnover. *Neurochem. Int.* **109**, 94–100 (2017).
66. Edelstein, A. D. et al. Advanced methods of microscope control using μ Manager software. *J. Biol. Methods* **1**, (2014).
67. Gandhi, S. et al. PINK1-associated Parkinson's disease is caused by neuronal vulnerability to calcium-induced cell death. *Mol. Cell* **33**, 627–638 (2009).
68. Valente, A. J., Maddalena, L. A., Robb, E. L., Moradi, F. & Stuart, J. A. A simple ImageJ macro tool for analyzing mitochondrial network morphology in mammalian cell culture. *Acta Histochem.* **119**, 315–326 (2017).
69. Deutsch, E. W. et al. The ProteomeXchange consortium in 2020: enabling “big data” approaches in proteomics. *Nucleic Acids Res.* **48**, D1145–D1152 (2020).

ACKNOWLEDGEMENTS

We would wish to thank the patients for the fibroblast donation. We would also like to thank the Francis Crick Institute Flow Cytometry, Advanced Light Microscopy, Advanced Sequencing, and Bioinformatics and Biostatistics STPs for their help and equipment in conducting and analysing the flow cytometry, fluorescence microscopy, and single-cell RNA-seq experiments. This research was funded in whole or in part by Aligning Science Across Parkinson's [ASAP-000509 and ASAP-000463] through the Michael J. Fox Foundation for Parkinson's Research (MJFF). For the purpose of open-access, the author has applied a CC public copyright license to all Author Accepted Manuscripts arising from this submission. G.S.V. acknowledges funding from the UCL-Birkbeck MRC DTP. S.G. acknowledges funding from the i2i

grant (The Francis Crick Institute), MJFox foundation, the Wellcome Trust, and is an MRC Senior Clinical Fellow [MR/T008199/1]. D.A. is funded by the National Institute for Health Research. R.P. holds an MRC Senior Clinical Fellowship [MR/S006591/1] and a Lister Research Prize Fellowship. H.A. acknowledges funding from the Kuwait University, Kuwait. M.H. acknowledges funding from UCB Biopharma, and Dr. Jim Love. N.P. acknowledges funding from Medical Research Scotland [PHD-50193–2020]. This work is supported by the Francis Crick Institute which receives funding from the UK Medical Research Council, Cancer Research UK, and the Wellcome Trust. Research at UCL Great Ormond Street Institute of Child Health benefits from funding from the NIHR Biomedical Research Centre at Great Ormond Street Hospital.

AUTHOR CONTRIBUTIONS

Conceptualisation: G.S.V., R.P. and S.G.; methodology: S.G., R.P., M.H.H. and A.Y.A.; investigation: G.S.V., M.L.C., J.R.E., Z.Y., A.I.W., N.P.H., C.L., R.S.S., D.M., J.P.L. and P.R.A. RNA-seq: S.S.; proteomics: R.S.N., and D.R.A.; HPLC: H.A., S.E. and S.H.; electrophysiology: O.K., S.S. and D.A.R.; resources: T.K.; writing—original draft: G.S.V.; writing—review & editing: S.G., R.P. and D.A.; funding acquisition: S.G.

FUNDING

Open Access funding provided by The Francis Crick Institute.

COMPETING INTERESTS

The authors declare no competing interests.

ADDITIONAL INFORMATION

Supplementary information The online version contains supplementary material available at <https://doi.org/10.1038/s41531-022-00423-7>.

Correspondence and requests for materials should be addressed to Rickie Patani or Sonia Gandhi.

Reprints and permission information is available at <http://www.nature.com/reprints>

Publisher's note Springer Nature remains neutral with regard to jurisdictional claims in published maps and institutional affiliations.



Open Access This article is licensed under a Creative Commons Attribution 4.0 International License, which permits use, sharing, adaptation, distribution and reproduction in any medium or format, as long as you give appropriate credit to the original author(s) and the source, provide a link to the Creative Commons license, and indicate if changes were made. The images or other third party material in this article are included in the article's Creative Commons license, unless indicated otherwise in a credit line to the material. If material is not included in the article's Creative Commons license and your intended use is not permitted by statutory regulation or exceeds the permitted use, you will need to obtain permission directly from the copyright holder. To view a copy of this license, visit <http://creativecommons.org/licenses/by/4.0/>.

© The Author(s) 2022